# Influence of the presence of solutes on the structural and dynamical properties of lipid membranes and water

*By*

**Upayan Baul**

**PHYS10201104006**

**The Institute of Mathematical Sciences, Chennai**

*A thesis submitted to the*

*Board of Studies in Physical Sciences*

*In partial fulfillment of requirements*

*for the Degree of*

**DOCTOR OF PHILOSOPHY**

*of*

**HOMI BHABHA NATIONAL INSTITUTE**

**June, 2016**

# Homi Bhabha National Institute

## Recommendations of the Viva Voce Board

As members of the Viva Voce Board, we certify that we have read the dissertation prepared by Upayan Baul entitled "Influence of the presence of solutes on the structural and dynamical properties of lipid membranes and water" and recommend that it maybe accepted as fulfilling the dissertation requirement for the Degree of Doctor of Philosophy.

_____ Date:

Chair - Ghanashyam Date

_____ Date:

Guide/Convener - Satyavani Vemparala

_____ Date:

Member 1 - Gautam I. Menon

_____ Date:

Member 2 - Rajesh Ravindran

_____ Date:

External Examiner - R. Sankararamakrishnan

Final approval and acceptance of this dissertation is contingent upon the candidate's submission of the final copies of the dissertation to HBNI.

I hereby certify that I have read this dissertation prepared under my direction and recommend that it may be accepted as fulfilling the dissertation requirement.

**Date:**

**Place:** Guide

# STATEMENT BY AUTHOR

This dissertation has been submitted in partial fulfillment of requirements for an advanced degree at Homi Bhabha National Institute (HBNI) and is deposited in the Library to be made available to borrowers under rules of the HBNI.

Brief quotations from this dissertation are allowable without special permission, provided that accurate acknowledgement of source is made. Requests for permission for extended quotation from or reproduction of this manuscript in whole or in part may be granted by the Competent Authority of HBNI when in his or her judgement the proposed use of the material is in the interests of scholarship. In all other instances, however, permission must be obtained from the author.

Upayan Baul

# DECLARATION

I, hereby declare that the investigation presented in the thesis has been carried out by me. The work is original and has not been submitted earlier as a whole or in part for a degree / diploma at this or any other Institution / University.

Upayan Baul

# List of publications arising from the thesis

- **Journal**

  1. **Interaction of multiple biomimetic antimicrobial polymers with model bacterial membranes**

     Upayan Baul, Kenichi Kuroda and Satyavani Vemparala

     *The Journal of Chemical Physics* **2014**, 141, 084902

  2. **Ion hydration and associated defects in hydrogen bond network of water: Observation of reorientationally slow water molecules beyond first hydration shell in aqueous solutions of MgCl$_2$.**

     Upayan Baul and Satyavani Vemparala

     *Phys. Rev. E* **2015**, 91, 012114

  3. **Effect of simple solutes on the long range dipolar correlations in liquid water.**

     Upayan Baul, J. Maruthi Pradeep Kanth, Ramesh Anishetty and Satyavani Vemparala

     *The Journal of Chemical Physics* **2016**, 144, 104502

  4. **Isosteric substitution in cationic-amphiphilic polymers reveals an important role for hydrogen bonding in bacterial membrane interactions.**

     Divakara S. S. M. Uppu, Mohini M. Konai, Upayan Baul, Priyank Singh, Tjalling K. Siersma, Sandip Samaddar, Satyavani Vemparala, Leendert W. Hamoen, Chandrabhas Narayana and Jayanta Haldar

     *Chemical Science* **2016**, 7, 4613

# Chapter in Book

1. [‡]**Membrane-Bound Conformations of Antimicrobial Agents and Their Modes of Action.**

Upayan Baul and Satyavani Vemparala

---

[‡]Not included in thesis

# List of conferences attended

1. **Fracture & Flow in Porous Media**

   Institute of Mathematical Sciences, Chennai, India, January, 2012

2. **Indo-US Symposium on Structure, Dynamics and Mechanics of Biological Membranes**

   Indian Institute of Science, Bangalore, Bangalore, India, December, 2012

3. **Bayes by the Bay - A Pedagogical Workshop on Bayesian Methods in Science**

   Pondicherry, India, January, 2013

4. **Current Trends in Biochemical and Biophysical Modelling**

   S.N. Bose National Centre for Basic Sciences, Kolkata, India, October 2013

5. **MD@50**

   Jawaharlal Nehru Centre for Advanced Scientific Research, Bangalore, India, August 2014

6. **Discussion Meeting on Water and Aqueous Solutions**

   Jawaharlal Nehru Centre for Advanced Scientific Research, Bangalore, India, January 2015

7. **APS March Meeting 2016**

   Baltimore, Maryland, United States of America, March 2016

*Dedications*

*This thesis is dedicated to*
*My Parents*


*Utpal Kr. Baul and Nipunika Baul*

# ACKNOWLEDGEMENTS

# Abstract

In this thesis, titled *Influence of the presence of solutes on the structural and dynamical properties of lipid membranes and water*, we report classical all-atom molecular dynamics (MD) simulation studies of two biological solvents, namely- phospholipid bilayers and water, and their interactions with flexible, amphiphilic, polycationic antimicrobial polymers and dissolved salts (ions) respectively.

For methacrylate polymers characterized by backbone amphiphilicity, we study the interactions of polymer aggregates with multiple model lipid membranes which include models for both mammalian and microbial membranes. We conclusively show that the polymers impact the structural properties of the microbial membrane models, with minimal effect on a mammalian one. For a model of *E. Coli* membrane, we suggest a mode of antimicrobial activity through polymer induced demixing of lipid species, and associated phase boundary defects. We also report that the flexible methacrylate polymers with no built-in facial amphiphilicity are capable of acquiring facial amphiphilicity in their membrane partitioned phase. For side-chain amphiphilic polymers, in collaboration with experiments, we show that the hydrogen bonding ability of polymers can impact their antimicrobial activity.

Our studies reveal the effect of both monovalent and divalent cations on the long-range dipolar orientational correlations in liquid water. Based on the observations, the ambiguous classification of ions as structure makers and breakers is challenged. The importance of the results is discussed in the context of hydrophobic aggregation. Finally, using a new selection criteria for water molecules, we show that strongly solvated ions such as $Mg^{2+}$ can induce reorientational slowing of water molecules beyond the first ion solvation shells. The slow water molecules are further shown to be de-localized. The results explain the contrasting observations from a class of experiments (FS-IR) and prior numerical simulations.

# Contents

# Synopsis

Fluid media such as cell membranes and water provide natural environments for diverse processes of biological and chemical relevance. Rich in their innate properties, they provide a solvating environment for solutes, ranging from proteins and macromolecules to dissolved ions. These solvent-solute interactions not only drive the conformations and conformational dynamics of the solute molecules, but also potentially have the ability to modulate the structural and dynamical properties of the solvents themselves. The response of solvents to the presence of solutes can be broadly classified into short-range (local) and long-range (global) effects. Short-range effects can be of extreme relevance, for example, in driving the stability of functionally viable biomolecular conformations. The presence of long-range effects, however, can impact processes involving a wider range of time scales, and spatial range of interactions that are considerably larger than molecular dimensions. Study of several such biologically relevant processes thus requires the understanding of the properties of solvents in molecular resolution, as well as changes in the same owing to their interactions with solute molecules.

In this synopsis, we report classical all-atom molecular dynamics (MD) simulation studies of two such biological solvents, namely- phospholipid bilayers and water, and their interactions with relevant solute molecules. We have studied the interactions of multiple flexible, amphiphilic polymers with model lipid bilayer patches. These polymers fall under the general class of membrane active polymers, and in particular antimicrobial polymers (AMPoly). They have the ability to interact with and disrupt / destabilize bacterial membranes. Accordingly, the lipid compositions of the bilayer patches have been chosen to mimic bacterial lipid bilayers. For liquid water, the solutes of interest are simple salts such as NaCl, KCl, CsCl and $MgCl_2$.

**Interactions of polymers with model lipid bilayers**

Lipid bilayers are formed by self-assembly of two layers of lipid molecules. The hydrophilic head groups of each layer remain exposed to hydrating water, and the lipid tails comprise the bilayers' hydrophobic core. Mammalian lipid bilayers have predominantly zwitterionic lipids in their outer leaflets, while bacterial bilayers have both zwitterionic and anionic lipids [1]. Further, in bacterial lipid bilayers, there is a greater abundance of zwitterionic lipids with spontaneous negative curvature (PE (phosphatidylethanolamine) head groups over PC (phosphatidylcholine)). As models for bacterial membrane patches, we have studied three lipid bilayers, abbreviated in the following as doPE-PG, poPE-PG and dpPE-PG. Lipids comprising them differ among one another through degree of (un)saturation of lipid tails. doPE-PG bilayer comprises of DOPE and DOPG lipids, with mono-unsaturations in all lipid tails. Each POPE and POPG lipid, comprising poPE-PG lipid bilayer, has a saturated and a mono-unsaturated lipid tail. All lipid tails of dpPE-PG lipid bilayer (DPPE and DPPG lipids) are saturated. We have studied doPC-PG lipid bilayer (DOPC and DOPG lipids) as a model for a mammalian lipid bilayer patch, but with similar electrostatics as its bacterial equivalent doPE-PG.
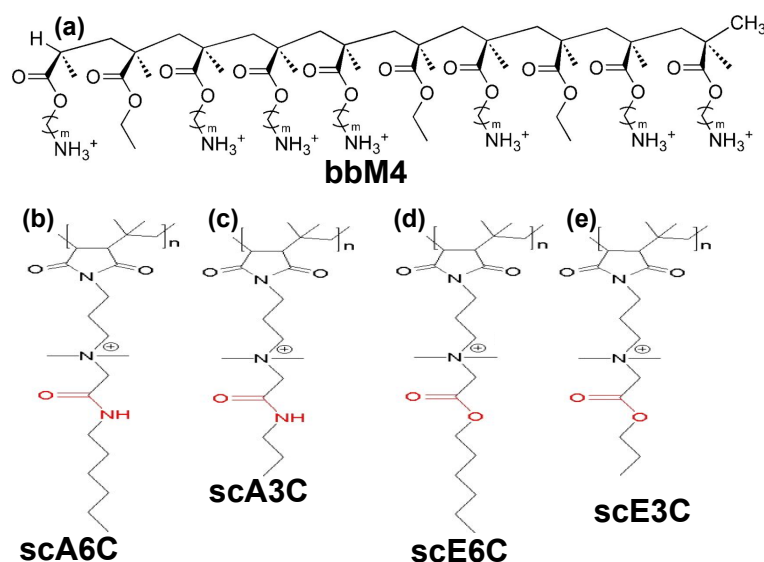


Figure 1: Chemical structures of the AMPoly studied. (a) Backbone (bb-) amphiphilicity, in which cationic and hydrophobic side chains are randomly distributed along polymer backbone. (b-e) Side chain (sc-) amphiphilicity, in which cationic and hydrophobic moieties are distributed along individual side chains.

AMPoly are characterized by the presence of both cationic and hydrophobic moieties. The chemical structures of the various AMPoly studied by us, along with the abbreviations used for them are shown in Figure 1. Polymer bbM4, with 4 carbon long spacer arms (m=4 in Figure 1(a)), belongs to a class of flexible AMPoly with methacrylate backbones. In them, cationic and hydrophobic side arms are distributed randomly along the polymer backbone. Prior MD simulation studies have reported the interactions of a single bbM4 polymer with poPE-PG model lipid bilayers [2]. In this synopsis, the co-operative interactions of multiple bbM4 polymers with model lipid bilayers is reported. Polymers scA6C, scA3C, scE6C and scE3C (Figure 1(b-e)), are characterized by side chain (SC) amphiphilicity. They are formed by identical monomers (alternating N-alkylmaleimide and isobutylene), in which charged and hydrophobic moieties are distributed to distinct regions in the side arms. The four polymers are equivalent in their electrostatic interactions, but differ in hydrophobic content. scA6C and scE6C have longer (6 carbon) hydrophobic side chain extensions compared to scA3C and scE3C (3 carbon). Further, scA3C and scA6C have amide functionality, while scE3C and scE6C have ester functional groups. The scA3C and scA6C AMPoly thus have greater ability to form hydrogen bonds with lipid molecules compared to their ester counterparts.

In aqueous environment, prior to their adsorption onto lipid bilayers, AMPoly can form aggregates. The aggregation behavior depends on polymer specific interactions with aqueous solutions. The stability of an AMPoly aggregate, when adsorbed onto a lipid bilayer leaflet is dependent upon the polymer - polymer, and polymer - lipid noncovalent interactions. Owing to favorable electrostatic interactions with anionic lipid head groups, the AMPoly can selectively recognize and adsorb onto bacterial bilayers over mammalian ones. While recognition is mediated by charged constituents, the energetically unfavorable exposure of hydrophobic moieties to water drives the partitioning of AMPoly into the lipid bilayers [1]. The ability to take up extended conformations at the bilayer interface is known to assist in the partitioning of membrane active molecules [2].

The conformations of partitioned polymers, as well as their influence on bilayer properties, depend upon a complex set of noncovalent interactions. These interactions not only involve the lipid and polymer molecules, but also interfacial water molecules and ions. Natural membrane active molecules, such as antimicrobial and cell penetrating peptides are capable of adopting facially amphiphilic (FA) conformations upon partitioning. In a FA conformation, the hydrophilic and hydrophobic moieties of an amphiphilic molecule are preferentially segregated to two sides of a secondary structure backbone, such as $\alpha$-helix or $\beta$-sheet [3]. For AMPoly with no *a-priori* secondary structure built into them, the ability to take up FA conformations in the membrane partitioned state is recognized as an essential criterion for antimicrobial action. Almost all effective AMPoly are envisaged to destabilize / disrupt bacterial lipid bilayers. The influence of the presence of partitioned AMPoly on the structural and organizational properties of lipid bilayers is thus of great interest.

We have studied the interactions of multiple (four) bbM4 AMPoly with model doPE-PG, poPE-PG, dpPE-PG and doPC-PG lipid bilayer patches. The bbM4 polymers were observed to form micellar aggregates in an aqueous environment with 0.15M sodium chloride. The initial configurations for the simulations were thus constructed by placing an aggregate of four bbM4 polymers close to the equilibrated lipid bilayer patches. The SC amphiphilic polymers were studied with poPE-PG lipid bilayer patches. No aggregation behavior was observed for the SC amphiphilic polymers in aqueous environments. Thus, the initial conformation for each SC polymer - model lipid bilayer simulation was constructed by dispersing 4 identical polymers close to an equilibrated poPE-PG bilayer patch. Important observations from the studies are summarized below.

- *Phased release of bbM4 AMPoly* : The bbM4 AMPoly were observed to be released from the micellar aggregates in a phased manner, when the bbM4 - bilayer nonbonded interactions became more favorable compared to bbM4 - aggregate nonbonded interactions. The phased release of polymers has also been observed to be
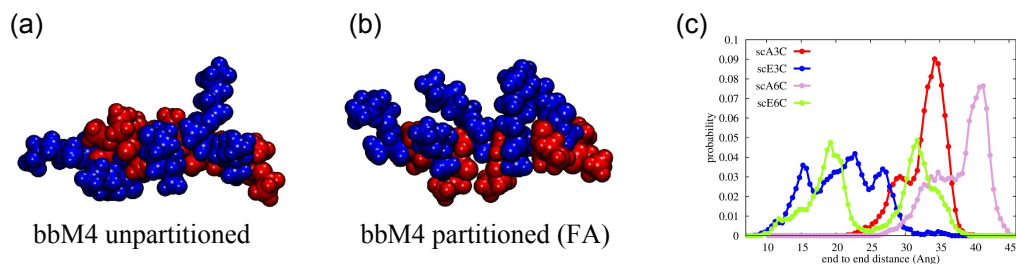
Figure 2: Representative conformations of a bbM4 polymer prior to (a) and after (b) membrane partition. In (b), the cationic (blue) and hydrophobic (red) side chains are segregated to two sides about the polymer backbone,- thus evidence of FA. (c) End to end distance distributions of the side chain amphiphilic polymers in their membrane bound states.

facilitated by the presence of PE- lipids with small head groups, and hence spontaneous negative curvature. This is in good agreement with the relative abundance of interfacial lipid-packing defects in the respective bilayers. Lipid-packing defect sites are regions at the bilayer-water interface, where hydrophobic bilayer constituents are transiently exposed to water. It has been suggested that membrane - active molecules are intrinsically capable of detecting and binding to such defects [4, 5].

- *Conformations of AMPoly* : AMPoly reported in this synopsis are flexible molecules with no built-in secondary structure. They have been observed to be unstructured in aqueous environments and at the bilayer - water interface prior to partition. However, upon partitioning into lipid bilayers, the bbM4 polymers have shown the ability to adopt FA conformations, as shown in Figure 2(a,b). Facial amphiphilicity for bbM4 polymers has also been observed to be facilitated by the presence of PE-lipid molecules. For bbM4 polymers partitioned into the doPC-PG lipid bilayer, the FA conformations have been less robust. For the AMPoly with SC amphiphilicity, our simulated times have been insufficient to identify the fully partitioned polymer conformations. However, the membrane bound conformations of the four SC amphiphilic polymers reported have been observed to differ with varying nature of functional groups (amide vs. ester), and varying length of hydrophobic end-group moieties. Amide polymers (scA3C, scA6C) were observed to take up more

extended conformations compared to their ester counterparts (scE3C, scE6C). Increasing the hydrophobicity (6C over 3C) is also observed to facilitate the adoption of extended conformations (Figure 2(c)).
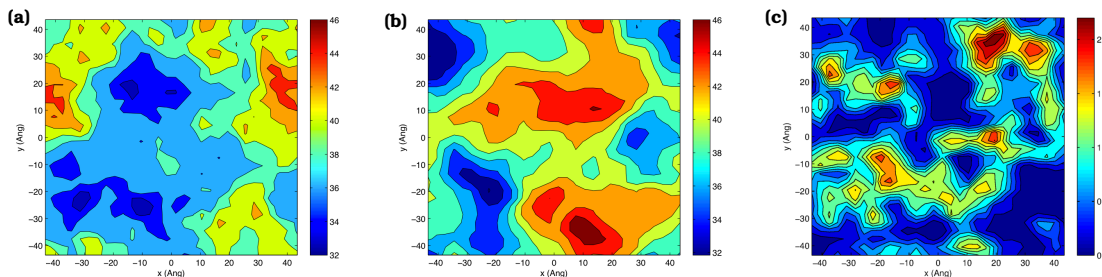


Figure 3: Local bilayer thickness profiles for (a) control poPE-PG and (b) bbM4 - poPE-PG systems. (c) Lateral (2D) number density profile for POPG lipids in the proximal leaflet for the bbM4 - poPE-PG system.

- *Lateral reorganization of bilayer leaflets* : When partitioned into model lipid bilayers with saturated lipid tails (poPE-PG and dpPE-PG), the bbM4 polymers have shown the ability to induce lateral reorganization and demixing of the lipid species. Owing to preferentially favorable interactions, the bbM4 polymers have been observed to sequester the PG- lipids in the respective bilayers, leading to the onset of coarsening. Such coarsening of the leaflets have been observed to induce considerable lateral inhomogeneity in bilayer properties, such as local bilayer thickness profiles (Figure 3). The observed changes in local thickness profiles with the presence of bbM4 polymers have been in good agreement with changes in lipid tail order parameters, such as deuterium order parameter ($S_{cd}$), tilt and splay angles. For multicomponent lipid bilayers, the induced phase demixing of lipid species', and associated phase boundary defects is a well known mode of bilayer destabilization. Such phase boundary defects include thickness, curvature and lipid packing order mismatches. Demixed bilayers are also susceptible to leakage of polar materials at the phase boundaries, as well as increased leakage of liposomes [6]. No such lateral inhomogeneities in bilayer thickness profiles have been observed with the bbM4 - doPE-PG and bbM4 - doPC-PG interactions. In a doPC-PG lipid bi-

6

layer, the bbM4 polymers maintain a passive presence, with no appreciable effect on bilayer properties. The scA3C and scA6C AMPoly have been observed to efficiently sequester the anionic POPG lipids, unlike their ester counterparts (scE3C, scE6C). All the SC amphiphilic polymers reported have equivalent electrostatic interactions with poPE-PG bilayer lipids. However, amide polymers have greater ability to form hydrogen bonds with the bilayer lipids. In the MD simulations, they have been observed to have strong hydrogen bonding interactions with POPG lipid molecules. Experimental results have indicated that the polymers with amide functionality have greater antimicrobial potency compared to their ester counterparts. These results emphasize that hydrogen bonding interactions can have a strong influence on the interactions of AMPoly with lipid bilayers.

**Influence of dissolved solutes on the properties of liquid water**

Liquid water is characterized by intricate and non-trivial structural and dynamical properties at the molecular resolution. The complexity can be attributed to the ability of water molecules to form an extensively connected network of hydrogen bonds, in which the four nearest neighbors of a water molecule arrange themselves in a nearly tetrahedral geometry [7]. This local structuring, in addition to the generally observed short-range structure in liquids, owing to excluded volume effects, has led to consensus in treating water as a highly structured liquid [8]. However, the definition of such structure is not without ambiguity [9, 10]. Pair distribution functions (PDFs) among atomic constituents have suggested that the structure of liquid water is short-range and the spatial distribution of water molecules are uncorrelated beyond a distance of $\sim(8$ - $10)\mathring{A}$ [10]. Effects of simple solutes, such as dissolved ions, on the structural properties of water have also conventionally been probed through their influence on PDFs, and other properties associated with positional correlations [7, 10]. Yet, PDFs yield a measure for density fluctuations alone and are devoid of information on orientational correlation, especially at longer separations. The mutual orientations of water molecules separated in space can be envisaged

through correlations involving the dipolar degree of freedom of water molecules. Compared to PDFs, the dipolar correlations have been observed to be considerably longer ranged [11, 12]. Study of the influence of simple ionic, as well as non-polar solutes on such correlations, provides a measure for a likely long-range structural response.

Structural correlations among water molecules, whose oxygen atoms are situated at $\mathbf{r_1}$ and $\mathbf{r_2}$, involving the dipolar degree of freedom can be defined as

$$\langle \hat{\mu}^i(\mathbf{r_1})\hat{\mu}^j(\mathbf{r_2}) \rangle \; = \; \frac{1}{2}\left( \delta^{ij} - \frac{r^i r^j}{r^2} \right) t(r) - \frac{1}{2}\left( \delta^{ij} - 3\frac{r^i r^j}{r^2} \right) l(r) \tag{1}$$

where $\hat{\mu}$ denotes the normalized dipole vector of a water molecule, indices $i, j$ denote directions in three-dimensional space, $\mathbf{r} = (\mathbf{r_1} - \mathbf{r_2})$, $r = |\mathbf{r}|$ and the angular brackets denote ensemble averages. The decomposed scalar functions $t(r)$ and $l(r)$, defined as

$$t(r) \;=\; \langle \hat{\mu}(\mathbf{r_1}).\hat{\mu}(\mathbf{r_2}) \rangle \tag{2}$$

$$l(r) \;=\; \langle \hat{\mu}(\mathbf{r_1}).\hat{\mathbf{r}}\,\hat{\mu}(\mathbf{r_2}).\hat{\mathbf{r}} \rangle \tag{3}$$

describe respectively the trace and longitudinal (traceless) parts of the tensorial correlations $\langle \hat{\mu}^i(\mathbf{r_1})\hat{\mu}^j(\mathbf{r_2}) \rangle$. Physically, $t(r)$ and $l(r)$ are measures for the statistical alignment of water dipole vectors spaced $r$ distance apart with respect to themselves and with respect to the radial vector separating them respectively. Both correlations show oscillatory solvation structure and are long-ranged compared to density correlations in water. $t(r)$ vanishes beyond $\sim 14\mathring{A}$ for solute free water. $l(r)$, oscillatory in nature and always positive, can be non-vanishing even at $\sim 75\mathring{A}$ separations, and decays exponentially beyond solvation region ($14\mathring{A}$) with largest correlation length of $\sim 24\mathring{A}$ [11].

The highly connected network of hydrogen bonds in liquid water is also extremely dynamic. It undergoes fluctuations at the picosecond timescale owing to incessant reorientational motions of water molecules [13]. A debated question in salt - water interactions is whether dissolved ions can influence the dynamical behavior of water molecules be-

yond their first solvation shells. Such an effect is defined as a long-range dynamical effect due to the presence of the ions. Recent experiments, using a combination of femtosecond time-resolved infrared (fs-IR) and dielectric relaxation spectroscopy, have shown the existence of a fraction of reorientationally slow water molecules well beyond the first solvation shells of strongly solvated ions [14]. These results have not been in agreement with other studies involving both experiments and simulation, according to which the effect on dynamics is confined to first solvation shell water molecules [15]. Using MD simulations, the reorientational dynamics of water molecules can be studied through auto-correlation functions of the unit dipole vector of a water molecule ($\hat{\mu}$), defined as

$$P_1(t) \quad = \quad \langle \hat{\mu}(t).\hat{\mu}(0) \rangle \tag{4}$$

$$P_2(t) \quad = \quad \langle \frac{1}{2}(3cos^2(\hat{\mu}(t).\hat{\mu}(0)) - 1) \rangle \tag{5}$$

We have studied the effects of NaCl, KCl, CsCl and $MgCl_2$ on the long-range structural ($t(r)$, $l(r)$) correlations at 0.15M and 1.0M salt concentrations. Influence of the presence of a single non-polar solute ($CH_4$) on the correlations is also reported, and compared to scenarios in which only a single salt molecule (NaCl / $MgCl_2$) is present in equivalent amounts of water. Effects of dissolved ions on the reorientational dynamics of water molecules have been studied by simulating $MgCl_2$ (2M, 3M, 4M) and CsCl (3M, 4M) salt solutions. Important results from the studies are summarized below.

- *Ions as structure makers / breakers* : Effects of dissolved ions on the correlations $t(r)$ and $l(r)$ have been observed to be considerably varied. While ions consistently reduce both the strength and the range of $l(r)$ correlations (Figure 4(e-h)), the effects on $t(r)$ have been observed to be dependent on concentration and salt species. At the smaller concentration of 0.15M, all salts result in an enhancement in $t(r)$ compared to that for solute free water, both for smaller and larger values of $r$ (Figure 4(a,b)). However, the enhancement is reduced at the higher concentration of 1.0M for all salts, with the presence of $MgCl_2$ further resulting in a reduced $t(r)$

9
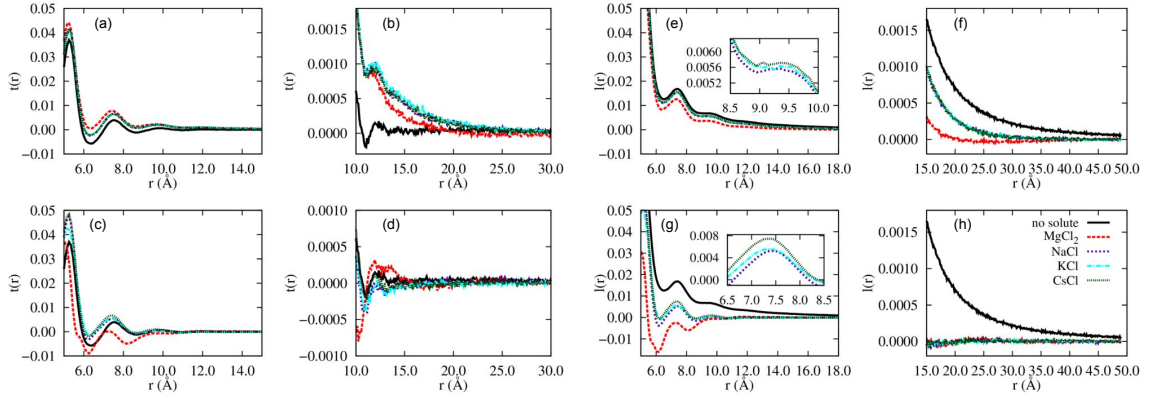
Figure 4: Plots for $t(r)$ correlations (a-d) and $l(r)$ correlations (e-h) at 0.15M and 1.0M salt concentrations. In all plots, the curve for solute free water is shown in (solid, black) line. The same are shown in (dashed, red), (dotted, purple), (dash-dot, cyan) and (small dots, green) for $MgCl_2$, NaCl, KCl and CsCl solutions respectively.

compared to that for solute free water (Figure 4(c,d)). These results bolster the criticism of the prevalent classification of ions along the lines of structure making and breaking, without defining an unambiguous connection between the observable(s) and structural changes [9]. The longest correlation length of $24\mathring{A}$, observed for $l(r)$ correlations in solute free water vanishes for all salts, even at 0.15M concentration. Further, the presence of salts at higher concentration has been observed to induce anticorrelations in $l(r)$ which is absent in solute free water. The the trend in relative effects of cationic species' studied (common anion $Cl^-$) is observed to be $Cs^+ < K^+ < Na^+ < Mg^{2+}$, indicating that the strongly solvated ions have greater influence on the dipolar correlations in liquid water.

- *Contrasting effects of ionic and non-polar solutes, and the hydrophobic effect* :
Contrary to ionic solutes, the presence of $CH_4$ has been observed to result in an enhancement of $l(r)$ correlations (Figure 5(b)). $l(r)$ correlations have been envisaged to result in long-range solvent mediated attraction between hydrophobic surfaces [11]. Further, presence of salts are known to cause a reduction in the attraction between solvated hydrophobes [16]. These results are thus in good agreement with trends observed in hydrophobic interactions, and can indicate at a possible origin of

10
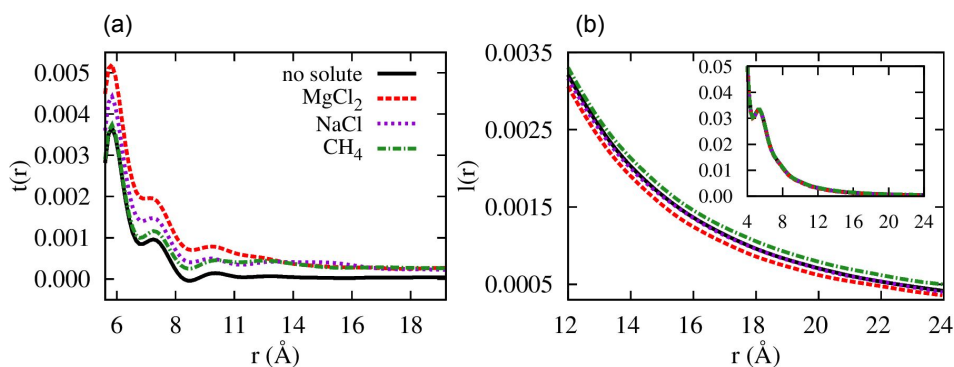
Figure 5: Plots for *t(r)* (a) and *l(r)* (b) correlations in presence of single solute molecules. The magnitude of effects are extremely small, as can be seen from the inset plot, showing the *l(r)* correlations over larger range in *r*.

the long-range component of the force between hydrophobic surfaces. Presence of a single $CH_4$ molecule has been observed to have no effect on the *t(r)* correlations compared to that for solute free water (Figure 5(a)).
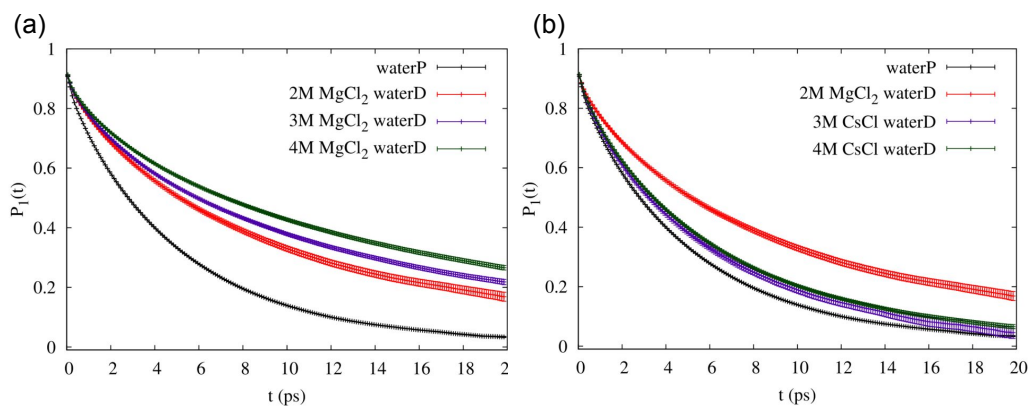


Figure 6: Plots for $P_1(t)$ for *waterD*. (a) Comparison for $MgCl_2$ solutions at the concentrations studied. (b) Comparison of 3M and 4M CsCl with 2M $MgCl_2$. The black curve in both figures is for solute free water (*waterP*). The error bars in all plots have been magnified 5 times.

• *Strongly solvated ions have long-range effects on reorientational dynamics* : The extended hydrogen bond network present in bulk water can be strongly perturbed by the presence of ions. At high salt concentrations, such a strong perturbation can result in in domains of water molecules connected through hydrogen bonds, with associated 'defect water molecules' at the domain boundaries. Defect water molecules are characterized by reduced number of hydrogen bonds, as well

11

as reduced tetrahedrality in the arrangement of nearest neighbors. Defect water molecules have been observed to be more numerous in presence of $MgCl_2$ than with CsCl. Defect water molecules, that are also not within the first hydration shell of any ion (*waterD*), undergo reorientational slowdown for $MgCl_2$ solutions (Figure 6(a)). The slowdown is observed to be enhanced at higher concentrations of $MgCl_2$. For dissolved CsCl ions (Figure 6(b)), no such concentration dependent effects have been observed. Compared to $MgCl_2$, the effects of CsCl on the reorientational dynamics have been observed to be marginal. Results for $P_2(t)$ have been observed to be in good agreement with those for $P_1(t)$, shown in Figure 6. The results demonstrate that strongly solvated ions such as $Mg^{2+}$ can have long-range effects on the dynamical behavior of water molecules.

# List of Figures

14

# List of Tables

# Chapter 1

# Introduction

A solvent is defined as a fluid, in which solutes can be dissolved, forming a solution. In nature, the most common solvent is liquid water, often known as the *universal solvent*. Water not only dissolves all polar and charged molecules, but also non-polar *hydrophobic* molecules to a limited degree. Owing to this unique property, water is the most abundant molecule observed in living organisms, transporting both nutrients and waste products from metabolic processes. A second class of molecules acting as solvents in living organisms are lipids. Lipids are one of the four major classes of biological macromolecules, the other three being proteins, nucleic acids and polysaccharides. Lipids form self-aggregated membranes, which do not dissolve polar and charged molecules, but provide favorable environments for small hydrophobic molecules, and amphiphilic molecules such as membrane proteins.

Both lipids and water are simple in their chemical composition compared to molecules such as proteins, nucleic acids and sugar. However, the simplicity is deceptive. They are rich in both structural and dynamical properties, which involve the collective behavior of a large number of molecules. These properties, and changes to them owing to the presence of solutes are at the heart of diverse processes of biological and chemical relevance. In this chapter, relevant structural and dynamical properties of lipid membranes and liquid

water will be briefly described. For liquid water, solutes of relevance to this thesis are simple salts such as NaCl, KCl, CsCl and $MgCl_2$. Studied solutes for lipid membranes belong to a general class of molecules, known as antimicrobial agents.

## 1.1 Lipid membranes

### 1.1.1 Self assembly of lipid molecules and the lipid bilayer

Phospholipids, dominant constituents of all lipid membranes, are amphiphilic molecules. They consist of a phosphate- containing hydrophilic *head* group, and two hydrophobic fatty acid chains, connected through a glycerol backbone. The fatty acid chains are commonly referred to as the *tails* of a lipid molecule. Phospholipids are intrinsically polymorphic molecules, and can adopt a wide range of self-assembled structures when exposed to water. The driving factor for such self-assembly is the hydrophobic effect, which minimizes the exposure of hydrophobic groups to solvating water molecules. A variety of such structures is shown in Figure 1.1. They can be lamellar or with curvature. Lipid monolayer, bilayer and stacked-bilayer phases are examples of lamellar self aggregates. Examples of curved structures include phases such as micellar, inverted micellar, hexagonal ($H_I$) and the inverted hexagonal ($H_{II}$) phase. The specific form of the aggregate depends upon lipid composition, as well as extrinsic factors such as temperature and relative abundance of hydrating water molecules [17].

In biology, the most relevant self-aggregated structure formed by lipid molecules is the lipid bilayer of cell. Along with membrane proteins and sterol lipids such as cholesterol, lipid bilayers are the universal constituents of both cytoplasmic and intracellular membranes. A lipid bilayer is formed by two layers of lipid molecules, also known as *leaflets*, with the hydrophilic head groups of each layer exposed to hydrating water. Their hydrophobic tails point toward the center of the lamellar sheet, and comprise the bilayer's
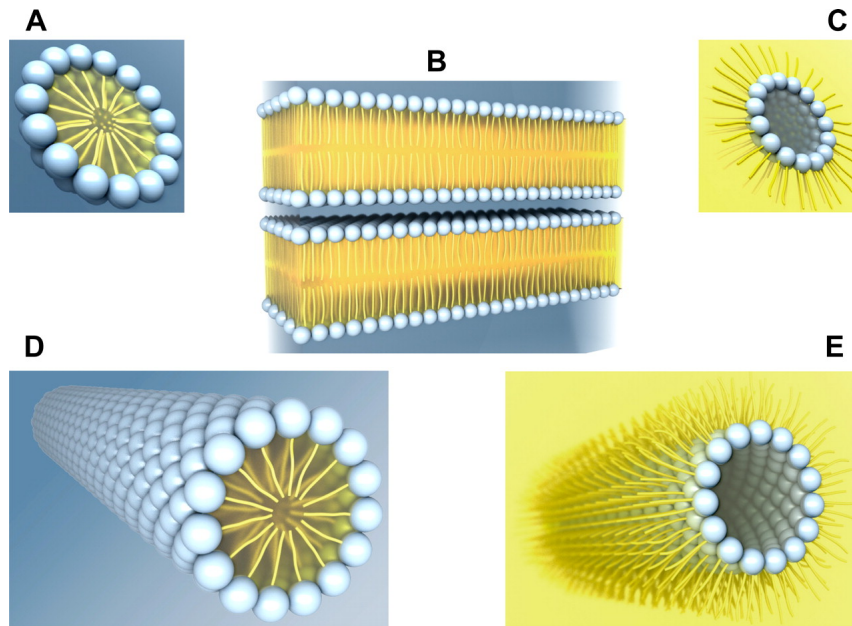
Figure 1.1: Schematic representations of various self-assembled lipid phases in presence of water (not shown). (A) micelle, (B) bilayers, (C) inverted micelle, (D) hexagonal, (E) inverted hexagonal. Courtesy [18].

hydrophobic core. The hydrophobic effect, at the heart of lipid self-assembly, also promotes the spontaneous merger of the free ends, thus leading to the formation of enclosed compartmental structures, or membranes.

The primary function of a lipid membrane can be described as containment and separation of cellular constituents. Most metabolic activities of living organisms take place in a controlled manner in specialized aqueous compartments,- the organelles and the cytoplasm. Lipid membranes, by virtue of their extremely hydrophobic core, provide very high permeability barriers to polar and charged molecules, thus preventing their passive transport, or diffusion, between the aqueous compartments. Similarly, the plasma membrane prevents non-selective exchange of molecules between cells and the extracellular matter. While generally acting as barrier to molecules such as water and dissolved ions, lipid molecules also participate in their selective transport through membrane channels. Membrane channels are comprised of proteins, or protein assemblies embedded in the lipid bilayer. Their functionality is critically dependent on lipid-protein interactions, and is a topic of considerable interest in the scientific community [19, 20]. Other functions

mediated by lipid membranes include signal transduction, protein sorting, endocytosis *etc*.

## 1.1.2    Phase behavior of lipid bilayers

The self-aggregated bilayer structure of lipid molecules encompasses multiple phases, characterized by properties such as lateral (in-plane) mobility of lipids and the conformations of lipid tails. Two phases common to all lipid bilayers in absence (or at low content) of sterol lipids such as cholesterol are the gel (or solid, $L_\beta$) and liquid-disordered (or liquid-crystalline, $L_\alpha$) phases. The two phases are connected through a first order, temperature driven phase transition, known as the main lipid bilayer phase transition. The critical temperature for the transition is known as the main transition temperature, or the melting point ($T_m$) [17, 21]. Apart from the gel and liquid-crystalline phases, lipid bilayers can also exist in subgel, ripple and liquid-ordered phases [21, 22]. The liquid-ordered phase is observed with the presence of cholesterol. The subgel and ripple phases are beyond the scope of this thesis and interested readers are referred to [22–25].

**The liquid-disordered and gel phases**

An ordinary lipid bilayer exists in the $L_\alpha$ phase above $T_m$ and in the $L_\beta$ phase below it. The phase transition is associated with changes in a large number bilayer properties. Density varies discontinuously across the main lipid bilayer phase transition. The thickness of a lipid bilayer is greater in the $L_\beta$ phase compared to $L_\alpha$. The $L_\beta$ phase corresponds to reduced hydration and a tighter packing of lipid head groups. The bending rigidity, or stiffness of a lipid bilayer is considerably greater in the $L_\beta$ phase, compared to $L_\alpha$ [17, 21, 26]. However, the most robust differences between the two phases are observed in the mobility of lipid molecules within the bilayer, and the order in the packing of lipid tails [17, 21].
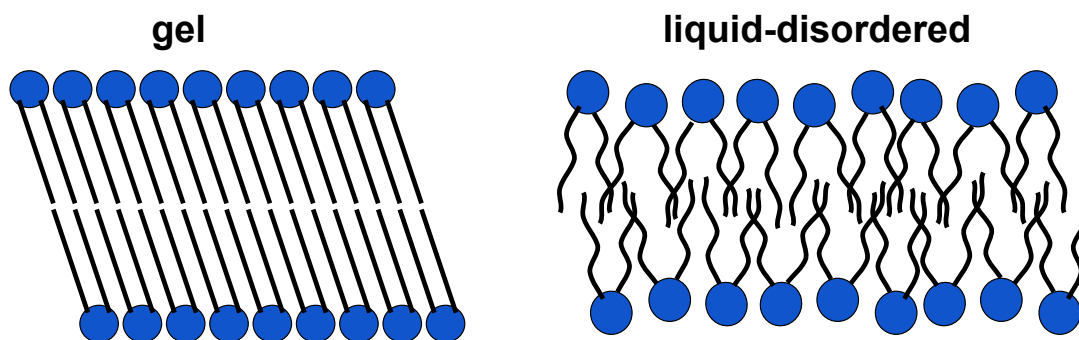
Figure 1.2: Schematic representation of the gel ($L_\beta$) and liquid-disordered ($L_\alpha$) phases of a lipid bilayer. The phases are characterized by ordered and disordered packing of the lipid acyl tails respectively. Considerable undulation fluctuations exist in the liquid-disordered phase.

In the $L_\alpha$ phase, the lipid molecules are highly mobile. They undergo rapid lateral translational diffusion within a bilayer leaflet. Individual lipid molecules can also move from one bilayer leaflet to the other, a motion known as *flip-flop* of lipids. Both the motions are highly restricted in the $L_\beta$ phase. The reduced mobility has important consequences on the viability of the lipid bilayer to function as a biological membrane. The fluid nature of lipid bilayers in their $L_\alpha$ phase allow for fluctuations and rapid reorganizations of lipid molecules, which are at the heart of the structural integrity of lipid membranes. Through such reorganizations, a lipid bilayer can rapidly self-heal defects and deformations of it, such as small transient pores. Such self-healing is highly restricted in the $L_\beta$ phase, whence the $L_\beta$ phase is often observed in the cell membranes of dead cells [21].

The main phase transition is associated with change in the entropy of the system through configurational reorganization of the system's components, especially the packing of lipid tails. In the $L_\alpha$ phase, there exists considerable disorder in the lipid tail conformations. The signatures of such disorder include rapid thermal motions, interdigitations among the lipid tails, presence of both *trans* and *gauche* conformations through which a lipid tail can fold back on itself *etc*. A transition to the $L_\beta$ phase with the reduction in temperature is associated with an enhancement of configurational order in the lipid tails. The acyl tails adopt *all-trans* conformations, undergo considerably reduced thermal fluctuations and do not interdigitate to any appreciable degree. The differences between lipid acyl

chain conformations observed for the two phases are schematically shown in Figure 1.2.

The phase behavior of lipid bilayers is predominantly governed by the van der Waals (vdW) interactions between tails of neighboring lipid molecules. vdW interactions favor the ordered alignment of lipid tails so as to maximize the number of contacts. At temperatures above $T_m$, thermal fluctuations can dominate over the vdW interactions, thus leading to disorder in lipid tail conformations. As the temperature is reduced below $T_m$, the gel phase becomes thermodynamically favorable, and the lipid tails adopt ordered conformations. $T_m$ for lipid bilayers depends on several factors, which include length of acyl chains and their degree of unsaturation, number of hydrating water molecules, pH *etc*. $T_m$ for a mixed lipid bilayer also differs from the $T_m$ for the corresponding single-component bilayers [21, 26, 27].

With increase in the length of lipid acyl chains the number of vdW contacts, and hence the strength of vdW interactions increases. Accordingly, for lipid bilayers with equivalent head group compositions, $T_m$ increases with longer acyl chains. Unsaturations in the lipid tails induce defects (kinks) in the regular ordered arrangements of lipid tails, and hence lead to a reduced $T_m$ [21]. pH and head group hydration affect $T_m$ primarily by modulating the hydrogen bonding among lipid molecules [28].

**Effect of cholesterol : the liquid-ordered phase**

Cholesterol is a lipid with unique chemical structure and effective shape (see Figure 1.3). It has a small, hydroxyl-containing head group, and a bulky and stiff hydrophobic tail region. The tail region has a steroid ring structure, unlike the fatty acid chains for conventional lipids. The length of the tail region is also considerably smaller compared to conventional lipids forming lipid bilayers. Owing to its unique structure, the presence of cholesterol disrupts both the $L_\alpha$ and $L_\beta$ bilayer phases [17, 29].

The bulky and stiff steroid ring structured tail of cholesterol prefers ordered arrangement
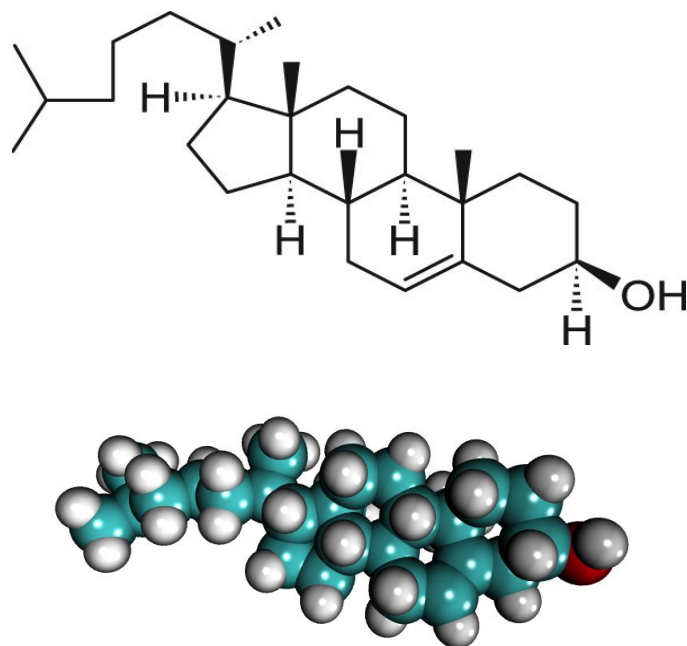
Figure 1.3: Chemical structure and all-atom representation of a cholesterol molecule. The figures show the molecule's hydroxyl-containing head group and steroid ring structured tail.

of lipid tails around it, thus enhancing the propensity for the $L_\beta$ phase. However, the $L_\beta$ phase is also characterized by positional ordering, and tight packing of lipid molecules. Owing to its small head group and short tail length, cholesterol can not pack effectively within the $L_\beta$ phase, allowing considerable conformational freedom to the neighboring lipid molecules. As a result of the opposing influences, cholesterol induces a distinct phase in a lipid bilayer, known as the liquid-ordered ($L_o$) phase. The $L_o$ phase has properties intermediate between the $L_\alpha$ and $L_\beta$ bilayer phases. It is characterized by positional disorder and high mobility of the lipid molecules, but with considerable order in the packing of the lipid tails and greater bending rigidity compared to the $L_\alpha$ phase [17, 29].

The influence of cholesterol on the lipid bilayer structure and organization is not fully understood. The phase behavior of a cholesterol containing bilayer is critically dependent upon the cholesterol concentration [17, 30]. The orientations of cholesterol molecules inside a lipid bilayer is also different for low and high concentrations of it. At low concentrations cholesterol molecules are envisaged to be highly tilted with respect to the bi-

layer normal. With increase in concentration the tilt angle decreases, and the cholesterol molecules align with the bilayer normal [31].

### 1.1.3 Trans-bilayer structure and lateral pressure profile

The trans-bilayer structure of model lipid membranes relates to the the probability of finding specific atomic constituents as a function of depth within the bilayer structure. The lipid bilayer is a highly heterogeneous structure, where composition and bilayer properties vary over sub-nanometer length scales. The interfacial regions of a lipid bilayer comprise of head group atoms and strongly bound water molecules. Toward the exterior, this region is followed by a nanometer thick region of strongly perturbed water, whose structure and dynamics vary widely from bulk behavior. The region is also characterized by high density of dissolved ions, which show strong propensities for localizing at the lipid bilayer - water interface. Toward the interior of the lipid bilayer, the interfacial regions are immediately followed by lipid glycerol groups, and a layer of ordered lipid tail atoms. The core of the lipid bilayer is comprised solely of lipid tail atoms, disordered in the $L_\alpha$ phase and ordered in the $L_\beta$ phase [17, 32].

While the core of the bilayer is essentially shielded from exposure to water, the same is not true for the hydrophobic groups immediately following the lipid head groups. Lipid bilayers actively try to minimize the exposure, thus minimizing the free energy cost of contact between hydrocarbon and water. This results in strong interfacial tension, or negative lateral pressure (attractive forces) in the narrow region comprised of the glycerol groups, and the topmost parts of lipid acyl tails. The tension acts to drive the head groups closer, resulting in imperfect screening of head group repulsions. The tension also leads to dense packing of lipid tails in the core of the bilayer, thus reducing their entropic freedom. The localized attractive lateral pressure is thus counteracted by positive lateral pressure (repulsive forces) at the interfacial region as well as the bilayer core. Figure 1.4 (a) shows a schematic representation of the relative magnitude and direction of forces

26
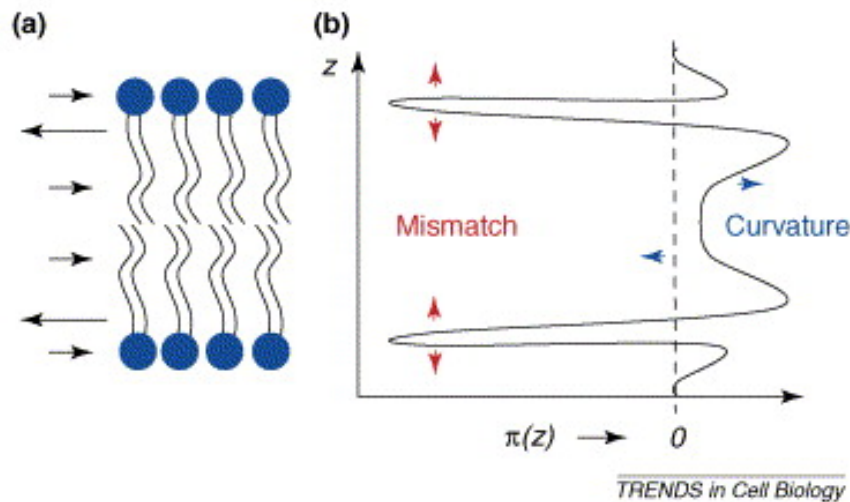
Figure 1.4: (a) Schematic showing the forces (arrows) that need to be balanced by pressure profile across a lipid bilayer. (b) The corresponding schematic lateral pressure profile ($\pi(z)$), shown as a function of position along bilayer normal (z). Strong tensions at the interfaces are balanced by positive pressures through the interior, which are greatest near the interfaces. The red arrows show that a mismatch in the (hydrophobic) thickness moves the regions of high pressure up or down along the membrane normal, and the blue arrows show how bending the membrane alters the pressure gradient within the bilayer. Courtesy [33].

required to counteract the forces due to lateral pressure at various depth within a lipid bilayer. The corresponding lateral pressure profile is schematically shown in Figure 1.4 (b). In equilibrium, the net lateral pressure across a lipid bilayer must sum up to zero [34, 35].

The lateral pressures inside a lipid bilayer are extremely high, measuring several hundreds of atmosphere. The pressure profile is also highly responsive to small changes in lipid bilayer structure and composition, and to the presence of solutes such as anesthetics [35,36]. Changes in lateral pressure profile can have strong influence on the conformations of membrane proteins. Asymmetry in the distribution of lateral pressures between bilayer leaflets results in spontaneous curvature, and can alter the elastic properties of a lipid membrane [17, 33, 34]. Experimental determination of the lateral pressure profile is extremely challenging, since it involves measuring local pressure differences at the sub-nanometer length scale [37]. In MD simulations, lateral pressure ($\pi(z)$) at a depth ($z$) is measured as the difference between the normal ($P_{zz}(z)$) and lateral ($[P_{xx}(z) + P_{yy}(z)]/2$) components of the pressure tensor (equation 1.1, angular brackets indicate ensemble av-

27

erage) [38].

$$\pi(z) = \langle P_{zz}(z) - \frac{1}{2}[P_{xx}(z) + P_{yy}(z)]\rangle \qquad (1.1)$$

### 1.1.4 Experimental determination of bilayer structure

In the $L_\beta$ phase, lipid bilayers are characterized by a high degree of positional order, as well as ordered, near crystalline packing of the lipid tails. Thus, structure of bilayers in the $L_\beta$ phase can be experimentally studied using diffraction methods, which result in several orders of diffraction peaks. Wide-angle X-ray experiments have been used to study the lateral packing of ordered lipid tails, from which structural parameters such as chain tilt angle, area per lipid *etc* can be obtained [39,40]. The wide-angle X-ray diffraction studies have shown that the lipid chains in the $L_\beta$ phase pack parallel to each other, and the lateral organization is approximately hexagonal [40].

Experimental techniques involving diffraction methods (*eg.* X-ray, neutron diffraction) can not be readily applied to determine accurate structures of lipid bilayers in their biologically relevant fully hydrated $L_\alpha$ phase. In the $L_\alpha$ phase the positional order in lateral packing of lipids is lost, the tails are conformationally disordered, and the overall bilayer is subject to considerable fluctuations. Accordingly, diffraction patterns obtained from them only contain a few order peaks [22,32,40]. Accurate determination of bilayer structural properties from such low-order diffraction data has been possible with the development of computational methods (*eg.* molecular dynamics) and theoretical models to account for undulation fluctuations in the $L_\alpha$ phase [22,32,40–43].

Electron density profiles as a function of depth along bilayer normal can be obtained using X-ray diffraction experiments [22,44,45]. In lipids, the phosphate groups are electron rich, and the technique can yield accurate estimates of the distribution of phosphate groups along the normal to the bilayer. Similar distributions for other lipid component groups can be obtained using neutron diffraction, with selective deuteration ($^1H \rightarrow {}^2H$) of

specific constituent groups [40]. The trans-bilayer structure, including the distributions of the various components, has been obtained to an appreciable degree of accuracy using combination of X-ray and neutron diffraction data [32, 42].

The fundamental structural quantity along the bilayer plane (transverse structure) targeted by experimental studies is the area per lipid molecule. Area per lipid for fully hydrated bilayers in $L_\alpha$ phase have been obtained using high resolution X-ray experiments, supplemented by theoretical modeling to account for undulation fluctuations [40, 43]. Other experimental methods to determine area per lipid molecule include Gravimetric X-ray [46, 47], liquid crystallography [40, 48] *etc*. For a detailed description of the experimental methods, readers are referred to review by Nagle and references therein [40].

The order in the conformations of lipid acyl tails is best characterized by order parameters computed using deuterium nuclear magnetic resonance spectroscopy ($^2$H NMR). $^2$H NMR measures the quadrupolar splittings ($\Delta\nu_Q$) associated with C–$^2$H bonds in the deuterated lipid acyl chains. $\Delta\nu_Q$ is related to bilayer and acyl tail order parameters ($S_{bilayer}$ and $S_{cd}$ respectively through

$$\Delta\nu_Q = \frac{3}{2}A_Q S_{bilayer} S_{cd} \tag{1.2}$$

where $A_Q$ is the quadrupolar coupling constant [49]. $S_{bilayer}$ and $S_{cd}$ have the same functional form, given by

$$S_{bilayer/cd} = \frac{1}{2}\left\langle 3Cos^2\Theta - 1 \right\rangle . \tag{1.3}$$

$\Theta$ represents the angle between applied magnetic field and the bilayer normal for $S_{bilayer}$, and the angle between the bilayer normal and the C–$^2$H bond for $S_{cd}$. $S_{cd}$ provides a good measure for chain mobility, average orientations of C–$^2$H bonds and order in lipid tails [49–52]. $S_{cd}$ is especially relevant since its measurement does not involve theoretical modeling,- whence it is often used as reference to parametrize computational models [49, 53].

### 1.1.5 Multi-component bilayers : lateral inhomogeneity

Lateral distribution of lipid species along the bilayer plane is an additional structural degree of freedom of mixed lipid membranes. Lipids are mobile molecules, which continuously exchange their neighbors by virtue of lateral diffusion. The dynamics allows for the possibility of co-localization of like lipid species into demixed phases, or nano-domains. The existence of such domains in presence of cholesterol, sphingolipids and proteins, or *rafts*, has been suggested to have significance in signaling and sorting pathways [54]. However, the existence of rafts is highly debated [55]. In functional mixed lipid membranes in absence of cholesterol, the lipids reside as mixed phases, where there is no preferential co-localization. Thus functional model membranes are characterized by lateral homogeneity or continuity of bilayer properties along bilayer plane. Interaction with membrane-active molecules, however, can induce demixed phases in model lipid membranes. Phase demixing is often associated with discontinuous variation of bilayer properties at the phase boundaries. Demixed bilayers are susceptible to destabilization. Large scale phase demixing can induce transition to non-bilayer lipid phases too. Phase boundaries are also prone to leakage [56, 57].

### 1.1.6 Continuum models for lipid membranes : the Fluid-Mosaic model

We conclude this section with a brief introduction to theoretical and computational models used to study model lipid membranes. In the following some important theoretical, continuum models will be introduced. Computational models, of greater relevance to this thesis will be described in section 2.2.

The bilayer structure of lipid membranes was known as early as 1925, through experiments by Gorter and Grendel [58]. In their experiments, the area of monolayers formed by lipid extracts from red blood cells was observed to be twice that of the surface area of

the cells providing the lipid extracts. This also led to the understanding that the thickness of lipid bilayers is negligibly small compared to the dimensions of the compartments they enclose. The lipid bilayer can thus be treated as a two-dimensional (2D) fluid, in which the lateral mobility of the constituents is key to functional viability [17].
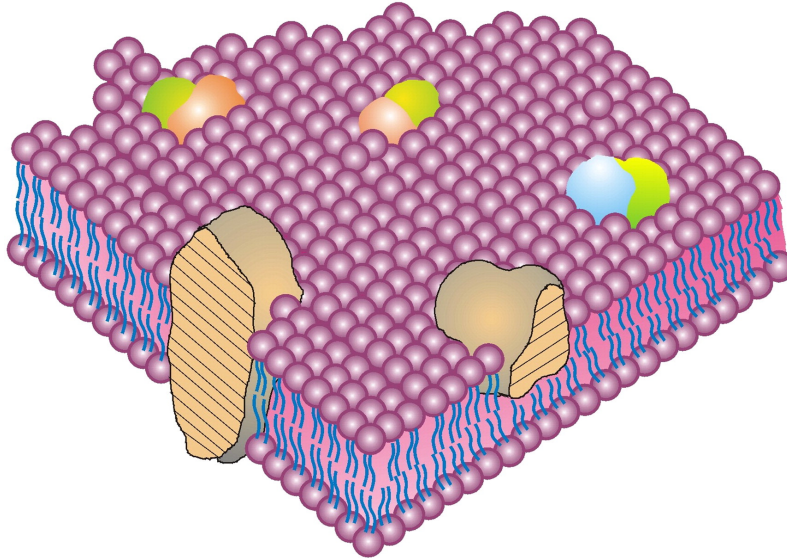


Figure 1.5: Schematic representation of the Fluid Mosaic membrane model. Courtesy [59].

The *Fluid-Mosaic* model (Singer and Nicolson, 1972) was the first model to describe the lateral organization of proteins and lipids in a biological membrane. In the Fluid-Mosaic model, the membrane is described as a pseudo 2D fluid, in which membrane proteins are dispersed in a multi-component, homogeneous lipid bilayer (Figure 1.5). The constituent molecules are characterized by a certain degree of *fluidity*, which is a measure for their lateral mobility. According to the model, the multi-component lipid membrane enables the variation of the solvation rate of membrane proteins through non-covalent interactions such as electrostatics, van der Waals, hydrogen bonding and hydrophobic shielding. Conceptually simple and capable of explaining qualitative properties of a vast majority of lipid membranes, the model however fails to describe several key features of membrane structure and function. These features include membrane protein assembly, trans-layer asymmetry in lipid composition and bilayer curvature, lateral heterogeneity and generally lipid-protein and lipid-lipid interactions [59, 60]. Subsequent modifications to the Fluid-Mosaic model, have often incorporated specific membrane properties. Notable examples

of such updated models include models by Israelachvili and Sackmann [17, 61, 62].

## 1.2 Antimicrobial - membrane interactions

### 1.2.1 Microbial membrane destabilizing (antimicrobial) agents

Antimicrobial agents are molecules that have the ability to selectively kill microbial cells over mammalian ones. Since their discovery, antibiotics have been the most effective drugs available to mankind for the treatment of bacterial infections. However, with the rapid growth of bacterial resistance to antibiotics in recent times [63], and especially with the emergence of multidrug-resistant bacteria, or *superbugs* [3], a lot of effort has been put into the development of alternate therapeutic agents that offer less susceptibility to the growth of bacterial resistance.

**Natural antimicrobial peptides**

Antimicrobial peptides (AMPs) have evolutionarily been part of the innate immunity system of eukaryotes, providing a broad spectrum of activity against invading pathogens [1, 64, 65]. AMPs are small peptides consisting of 12 to 100 amino acids [66]. While a small number of them are known to be exclusively negatively charged [67], AMPs are typically composed of cationic and hydrophobic residues [3]. All AMPs are inherently membrane active and the complex interactions involved can lead to considerable conformational changes in the agents, while also inducing structural rearrangements of membrane lipids. Such structural modifications can trigger series of events enabling the agent to affect the structural integrity of the microbial membrane or translocate to the interior of the microbial cell. The predominant dependence of the antimicrobial action on the general lipid composition of microbial membranes, in contrast to the antibiotics which target specific metabolic pathways and proteins, makes the AMPs considerably less sus-

32

ceptible to microbial resistance development through gene mutation [3, 68]. For the same reason, antimicrobial activity of AMPs is not restricted solely to bacteria but often extends to fungi and viruses [66]. In addition to direct microbe killing, in higher eukaryotes the AMPs are also involved in the orchestration of immunomodulatory responses triggered by the presence of pathogenic species, hence they are also termed as host defense peptides [3, 65, 66].



(A) α-helical

Magainin-2
DOI:10.2210/pdb2mag/pdb

(B) β-sheet

β -defensin 1
DOI:10.2210/pdb1kj5/pdb

(C) extended

Indolicidin
DOI:10.2210/pdb1g89/pdb

(D) loop

Gramicidin
DOI:10.2210/pdb1mag/pdb
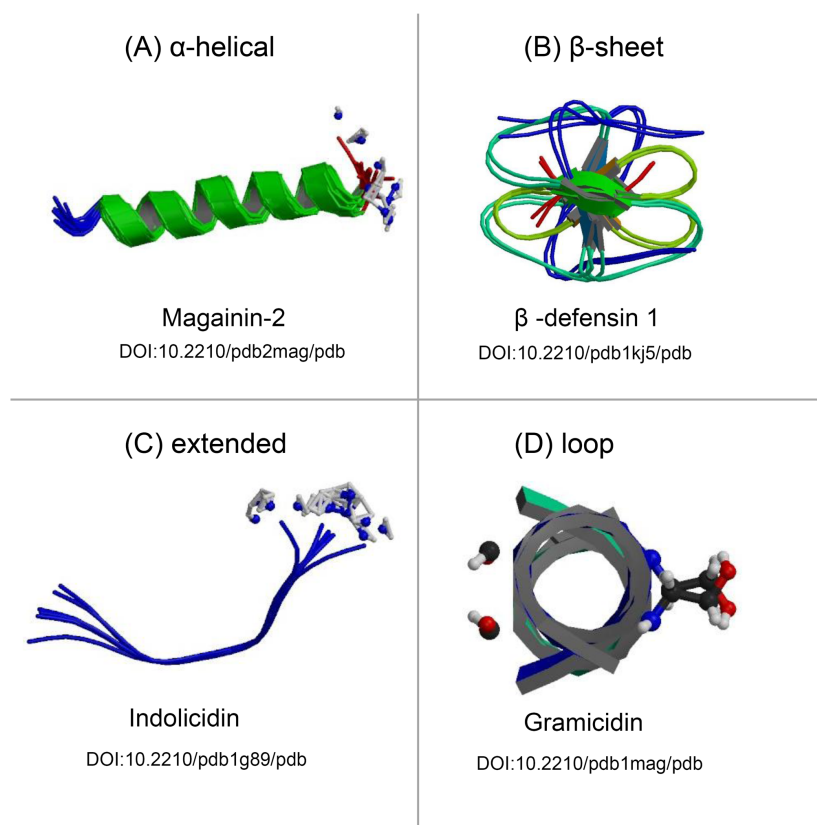
Figure 1.6: Representative molecules from the various structural classes of AMPs. The PDB ids for (A)-(D) are 2MAG, 1KJ5, 1G89 and 1MAG respectively. Courtesy [69].

The secondary structural conformations of AMPs can be broadly classified into four classes: $\alpha$-helical, $\beta$-sheet, loop structured and extended or unstructured [66, 70] (Figure 1.6). Over the past two decades, considerable effort has been put in to probe the relationship between their secondary structure and mode of antimicrobial action. Vast majority of AMPs are known to act through the direct targeting of structural integrity of the microbial membrane itself [71, 72],- generically termed as membranolytic modes. Several models have been proposed to describe the membranolytic modes, and are briefly

described in section 1.2.3. Models generally account for the destabilization of the lipid bilayer through the formation of transmembrane pores, or through induced reorganizations of bilayer lipids. While well defined extended secondary structures have indeed been observed to often facilitate specific modes of action, the very existence of such structures have not emerged as essential to antimicrobial activity [73, 74]. Instead, the ability to take up amphiphilic conformations in which the hydrophilic and hydrophobic components are spatially segregated, also known as *facially amphiphilic* (FA) conformations, has been recognized as key to antimicrobial activity [3]. FA conformations of antimicrobial agents are closely related to trans-bilayer structure and bilayer-agent interactions. They are detailed in section 1.2.2.

**Synthetic antimicrobial polymers and oligomers**

In spite of distinct advantages over antibiotics, therapeutic use of AMPs has been limited by several key factors. These include high manufacturing costs, susceptibility to proteolysis, pH dependence of activity and high levels of toxicity to host cells at concentrations that are required to treat infections [71, 75]. Further, the secondary structural features of AMPs can be preserved only with a few amino acid substitutions. AMPs are thus also ill-suited for a rigorous study of relationship between the secondary structure and antimicrobial activity [76]. Some of these issues have been overcome through the rational design of polymeric / oligomeric molecular structures (AMPoly) that mimic the essential structural features of AMPs.

Design principles can be broadly classified into two classes. The first includes molecules with *built-in* secondary structural conformations such as $\alpha$-helix or $\beta$-sheet, while for the other involves molecules with flexible backbones, thus allowing for large scale changes in conformations with varying environment. Molecules with *built-in* secondary structure include structures with biotic backbones such as peptoids and $\beta$-peptides, as well as molecules such as phenylene ethynylenes, arylamides and polynorbornenes which have

abiotic backbones [77–83]. The structural properties of such molecules, including their secondary structure forming properties can be varied over a wider range compared to AMPs. They have been extensively used to study structure-function relationships in antimicrobial agents. A vast amount of data has reinforced the understanding that greater property for secondary structure does not lead to greater activity against microbes. Facial amphiphilicity, along with other characteristics such as molecular weight and relative content of hydrophobic to cationic groups have been identified as key attributes to the design principle. Toxicity against mammalian cells has generally been observed to increase with higher molecular weight. Activity against both mammalian and bacterial cells have been observed to increase with increased hydrophobic content [84].

The importance of the said factors over in-built conformational rigidity has been reinforced with the development of functional AMPoly with flexible backbones. Aided by availability of vast polymer design libraries, a large variety of flexible AMPoly have been designed with potential antimicrobial activity. Notable examples studied extensively include methacrylate copolymers [85] and nylon-derivatives [86]. Structure - function studies on such polymers, along with the effect of overall charge and hydrophobic content, has also involved the effect of distribution of hydrophobicity over the molecular structure [84]. AMPoly have been designed by distributing the charge and hydrophobicity either along the backbone or side chains [84, 87–89]. In the case of the former, a further design element could be the arrangement of these cationic and hydrophobic monomers (random, alternating and block). In a very recent study, the distribution of amphiphilic groups has also been extended to radial symmetry. Flexible AMPoly are unstructured in aqueous phase, forming aggregates or adopting random coiled structures. However, functional flexible AMPoly are expected to have the ability to adopt FA conformations upon interaction with lipid membranes. Trends in antimicrobial and hemolytic activities of flexible AMPoly with respect to structural attributes such as molecular weight and hydrophobic content have been generally been observed to be in qualitative agreement with those observed with AMPs and AMPoly with rigid backbones [84]. However, a notable

35

variation observed for methacrylates and nylon-3-based random copolymers is that their antimicrobial activities can level-off, or even decrease, at very high hydrophobic contents. This is generally attributed to formation of strongly bound, stable AMPoly aggregates in the aqueous phase. Formation of such aggregates can lead to a reduction in the number of agent molecules available for membrane interactions [84, 90, 91].

## 1.2.2   Selectivity and membrane binding of antimicrobial agents

All antimicrobial agents must have the ability to selectively interact with and disrupt microbial membranes over mammalian ones. At the heart of the selectivity lies the differences in the lipid composition between the two. Both the outer and the inner leaflets of microbial lipid bilayers have a high population of anionic lipids such as phosphatidyl-glycerol (PG) and cardiolipin. In contrast, negatively charged lipids largely reside only in the inner leaflet of mammalian membranes, with head groups facing the cytoplasm. The lipid composition of the outer leaflet of eukaryotic cell membranes is predominantly zwitterionic, comprising of lipids such as phosphatidylcholine (PC) and sterol molecules such as cholesterol [1, 92]. The cationic moieties common to almost all antimicrobial agents interact favorably with the anionic lipid head groups of the microbial membranes through long range electrostatic interactions. This results in the selective recognition, and adsorption of the agents at the microbial membrane - water interface. Following adsorption, the penetration of an agent molecule into the membrane interior is driven by its hydrophobic constituents. The hydrophobic constituents remain exposed to interfacial water while adsorbed on the membrane, but attain energetically favorable environment on penetration into the membrane's hydrophobic interior. The membrane interior, however, provides energetically unfavorable environment for the charged, hydrophilic groups. Only an ability to attain a FA conformation enables easy partitioning of the antimicrobial agents into the membrane interior.

In a FA conformation, shown in Figures 1.7 (a and c), the charged / polar and hydrophobic
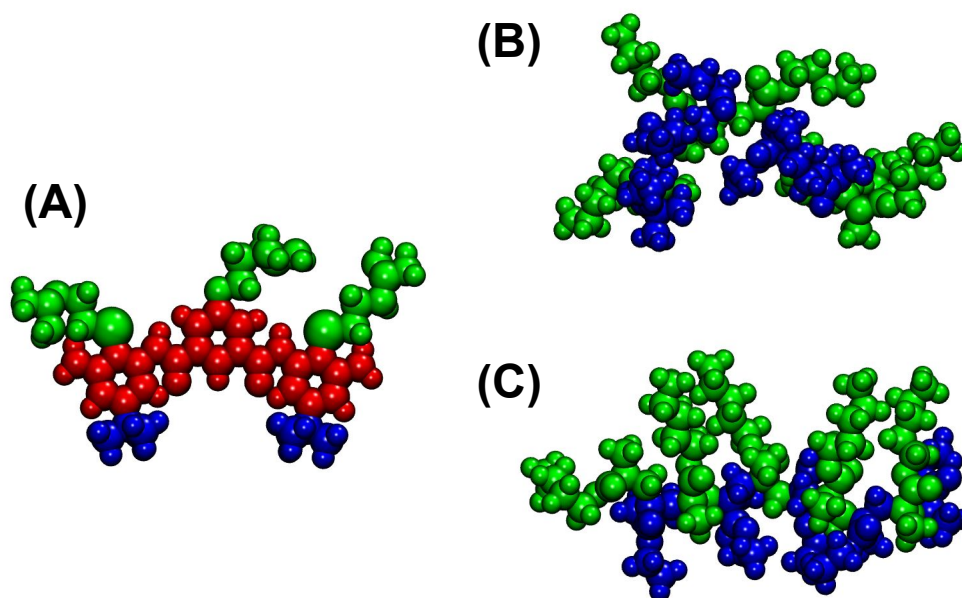
Figure 1.7: Conformations of AMPoly based on (A) rigid scaffold like arylamide with in-built facial amphiphilicity in solution and in membrane, (B) flexible backbone like methacrylate polymers in solution with no facial amphiphilicity, and (C) acquisition of facial amphiphilicity of the methacrylate polymer in the membrane. The charged and hydrophobic moieties are shown in green and blue respectively. For the arylamide the rigid, ring-structured backbone is additionally shown in red.

constituent of an antimicrobial agent are spatially segregated to two sides of a secondary structural conformation. In AMPs and AMPoly such as arylamides 1.7 (a), with rigid backbones having built-in secondary structure, the secondary structural conformations can be $\alpha$-helices or $\beta$-sheets. These molecules, by virtue of their structural design can retain their secondary structural conformation, hence facial amphiphilicity even in the aqueous phase [76]. However, extensive data indicates that the ability to attain FA conformations is only relevant at the membrane partitioned state. Stringent design strategies, resulting in well structured $\alpha$-helices in the aqueous phase has been observed to enhance toxicity to mammalian cells. Imperfect helicity, resulting in well organized $\alpha$-helical conformations in membranous environment, but with reduced secondary structural propensities in the aqueous phase has often been observed to increase selectivity [3]. In absence of a secondary structural conformation such as an $\alpha$-helix or a $\beta$-sheet, facial amphiphilicity can appear about a structural backbone, such as the polymeric backbone. Figures 1.7 (b

and c) depict the advent of facial amphiphilicity in a flexible methacrylate copolymer. In the aqueous phase (Figure 1.7 (b)), the charged and hydrophobic moieties are randomly distributed, while in the membranous phase (Figure 1.7 (c)), they can be observed to be preferentially distributed about the polymer backbone.

The importance of FA conformations can be related to the trans-bilayer structure in a lipid bilayer. The interfaces of a lipid bilayer are comprised of hydrophilic head groups and interfacial water, which is immediately followed by the hydrophobic core. In the initial partitioned FA conformations, the cationic / hydrophilic groups of an antimicrobial agent can reside in the vicinity of the lipid head groups, while the hydrophobic constituents are buried deeper into the membrane interior. The conformation thus leads to energetically favorable interactions, while also allowing for maximal agent-lipid interactions. However, the initial partitioned conformation of the agent, generally speaking, is only a metastable one, with further evolution of the system being dependent on a variety of structural effects. The fundamentally important criterion for the antimicrobial agents is the ability to form energetically favored global conformation and orientation, as well to form supramolecular aggregates, especially for pore forming agents.

**Interfacial lipid-packing defects**

In addition to favorable long-range electrostatic interactions, the ability of antimicrobial agents to recognize and bind to interfacial lipid-packing defects has been suggested as a mechanism for selectivity. The interfacial region of a lipid bilayer is a highly dynamic, and the sub-nanometer structure of the lipid bilayer-water interface is subject to constant dynamical fluctuations. Such fluctuations often result in transient exposure of hydrophobic lipid tail group atoms to interfacial water. Regions of hydrophobic exposure are defined as interfacial lipid packing defects. Defect regions provide favorable binding sites to the hydrophobic groups of molecules adsorbed at the lipid bilayer interface. It has been suggested that binding to defect sites facilities the partitioning of membrane-

active molecules [5]. The area of defect regions have been shown to be enhanced in the presence of conical lipids with smaller head groups, and positive curvature (convex interface) [4]. Conical lipids with PE head groups are dominant constituents of bacterial lipid membranes. Their mammalian counterparts with PC head groups are approximately cylindrical in effective shape. This difference in head group composition leads to greater abundance of packing defects in bacterial membranes compared to mammalian ones, and can be envisaged to contribute of selectivity of antimicrobial agents.
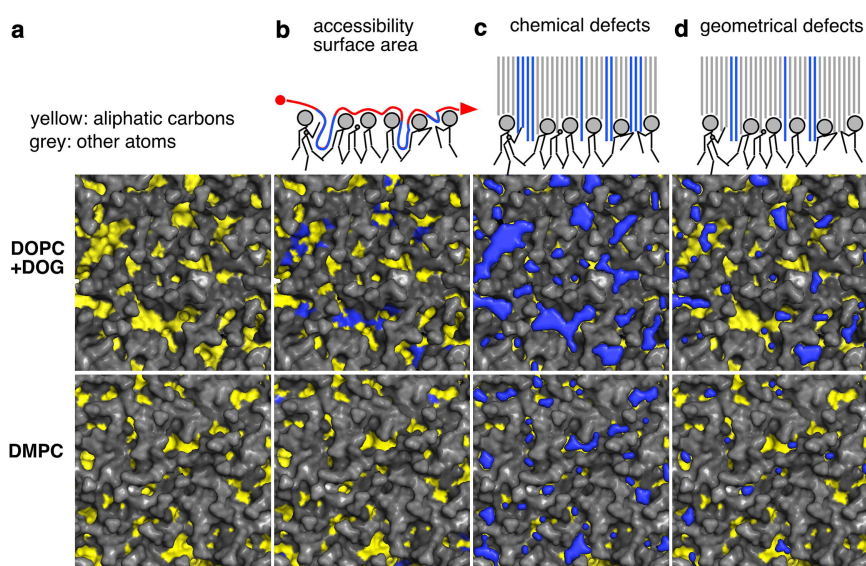


Figure 1.8: Schematic showing the definitions and identifications of interfacial lipid packing defects. Column (a) shows snapshots of the surface of DOPC/DOG and DMPC bilayers with polar heads in gray and aliphatic carbon atoms in yellow. Column (b) shows the defects identified using accessible surface area calculations (probe radius 3 $\mathring{A}$). Columns (c) and (d) show chemical and geometrical defects respectively, computed using a grid size of 1 $\mathring{A} \times 1$ $\mathring{A}$. In columns (b)-(d), defects are shown in blue. Courtesy [4].

Interfacial lipid packing defects have been categorized into chemical and geometrical defects, based on the relative depth of the defect sites with respect to the nearest glycerol backbone. By definition, all lipid packing defects resulting in hydrophobic exposure are defined as chemical defects. Defects that involve exposure of hydrophobic tails at locations deeper than the position of nearest glycerol atoms are defined as geometrical defects [4]. Figure 1.8 schematically shows interfacial lipid packing defects identified using a grid-based Cartesian scheme [4], both in presence and absence of conical lipid species (DOG). Transient hydrophobic exposures can also be identified using water accessible

39

hydrophobic surface area calculations. Figure 1.8 also portrays quantitative differences between hydrophobic exposures obtained using both approaches.

## 1.2.3 Models of antimicrobial action
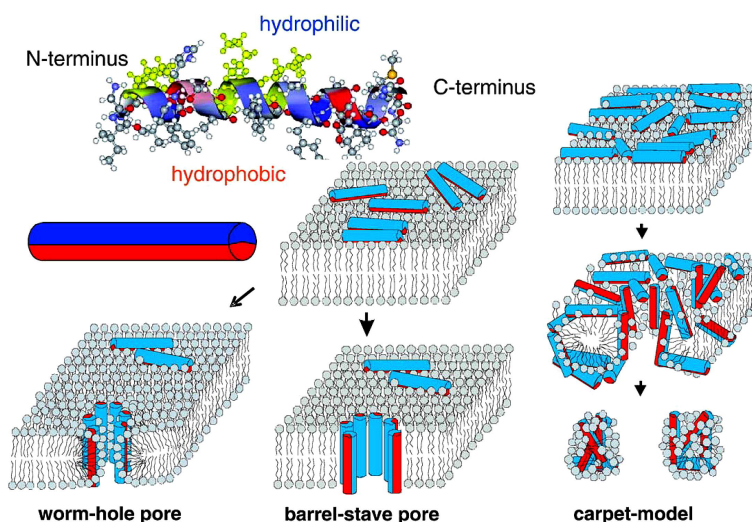


Figure 1.9: Schematic description of three well-documented membrane-active modes of action of AMPs. In the facially amphiphilic, membrane-bound conformation, the hydrophilic and hydrophobic moieties of the agent are depicted in blue and red respectively. Courtesy [93].

The lipid membrane - water interface provides a complex environment in which the structural and dynamical properties of the membrane, hydrating water and ions can all play critical roles in the interactions of antimicrobial agents. Understanding the mode of action as well as the structure - function relationship of antimicrobial agents is intrinsically a daunting task. The antimicrobial agents interact with lipid membranes in both non-specific (eg. electrostatic, hydrophobic) as well as specific (eg. hydrogen bonding) ways. All of these interactions contribute to the changes in agent conformations, and the properties of the membranes. Many effective antimicrobial agents are also known to act through multiple modes of action, which is a further barrier in understanding their structure - function relationships [3, 66, 68].

Several models have been proposed to explain membranolytic activity of antimicrobial agents. All such models require the ability of the agents to adopt FA conformations

in their membrane-bound states. Further, it is recognized that antimicrobial activity involves co-operative concerted action of multiple agent molecules. Three well documented models that involve membrane permeabilization or disintegration are barrel-stave [94], toroidal-pore (or worm-hole pore) [95, 96] and carpet [66, 95]. A schematic description of these models is shown in Figure 1.9. In both barrel-stave and toroidal models, transmembrane pores are the result of co-operative interactions of AMPs and typically have been observed at low peptide concentration, while in the carpet model, the AMPs disrupt the membrane integrity in multiple sites on the bacterial membrane through micellization and is known to occur at high concentration of AMPs. In the barrel-stave model, the AMPs, typically helical molecules, align along the membrane normal and form aggregates in the form of transmembrane pores with the hydrophobic residues interacting with the non-polar lipid chains, while the hydrophilic peptide residues line the lumen of the pore. In the toroidal pore model, the AMPs induce the bending of the lipid head-groups in a toroidal mode, after binding to them, and form transmembrane pores and unlike barrel-stave model, the lumen of the pore is lined with both the peptide residues as well as the lipid head groups. AMPs like magainin, melittin and protegrins have been shown to disrupt the membrane in toroidal mode [97, 98] , while helical peptides like alamethicin are known to function through barrel-stave mode [99, 100].

Less idealistic variants of the toroidal-pore models have been suggested such as the disordered toroidal-pore [101] and aggregate [102] models. The disordered toroidal-pore model differs from the original primarily in the orientations of the AMPs. While the partitioned AMPs are still tilted, the tilt angles are considerably smaller for most peptides as well as broadly distributed. In this model, relatively few peptides lining the interior of the pore are actually oriented perpendicular to the membrane interface while most lie relatively parallel to it. The pore formation is essentially a stochastic process with the majority of the AMPs clustered close to the outer leaflet of the bacterial membrane [101] . In the aggregate model, the AMPs form micellar aggregates with the membrane lipids and reorient without a preferential orientation to span the microbial membrane. This can

lead to a diverse range of peptide aggregate sizes and as a consequence, wide range in pore radii and characteristics. A notable difference of aggregate model from the previous mechanisms is in exhibiting negative, rather than positive curvature strain across the membrane. All the above modes, especially the latter two, can also account for the translocation of the AMPs across the microbial membranes through the collapse of transient pores. In addition to the above models, a more specific mechanism of antimicrobial action by polycationic flexible antimicrobial agents has also been recently suggested [56] which involves polymer-induced sequestering of anionic lipids leading to lipid phase separation in the microbial membrane. This can lead to demixing of the lipid domains and associated phase boundary defects.

## 1.3 Structural and dynamical properties of liquid water

### 1.3.1 Structure of a simple monoatomic model liquid

Liquids are characterized by spatially short range order (structure), which is lost at larger spatial separations. In other words, the packing of liquid molecules or atoms are correlated over short distances, but uncorrelated beyond. The order over short separations for a simple liquid is brought about by various non-covalent interactions which include non-specific excluded volume and electrostatic interactions. However, unlike the case of solids, molecules in a liquid have too much thermal energy to be held onto fixed positions. The liquid molecules can move relative to one another, thus destroying long-range correlations in their packing.

The extent of structure in liquids is commonly probed by measuring radial or pair distribution function(s) (*RDF* or $g(r)$) among its atomic constituents. $g(r)$ represents the probability of finding an atom at a spatial separation $r$ from another. For a perfectly crystalline solid, a plot of $g(r)$ vs. $r$ yields sharp delta function peaks at separations determined

by lattice spacings. On the other hand, $g(r)$ for an ideal gas is always constant, since two ideal gas atoms are completely non-interacting and all separations between them are equally likely. As a convention, $g(r)$ for an ideal gas is normalized to unity. As can be expected, for liquids the behavior of $g(r)$ is intermediate between solids and gases. Figure 1.10 shows $g(r)$ for a monoatomic model liquid interacting through Lennard-Jones interactions only. The plot can thus be studied as a minimalistic description of structure of a liquid.
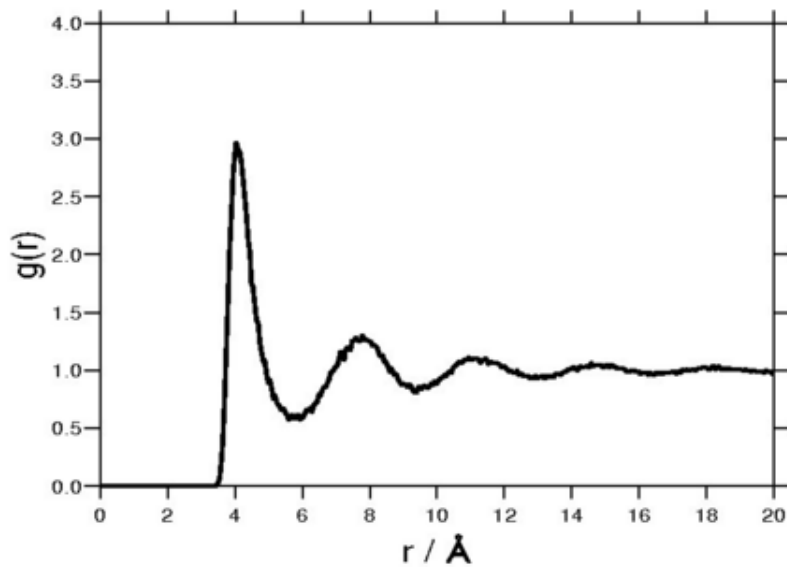


Figure 1.10: Radial (pair) distribution function for a model Lennard-Jones fluid. Courtesy [103].

Upto a minimum separation, the van der Waals diameter, $g(r)$ is necessarily zero. This region indicates that the overlap of two atoms is forbidden owing to excluded volume interactions. The forbidden region is immediately followed by a sharp peak, a region occupied by the nearest neighbors of an atom. At the origin of this peak lies the tendency of atoms to diffuse into the space occupied by the other atoms. The height of the first peak is strongly dependent on the specific nature of the interactions between the atoms. The high occupancy of the first peak region leads to a reduced availability of atoms in the region immediately following the first nearest neighbors. The first peak is thus followed by the minimum in $g(r)$. The resultant shell-like packing repeats itself over a few molecular diameters, with monotonic decrease of peak heights and broadening of the peaks, until at

larger separations $g(r)$ approaches its limiting value of unity [103, 104].

## 1.3.2 Unique properties of water
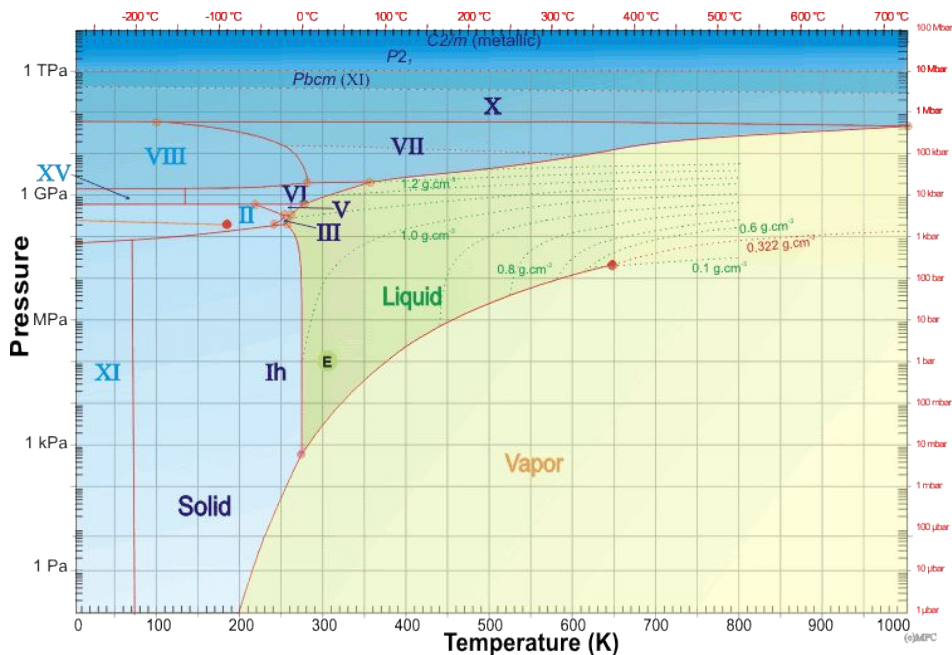


Figure 1.11: The pressure - temperature phase diagram of water, showing conventional (solid, liquid, vapor / gas) as well as exotic ice phases. Ice phases denoted through light-blue fonts have ordered network of hydrogen bonds, and appear at lower temperatures compared to the ice phases with disorder in their hydrogen bond network. Courtesy [105].

Albeit more complex than the model monoatomic liquid discussed above, a water molecule is simple in its chemical composition. It is formed by an oxygen (O) atom covalently bonded to two hydrogen (H) atoms. In spite of the apparent simplicity of molecular structure, however, water can be hardly characterized as a *simple* or *ordinary* liquid. Compared to other liquids of similar molecular geometry (eg. carbon dioxide ($CO_2$)), water has an unusually complex phase diagram which is still not completely understood. The known phase diagram for water is shown in Figure 1.11. In addition to the common liquid and gaseous (or *vapor)* phases, water can exist in multiple, often metastable solid or *ice* phases which are structurally distinct. These phases are separated by phase boundaries that share multiple triple points, and at least one critical point [105]. However, as can be seen from

44

Figure 1.11, the structurally exotic phases of water are mostly observed under extreme environmental conditions of very high or very low temperature and pressure.

The phase of water most pertinent to biological processes is its liquid phase. Not only is water the most abundant liquid on Earth's surface, contributing to the sustenance of habitable climate, it also accounts for ≥70% of the total mass of cellular contents. Most of the metabolic processes in living organisms thus take place in an aqueous environment. At the heart of its importance in biological processes is the ability of water to act as a universal solvent. Almost all known substances are soluble in water, albeit to varying degrees. Further, water can induce aggregation of molecules that have low aqueous solubility. In cellular processes the role of water ranges from transport of molecules, repulsion between as well as fusion of biological membranes, function of membrane channels, to inducing relevant conformations in proteins and nucleic acids [106–110]. Understanding the properties, and interactions of water under ambient conditions is essential to the understanding of complex biomolecular processes.
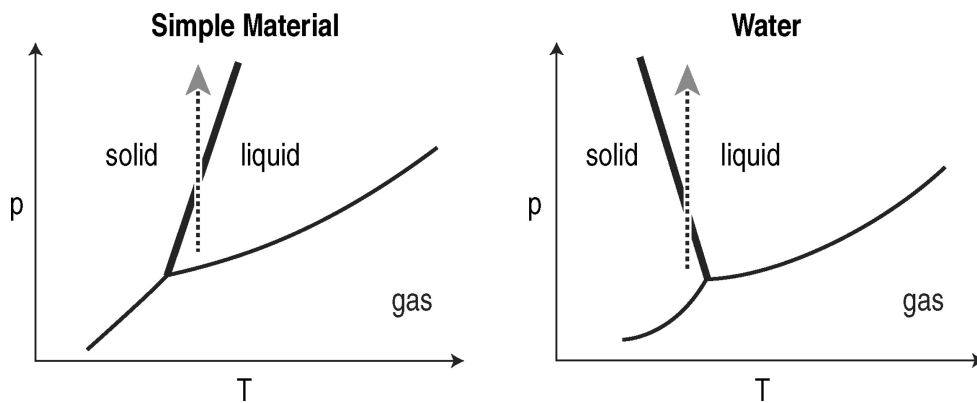


Figure 1.12: The simplified pressure - temperature phase diagram of a simple material (left) and water (right). Courtesy [111].

Even under ambient conditions of temperature and pressure, the properties of water are unique. This can be easily appreciated from the simplified phase diagrams shown in Figure 1.12. The phase boundary between the liquid and solid phases of water has a negative slope in the pressure - temperature phase diagram, while the same for ordinary materials is characterized by a positive slope. Thus water expands upon freezing, and

has a density maximum above its freezing point. Example of other unique properties of liquid water includes high values of melting and boiling points, heat capacity, dielectric constant and surface tension, as well as a unusually high mobility of $H^+$ and $OH^-$ ions through it [111, 112].

Many of the unique macroscopic properties of water originate from its microscopic structure and dynamics [10, 113]. In section 1.3.1, structure of a model liquid was discussed in terms of $g(r)$. While structure based on $g(r)$ is relevant for all liquids, a description based solely on $g(r)$ is often inadequate for more complex liquids [10]. For example, the $g(OO, r)$, or the oxygen-oxygen pair distribution function for liquid water indicates that water has structure reminiscent of considerably simpler liquid argon [10]. The limitation of $g(OO, r)$ in describing water structure is expected, since $g(OO, r)$ is devoid of information on the relative orientations of water molecules. In addition to the excluded volume effects, water structure can be attributed to the ability of water molecules to form an extensively connected network of hydrogen bonds. A water molecule has two partially polarized OH-arms, and two lone pairs. Each water molecule can thus participate in the formation of four hydrogen bonds, through which the four nearest neighbors of a water molecule arrange themselves in a nearly tetrahedral geometry [7, 114–116].

Though generally described as a structured liquid, the precise definition of structure of water is not without ambiguity [9, 10]. Owing to its overwhelming importance, structure of water has been probed over the years using a variety of definitions, which include bulk and thermodynamic, as well as molecular properties. Bulk and thermodynamic properties used to characterize water structure include quantities such as stiffness, openness, deficit of molar entropy with respect to ideal gas phase *etc* [117, 118]. A discussion of these properties is beyond the scope of this thesis. Interested readers are referred to review by Marcus [10] and references therein. In the two sections which follow, some relevant structural properties of water, spatially both short- and long-range, based on molecular packing and orientations will be discussed.

### 1.3.3 Short-range structure of liquid water

**Partial pair correlation functions**

The primary reason why $g(OO, r)$ for liquid water provides a limited measure of water structure is because it is dominated by the strong short-range repulsive interactions owing to excluded volume effects. However, a combination of the three possible pair correlations for water molecules, namely $g(OO, r)$, $g(OH, r)$ and $g(HH, r)$, can collectively provide considerably enhanced information on the molecular arrangements in liquid water. The three pair correlations, computed numerically using multiple models for water, as well as from neutron diffraction experiments (dotted lines) are shown in Figure 1.13. The $g(OO, r)$ can be observed to qualitatively resemble the same for a model liquid, shown in Figure 1.10. The first peak represents the most probable separation between two first nearest neighbor water molecules' oxygen atoms. The following weaker and broader peak corresponds to the same between two second nearest neighbor water molecules.

The $g(OH, r)$ correlation function is especially relevant owing to the information it provides on the hydrogen bonding in water molecules. The first peak in a $g(OH, r)$ curve has contributions only from the covalent OH-bonds. The second peak, with similar height as the first, indicates that H atoms from neighboring water molecules cluster around the O atoms of a water molecule. Together, the combination of $g(OO, r)$, $g(OH, r)$ and $g(HH, r)$ provides information not only on the spatial distribution of atomic species' in liquid water, but also the relative orientations of water molecules at small separations [119]. The drawback, however, is that the information on orientations is severely lost for separations greater than the second nearest neighbor distance. Correlations involving the mutual orientations of water molecules have been observed to be considerably longer ranged [11, 120].

Experimentally, a pair correlation function is computed in an indirect manner. Using experimental techniques such as X-ray and neutron scattering, one can compute the static
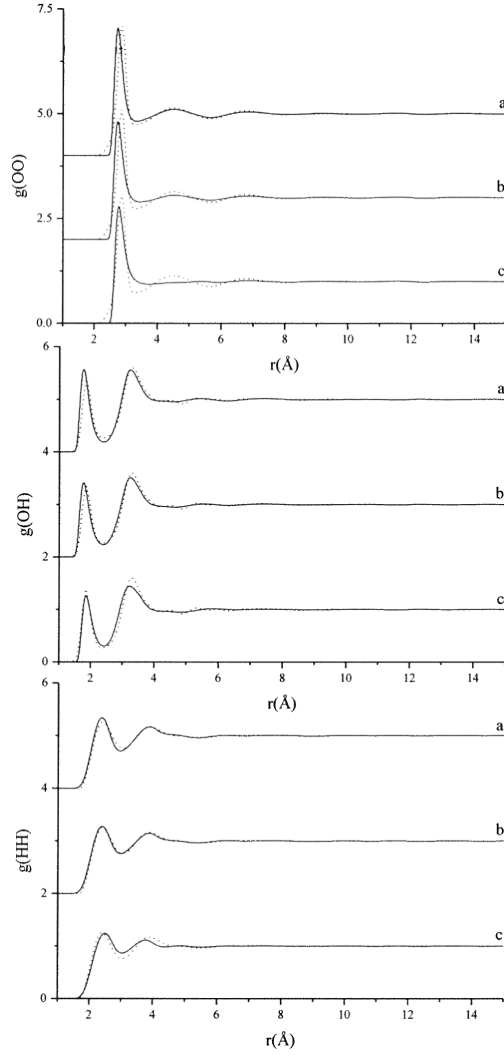
Figure 1.13: $g(OO, r)$, $g(OH, r)$ and $g(HH, r)$ pair correlation functions in liquid water, obtained with multiple computational water models ((a) SPC/E, (b) SPC, (c) TIP3P) and experiment. The solid and dotted lines represent results from numerical computations and neutron diffraction respectively. Curves are shifted by 2 units along vertical axis for clarity. Courtesy [121].

structure factor ($S(\mathbf{q})$) associated with the distribution of the relevant atoms. Here, $\mathbf{q}$ is a vector in the reciprocal space. The static structure factor is related to the pair distribution function through

$$S(\mathbf{q}) = 1 + \rho \int_V g(\mathbf{r}) exp(-i\mathbf{q}\mathbf{r}) d\mathbf{r} \tag{1.4}$$

where $\rho$ represents density. $g(r)$ can thus be computed through Fourier transformation of $S(\mathbf{q})$. However, the procedure is plagued by spurious structure appearing from artefacts in the data [119]. Accurate measurement of pair correlations has been possible with the development of novel modeling techniques used to interpret the experimental data, such

as reverse monte carlo and empirical potential structure refinement [119, 122, 123]. Co-ordination numbers can be obtained by integrating $g(r)$ correlations (upto a desired maximum separation $r_{max}$). Considering $r_{max}(OO) = 3.36\text{Å}$, mean coordination number of a molecule in liquid water, or the average number of nearest neighbors, has been estimated to be greater than four [119]. A coordination number greater than four immediately indicates that the regular tetrahedral packing associated with four hydrogen bonds per water molecule, observed in ice, is distorted in liquid water.

**Average number of hydrogen bonds**
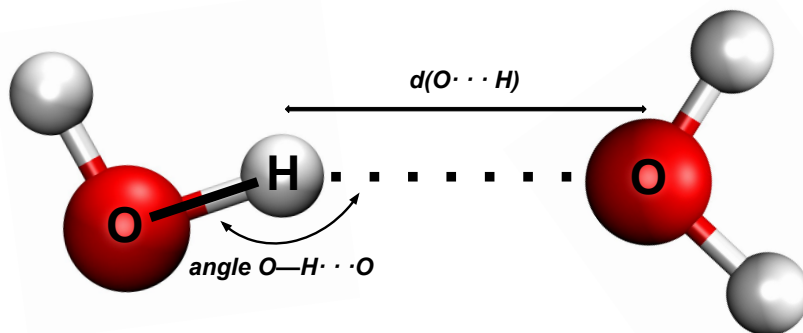


Figure 1.14: Schematic showing hydrogen bond between two water molecules. A geometric definition of hydrogen bond (see text) involves the separations and angle between the three indexed atoms (O, H, O).

For liquid water, the average number of hydrogen bonds per water molecule is less than four. The precise estimate of the number of hydrogen bonds, however, is complicated since the criteria for the definition of a hydrogen bond is not unambiguous. Popular definitions of a hydrogen bond are based on energetic [124] and geometric [124, 125] measures. Geometric definitions of hydrogen bond are based on defining cut-off values to distance $d(O \cdots H)$ and angle $O\text{---}H \cdots O$, and sometimes also to the distance $d(O \cdots O)$ (see Figure 1.14). "—" between two atoms indicates a covalent bond, while "$\cdots$" indicates that the atoms belong to neighboring water molecules. The energetic definition requires the energy associated with a hydrogen bond to be more negative with respect to a defined value.

Both sets of definitions have indicated that all the hydrogen bonds in liquid water are not equally strong. Extended X-ray absorption and X-ray Raman scattering spectroscopic measurements have indicated that hydrogen bonds in water can belong to two distinct subensembles, namely *strong* and *weak* [10, 126]. The explanation of the same is not without ambiguity, and two popular explanations have been suggested for the spectral signatures. In one explanation, the molecules in liquid water are envisaged to belong to two subensembles. The majority are characterized by two hydrogen bonds per water molecule, while relatively smaller number of water molecules maintain a tetrahedral coordination and form four hydrogen bonds per water molecule [10, 127, 128]. The alternate explanation involves mostly distorted tetrahedral arrangement of water molecules. The *weak* hydrogen bonds in this view are characterized by longer (larger $d(O\cdots H)$) and more bent hydrogen bonds [10, 129, 130]. With divided opinions in the explanation of the local hydrogen bonding environment and packing of water molecules, the average number of hydrogen bonds per water molecule is estimated to be ~(2.8 - 3.6), including both *strong* and *weak* hydrogen bonds.

**Tetrahedral packing of water molecules**
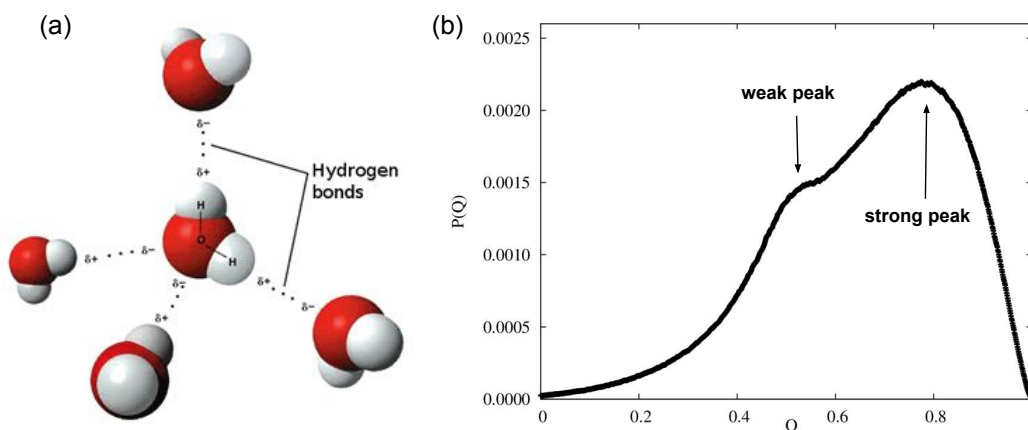


Figure 1.15: (a) Tetrahedral arrangement of water molecules, showing ideal hydrogen bonding among nearest neighbors (Courtesy [131]). (b) Representative probability distribution of local tetrahedral order parameter (Q), showing the two peaks corresponding to the bimodal nature.

It is generally accepted that water molecules pack in a nearly tetrahedral arrangement (see Figure 1.15(a)), maximizing the number of hydrogen bonds [7, 114, 116]. With increase in temperature, the tetrahedral packing is expected to be reduced, or skewed, and this is associated with a reduction in the average number of hydrogen bonds per water molecule. Experimental determination of tetrahedrality of water is an indirect process. Using scattering experiments, tetrahedrality and its temperature dependence is inferred from the behavior of the second peak in $g(OO, r)$ [132]. Computer simulations, however, allow for direct determination of tetrahedrality from the spatial packing of water molecules.

The tetrahedrality for a water molecule (indexed $i$) can be quantified using a local, or on-site order parameter ($Q_{(i)}$), defined as

$$Q_{(i)} = 1 - \frac{3}{8} \sum_{j=1}^{3} \sum_{k=j+1}^{4} \left( cos\Psi_{jik} + \frac{1}{3} \right)^2 \qquad (1.5)$$

where $j, k$ are used to index the four nearest neighbors of molecule $i$. $\Psi_{jik}$ are angles subtended at the location of the O atom of the $i$'th molecule, by lines joining it to the O atoms of its neighbors ($j, k$). $Q$ takes the value of 1 for ideal tetrahedral structures and 0 for ideal gas.

Consistent with the discussion on *strong* and *weak* hydrogen bonds above, the probability distribution of $Q$ is bimodal for liquid water (Figure 1.15(b)). The distribution of $Q$ shows that in liquid water there are two major subensembles of water molecules, one corresponding to greater local tetrahedral arrangement compared to the other. With increase in temperature, the number of water molecules contributing to the peak corresponding to greater tetrahedral arrangement decreases monotonously [7]. The temperature variation of $Q$ is thus consistent with reduction in water structure with increase in temperature.

The measure for tetrahedrality discussed above is essentially local, and is not a function of spatial separation ($r$). Recently, space dependent correlations have been proposed which involve the mean and variance of the local tetrahedral order parameter $Q$. Such correla-

tions have indicated that on increasing the temperature of water, tetrahedral order in water is distorted owing to the tendency of a fifth neighboring water molecule to be incorporated within the coordination shells of water molecules [7]. The space-dependent correlations based on $Q$, however, are short-range and decay within radial separations $<10\text{Å}$.

### 1.3.4 Long-range structure of liquid water

As described above, intermolecular correlations in liquid water have generally been characterized through correlations involving short range density fluctuations. The studies have suggested [11, 133–136] that at ambient conditions, the structure of liquid water is short range and the spatial distribution of water molecules are uncorrelated beyond a distance of $\sim(8\text{-}10)\text{Å}$. Correlation such as $g(r)$ are devoid of information on orientational correlations, especially at longer separations. Recent numerical and experimental results have suggested that such a description of order or structure in liquid water is incomplete and there exists considerably longer ranged orientational correlations in water that can be studied through dipolar correlations.

Experimental observations of such long-range dipolar or angular correlation are not accessible to conventional spectroscopic techniques owing to the lack of positional ordering at longer length scales. Recently they have been studied by the use of second-harmonic, or hyper-Rayleigh light scattering (HRS) experiments, which can probe non-centrosymmetric orientational fluctuations in polar liquids [12, 137–139]. Results have indicated that the range of the orientational correlations are at least an order of magnitude larger than the length scale of density fluctuations. Also, the nature of their decay is not diffusional, but has the characteristics of a propagating wave [140]. The nature of molecular interactions leading to such long-range correlations is not known without ambiguity. HRS data have been best interpreted through a distribution in molecular (dipolar) orientations that take the form of a transverse random vector field. Based on the assumption, the correlations are envisaged to arise owing to dipole-dipole interactions, which decay

as $r^{-3}$ at long-range [12, 139]. On the contrary, computational studies have indicated that long-range orientational correlations in liquid water are not a consequence of long-range dipole-dipole interactions, and decay at long-range in an exponential manner [11]. Direct quantitative comparison of results from HRS experiments and numerical computations is challenging since (a) system dimensions studied using HRS are well beyond the scope of atomistic simulations [139] and (b) HRS does not provide explicit information of microscopic correlations among molecular dipoles [140].

Computational studies of indicate that the long-range nature of orientational correlations originates from fluctuations of the underlying hydrogen bond network of water and is not a consequence of long-range electrostatic interactions [11]. While hydrogen bonding interactions are intrinsically short range, the fluctuations of the hydrogen bond network are restricted by topological constraints [125, 141]. The entropy of hydrogen bond network thus has contributions from both single-water and collective dynamics [142, 143]. In a statistical description of liquid water, the hydrogen bond fluctuations need to be consistent with a "sum rule", which states that sum of density of dangling bonds (i.e., a water molecule's bond arms which are not hydrogen bonded to any other molecule) and twice the density of hydrogen bonds should be equal to four times the density of water molecules [141]. The dynamics of the hydrogen bond network of water, governed by orientational fluctuations of water molecules, thus results in orientational correlations that are substantially long-range compared to the length scale ($\sim 2\mathring{A}$) of hydrogen bonding interactions [11, 141, 144].

Mutual orientations of water molecules separated in space can be studied computationally through correlations involving dipolar and higher order multipole (*eg*. quadrupole) moments of the constituent molecules [11, 120, 145, 146]. Studies have shown that correlations involving quadrupolar fluctuations in liquid water disappear within a separation of $\sim 3\mathring{A}$ [11, 120]. Two well studied correlations involving dipolar orientations of two water molecules separated at a distance $r$ involve (a) alignment of the dipoles with respect to
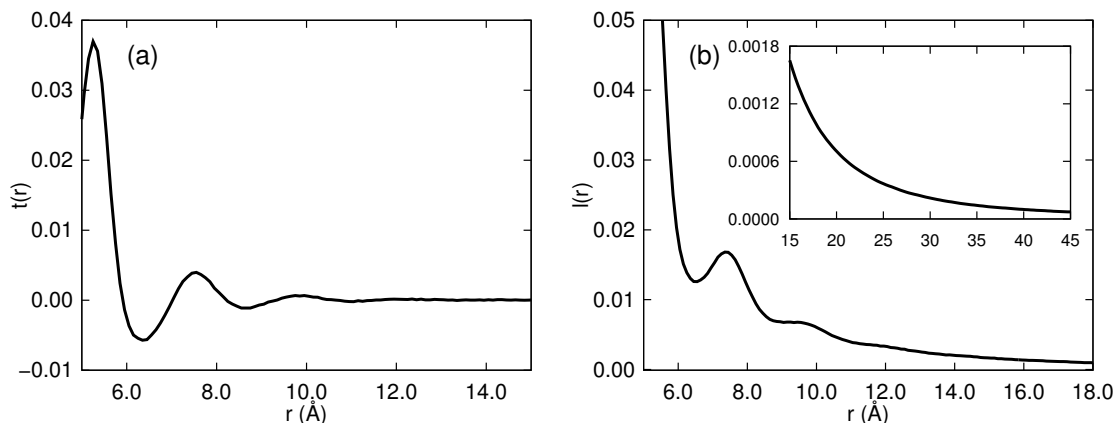
Figure 1.16: (a) $t(r)$ and (b) $l(r)$ correlations computed for liquid water (at 298 K and 1 atm, with TIP4P-Ew model for water. The inset plot of (b) shows the exponential decay of $l(r)$ correlation beyond the solvation shell region.

themselves (trace correlations, or $t(r)$), and (b) alignment of the dipoles with respect to the radial vector separating them (traceless or longitudinal correlations, $l(r)$) [11]. Both of these correlations show oscillatory solvation structure and are longer ranged compared to density correlations in water. They are shown in Figure 1.16. $t(r)$ correlations vanish beyond $\sim 14\mathring{A}$ in liquid water in compliance with rotational symmetry. A non-vanishing $t(r)$ at long separations would induce spontaneous polarization in liquid water, characterized by a large dipole moment of the system in general, or of large orientationally correlated domains. $l(r)$ correlations are oscillatory in nature and always positive for water in the absence of solutes, or impurities. $l(r)$ is reported [11] to be non-vanishing even at $\sim 75\mathring{A}$ separations, and decays exponentially beyond solvation region ($14\mathring{A}$) with largest correlation length of $\sim 24\mathring{A}$. The long-range nature and oscillatory decay of orientational correlations have also been evidenced through angular correlation functions computed using classical density functional theory calculations [140].

The presence of long-range correlations in liquid water, and the influence of solutes on them can be of crucial relevance in the understanding of complex biologically relevant processes which involve long-range interactions, likely mediated by water or aqueous solutions. Examples of such processes include hydrophobic aggregation [16] and the Hofmeister series [147]. The mathematical definitions of the correlations $t(r)$ and $l(r)$

will be elaborated in section 2.4.

### 1.3.5 Introduction to water dynamics

The extensively connected network of hydrogen bonds in liquid water, which is at the heart of its structural properties, is also highly dynamic in nature. Water molecules incessantly exchange their hydrogen bond partners through reorientational motions, whence the local hydrogen bond network rearranges at the picosecond time-scale [148]. The disruption of existing hydrogen bonds and formation of new ones is known to take place in ice too [114, 149]. Recent progress in understanding the dynamics of the hydrogen bond network has, however, shown that the mechanisms involved for the two phases have characteristic differences. In ice, the water molecules are strongly constrained against translational motion. Exchange of hydrogen bond partners for a water molecule in ice is thus restricted to the nearest neighbors. In the liquid phase, the occupancy of the first solvation shells of water molecules (nearest neighbors) continuously changes owing to diffusion. This rearrangement is associated with fluctuations in the coordination number of water molecules about its mean value, close to four. It is now understood that such fluctuations play a critical role in the rearrangement of hydrogen bonds liquid water,- coupling the translational and rotational degrees of freedom and imparting collective nature to reorientational dynamics [148, 150].

The complex nature of water molecules' reorientational motion, and and the influence of solutes on the same is extremely relevant in the study of various processes in chemistry and biology. In a statistical description of liquid water, the dynamics of the underlying hydrogen bond network imbibes liquid water with a very large configurational entropy [11]. The reorientational motion of water molecules are critical to several chemical reaction pathways, such as acid dissociation, proton transport and $S_N2$ reactions [112, 148]. Dynamics of water molecules in the solvation shells of biomolecules are known to modulate their conformations, as well binding to other molecules [110, 113, 151]. The reorien-

tational motion of water molecules is also necessary to the transport of water and ions through membrane channels, often in a manner similar to single-file diffusion [108, 109, 152]. For these reasons, the dynamical behavior of liquid water has been probed extensively using both experimental and computational techniques.

### 1.3.6 Experimental study of water dynamics

Experimental methods to study the dynamical behavior of liquid water (and aqueous solutions) can be broadly classified into two classes, techniques which probe the collective dynamics of water molecules, and those which provide information on the dynamical behavior of single water molecules. Examples of the former include dielectric relaxation at terahertz frequencies (DR) and optical Kerr-effect spectroscopy [153, 154]. Dynamics of single water molecules are best studied to date using femtosecond time-resolved infrared pump-probe spectroscopy (fs-IR) [155–157]. Other techniques belonging to the latter class include NMR (through measurement of spin-lattice relaxation time) [158, 159] and quasi-elastic neutron scattering [160].

DR spectroscopy studies the propagation of a (0-1) terahertz pulse and its frequency dependent refraction and absorption upon passing through liquid water [14, 157]. Refractions by water molecules cause delay in propagation, while absorptions reduce the amplitude of the pulse. The dipoles corresponding to water molecules keep reorienting under the influence of the externally applied oscillatory electric field (pulse). An inability to do so (at resonant frequencies) results in the observation of strong absorption peaks. DR spectroscopy for liquid water is observed to result in two such absorption peaks at frequencies of 20 gigahertz (stronger) and 0.6 terahertz (weaker). The 20 gigahertz absorption peak corresponds to the slower time-scale in water reorientations, and maps to the Debye relaxation time ($\approx 8$ ps). The physical origin of the faster absorption peak around 0.6 terahertz is debated [161], but is often ascribed to reorientations of under-coordinated water molecules with relaxation time $\approx 250$ fs [14].

fs-IR technique uses two successive short pulses to probe the reorientational dynamics of water molecules. The first pulse, termed the *pump* or excitation pulse, is used to excite OD-stretch modes in a mixture of HDO and $H_2O$. The pump pulse preferentially excites OD bonds which are aligned to its polarization axis, thus resulting in a *tagged* sub-ensemble of molecules. Using the second (*probe*) pulse, it is thus possible to measure signals coming from tagged molecules, both parallel and perpendicular to the excitation axis. A comparison of the two yields the anisotropy decay as a function of duration between the pulses, or the delay time. The temporal resolution of the technique ($\sim$ 150 fs) is high enough to study the anisotropy decay resulting from the reorientational motion of individual water molecules. The technique, however, is limited in the measurement of collective reorientational modes, since the lifetime of the excited vibrational modes is less than 10 ps, beyond which the tagged nature of the molecules is lost [14, 148].

### 1.3.7 Mechanism of water reorientation

The experimental techniques described above can measure the time-scales corresponding to the reorientational motions of water molecules, both collective and single molecule. Experiments, however, are limited in the description of the underlying mechanism(s) involved in the reorientations of water molecules through which they break hydrogen bonds, and successively form new ones [148]. A mechanistic description of the reorientational motions of molecules in liquid water, which is consistent with the experimentally obtained relaxation times, has been obtained recently through the use of computer simulations [13, 150]. This mechanism is known as the *extended jump mechanism* (EJM), and states that an exchange of hydrogen bond partners by the (hydrogen bond donor) OH arm a water molecule primarily involves a large amplitude jump in the orientation of the OH arm [150]. Prior to the EJM mechanism, the reorientations of water molecules was envisaged to take place through the Debye diffusive model [162]. In the following, the two mechanisms are briefly outlined.

**The Debye diffusive model**

The Debye diffusive model describes the reorientations of water molecules through over-damped rotational Brownian motion [13, 162]. A water molecule is not allowed to rotate freely since the hydrogen bonds with its neighbors impose strong restoring torques on it. According to the Debye diffusive model, reorientational motion of a water molecule is initiated by the rupture of one of the hydrogen bonds formed by its donor OH arms. The *free* OH arm (and hence the water molecule) then reorients through infinitesimally small angular displacements in search of a new hydrogen bond acceptor. Conceptually appealing, the model however fails to justify several experimental and computational observations, such as

- Free OH arms in bulk liquid water have generally been observed to be highly unstable, not in good agreement with the presence of diffusing free OH arms [163].

- Trajectories from MD simulations of liquid water indicate that reorientations of water molecules are characterized by sporadic large angle *jumps*, as shown in Figure 1.17 [13].

- The model severely underestimates the characteristic reorientation time corresponding to the second order reorientational autocorrelation function (see section 2.5) of water molecules [13, 150].

- The ratio of characteristic reorientation times obtained from first and higher order reorientational autocorrelation functions deviate from the theoretical values based upon ideal diffusive picture [13, 150].

**The extended jump mechanism (EJM) for water reorientations**

According to the EJM, three processes contribute to the reorientational dynamics in liquid water. They are (a) libration of hydrogen bonded OH arms, (b) large amplitude angular

58
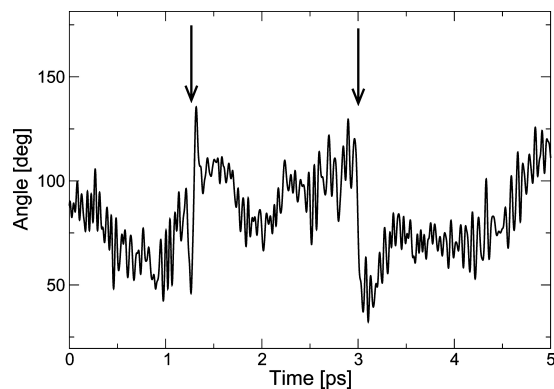
Figure 1.17: Time evolution of the angles between a selected OH-bond of a water molecule and a laboratory frame axis. The arrows indicate the presence of intermittent large angle jumps, separating intervals over which the angular displacements are relatively small. Courtesy [13].

jumps by donor OH arms in trading hydrogen bond acceptors, and (c) frame reorientation [150]. The time-scales corresponding to the three individual processes increases from (a) to (c). They are briefly described in the following. A detailed description of the processes can be found in review by Laage *et.al* [148], and references [13, 150].

Libration corresponds to the inertial wobbling motion of a hydrogen bonded OH arm, within a cone whose axis is the hydrogen bond donor-acceptor direction. The freedom for its inertial rotational motion is strongly constrained owing to restoring torque from the hydrogen bond. The semi-vertical angle of the cone is thus dependent on the strength of the hydrogen bond, and decreases with increased strength. The librational motions are extremely rapid, with sub-picosecond time-scale. The overall reorientations caused by librational motions are small. The noisy, small angle fluctuations shown in Figure 1.17 arise from librations.

Large amplitude angular jumps is the most important aspect of the EJM. The pathway corresponding to such jumps is schematically shown in Figure 1.18, where $O^\star H^\star$, the donor OH arm of a water molecule, trades its hydrogen bond with $O^a$ for one with $O^b$. For a majority of such events, the water molecule with $O^b$ is initially situated in the second solvation shell of the water molecule with $O^\star$.

Owing to inherent fluctuations in the hydrogen bond network, the water molecule with

59
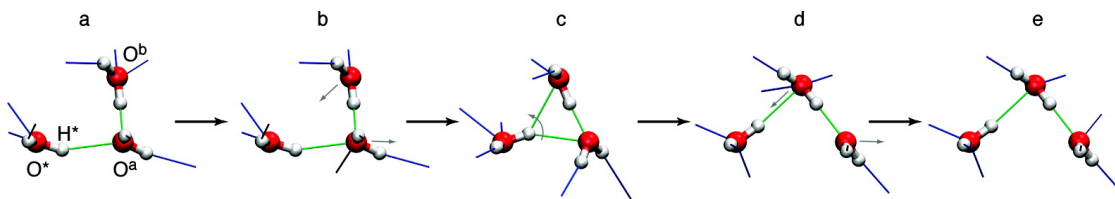
Figure 1.18: Schematic representation of the jump mechanism involved in EJM. The pathway, along with the individual states (a-e) are described in the text. Green lines represent hydrogen bonds formed between the three water molecules shown in the figure. Blue lines represent hydrogen bonds formed with surrounding water molecules (not shown). Courtesy [13].

$O^a$ gets transiently over coordinated while that with $O^b$ gets under coordinated. Such a situation is shown through transition from state (a) to (b) in Figure 1.18. This induces motions away from and towards $O^\star$ for water molecules with $O^a$ and $O^b$ respectively, with an associated reduction in strength of $(H^\star \cdots O^a)$ hydrogen bond. When $O^a$ and $O^b$ are equidistant from $O^\star$, the $O^\star H^\star$ arm can reorient through a large amplitude angular jump, in the process breaking the hydrogen bond with $O^a$, and forming one with $O^b$ (Figure 1.18(d)). The transition state for the event is shown in Figure 1.18(c), where $H^\star$ forms a symmetric bifurcated hydrogen bond with both $O^a$ and $O^b$. The presence of this transition state is known to considerably reduce the free energy barrier associated with the disruption of the hydrogen bond $H^\star \cdots O^a$. Subsequently, the water molecule with $O^b$ replaces the the water molecule with $O^a$ in the first solvation shell of the water molecule with $O^\star$ (Figure 1.18(e)). It is important to note that every large angle jump does not lead to a change of hydrogen bonding partners. A hydrogen bond broken through a large amplitude jump can be reformed immediately owing to restoring torques. The jump mechanism for exchange of hydrogen bonds take place at the picosecond time-scale.

The third component in EJM involves the slow reorientations of intact hydrogen bond axes between successive hydrogen bond exchanges. This motion arises since the water molecules do not remain frozen between jumps, and hydrogen bonded water molecules can undergo coupled reorientational motion through the tumbling motion of the local molecular axis. This process also takes place at the picosecond time-scale, but is slower compared to the hydrogen bond exchange (jump) dynamics.

## 1.4  Overview of the thesis

The rest of the thesis is organized as follows:

The molecular dynamics (MD) simulation technique is described in Chapter 2, with a description of the various bonded and non-bonded interactions between constituent sites. Classical atomistic models used for lipids and water in the reported studies are detailed, followed by a brief description of some relevant computational observables.

In Chapter 3, the interactions of multiple cationic synthetic random antimicrobial polymers based on methacrylates (bbM4 polymers) with a model bacterial membrane consisting of POPE and POPG lipids is described. The results show that the cationic polymers form a micellar aggregate in water phase and the aggregate, when interacting with the bacterial membrane, induces clustering of oppositely charged anionic lipid molecules to form clusters and enhances ordering of lipid chains. The model bacterial membrane, consequently, develops lateral inhomogeneity in membrane thickness profile compared to polymer-free system. The individual polymers in the aggregate are released into the bacterial membrane in a phased manner. The partitioned polymers preferentially adopt facially amphiphilic conformations at lipid-water interface, despite lacking intrinsic secondary structures such as $\alpha$-helix or $\beta$-sheet found in naturally occurring antimicrobial peptides.

In Chapter 4, the study of membrane interactions of bbM4 polymers is extended to lipid membranes of varying composition. The model membranes studied differ in the composition of the lipid head groups, as well as the degree of saturation in the lipids' acyl tails. The influence of varying lipid composition on the observations from Chapter 3, such as facially amphiphilic conformations of the polymers, phased release from the aggregate and the mechanism of antimicrobial action through lateral inhomogeneity in membrane properties is discussed.

Chapter 5 describes the importance of hydrogen bonding in antimicrobial polymer - bac-

terial membrane interactions. The antimicrobial polymers described in this chapter are characterized by side chain amphiphilicity. The interactions of multiple polymer types with model bacterial membranes consisting of POPE and POPG lipids is described. The polymers differ in their hydrogen bonding abilities, as well as their relative hydrophobic contents. Insertion of the polymers into the membranes, governed by polymer - membrane energetics, is observed to be dependent on hydrophobic content. The membrane - bound polymer conformations, and the relative influence on lipid bilayer properties is observed to be driven by hydrogen bonding interactions.

Chapter 6 describes the influence of simple salts such as sodium chloride (NaCl), potassium chloride (KCl), caesium chloride (CsCl) and magnesium chloride ($MgCl_2$) on the long-range dipolar correlations in liquid water. Observed effects are explained through orientational stratification of water molecules around ions, and their long range coupling to the global hydrogen bond network by virtue of the sum rule for water. Inadequacy of the notion of structure making and breaking by dissolved ions in explaining the observations is discussed. The observations for single hydrophilic solutes are contrasted with the same for a single methane ($CH_4$) molecule. We observe that even a single small hydrophobe can result in enhancement of long range orientational correlations in liquid water,- contrary to the case of dissolved ions, which have been observed to have a reducing effect. The observations are discussed in the context of hydrophobic effect.

Chapter 7 describes the effects of dissolved caesium chloride (CsCl) and magnesium chloride ($MgCl_2$) at moderate to high concentrations on dynamical properties of water molecules. Results reveal that the presence of strongly solvated ions ($Mg^{2+}$) can induce reorientational slowdown of water molecules which are beyond the first ion solvation shells. The observation is explained through ion-induced perturbations in the hydrogen bond network of water, leading to the formation of bulk-like domains with 'defect sites' on boundaries of such domains. In contrast, addition of CsCl to water does not perturb the hydrogen bond network of water significantly even at higher concentrations.

# Chapter 2

# Methods

## 2.1   Molecular dynamics simulation

Molecular Dynamics (MD) is a computer simulation method which involves solving Newton's equation of motion for a system with $N$ interacting particles. MD simulation is one of the standard techniques used to study biomolecular systems, which in principle is capable of affording a detailed view of the natural dynamics of the systems under study. Data obtained from experimental techniques are generally robust. The interpretations of experimental data, however, are often dependent on the models used to analyze the data. The development of accurate models requires knowledge of the structure and dynamics of the systems, which is often beyond the scope of existing experimental techniques. Experiments and MD simulations are thus complementary techniques, together providing information on both average properties of a system, and the underlying interactions responsible for the same. The applicability of MD to complex biomolecular systems, and the accuracy of the inferences from it are critically dependent on several factors. These include system sizes and simulation times, choice of initial configurations, accuracy of the interaction potentials (force fields) and choice of ensembles and boundary conditions.

Biomolecular systems are characterized by the presence of complex *many-body* interac-

tions, which can lead to correlations that are long-range in both space and time. A realistic study of a given property of such systems thus requires that the spatial dimensions be considerably larger than (*at least* twice, with periodic boundary conditions) the spatial range of the longest correlation length. The issue is severely restrictive, since the nature and range of such correlations are often not known *a priori*. A method conventionally used to estimate the minimum required system size is *system size scaling*. With system size scaling the desired properties, or *observables*, are computed from simulations involving increasingly larger systems, with convergence of the results used as a measure for adequacy. Further, the mechanistic processes in complex biomolecular systems are generally distributed over a wide range of time-scales. For example, in a multi-component lipid membrane, bond vibrations take place over femtoseconds, while reorganizations of membrane lipids can be distributed over nanoseconds to tens or hundreds of microseconds, depending on the specific process. Intrinsic to MD simulations is the ergodic hypothesis, which implies that time-averaged molecular properties obtained from *adequate* sampling in time approach the experimentally measurable ensemble averages [164]. In other words, computing an observable using MD requires that within the analysis time, the property is averaged over all microstates relevant to the observable. Rational choice of initial configuration is necessitated by the inherently complex nature of free energy landscape, common to most relevant biomolecular systems. Limited in simulation time, conventional MD simulation requires fast relaxation of the initial configuration to the immediate neighborhood of global free energy minima, or *equilibration*. An erroneous choice of initial configuration can cause a system's dynamical evolution to be confined to a local free energy minimum, thus resulting in wrong estimates for the computed observables.

These restrictions have been appreciably, albeit partially, overcome through (a) rapid development in computer hardware, and development of dedicated, highly scalable programs or packages such as NAMD [165], GROMACS [166], Amber [167], LAMMPS [168]. (b) availability of extensive database [169] for high resolution structures of biomolecular conformations, and servers [170] and softwares [171] capable of generating relevant

64

initial conformations.

## 2.1.1 Interactions in MD

As described above, MD involves time evolution of $N$ body systems. The instantaneous evolution of a *site*[1] is determined by the force acting on the same owing to its interactions with the rest $(N-1)$ sites. The force on $n^{th}$ site $(F_n)$ can be described as

$$F_n = -\nabla V_n \tag{2.1}$$

where $V_n$ is the net potential through which the site $n$ interacts. $V_n$ can have contributions from both bonded and non-bonded interactions. A force field is a description of $V_n$, both in terms of explicit mathematical formalism, and the interaction parameters. Several highly optimized force fields exist for biomolecular systems, which include CHARMM [172], Amber [167], OPLS [173] etc. The following description would be based on the CHARMM force field, which has been used for the studies included in this thesis.

The potential function $V$ can be expressed as

$$
\begin{aligned}
V = & \sum_{bonds} k_{ij}(r_{ij} - b_0)^2 + \sum_{angles} k_{\theta_{ijk}}(\theta_{ijk} - \theta_0)^2 + \sum_{Urey-Bradley} k_{u_{1-3}}(r_{1-3} - u_0)^2 \\
& + \sum_{dihedrals} k_{\phi_{ijkl}}[1 + cos(n_{ijkl}\phi_{ijkl} - \phi_0)] + \sum_{impropers} k_{\omega_{ijkl}}(\omega_{ijkl} - \omega_0)^2 \\
& + \sum_{non-bonded} \left( \varepsilon_{ij}\left[ \left(\frac{R_{min_{ij}}}{r_{ij}}\right)^{12} - \left(\frac{R_{min_{ij}}}{r_{ij}}\right)^6 \right] + \frac{1}{4\pi\epsilon_0\epsilon_r}\frac{q_iq_j}{r_{ij}} \right)
\end{aligned}
\tag{2.2}
$$

---

[1] A site can be an atom or a *bead* representing a collection of atoms, depending on the system resolution. Discussed in section 2.2.
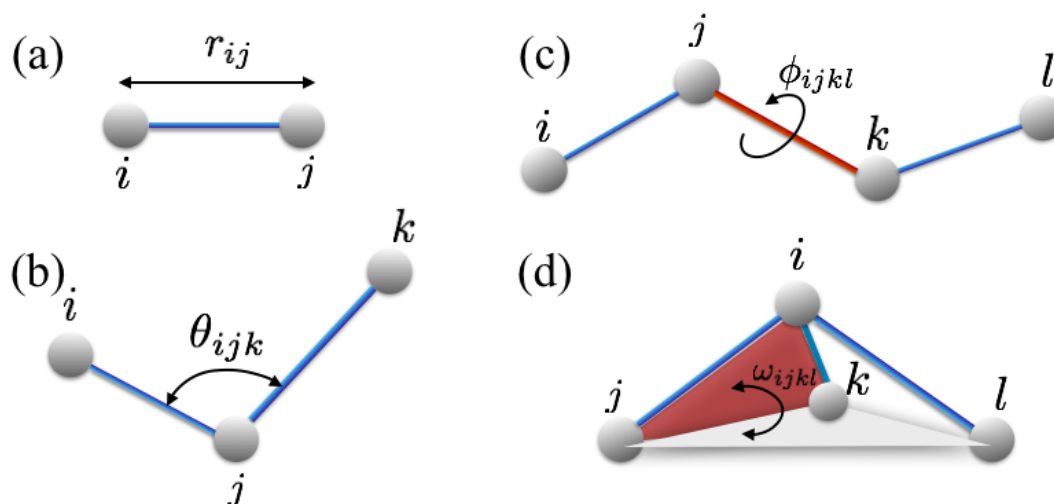
Figure 2.1: Schematic description of the bonded interactions between sites.

**Bonded interactions**

The first term in equation 2.2 represents the bond energy between two covalently bonded sites $(i, j)$, described through a harmonic bond potential. $r_{ij}$ is the instantaneous separation between the pair, $b_0$ is the reference bond length, and $k_{ij}$ is the force constant associated with the bond (Figure 2.1(a)). The harmonic bond potential is a Taylor approximation about the reference bond length.

The second and third terms in equation 2.2 together describe the angular vibrational modes, corresponding to the fluctuations in the angle between two consecutive bonds (Figure 2.1(b)). The second term is also represented as a harmonic potential, involving instantaneous angle $(\theta_{ijk})$, reference angle $(\theta_0)$ and the force constant $(k_{\theta_{ijk}})$. The third, Urey-Bradley term is specific to CHARMM force fields. The Urey-Bradley term additionally restrains the motions of the two bonds associated with an angle. With reference to Figure 2.1(b), the term can be written as $\sum k_{u_{ik}}(r_{ik}-u_0)^2$, where $k_{u_{ik}}$ is the harmonic force constant, $r_{ik}$ is the instantaneous separation between the pair $(i, k)$ and $u_0$ is the reference separation.

The fourth, or the dihedral term constrains the rotation around a bond (bond between sites

($j, k$) in Figure 2.1(c)). The potential involves the angle ($\phi_{ijkl}$) between planes containing sites ($i, j, k$) and ($j, k, l$). The multiplicity ($n_{ijkl}$) is a non-zero positive integer which specifies the number of minima observed with 360° rotation about the bond. The dihedral interactions are optimized to reproduce the experimentally observed energy differences between *trans* and *gauche* conformations, as well as the rotational energy barrier. The dihedral potential is often written as a sum of multiple potentials with varying multiplicity and / or reference angle ($\phi_0$).

The fifth term in equation 2.2 involves improper torsion angle ($\omega_{ijkl}$) between four atoms whose bond connectivity is shown in Figure 2.1(d). Such interactions are used to maintain planarity in the molecular structure. The potential can be represented as a harmonic function.

**Non-bonded interactions**

The non-bonded term in equation 2.2 is a combination of van der Waal and electrostatic interactions. In theory, each pair of sites ($i, j$) interacts through such interaction. In MD simulations, however, these interactions are often omitted, or scaled for sites interacting through bonded interactions. Sites interacting through bonded interactions can be separated by a maximum of three covalent bonds (for dihedral interactions). The omission or scaling of non-bonded interactions thus applies to pairs of sites separated by three covalent bonds, or less [174]. The explicit procedure for the same, varies with the force fields and the simulation packages.

The first non-bonded term represents the dispersion, or van der Waals interaction between site pairs ($i, j$). In equation 2.2, this is modeled as a 6-12 Lennard Jones (LJ) potential. The interaction potential is zero at infinite separation. As the separation is reduced, the interaction turns attractive and attains a minimum at a critical separation equal to the collision diameter. As the separation is further reduced, the interaction turns strongly repulsive, which prevents overlap between sites. The nature of the interaction is schematically

67

shown in Figure 2.2. Though in principle a long-range interaction, for all practical purposes the interaction can be considered as short-range. For computational efficiency, the LJ interactions are invariably truncated beyond a cut-off separation. To avoid singularities in the first (force) and higher derivatives of the potential, the truncation is implemented through an associated *switch* function, which takes the potential to zero continuously between switch and cut-off distances (Figure 2.2). The switch distance is necessarily smaller than the cut-off distance.
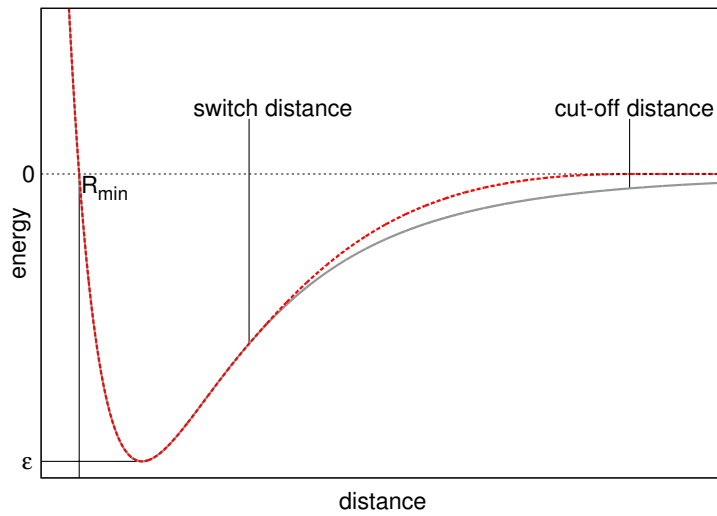


Figure 2.2: Plots showing the nature of LJ interactions, without (continuous, gray) and with (dashed, red) switch function. The parameters corresponding to the interaction potential are shown in the figure.

In equation 2.2, the two-body LJ interaction potential is characterized through two parameters, $\varepsilon_{ij}$ and $R_{min_{ij}}$. The former represents the well depth of the potential, and the latter corresponds to the separation at which the LJ curve intersects the x-axis (Figure 2.2). The force fields generally assign the parameters for interactions between identical sites, from which the pair potential parameters between non-identical sites are derived according to the Lorentz-Berthelot mixing rule [175]. According to the Lorentz-Berthelot mixing rule,

$$\varepsilon_{ij} = \sqrt{\varepsilon_{ii}\varepsilon_{jj}} \quad \text{and} \quad R_{min_{ij}} = \frac{1}{2}\left(R_{min_{ii}} + R_{min_{jj}}\right) \tag{2.3}$$

The second non-bonded term is the electrostatic interaction (Coulomb) potential, where

$(q_i, q_j)$ are the charges of sites $(i, j)$, separated by distance $r_{ij}$. $\epsilon_0$ and $\epsilon_r$ are the permittivity of free space, and relative permittivity of the medium respectively. Coulomb interactions are essentially long range, and hence the most difficult to compute in an MD simulation. All pairs of sites $(i, j)$ in a system interact through Coulomb interactions. Further, in a system with periodic boundary conditions, the sites interact through Coulomb interactions with all periodic images too. The computation of Coulomb interactions in a periodic system thus requires special techniques such as the *Ewald summation*, which is briefly outlined below. Interested readers are referred to book by Frenkel & Smit [176] for a detailed derivation.
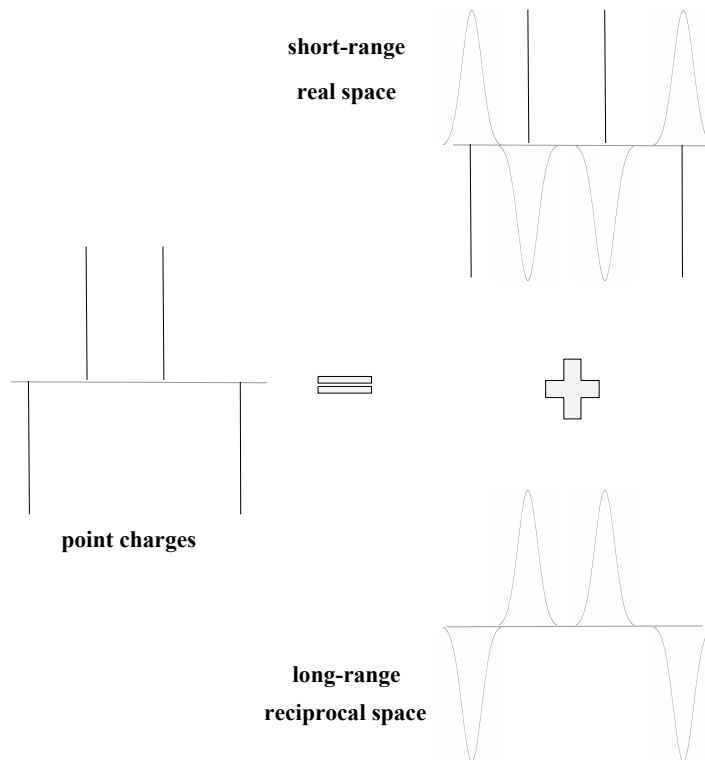


Figure 2.3: The Ewald summation scheme for computing electrostatic interactions between point charges. The short-range screened interactions are computed in direct space. The contributions from the complementary screening charge distribution is computed in the reciprocal space.

**The Ewald Summation :**

For a system with $N$ point charges $q_i$ within a cubic box with side length $L$ with periodic

boundary conditions, the Coulomb interaction energy for the system ($U_{Coul}$) is given by

$$U_{Coul} = \frac{1}{2} \sum_{i=1}^{N} \frac{q_i}{4\pi\epsilon_0\epsilon_r} \left( \sum_{j,\mathbf{n}}' \frac{q_j}{|\mathbf{r}_{ij} + \mathbf{n}L|} \right) \tag{2.4}$$

where $\mathbf{n}$ represents periodic images. The prime on the second summation indicates that the sum is over all $j$, except $j = i$ when $\mathbf{n} = \mathbf{0}$, thus excluding self interaction. The sum in equation 2.4 is only conditionally convergent [176], and can not be used in an MD simulation. The reason for it is that the potential generated by an un-screened point charge falls of as $r^{-1}$, and is essentially long-range. The Ewald summation scheme is schematically shown in Figure 2.3. In Ewald summation, short-range screened electrostatic interactions are computed in real space, while the long-range contributions from the complementary screening charge distribution is computed in the reciprocal space. The procedure is demonstrated with a simplified scenario.

Let us consider a point charge $q_i$ at a position $\mathbf{r_i}$. The charge density can be written as a delta function

$$\begin{aligned} \rho(\mathbf{r}) &= q\delta(\mathbf{r} - \mathbf{r}_i) \\ &= (\rho(\mathbf{r}) - q\rho_{Gauss}(\mathbf{r})) + q\rho_{Gauss}(\mathbf{r}) \ . \end{aligned} \tag{2.5}$$

Here $\rho_{Gauss}(\mathbf{r})$ is a Gaussian distribution given by

$$\rho_{Gauss}(\mathbf{r}) = \left(\frac{\alpha}{\pi}\right)^{\frac{3}{2}} exp\left(-\alpha |\mathbf{r} - \mathbf{r}_i|^2\right) \ .$$

$(\rho(\mathbf{r}) - q\rho_{Gauss}(\mathbf{r}))$ represents a screened charge distribution, whence the electrostatic potential corresponding to it ($\phi_1(r)$) is short-range. It can be shown that $\phi_1(r)$ take the form [176]

$$\begin{aligned} \phi_1(r) &= \frac{q}{4\pi\epsilon_0\epsilon_r |\mathbf{r} - \mathbf{r}_i|} \left(1 - erf\left(\sqrt{\alpha} |\mathbf{r} - \mathbf{r}_i|\right)\right) \\ &= \frac{q}{4\pi\epsilon_0\epsilon_r |\mathbf{r} - \mathbf{r}_i|} erfc\left(\sqrt{\alpha} |\mathbf{r} - \mathbf{r}_i|\right) \end{aligned} \tag{2.6}$$

where $erfc(x)$ is the complementary error function, and

$$erf(x) = \left(\frac{2}{\sqrt{\pi}}\right) \int_0^x exp(-y^2)dy .$$

Now, considering all periodic images (**n**) of the point charge $q$, and with box length $L$, the charge density is given by

$$\rho(\mathbf{r}) = \sum_{\mathbf{n}} q\delta\left(\mathbf{r} - (\mathbf{r}_i + \mathbf{n}L)\right) .$$

Considering identical Gaussian charge distributions as in equation 2.5, the electrostatic potential due to the overall screened charge distribution ($\Phi_1$) can be written as

$$\Phi_1(r) = \sum_{\mathbf{n}} \frac{q}{4\pi\epsilon_0\epsilon_r |\mathbf{r} - \mathbf{r}_i - \mathbf{n}L|} erfc\left(\sqrt{\alpha}|\mathbf{r} - \mathbf{r}_i - \mathbf{n}L|\right) \qquad (2.7)$$

As for equation 2.6, the term in the *r.h.s.* of equation 2.7 is also short-range and the sum can be computed in direct space by defining appropriate distance cut-off.

The potential $\phi_2(r)$ corresponding to the term $q\rho_{Gauss}(\mathbf{r})$ in equation 2.5 is given by

$$\phi_2(r) = \frac{q}{4\pi\epsilon_0\epsilon_r |\mathbf{r} - \mathbf{r}_i|} erf\left(\sqrt{\alpha}|\mathbf{r} - \mathbf{r}_i|\right) . \qquad (2.8)$$

Whence, considering all periodic images, the electrostatic potential due to the complementary screening charge distribution ($\Phi_2$) can be written as

$$\Phi_2(r) = \sum_{\mathbf{n}} \frac{q}{4\pi\epsilon_0\epsilon_r |\mathbf{r} - \mathbf{r}_i - \mathbf{n}L|} erf\left(\sqrt{\alpha}|\mathbf{r} - \mathbf{r}_i - \mathbf{n}L|\right) . \qquad (2.9)$$

Unlike $\Phi_1(r)$, $\Phi_2(r)$ does not convergence rapidly. Its Fourier transformed variable ($\Phi_2(\mathbf{k})$) is computed in the reciprocal space using the Poisson equation, and $\Phi_2(r)$ can be retrieved

71

using inverse Fourier transformation of $\Phi_2(\mathbf{k})$ [176].

$$\Phi_2(r) = \sum_{\mathbf{k}} \frac{q}{L^3 \epsilon_0 \epsilon_r k^2} exp\left(-i\mathbf{k}.(\mathbf{r} - \mathbf{r}_i)\right) exp\left(-k^2/4\alpha\right) \qquad (2.10)$$

Here, $\mathbf{k}$ is the reciprocal lattice vector. The sum converges rapidly in the reciprocal space.

The procedure can be easily generalized to a system with $N$ point charges $q_i$. In MD simulations, the electrostatic interactions are computed with the particle mesh Ewald (PME). In PME, the calculation in reciprocal space is done using fast Fourier transforms using charges assigned to discrete grid points. The implementation of the same can be found in references [177, 178], and is beyond the scope of this thesis.

### 2.1.2   Choice of ensemble

Molecular simulations can be performed in a variety of ensembles. These include the common ensembles used in statistical mechanics as microcanonical (NVE), canonical (NVT), isothermal isobaric (NPT) and grand canonical ($\mu$VT) [2]. Depending upon the specifics of the systems, simulations can also be performed in other ensembles whose thermodynamics are not as straight forward. For systems which interact only through short-range interactions, the ensembles are equivalent (in the thermodynamic limit). With the presence of long-range interactions, however, the measured microscopic observables and the thermodynamics of the systems crucially depend upon the choice of ensemble [179]. For comparisons with experimental results, both quantitative and qualitative, effort should be made to perform molecular simulations at the experimentally relevant ensembles [106, 180].

The choice of appropriate ensemble to simulate a model lipid bilayer patch had been a

---

[2]N : number of particles, V : volume, E : internal energy, T : temperature, P : pressure, $\mu$ : chemical potential, A : surface area.

topic of considerable controversy in the scientific community. Simulating a model lipid bilayer in the NPT ensemble, with the application of isotropic pressure[3] is equivalent to simulating the bilayer under the conditions of zero surface tension. In the procedure, the dimensions of the simulation box are allowed to change along all three orthonormal axes of the reference frame. Parametrized correctly, the procedure can produce correct estimates for observables, especially the area per lipid molecule [180, 181]. Arguments against NPT ensemble were based upon (a) finite-size effects arising from periodic boundary conditions [182], and (b) non-zero values of surface tension observed for lipid monolayer systems [183]. Consequently, model lipid bilayer patches have often been simulated by maintaining constant surface area ($NP_zAT$ ensemble [4]) and using anisotropic pressures along directions parallel and perpendicular to the plane of the bilayer.

Unlike a lipid monolayer which has non-zero surface tension, a lipid bilayer in equilibrium is essentially *unstressed*, and is characterized by zero surface tension [180, 184]. Finite-size effects can lead to suppression of large wavelength undulations along the bilayer plane. The issue has vastly been overcome through rapid development in hardware and softwares capable of simulating appreciably large model bilayer patches, and the development of force fields capable of reproducing tensionless bilayers in the NPT ensemble [185]. All model bilayer patches reported in this thesis were simulated in the NPT ensemble, with application of isotropic pressure.

Choice of ensemble is also relevant in simulating liquid water. NPT (or very long NVT) simulations can produce correct values of properties such as the density of the liquid. The maintenance of constant pressure and temperature, however, couples the dynamics of the system to those of the external *baths* [186]. Accordingly, to study the structure and dynamics of liquid water, systems are conventionally equilibrated in NPT (or NVT) ensemble and the production run to compute observables is carried out in the NVE ensemble.

---

[3] equal pressure along directions parallel and perpendicular to the plane of the bilayer
[4] z indicates direction normal to the bilayer plane.

## 2.2 Computational models

A computational model involves,- (a) complete description of the structure of the system under study in the desired resolution, and (b) description of the interaction parameters discussed in section 2.1.1, along with parameters such as mass and charge of the sites. If the partial charges on the sites are allowed to be redefined during the course a simulation with change in local environment, the model is described as a *polarizable* computational model [187]. The studies reported in this thesis involve models with fixed charges assigned to the interaction sites, or *non-polarizable* models. Hence, the discussion of models for the relevant molecules would be limited to the non-polarizable models.

Two dimensional continuum models, such as the Fluid-Mosaic model, were briefly introduced in section 1.1.6. Such models are not useful for computational studies such as MD, since they involve no explicit description of the systems in terms of their internal composition and structure. In the following we discuss two types of computational models conventionally used in MD simulations, which differ in their resolution of internal structure. The first, *atomistic* computational models, afford resolution in atomic detail. The second class of models discussed are known as *coarse-grained* models. Coarse-grained models provide reduced resolution compared to atomistic models, but allow the sampling of larger length and longer time-scales.

### 2.2.1 Atomistic computational models

Atomistic, or *all-atom* models are robust computational models, in which the chemical structure of all constituents are effectively reproduced. In such models, each interacting site represents a constituent atom, bonded to others in accordance with chemical composition. Figure 2.4 shows snapshot of a multi-component model lipid membrane patch, with constituent molecules described in atomistic detail. The atoms interact with one another through appropriately parametrized bonded and non-bonded interactions. The interaction
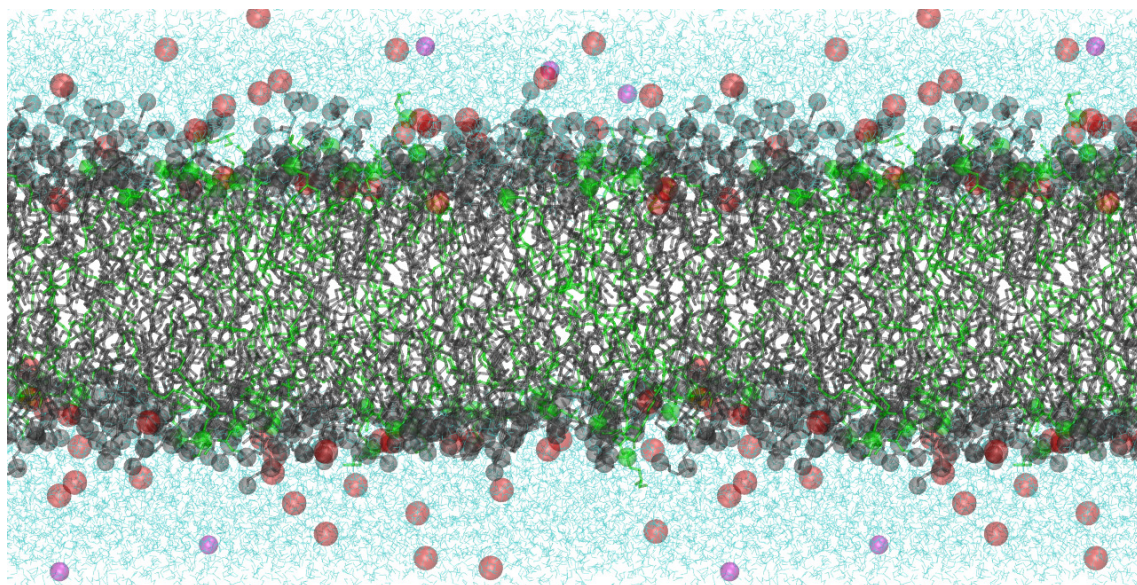
Figure 2.4: Snapshot showing an atomistic multi-component model lipid bilayer. The lipid species are colored gray and green. The hydrating water molecules are shown in cyan. The dissolved ions are shown through spheres (cations : red, anions : magenta). The hydrogen atoms for the lipid molecules have not been shown for clarity.

parameters are generally *effective* ones, which are optimized with respect to experimentally measurable structural and thermodynamic properties, as well as data from quantum mechanical calculations [133, 135, 172, 188].

Very detailed in description, atomistic models are computationally expensive [189]. With radical improvement in computational facilities over the past decades, atomistic models can now be used to study model biomolecular systems with spatial dimensions of tens of nanometers and over time-scales of hundreds of nanoseconds. Highly optimized parameters exist for proteins, lipids, nucleic acids and carbohydrates, along with optimized parameters for water and relevant ions [135, 172, 188, 190, 191]. Further, using dedicated programs such as CGenFF, parameters for arbitrary organic molecules can be obtained with appreciable accuracy [192, 193].

All studies reported in this thesis involve atomistic description. The structure of relevant molecules, and the models used for them are described briefly in the following.
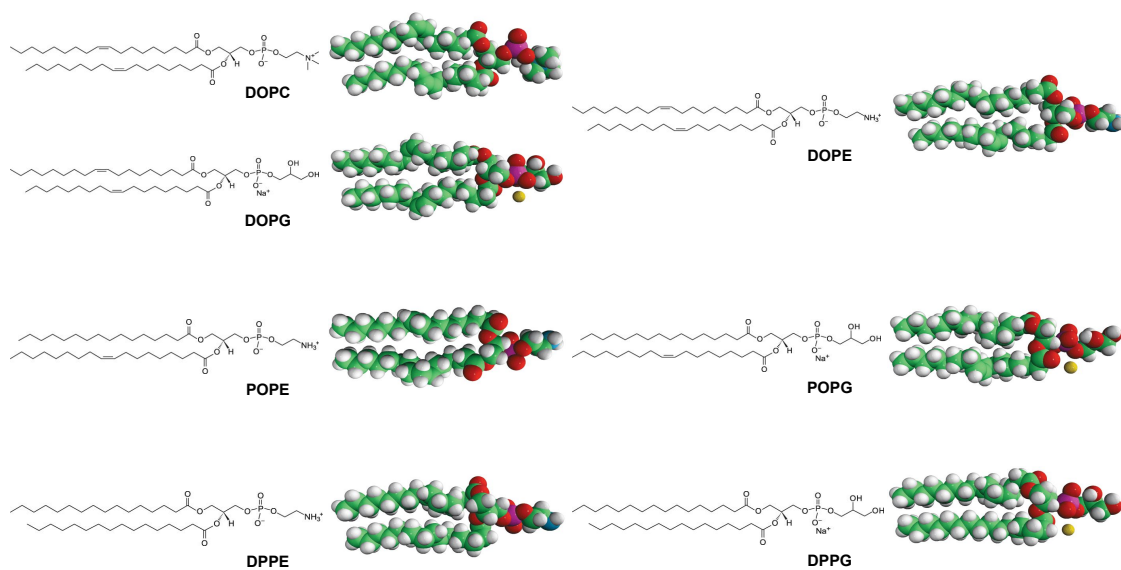
Figure 2.5: Chemical structures (left panels) and atomistic model representations (right panels) of lipids used in the studies reported in this thesis. The PG- lipids are shown as their sodium salts, emphasizing their anionic nature. The rest of the lipids are zwitterionic ones.

**Atomistic models for studied lipids**

All lipid species used to construct the mixed lipid membranes discussed in this thesis are shown in Figure 2.5. Abbreviations used for the individual lipid species are also shown with their chemical structure and atomistic representations in the figure. These lipids differ among one another through their head-group composition, which can be formed of phosphatidylethanolamine (PE), phosphatidylcholine (PC) or phosphatidylglycerol (PG) groups. PE and PC are overall neutral, whence the lipids with these head-groups are zwitterionic ones. The PG head-group is negatively charged, and characterizes the anionic lipids studied. PE and PC head groups, though equivalent in long-range electrostatics, differ in through hydrogen bonding, and their cross sectional area. PE groups have primary amines as their terminal moieties, and hence greater hydrogen bonding ability compared to PC groups which have tertiary amines. The cross section of PC groups is considerably larger than PE groups. Thus PC-lipids are often characterized by cylindrical effective shape, while PE-lipids are conical and have spontaneous negative curvature [17, 194].

The studied lipids also differ among one another through the degree of (un-)saturation

of their acyl chains. DOPE (1,2-dioleoyl-sn-glycero-3 phosphoethanolamine), DOPC (1,2-dioleoyl-sn-glycero-3 phosphocholine) and DOPG (1,2-dioleoyl-sn-glycero-3 phosphoglycerol) lipids have mono-unsaturations in all lipid tails. Each POPE (1-palmitoyl-2-oleoyl phosphatidylethanolamine) and POPG (1-palmitoyl-2-oleoyl phosphatidylglycerol) lipid has one saturated and one mono-unsaturated tail, while lipid tails in DPPE (1,2-dipalmitoyl-sn-glycero-3 phosphorylethanolamine) and DPPG (1,2-dipalmitoyl-sn-glycero-3 phosphoglycerol) lipids are all saturated.

CHARMM (C36) force fields have been used for the lipids in all studies described in this thesis [172].

**Atomistic models for water**

Computational models used for simulating water are diverse, which emphasizes the complexity in reproducing all the properties of liquid water through a small number of interaction parameters. A description of various water models is beyond the scope of this thesis. Interested readers are referred to London South Bank University's detailed database on water models [195], as well as a review of water models and references therein [196]. In the studies discussed in this thesis, water molecules have been represented through *three-site* TIP3P [135] or *four-site* TIP4P-Ew [133] water models. The water models are shown in Figure 2.6.



(a)　　　　　　　　　(b)
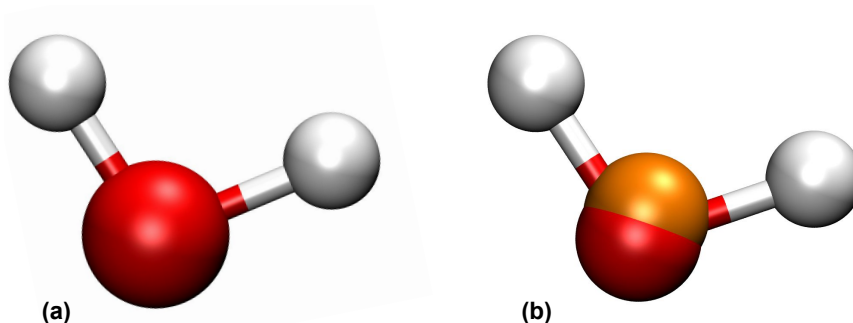
Figure 2.6: (a) Three-site (eg. TIP3P) and (b) four-site (eg. TIP4P-Ew) water models. The oxygen and hydrogen sites are colored in red and silver respectively. In (b), the sphere shown in orange corresponds to the site with partial negative charge. The spheres showing the atoms (sites) are not to scale.

In three-site TIP3P water model, the sites represent the oxygen and two hydrogen atoms. Mass and partial charges are assigned to the respective sites, with vdW interactions dominated by the the interactions of the central oxygen atom site. In the four-site TIP4P-Ew model, the masses are assigned to the designated sites for oxygen and hydrogen atoms. While the sites corresponding to the hydrogen atoms are also assigned partial positive charges, the negative charge is assigned to a fourth site which lies along the bisector of the H−O−H angle. This fourth site, however, does not interact through vdW interactions. Both the models are non-polarizable ones, in which the assigned partial charges to the sites are not allowed to change with the local environment. The separation between the sites, or bond lengths are also held rigid during the simulations.

### 2.2.2 Coarse-grained computational models
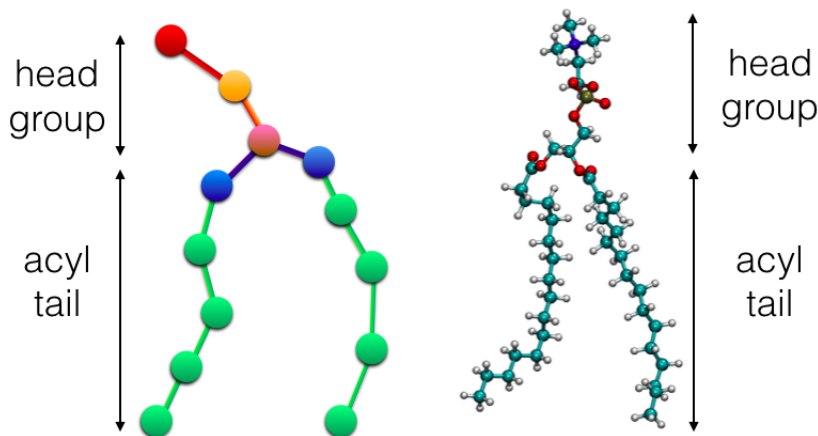


Figure 2.7: Schematic showing the coarse-graining of an atomistic lipid model. In the coarse grained model, groups of atoms from the all-atom description are replaced by *beads* with effective interactions.

Owing to their robust descriptions, atomistic models are computationally expensive. This limits their applicability in studying several processes, which include large-scale reorganizations of bilayer lipids, mechanics of membrane fusion, large-scale changes in membrane protein conformations, pore formation by membrane destabilizing agents *etc*. Coarse-grained computational models, well parametrized, are useful in the study of such processes. In a coarse-grained description, groups of atoms are represented through single

*beads*, thus reducing the number of interaction sites appreciably. Figure 2.7 schematically describes the process of coarse graining of a lipid molecule. The interactions between explicit atoms are replaced by effective interactions (bonded and non-bonded) between the sites. Coarse-grained biomolecular simulations also require the use of coarse-grained water models. In a coarse-grained water model, multiple water molecules are represented through a reduced number of sites [197, 198]. Polarizable and non-polarizable water models used with MARTINI coarse-grained force-fields are shown in Figures 2.8 (A) and (B) respectively. With coarse-graining it is possible to achieve ∼(4-5) fold increase in the length and time-scales that can be sampled in the simulations, compared to atomistic MD [189, 199, 200].
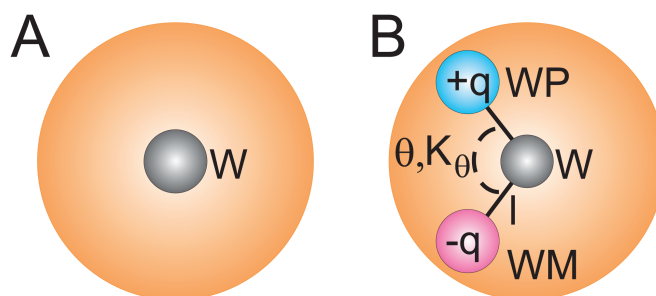


Figure 2.8: Coarse-grained water models : (A) original non-polarizable, and (B) polarizable MARTINI water models. The orange shaded regions indicate vdW radii of the central sites. With the polarizable model, water molecules interact through electrostatic interactions in addition to the vdW interactions for the non-polarizable model. Courtesy [198]

Parametrization of a coarse-grained model is intrinsically a complex process, in which several rapidly fluctuating degrees of freedom are averaged over. This generally requires detailed prior knowledge of structural and dynamical properties in atomistic resolution. A further complexity in coarse-graining is the transferability of parameters, which are generally applicable over a small range of environmental conditions such as temperature and pressure. With the development of coarse-grained models such as MARTINI, however, transferability issues have largely been overcome for commonly studied model lipid membranes [199]. Coarse-grained models partially bridge the gap between atomistic and mesoscopic / continuum descriptions, however sacrificing information on detailed local structure in the process.

## 2.3 Observables : lipid bilayer properties

### 2.3.1 Order in lipid tails

The extent of *order* in the packing of lipid tails is important in understanding the phase behavior of a lipid bilayer. The main lipid bilayer phase transition is associated with change in the entropy of the system through reorganization of the system's components. While also reflected in structural parameters such as area per lipid and bilayer thickness, the changes in conformational entropy is best understood through changes in the order in lipid tails. The lipid acyl tail order parameter or the deuterium order parameter ($S_{cd}$) is defined as

$$S_{cd} = \frac{1}{2} \left\langle 3Cos^2\theta - 1 \right\rangle \qquad (2.11)$$

where $\theta$ is the angle between a C–H (C–$^2$H in experiments) bond and the membrane normal. $S_{cd}$ can vary in the range [-0.5, 1]. A higher value of $S_{cd}$ indicates increased ordering of the lipid acyl chains. Along with computational methods, $S_{cd}$ can be computed using $^2$H NMR, and is used extensively in the parametrization of computational models. It is highly sensitive to structural parameters such as tail length and degree of unsaturation [49].

Other structural parameters related to the conformations and interdigitation in lipid tails include tilt and splay angles. Tilt angle can be defined as the angle between the membrane normal and a vector connecting a lipid head group atom and carbon atom of the lipid chain. The splay angle is measured as the angle between two vectors, each connecting a lipid head group or glycerol atom and equivalent carbon atoms along the two lipid tails. The definitions are schematically illustrated in Figure 2.9. Increased tilt or / and splay angles indicate greater interdigitation of the lipid tails.
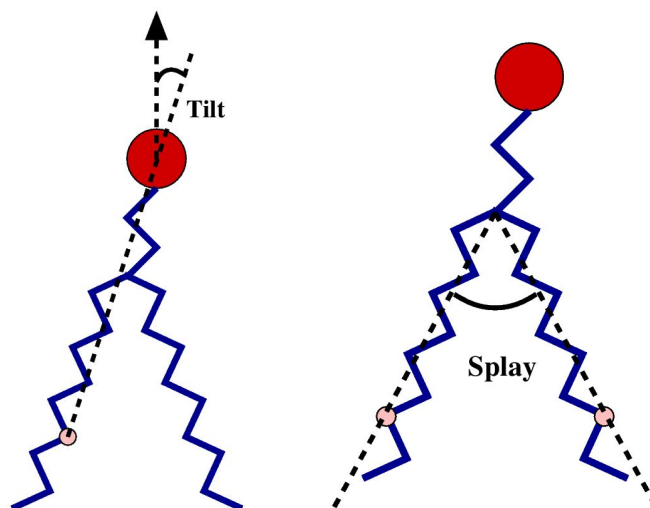
Figure 2.9: Schematics showing tilt and splay angles for a lipid molecule, as a function of position of C atom(s) (pink beads) along acyl chain (blue lines). An atom in the head-group / glycerol backbone can be considered as reference.

## 2.3.2 Trans-bilayer structure and bilayer thickness

The distribution of atomic constituents as a function of depth within a bilayer describes the trans-bilayer structure. Simulation data obtained with well parametrized atomistic computational models can provide the best descriptions of the trans-bilayer structure. The methodology for computing the distributions for individual atom types is essentially simple. For each configuration (frame), the system is divided into slabs of small, finite width ($\sim 1\mathring{A}$) along the bilayer normal. The density of desired atom type(s) is then computed for the individual slabs. Averaged over appreciable number of uncorrelated system configurations, the densities for the individual atomic constituents can be obtained as distributions that account for the fluctuations in a bilayer. A plot showing component densities as a function of depth along bilayer normal is known as the *density profile* for the bilayer. The average thickness of a bilayer can be obtained directly from the density profile. For studies reported in this thesis, average bilayer thickness has been defined as the separation between the peaks for phosphate groups in the individual bilayer leaflets. In computing the probability distributions of average bilayer thickness, the thicknesses obtained from each system configurations analyzed were binned.

Of greater relevance to the studies reported is the lateral bilayer thickness profile, or the distribution of local bilayer thickness over the plane of the bilayer. The same can be obtained easily using a grid-based Cartesian scheme. The plane of the bilayer is divided into small grids ($2\mathring{A} \times 2\mathring{A}$ in the studies reported). For a given system configuration and for each cell in the grid, phosphate groups are identified in the two leaflets that occupy the grid or lie closest to it (in the plane parallel to the bilayer). Local bilayer thickness for the grid point is then defined as the separation along bilayer normal between the identified phosphate groups in the two leaflets. The thickness distribution thus obtained is averaged over time, or uncorrelated system configurations.

### 2.3.3 Interfacial lipid-packing defects

The interfacial lipid-packing defects were identified using a grid-based Cartesian scheme. The procedure is briefly outlined below. Interested readers are referred to supporting material of reference [4] for details.

The lipid-packing defects are identified separately for the individual bilayer leaflets. The plane of a bilayer leaflet is divided into $1\mathring{A} \times 1\mathring{A}$ grid cells. For each cell one can envisage a circular disc in the bilayer plane, with radius equal to half diagonal length ($\sim 0.7\mathring{A}$) and centered at the center of the grid cell. For every grid cell, the leaflet is scanned starting from the aqueous phase towards the bilayer center. The first bilayer atom to have a van der Waal overlap with the disc (computed using on-plane or 2D separation between atom and grid cell centers) is identified. If the atom identified is a polar lipid head group atom, the cell is defined as *non-defect*. However, if the atom is an aliphatic one, its depth within the bilayer relative to the *sn-2* carbon of the nearest glycerol group is determined. If the atom is observed to reside more than $1\mathring{A}$ deeper within the bilayer relative to the *sn-2* carbon, the grid cell is defined as a *geometrical defect*, else as a *chemical defect*.

Following the assignment of all grid cells for a leaflet, the clustering of the defect cells is

computed using cluster multiple labeling technique due to Hoshen and Kopelman [201], accounting for periodicity of the simulation box. The area corresponding to each cluster is obtained, which is binned to obtain the probability distributions of interfacial lipid packing defects as a function of defect surface area. It is important to note that geometrical defects are a sub-category of chemical defects, whence in identifying the clusters of chemical defects, the geometrical defects are also included.

## 2.4    Observables : long-range structure of liquid water
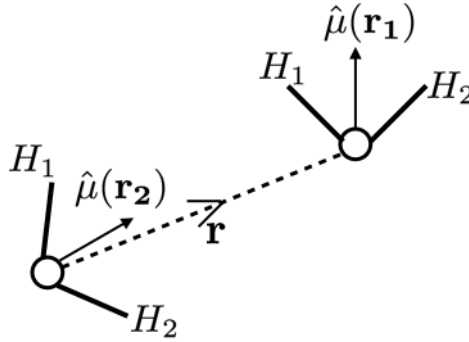


Figure 2.10: Schematic diagram showing the vectors used to define correlations $t(r)$ and $l(r)$. $\hat{\mu}$ for a water molecule is defined as unit vector along the bisector of $\angle H_1OH_2$. It is important to note that the figure does not represent any *preferred* orientations.

Let $\hat{\mu}$ denote the normalized dipole vector of a water molecule. Statistical correlations among any two water molecules, whose oxygen atoms are situated at $\mathbf{r_1}$ and $\mathbf{r_2}$, involving the dipolar degree of freedom can be formulated as

$$\langle \hat{\mu}^i(\mathbf{r_1})\hat{\mu}^j(\mathbf{r_2}) \rangle = \frac{1}{2}\left(\delta^{ij} - \frac{r^i r^j}{r^2}\right)t(r) - \frac{1}{2}\left(\delta^{ij} - 3\frac{r^i r^j}{r^2}\right)l(r) \qquad (2.12)$$

where indices $i, j$ denote directions in three-dimensional space, $\mathbf{r} = (\mathbf{r_1} - \mathbf{r_2})$, $r = |\mathbf{r}|$ and the angular brackets denote ensemble averages [11]. The decomposed scalar functions

$t(r)$ and $l(r)$, defined as

$$t(r) = \langle \hat{\mu}(\mathbf{r_1}).\hat{\mu}(\mathbf{r_2}) \rangle \tag{2.13}$$

$$l(r) = \langle \hat{\mu}(\mathbf{r_1}).\hat{\mathbf{r}}\, \hat{\mu}(\mathbf{r_2}).\hat{\mathbf{r}} \rangle \tag{2.14}$$

describe the trace part and the longitudinal (traceless) part of the tensorial correlations $\langle \hat{\mu}^i(\mathbf{r_1})\hat{\mu}^j(\mathbf{r_2}) \rangle$. Physically, $t(r)$ and $l(r)$ are measures for the statistical alignment of water dipole vectors spaced $r$ distance apart with respect to themselves and with respect to the radial vector separating them respectively (see Figure 2.10). A linear combination of them in the form of $\frac{1}{2}(t(r) - l(r))$ gives correlations transverse to the vector $\mathbf{r}$ [12].

$t(r)$ and $l(r)$ correlations in liquid water have been studied for a variety of non-polarizable as well as polarizable models of water, including (TIP5P, TIP3P) [11] and (SPC/E, swm4-DP) [120]. Any structural observable for water should vary monotonically with pressure and temperature (above 4°C) [10]. In a recent study, both $t(r)$ and $l(r)$ correlations have shown small, but monotonic effects due to changes in temperature and pressure (density) [120]. As described in section 1.3.4, both correlations show oscillatory solvation structure. The correlation $l(r)$ is especially long-range and decays exponentially beyond solvation region.

A third correlation of interest in studying long-range structure of liquid water is oxygen - dipole correlation ($d(r)$). $d(r)$ is defined as

$$d(r) = \langle \hat{\mu}(\mathbf{r_1}).\hat{\mathbf{r}}\rho(\mathbf{r_2}) \rangle \tag{2.15}$$

where $\rho(\mathbf{r})$ is the density field for oxygen atoms (or, equivalently, water molecules) and takes a value of 1 or 0 depending on presence or absence of oxygen atom at position $\mathbf{r}$ [11]. The correlation $d(r)$ represents the propensity for alignment of the dipole vector of a water molecule to the radially outward direction, when observed from the position of another water molecule. This correlation also shows oscillatory solvation structure at

radial separations below $14\mathring{A}$ and vanishes beyond the same [11].

## 2.5 Observables : reorientational dynamics of water molecules
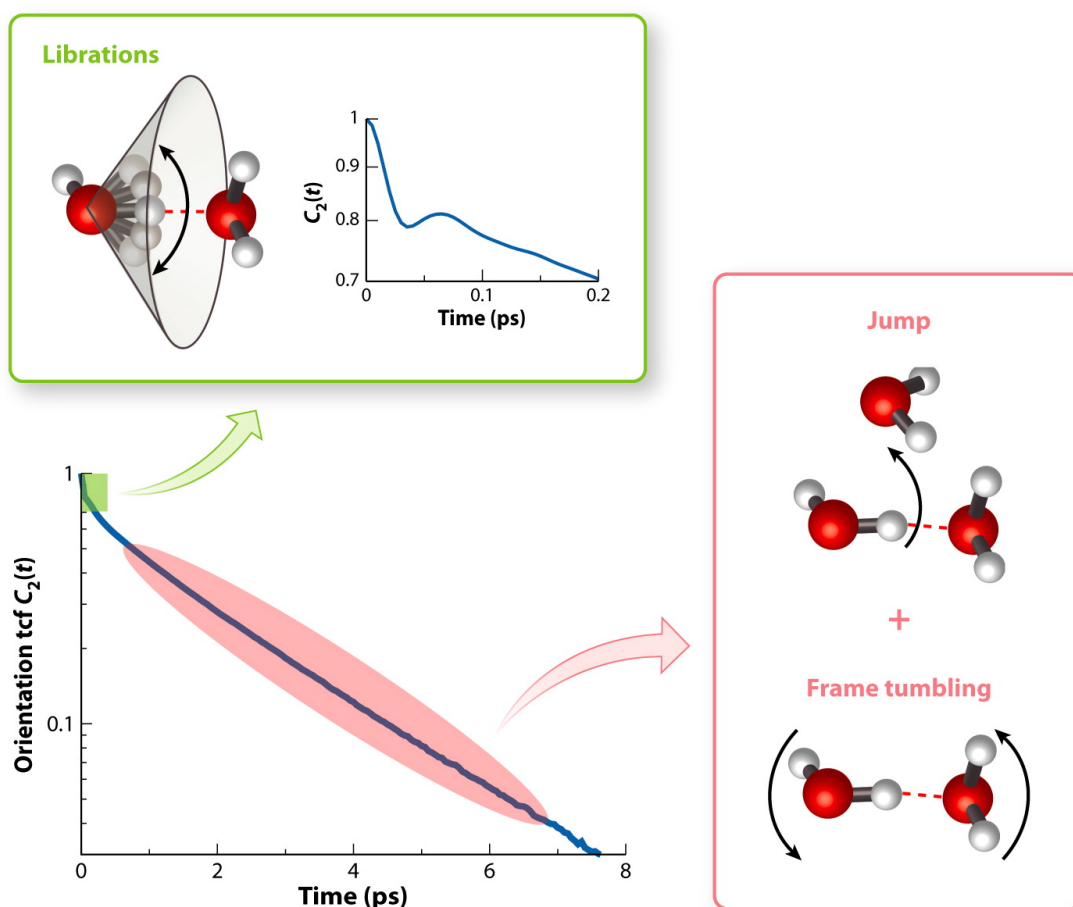


Laage D, et al. 2011.
Annu. Rev. Phys. Chem. 62:395–416

Figure 2.11: Reorientational autocorrelation function $P_2(t)$ of molecules in liquid water, shown as a logarithmic plot. The region highlighted in green has contributions from the fast, sub-picosecond librational motion. This initial decay is non-exponential. The decay of the correlation at the picosecond time-scale (highlighted in red) has contributions from angular jumps and frame reorientations, and can be fit to an exponentially decaying function. Courtesy [148].

The reorientational dynamics of individual water molecules can be studied qualitatively using reorientational autocorrelation functions. For any *body-set* vector of a water molecule

$(\mu)$, the $n^{th}$ order reorientational autocorrelation function $(P_n(t))$ is given by

$$P_n(t) = \langle \wp_n \left[ \mu(t).\mu(0) \right] \rangle \qquad (2.16)$$

where $\wp_n$ is the Legendre polynomial of rank $n$. The angular brackets indicate ensemble average. The reorientational autocorrelation functions provide a measure for the rate at which the memory of the initial orientation (orientation at time $t = 0$) is lost. Long-time decays of the functions $P_n(t)$ are exponential in nature. The behavior of the correlation $P_2(t)$ for liquid water at ambient conditions is shown in Figure 2.11 in the logarithmic scale.

As discussed in section 1.3.5, reorientational dynamics of molecules in liquid water has contributions from three processes. These are libration, large amplitude angular jumps and frame reorientation. The first process has a sub-picosecond time-scale, while the latter two occur at the picosecond time-scale. A reorientational autocorrelation function can not provide good quantitative description of the individual processes. Further, it can not distinguish between the contributions due to large amplitude angular jumps and frame reorientations. However, such correlations provide a computationally inexpensive qualitative description of the reorientational dynamics of individual water molecules. They are also extremely useful when used in a comparative manner, and can identify the effects of local environment (eg. presence of solutes and interfaces) on the overall reorientations of water molecules [113, 148, 202]. The librational motions of the body-set vector $\mu$ contributes to the initial sub-picosecond fast decay of reorientational autocorrelation functions, shown in Figure 2.11 through the region highlighted in green. The longer, picosecond time-scale exponential decay (highlighted red in Figure 2.11) is due to the angular jumps and frame reorientations.

These correlation functions will be used in Chapter 7. For the reported study, the vector $\mu$ was chosen to be the unit dipole vector $(\hat{\mu})$ of a water molecule, whence the correlations

studied ($P_1(t)$, $P_2(t)$) were defined as

$$P_1(t) = \langle \hat{\mu}(t).\hat{\mu}(0) \rangle \tag{2.17}$$

$$P_2(t) = \langle \frac{1}{2}(3cos^2(\hat{\mu}(t).\hat{\mu}(0)) - 1) \rangle \; . \tag{2.18}$$

# Chapter 3

# Interaction of multiple methacrylate polymers with model bacterial membrane

## 3.1 Introduction

### 3.1.1 Methacrylate polymers

Methacrylate polymers consist of cationic and hydrophobic side chains distributed along a flexible backbone. The chemical structure of methacrylate copolymers is shown in Figure 3.1. They exhibit a broad spectrum of activity against both Gram-positive and Gram-negative bacteria and have been observed to be similarly active against both drug-resistant (MRSA) and drug-susceptible strains of *S. aureus* [2]. Further, their bactericidal activity (tested against *E. coli* and *S. aureus*) has been revealed to be equal in both the stationary and the exponential growth phases of the bacteria [203], thus rendering them less likely to be susceptible to bacterial resistance development through dormancy [84]. Experimental results showed that bacterial resistance was developed against antibiotics like

Ciprofloxacin and Norfloxacin, while no resistance was found in the case of methacrylate polymers in case of *E. coli* [84, 203].
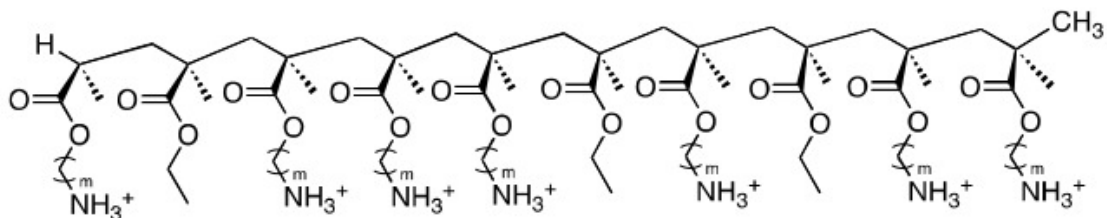


Figure 3.1: Chemical structure of methacrylate polymers. bbM4 polymers are characterized by aminobutylene (m=4) cationic side chains.

Various structural aspects of methacrylate polymer design has been systematically studied with the view to optimize the polymers for maximum bactericidal activity and minimum toxicity to host cells [2, 84, 85, 90, 203–209]. The chemical structure of cationic amine groups (primary, tertiary and quarternary amines) in the charged monomers has been observed to have a considerable impact on the bactericidal activity of methacrylate antimicrobial polymer, with polymers having primary amines being most active and those with tertiary amines being inert in comparison [205, 206]. These observations indicate that the role of the charged moieties for methacrylates is not confined to the recognition of, and attachment to bacterial anionic lipid head groups through electrostatic interactions only. The amine groups likely form complexes with polar lipid head groups through a combination of electrostatic interactions and hydrogen bonding.

Increase in hydrophobic content for methacrylate AMPoly has been observed to enhance both antimicrobial and hemolytic potency of the polymers. The balance between charge and hydrophobicity is thus pivotal to the design of effective, non toxic methacrylates. The hydrophobic content of methacrylate copolymers can be varied in multiple ways such as the ratio of charged to hydrophobic monomers for a given polymer length and the length of the alkyl side chains. Polymers with short alkyl side chains have been observed to yield greater selectivity in their antimicrobial action compared to those with longer alkyl side chains [90]. With the increase in relative number of hydrophobic monomers compared

to charged ones, both antimicrobial and hemolytic activities of methacrylate copolymers have been observed to show an enhancement followed by saturation behavior at high values of hydrophobic content, the trend in hemolytic toxicity being most pronounced at high molecular weights [90]. Generally, low molecular weight methacrylate copolymers have been observed to be less hemolytic.

## 3.1.2 MD simulations of methacrylate polymers

Systematic simulation studies of methacrylate polymers have been performed, which helped in the understanding of design strategies and possible modes of action [2, 204]. In the first simulation study using methacrylates, the effects of design parameters such as ratio of cationic to hydrophobic units, polymer length and sequential distribution of monomers on the conformations of the antimicrobial polymer and their interactions with a lipid bilayer were studied in water and in the presence of an equilibrated dioleoyl phosphatidylcholine (DOPC) bilayer patch [204]. In aqueous environment, polymers with greater charge content were observed to take up more extended conformations. With increase in hydrophobicity, the conformations in water were observed to be dependent on the placement of hydrophobic units,- alternating polymers adopting crescent like conformations, while block copolymers depicting considerably wider variety in their backbone conformations. Though the simulations in the presence of DOPC bilayer were very short (< 10 ns), partial insertion into the bilayer was observed for polymers with high hydrophobicity, thus indicating that hydrophobicity, as in all AMPs, was the key factor contributing to the bilayer insertion of methacrylates. Further computational effort was thus directed at understanding the bacterial membrane bound conformations of methacrylate AMPoly.

Experimental observations of greater activity of primary ammonium groups [205] and dependence of antimicrobial activity to hemolytic toxicity on the relative content of cationic and hydrophobic comonomers [90] dictated the choice of methacrylate polymers for further simulation study. Three methacrylate AMPoly with ethylene (bbM2), butylene
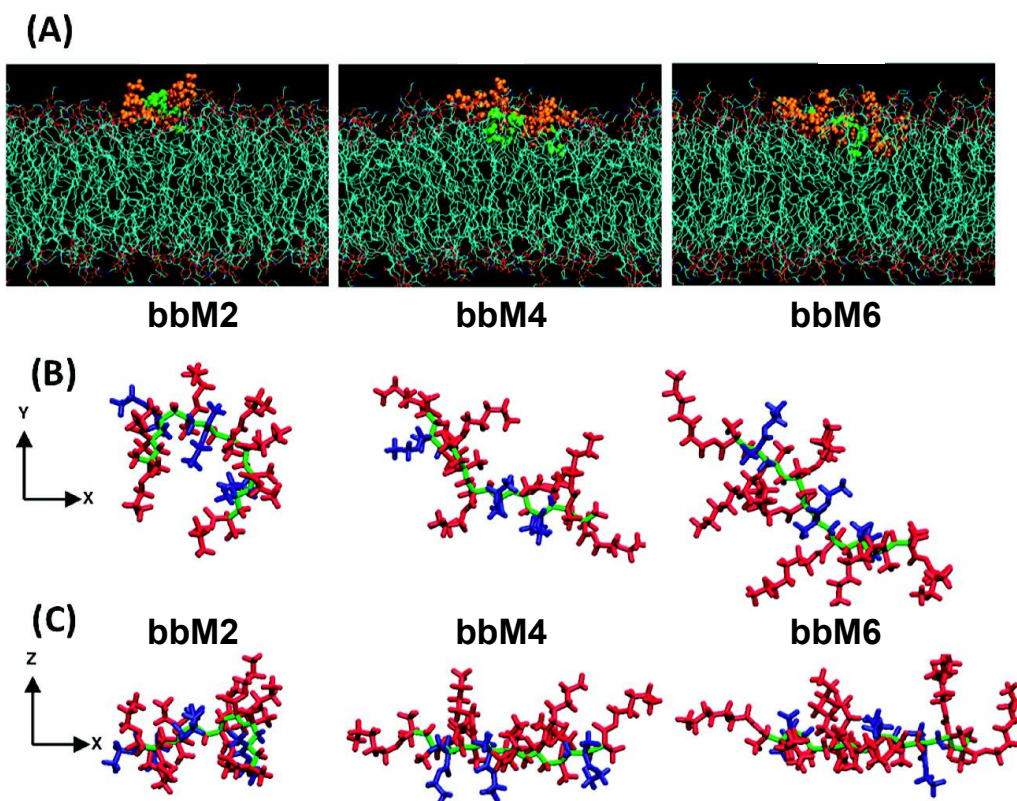
Figure 3.2: (A) Snapshots showing bacterial membrane interactions of bbM2, bbM4 and bbM6 AMPoly. (B,C) Membrane-bound conformations of the polymers in the XY and XZ planes respectively (Z axis is along normal to the membrane). Modified with permission from [2].

(bbM4) and hexylene (bbM6) spacer groups arms were studied to understand the effect of varying spacer group lengths [2]. The membrane patch was chosen to comprise of zwitterionic POPE and anionic POPG lipids (see section 2.2) in 7:3 ratio, which is a conventionally used model for Gram-negative bacterial membranes, mimicking the inner membrane in *E. coli* [210]. A membrane patch with this composition will be referred to as **poPE-PG** in the rest of the thesis. In aqueous phase, all the polymers were observed to adopt compact structures with side arms oriented randomly about the polymer backbones, the membrane bound conformations for the same were observed to vary considerably (Figure 3.2). While bbM2 polymers retained compact conformations along membrane interface, bbM4 and bbM6 were observed to adopt considerably stretched ones, maximizing the contacts with lipid atoms. This was also reflected in the membrane partitioning affinity of the polymers with bbM2 being considerably less partitioned at the end of 100 ns compared to bbM4 and bbM6. The latter ones also exhibited the ability to adopt FA con-

formations in the membrane bound phases with pendant ammonium groups localized near the lipid head group atoms and the hydrophobic side chains penetrating deeper into membrane interior,- thus leading to spatial segregation of cationic and hydrophobic groups to two sides of polymer backbone [2]. The polymer backbones were observed to be oriented parallel to the membrane interface, the conformation thus efficiently mimicking the *snorkeling* effect [84, 208, 211, 212].

As shown in Figure 3.2(C), facial amphiphilicity was observed to be most robust for the bbM4 methacrylate polymers. Experimental results also showed that the bbM4 polymers are effective antimicrobial agents, with low toxicity to host cells [2]. However, the previous MD simulations were limited to interaction of a single flexible polymer chain with bacterial membrane. In the following, as well as in Chapter 4, the interactions of multiple bbM4 polymers with bacterial membranes are discussed. In the rest of this chapter, the interactions of an aggregate of four bbM4 polymers with a poPE-PG membrane will be described. In Chapter 4, key observations from the study of the bbM4 - poPE-PG interactions will be discussed in the context of varying membrane compositions. The content of this chapter is published in reference [213].

## 3.2   Model and Simulation method

Two model bacterial membrane patches with (bbM4-membrane) and without (control) the AMPoly aggregate were simulated. The starting configuration of bacterial membrane for both the systems were taken from a pre-equilibrated poPE-PG membrane patch consisting of 90 POPE and 38 POPG lipid molecules per leaflet, mimicking bacterial membrane composition [214], which was constructed using CHARMM- GUI's Membrane Builder module [170, 215]. POPE(70%)-POPG(30%) is a good model for Gram-negative bacteria that mimics the inner membrane lipid composition of *E. coli* [216]. Forty water molecules per lipid molecule were added to simulate a fully hydrated bilayer system and 82 $Na^+$ and

6 Cl$^-$ ions were added to the system to achieve a salt concentration of 150 mM. The prepared bilayer was subjected to planar, harmonic and dihedral restraints, which were gradually reduced to zero over 0.8 ns. The bilayer system was then equilibrated for 15 ns in isothermal- isobaric (NPT) ensemble (T=310.15 K, P= 1 atm).
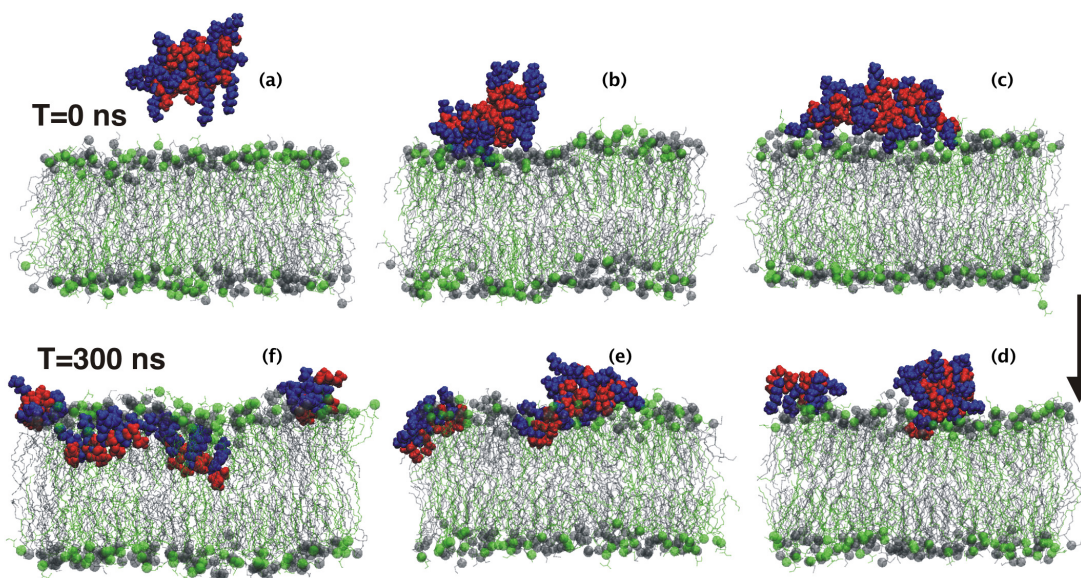


Figure 3.3: Snapshots of partitioning of antimicrobial polymers bbM4 aggregate into a poPE-PG lipid membrane. Water and ions are not shown for clarity. The cationic and hydrophobic groups of bbM4 polymers are shown in blue and red respectively.

A stable aggregate with 4 bbM4 polymers (P1, P2, P3, P4) was extracted from a 40 ns long MD simulation of the AMPoly dispersed in a box of water and simulated for 40 ns. To construct bbM4-membrane system, the aggregate of four bbM4 polymers was placed about 12 $\mathring{A}$ away from one of the bilayer leaflets (which is referred to as upper leaflet in section 3.3) along membrane normal, in the water phase (see Figure 3.3). Additional water molecules were added to the system to prevent the interaction of the aggregate with the lower leaflet of bilayer image along the bilayer normal. The total charge of the bbM4-aggregate was +20e and with the addition of required number of counterions, the number of sodium and chlorine ions in the bbM4-membrane system were 82 and 26 respectively to maintain 150 mM salt concentration. The two systems, bbM4-membrane and control were further simulated for 300 ns each and the analysis in this work was done over 50 ns (250-300 ns) of simulations, unless otherwise stated. Both systems were simulated for an

additional 20 ns (300 - 320 ns) over which the lateral pressure profiles were computed.

Simulation package NAMD2.8 [165] was used to perform all simulations. CHARMM forcefield CHARMM 36 [172], which has been optimized to simulate tensionless bilayers, was used for POPE and POPG lipid molecules. The interaction parameters for bbM4 polymers were taken from previous published work [2, 204]. TIP3P [135] water model was used to simulate water and standard CHARMM parameters were used for Na$^+$ and Cl$^-$ ions [191]. A time step of 2.0 fs was used in all simulations. The two systems were simulated at 310.15 K, ensuring that the temperature was above the main transition temperature of both POPE and POPG lipid molecules [217]. All simulations were performed at 1 atm pressure, maintained through Langevin Piston [218]. Long-range electrostatic interactions were handled using particle mesh Ewald method and Lennard-Jones interactions were smoothly truncated at a cutoff of 12 $\mathring{A}$ through the application of switching function between 10 $\mathring{A}$ and 12 $\mathring{A}$. Visual Molecular Dynamics (VMD) [171] was used extensively for visualization and analyses.

Cluster multiple labeling technique due to Hoshen and Kopelman [201] was used to statistically study the phase demixing and consequent clustering of POPG lipids at the bilayer leaflets. The algorithm is an efficient means of identifying clusters of contiguous cells on a grid where each cell can be either *occupied* or *unoccupied*. The the plane of the bilayer perpendicular to the membrane normal was divided into a 2-dimensional grid of cells, with cell size of 2$\mathring{A}$ × 2$\mathring{A}$ for both leaflets. A cell was defined to be occupied if any of the POPG head group atoms were observed to be located within its confines and unoccupied otherwise. Periodic boundary condition was incorporated in defining the clusters and the grid occupancy was averaged over 250 ps in each analysis. The averaging time was chosen to allow the vibrational motion of the lipid molecules to affect the grid occupancy while avoiding effect due to large scale diffusive motion of lipids.

95

## 3.3 Results

### 3.3.1 Interaction of bbM4 aggregate with poPE-PG membrane
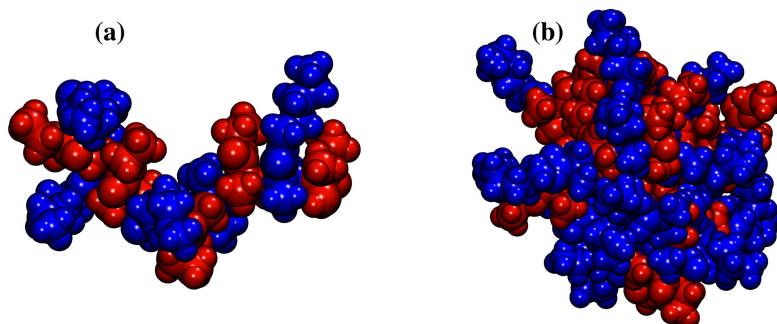


Figure 3.4: Configuration of (a) a single bbM4 polymer and (b) an aggregate of four bbM4 polymers in solution. The cationic and hydrophobic components are colored blue and red respectively.

The multiple bbM4 polymers form an aggregate in solution phase (0.15M NaCl solution), in an almost micellar structure, with hydrophobic groups buried inside the aggregate and the cationic arms exposed to water. Solution structures of an individual bbM4 AM polymer as well as the aggregate of four such polymers are shown in Figure 3.4. It is to be noted that the cationic and hydrophobic groups for the bbM4 polymers, both individually and within the aggregate, are randomly distributed along the polymer backbone and do not display any pronounced facial amphiphilicity. The formation and stability of such aggregate depends on the hydrophobic content of the individual AM polymers. Previous studies involving methacrylate polymers demonstrated that the antimicrobial activity of the copolymers increases as the hydrophobic content is increased, but levels off when the polymers are highly hydrophobic [2]. This was attributed to strong hydrophobic aggregation of polymer chains in water, which reduces the number of AM polymer chains available for possible disruption of bacterial membranes. Over first 10 ns of simulation time, the aggregate of bbM4 copolymers placed in water reaches the bacterial membrane surface via attractive electrostatic interactions between the solvent-exposed cationic groups of AM polymers and the anionic lipid molecules (POPG) (Figure 3.3(b)). The aggregate

of four bbM4 polymers adopts a more extended form, in the vicinity of the membrane, with increase in number of contacts between cationic charged groups of bbM4 polymers and anionic lipid POPG (Figure 3.3(c)). The extended form of aggregate remains relatively stable and in contact with membrane for further 20 ns.
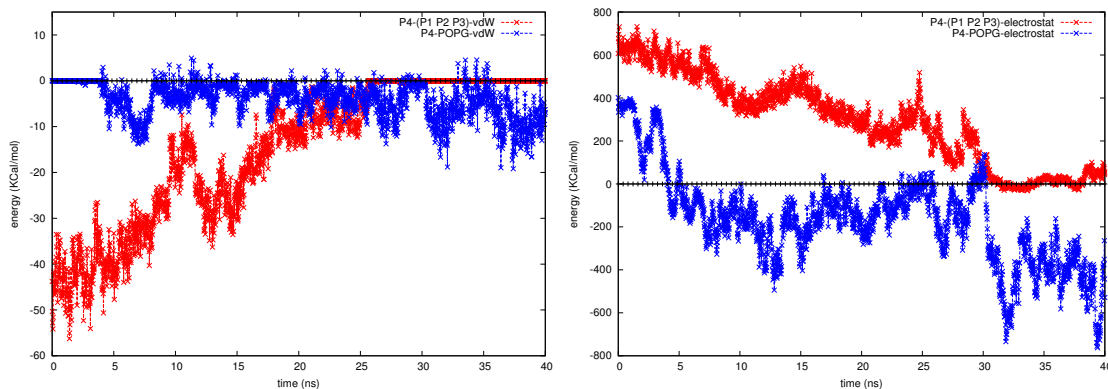


Figure 3.5: Pair interaction energies between the polymer P4 and aggregate and P4 and POPG lipid molecules as a function of time, before polymer P4 leaves the aggregate. The energies include van der Waals and electrostatic terms.

With the increase in number of contacts between the cationic groups of the bbM4 polymers in the aggregate and the anionic lipid head groups, a single polymer in the aggregate may experience competing forces: attractive van der Waals interactions from other polymers in the aggregate and attractive electrostatic interactions with the oppositely charged anionic lipid head groups of the bacterial membrane. This can be seen from the pairwise interaction energies (Figure 3.5) of P4 polymer with other three polymers in the aggregate and also with POPG head groups in the bacterial membrane. As the attractive electrostatic interactions between P4 and POPG head groups increases, the corresponding van der Waals interaction between P4 and the aggregate decreases. A polymer dissociates from the aggregate, when the polymer-lipid interactions are more favorable than the polymer-polymer interactions. This indicates that "weak aggregation"is important for polymer insertion and membrane disruption; otherwise, a very stable aggregate of hydrophobic polymers may not disintegrate, which is in agreement with the leveling off of activity for highly hydrophobic polymers observed earlier [2, 90]. In addition, polymer aggregation in solution phase could favor faster binding to lipid bilayer. The high den-
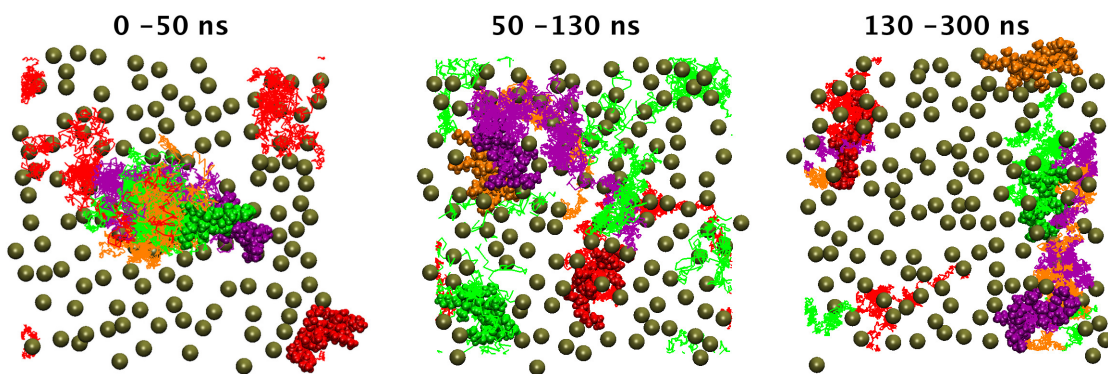
Figure 3.6: Trajectories of centers-of-mass of the four polymers (P1: magenta, P2: orange, P3: green and P4: red) in three different time intervals (top view). The phosphorous atoms of the lipid head groups are shown in tan.

sity of cationic groups provides more binding contacts to the anionic lipids in the lipid bilayer, increasing the affinity of aggregate for bacterial membranes. From the trajectory of the center-of-mass of the four polymers on the lipid surface (Figure 3.6), it can be seen that the AM polymers disassociate from the aggregate in a phased manner. The polymer P4 gets released into the bacterial membrane within first 50 ns, followed by release of polymer P3 around 160 ns. A similar dispersion of antimicrobial lipopeptides from an aggregate into a bacterial membrane was observed in coarse-grained simulations as well [219].

## 3.3.2 Acquired amphiphilic conformations of bbM4 polymers

Facial amphiphilicity is one of the key factors for potent antimicrobial action of naturally occurring AMPs. The bbM4 AMPoly have no in-built facial amphiphilicity built into them *a-priori*. However, the polymers that partition into the bacterial membrane acquire FA conformations, with well-separated cationic and hydrophobic groups, in agreement with previous work [2, 204]. The density profiles of various components of the system, along the membrane normal, are shown in Figure 3.7. The partitioned polymers (P3 and P4) are inserted into the bacterial membrane, with well separated peaks of average location of cationic and hydrophobic groups, clearly suggesting the acquired amphiphilicity. This is not the case with polymers P1 and P2, which are still bound together and have
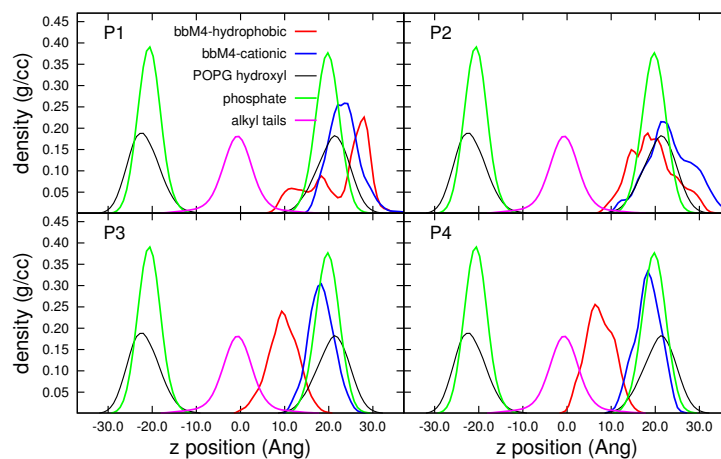
Figure 3.7: Density profiles of various components of simulation along the direction of membrane normal (z-axis). The profiles are computed over 50 ns (250-300 ns). The partitioned polymers (P3 and P4) exhibit distinct amphiphilicity (spatial separation of red and blue peaks). The profiles of the polymers are multiplied by 6.2, for visual clarity.

not partitioned fully into the bacterial membrane. The hydrophobic side chains of polymers P3 and P4 are buried inside the hydrophobic tail groups of the bacterial membrane while the cationic side chains of the partitioned polymers interact with the head groups of the membrane. This conformation of the partitioned polymers is reminiscent of the snorkeling effect of certain transmembrane proteins [220] and amphipathic helices [221].

Two parameters are defined to characterize the onset of acquired amphiphilicity as well as location of constituent groups with respect to membrane head groups in partitioned AM polymers. The time evolution of the center of mass location of cationic and hydrophobic groups shown in Figure 3.8(a) clearly demonstrates this acquired amphiphilicity, for P3 and P4 polymers, after they partition into the bacterial membrane and this acquired facial amphiphilicity persists throughout the simulation time scale. The hydrophobic side chains of partitioned polymers experience a flip, just before the polymers are partitioned into the bilayer. This can also be visually seen in Figure 3.3(d-e) for one of the polymers. A dipole vector for a polymer is defined as a vector joining the center of mass of cationic and hydrophobic groups and the time evolution of projection of unit dipole vector along

99
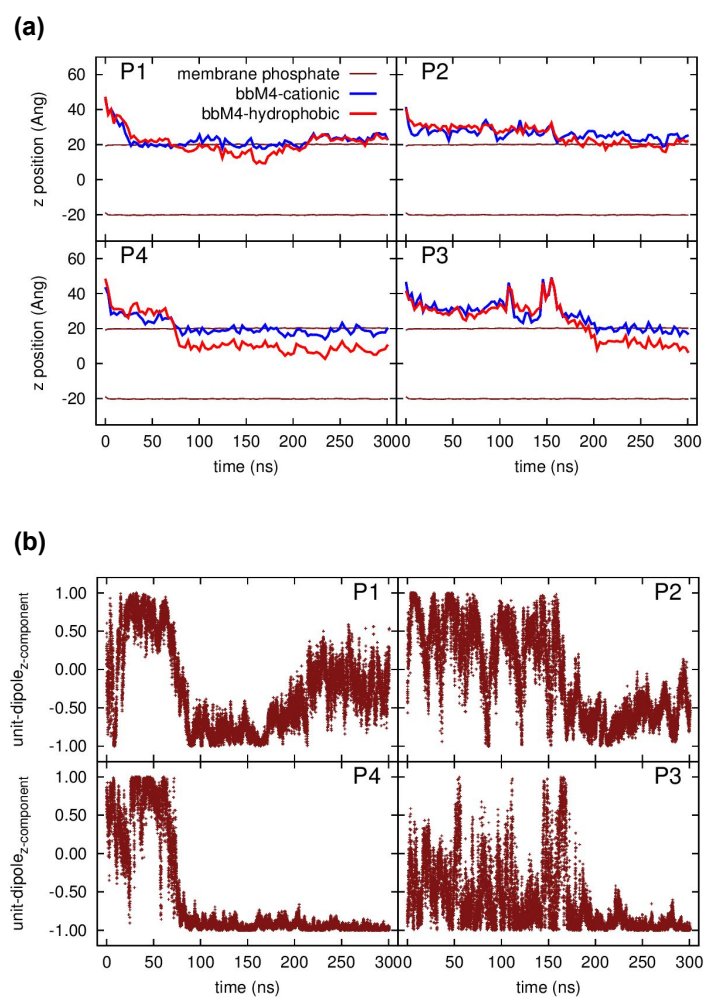
Figure 3.8: Time evolution of (a) center of mass positions of copolymer cationic (blue) and hydrophobic (red) groups. Brown lines denote membrane leaflet-water interfaces. (b) Unit dipole vector of bbM4 AM-Poly, projected along the membrane normal. The dipole is computed as a vector joining the center of mass of cationic and hydrophobic groups.

the membrane normal, for each of the four polymers, is shown in Figure 3.8(b). The projection has the value of ∼ -1 when the partitioned polymer acquires facial amphiphilicity. It can be seen from the plots that the projection, and hence the direction of the dipole vector fluctuates significantly when the polymers are in the solution phase. As the polymers partition into the membrane (P4 and P3), the projection attains a value of -1 and fluctuates around that value. The results shown in Figure 3.8, along with the density profiles computed over 50 ns (250-300 ns) of simulations (Figure 3.7) strongly suggest the acquired facial amphiphilicity of AM polymers, once they partition into the bacterial membrane.

100

Snapshots of a copolymer P4 before and after insertion into the bacterial membrane are
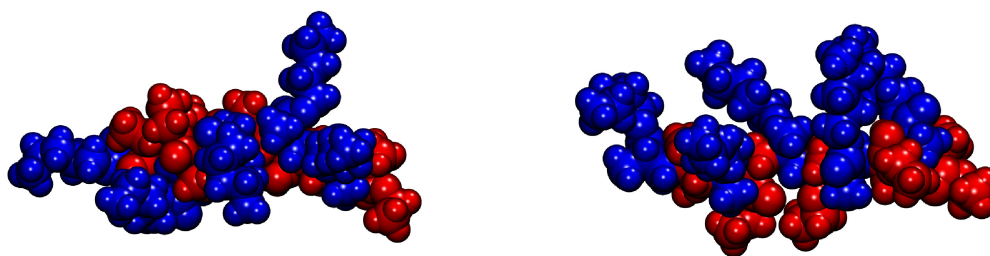


Figure 3.9: Snapshots of polymer P4 before (left) and after (right) insertion into the bacterial membrane. Cationic and hydrophobic arms are colored blue and red respectively.

shown in Figure 3.9. The cationic (red) and hydrophobic (blue) groups which were randomly distributed spatially before insertion, adopt a very distinct amphiphilic structure after partitioning into the bacterial membrane. The density profiles, in Figure 3.7, suggest that the most likely location of cationic side chains of the partitioned polymers is in proximity to the hydroxyl groups of POPG. We measured the radial distribution function,
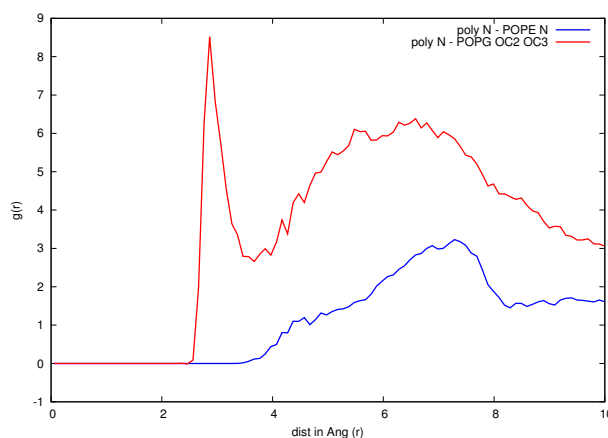


Figure 3.10: Preference of the cationic groups of partitioned polymer to bind to POPG lipid molecules. The amide groups of polymer are found to form strong attractive interactions with the hydroxyl groups of POPG. The radial distribution data is computed over 20 ns (280-300 ns).

$g(r)$, between primary ammonium groups of the polymer and the head groups of POPE and POPG lipid molecules and the results are shown in Figure 3.10. The $g(r)$ results clearly suggest that cationic groups preferentially bind to POPG phosphate groups over POPE, possibly due to the formation of favorable hydrogen bonding interactions between

101

primary ammonium groups of the polymer and the phosphate and hydroxyl groups of POPG.

### 3.3.3 Lateral inhomogeneity in membrane with bbM4 interactions
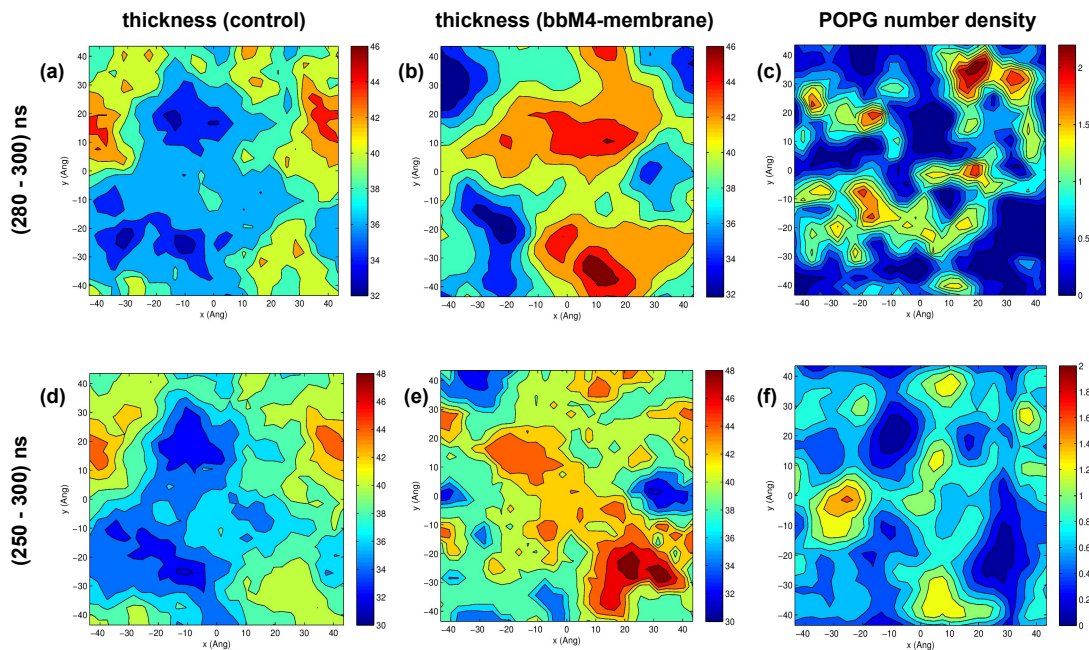


Figure 3.11: Contour plots depicting thickness profile across the plane of the membrane for control simulation (a) and in presence of bbM4 AMPoly (b). (c) 2D number density of POPG lipid molecules combining both leaflets. Results shown in top panel (a-c) have been computed over 20 ns (280-300 ns) of simulation. Bottom panel (d-f) shows same plots when computed over computed over 50 ns (250-300 ns). Comparisons of ((b) and (a)) and ((e) and (d)) figures indicate that POPG rich regions have a lower value of thickness for the bbM4 - membrane system.

Clustering of anionic and zwitterionic lipids into separate phases has been suggested to promote antimicrobial activity through introduction of phase boundary defects such as mismatch in bilayer thickness and curvature, leading to increased leakage of liposomes [6, 222]. The simulation time scales in this work do not allow us to observe the global phase separation of the membrane in the presence of AM polymers. However significant inhomogeneity in membrane thickness has been observed in bacterial membrane over 300 ns of time scale, with the partitioning of bbM4 AMPoly, in contrast to the control simulation. Thickness profile, across the plane of the membrane, in the presence and absence of bbM4 AMPoly is calculated and shown in Figure 3.11 along with two

dimensional number density of POPG lipid molecules for the bbM4-membrane system (considering both leaflets). The plane of the bilayer, perpendicular to the membrane is divided into bins of $2\mathring{A} \times 2\mathring{A}$ and distance between the phosphate groups of upper and lower leaflets of the membrane is computed. In Figure 3.11(a-c) the data is averaged over 20 ns (280-300 ns) of simulation for both the systems. Plots of data averaged over 50 ns (250-300 ns) are shown in Figure 3.11(d-f). A comparison of plots over last 20 and 50 ns suggest that the lipid molecules are still diffusing and that the present results are in the regime of onset of coarsening. The 2D number density plot of POPG molecules clearly indicates mapping of POPG-rich regions with lower membrane thickness.
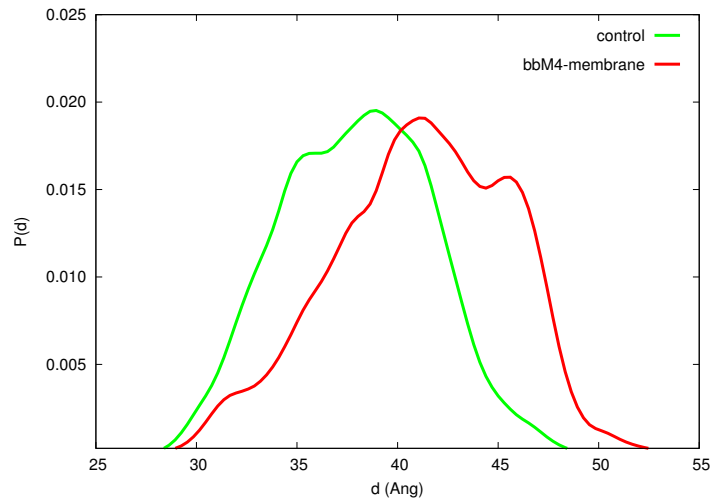


Figure 3.12: Probability distribution of bilayer thickness for control simulation (green) and in presence of bbM4 polymers (red) over 50 ns (250-300 ns) of simulation.

In the following, the lipid tail ordering and consequently the enhanced thickness of POPE-rich regions will be discussed. The distribution of overall bilayer thickness, computed over 50 ns (250-300 ns), for both control and bbM4-polymer systems is also shown in Figure 3.12. The data clearly indicates the shift of average bilayer thickness to higher values in the presence of multiple bbM4 polymers. The average bilayer thickness, measured over 50 ns (250-300 ns), for control and bbM4-membrane systems have been found to be $(38.09 \pm 0.07$ and $40.85 \pm 0.13)\mathring{A}$ respectively. However, the bacterial membrane, with the bbM4 AMPoly inserted, clearly shows considerable non-uniformity, with local values of thickness ranging from $32 - 46\mathring{A}$. The area per lipid for the bbM4-membrane sys-

tem (($60.65 \pm 0.07$)$\mathring{A}^2$) has accordingly been observed to be smaller compared to control bilayer (($64.49 \pm 0.09$)$\mathring{A}^2$).
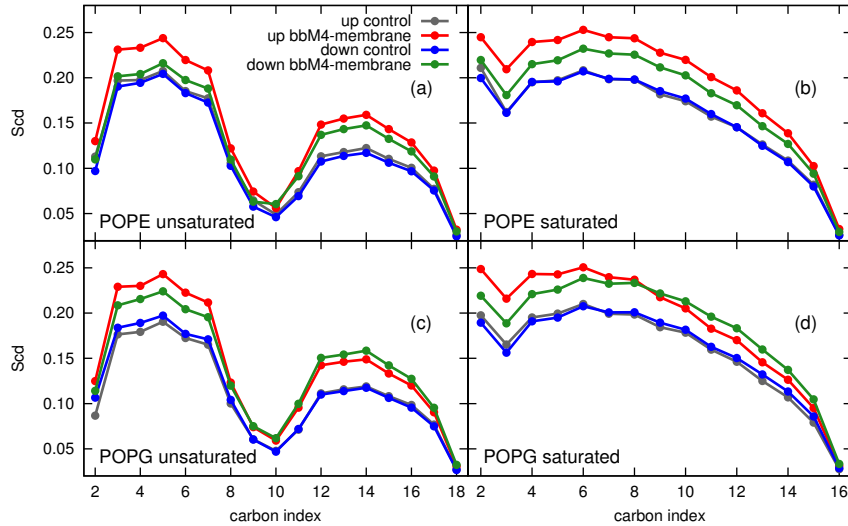


Figure 3.13: $S_{cd}$ values plotted versus the lipid tail carbon atoms. (a) POPE - sn1, (b) POPG - sn1, (c) POPE - sn2, (d) POPG - sn2 tails. The carbon atoms have been indexed starting from the one closest to head groups. Blue and red curves correspond to control and bbM4 - membrane systems at T=300 ns respectively.

To understand the origin of this lateral inhomogeneity and general enhancement in the membrane thickness, we computed the lipid acyl tail order parameter or the deuterium order parameter ($S_{cd}$), defined in equation 2.11, for lipids in both upper (where bbM4 polymers partitioned) and lower leaflets of the bacterial membrane, and compared with the control membrane system. A higher value of $S_{cd}$ indicates ordering of the lipid chains. $S_{cd}$ values have been computed for both POPE and POPG lipids and for the saturated (sn-1) and unsaturated (sn-2) lipid tails and the results are shown in Figure 3.13. The data clearly indicates the enhanced lipid order in the presence of AM polymers for both POPE and POPG lipid molecules. It is also seen that the lipid molecules in the upper leaflet, where the bbM4 polymers have partitioned, experience higher ordering compared to the lipid molecules in the lower leaflet.

Two angles were computed to further characterize the increased order in the membrane

104
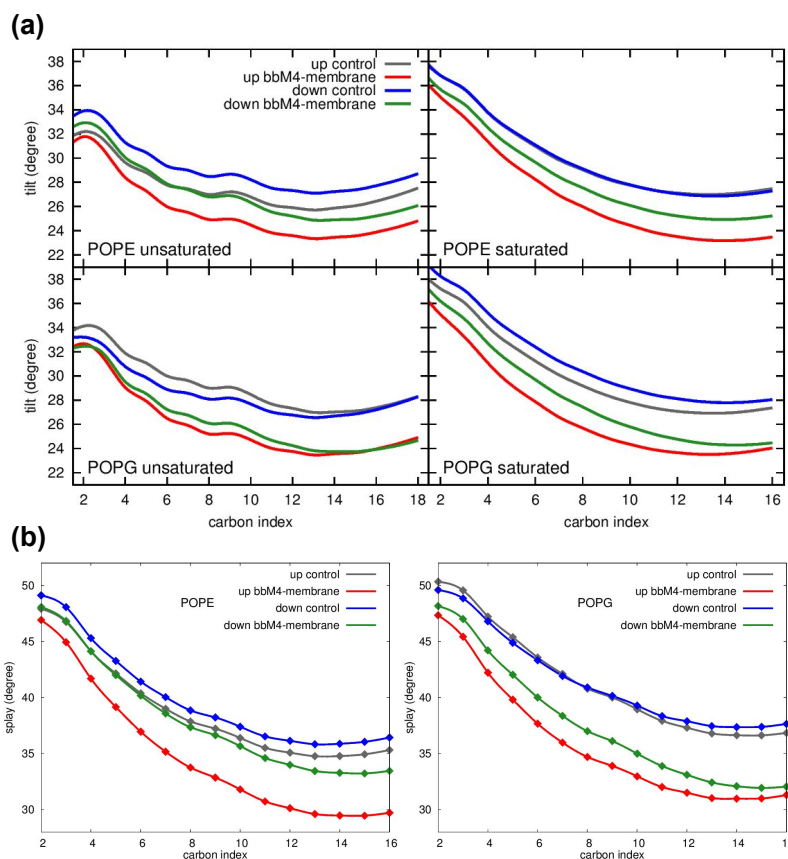
Figure 3.14: (A) Tilt and (B) splay angles of the POPE and POPG lipid chains for bbM4-membrane and control systems, averaged over 50 ns (250-300 ns) of simulation. The tilt and splay angles are computed for each carbon atom along the lipid chain.

lipid tails in the presence of partitioned bbM4 polymers. The tilt angle was measured as the angle between the membrane normal and the vector connecting phosphorous atom of the lipid head group and carbon atoms of the lipid chain. The splay angle was measured as the angle between two vectors, each connecting phosphorous atom of the lipid head group and equivalent carbon atoms along sn-1 and sn-2 lipid tails. The per carbon definitions for the tilt and splay angles were used to envisage the depth within the membrane interior to which the lipid tail ordering is affected, since the bbM4 AMPoly do not adopt transmembrane conformations. The tilt and the splay angles as a function of carbon atoms along the lipid chain and averaged over 50 ns (250-300ns) are shown in Figures 3.14(A) and 3.14(B) respectively. Both tilt and splay angles for lipid chains of POPE and POPG have significantly reduced values in the presence of bbM4 polymers. It can also be observed from the figures that the reduction of tilt and splay angles is more pronounced in

the upper leaflet of the bacterial membrane, where two bbM4 polymers P3 and P4 are fully partitioned.
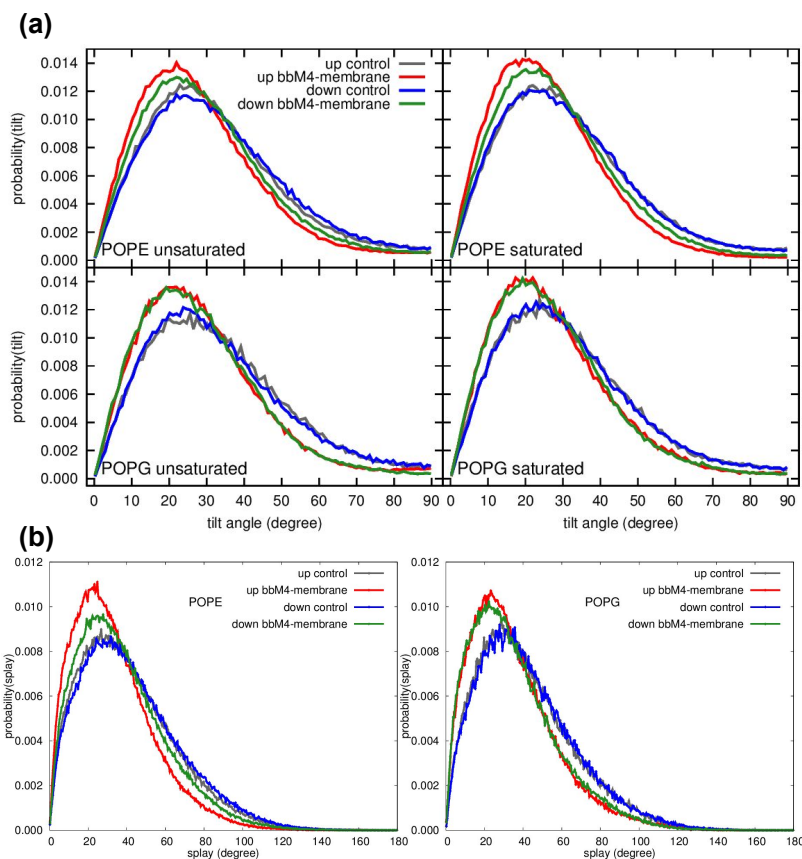


Figure 3.15: Probability distribution for (A) tilt and (B) splay angles of the POPE and POPG lipid chains for bbM4-membrane and control systems, averaged over 50 ns (250-300 ns) of simulation. Tilt angle is defined here as the angle made by the principal axis of inertia of a lipid tail with the bilayer normal. Splay angle is defined as the angle between the principal axes of inertia of sn-1 and sn-2 lipid tails.

Overall tilt and splay angles for the lipid chains were also computed taking the principal axes of inertia of the lipid tails into consideration. For this analysis, tilt angle for a lipid tail (sn-1/sn-2) was defined as the angle made by its principal axis of inertia (corresponding to the smallest eigenvalue of the moment of inertia tensor) with membrane normal. The splay angle for a lipid molecule was defined as the angle between the principal axes of inertia for the sn-1 and sn-2 tails. The distribution for both angles, measured over 50 ns (250-300ns) are plotted in Figures 3.15(A) and 3.15(B) respectively. They clearly suggest enhanced lipid chain packing of POPE lipid molecules, in particular, in the presence of bbM4 copolymers. The enhanced $S_{cd}$ and reduced tilt angles suggest en-

hanced conformational ordering of the lipid chains and can explain the observed increase in bilayer thickness and consequent lateral inhomogeneity of membrane thickness across membrane surface. Experiments by Epand *et. al.* have suggested that the flexible AMPoly can induce global phase separation with POPE changing phase from liquid-disordered to a liquid-ordered phase [6].
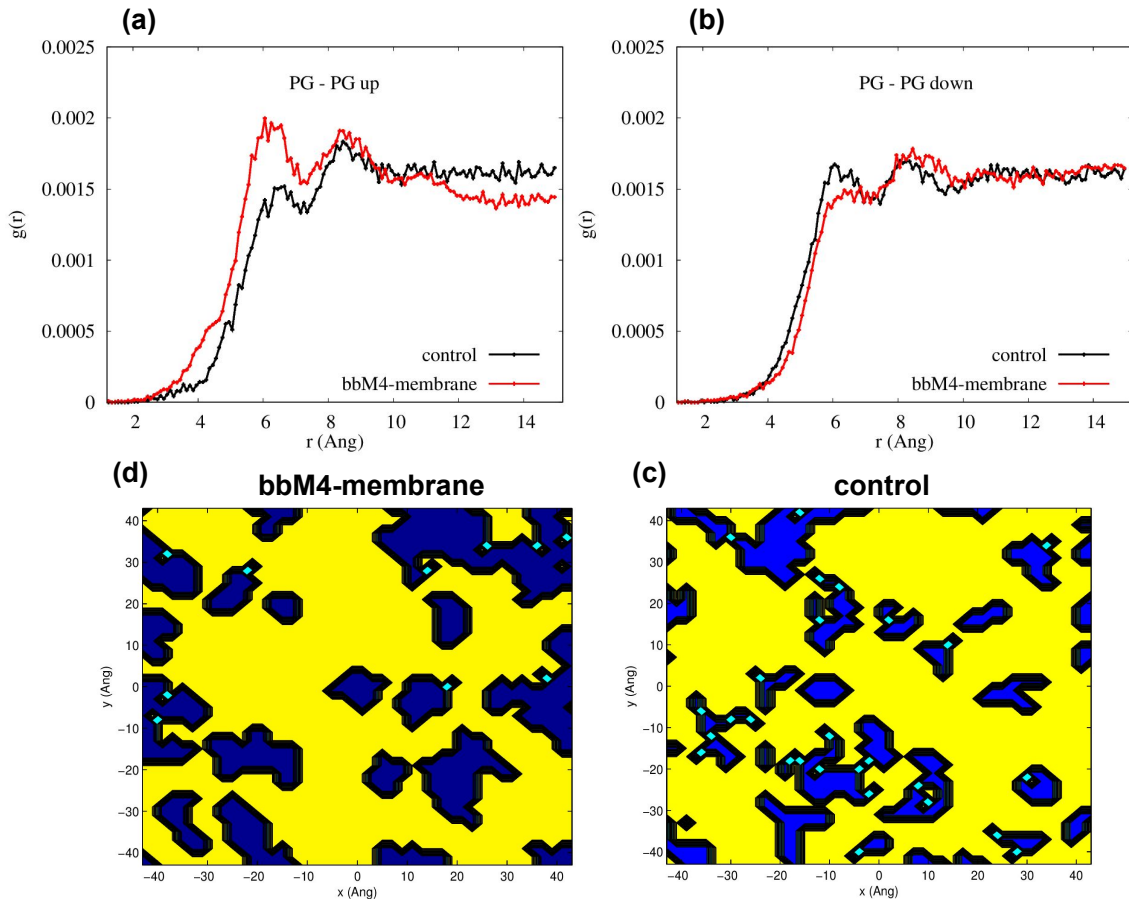


Figure 3.16: Clustering of POPG lipid molecules shown through (a)-(b): 2D g(r) plots measured between the phosphate groups of POPG-POPG molecules, averaged over 20 ns (280-300 ns) and (c)-(d): results from cluster labeling algorithm of Hoshen and Kopelman for the upper leaflets of bbM4-membrane and control systems.

To probe the possible clustering of anionic POPG lipid molecules due to presence of bbM4 polymers, two sets of analysis were carried out. A 2D g(r), averaged over 20 ns (280-300 ns) is computed between the headgroups of POPG lipid molecules for both upper and lower leaflet. Additionally, the clustering of anionic POPG lipid molecules was analyzed using cluster multiple labeling technique due to Hoshen and Kopelman [201], described in section 3.2, for both bbM4-membrane and control systems. The results

107

are shown in Figure 3.16. The 2D g(r) results for the upper leaflet (Figure 3.16(a)) clearly show that for a given POPG lipid molecule, the probability of finding other POPG molecules around 6 $\mathring{A}$ is enhanced for the bbM4-membrane system compared to the control simulations. No similar enhancement was observed for the lower leaflet (Figure 3.16(b)), where there are no AMPoly present. The cluster algorithm results show that for bbM4-membrane systems, the cluster sizes of the POPG lipid molecules is considerably larger than the case of control system (only upper leaflet results are shown in Figure 3.16(c)-(d)). The results also show that in the absence of AMPoly, the POPG lipid molecules are more uniformly distributed and the clustering is significantly increased with the presence of AMPoly. The plots clearly indicate the existence of localized POPG-rich domains in the bbM4-membrane system while the distribution for the control bilayer can be seen to be more delocalized as well as sparse. This indicates the possibility of clustering of POPG molecules into nanodomains en route to phase demixing of POPE and POPG lipids in presence of bbM4 polymers. Formation of such preferentially enriched clusters by components of a system are well known in literature [223]. The largest clusters in the upper leaflets for bbM4-membrane and control systems, at the end of 300ns, were estimated to include 13 and 7 POPG molecules respectively. Due to limited computational time scales, complete phase separation is not observed in present simulations. It can however be noted that the results presented here clearly point towards coarsening of the bacterial membrane by the partitioned AM polymers. Similar lateral organization and induced growth of POPG clusters were observed in a coarse-grain simulation of membrane-bound alpha-helical AM peptides from Latarcin family [216].

The curvature of a bilayer has been suggested to be intrinsically related to the balance between lateral pressures over the individual leaflets [34, 35]. Lateral pressure profiles are difficult to measure experimentally, but simulations have been used to compute the pressure profiles across the membrane [38, 224] and their dependence on changes in membranes due to presence of molecules such as cholesterol [225], alcohol [36, 226] and proteins [227]. The lateral pressure profiles for both control and bbM4-membrane systems
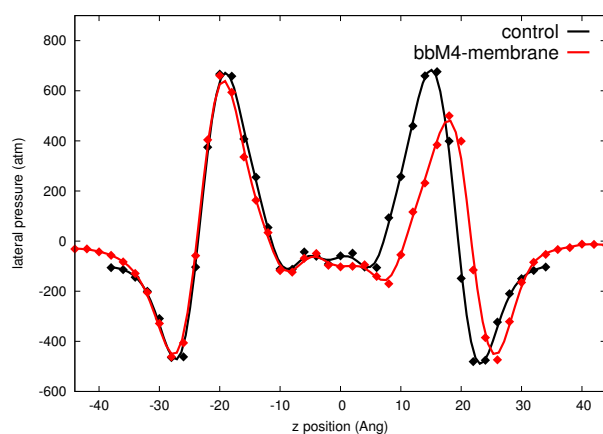
Figure 3.17: Plots for lateral pressure profile for control bilayer (black) and bilayer with partitioned polymers (red) computed over 20 ns (300-320 ns). The leaflet of the bilayer in which the polymers partition corresponds to positive values of the abscissa. The presence of the polymers induces considerable imbalance in lateral pressures over the two leaflets.

have been computed over 20ns (300-320 ns) using equation 1.1. The results of lateral pressure profile are shown in Figure 3.17. In the absence of bbM4 AMPoly, the profile has well-understood peaks corresponding to attractive (negative pressure) and repulsive (positive pressure) interactions in the bilayer. The presence of the AM polymers affects the pressure profile of bacterial membrane quite significantly. The negative peak close to the head group of bacterial membrane ($20\,\mathring{A}$) is considerably reduced. The location of the negative peak coincides well with the presence of cationic groups of partitioned AMPoly. The pressure in the acyl chain region (about $10\,\mathring{A}$) is lowered with the presence of AM polymers. In an earlier simulation with cholesterol in dipalmitoyl phosphatidylcholine (DPPC) membrane, a similar increase in the negative compressing pressure component in the acyl chain region has been observed [225]. This change was attributed to the increased lipid tail ordering caused by the presence of cholesterol. As shown in Figures 3.13, 3.14 and 3.15, the bbM4 polymers increase the ordering of the lipid molecules in the current simulations, thereby increasing the attraction between the lipid chains and causing the lowering of pressure in the acyl region. The changes in the lateral pressure profile due to presence of AM polymers can significantly effect the curvature of the membrane, making it more susceptible to disintegration.

## 3.4 Discussion

The effect of interaction of multiple copolymer mimics of AMPs with a model bacterial membrane (poPE-PG) has been investigated through atomistic molecular dynamics simulation. The polymers considered in this study have a flexible backbone and contain both charged and hydrophobic units and have been shown experimentally to be effective against a broad-spectrum of Gram-positive and Gram-negative bacteria [2]. The aggregate of the polymers travels to the bacterial membrane from water phase and is seen to induce lateral phase separation in a bacterial membrane through cooperative recruitment of anionic POPG lipid molecules. The clustering of the anionic POPG lipid molecules on the upper leaflet, where the polymers are present, leads to coarsening of membrane lipids and inhomogeneity in membrane thickness.

Polymers partition into the bacterial membrane in a phased manner and this release depends on the delicate balance between polymer-polymer interactions in the aggregate and polymer-lipid interactions. Analysis of lateral pressure profiles across the bacterial membrane, distribution of thickness of the bilayer, change in lipid-order parameters and density profiles along the membrane normal suggest that the partitioned antimicrobial polymers affect the structure of the bilayer significantly. Experiments involving similar polymers with conformational backbone flexibility and presence of multiple cationic groups have been shown to promote domain formation in bacterial membranes [6, 56, 222, 228] and it has been suggested that this lowers the membrane permeability barrier due to packing defects. The results of this study support such mechanism of antimicrobial action. A recent all-atom simulation of involving interactions of aggregate of synthetic AM peptide, C16-KGGK, with bacterial membranes showed similar evidence of increased order of lipid molecules and lateral reorganization with partitioning of the peptides [229].

In addition the present results also indicate that the release of antimicrobial polymers into the bacterial membrane depends on two additional aspects: (1) weak interactions within the aggregate, which can be overcome by polymer-lipid interaction (2) availability of

anionic lipids to coarsen the membrane aiding the subsequent release of polymers. From the time evolution of the trajectory of the center of mass of each polymer, it is seen that the two of the four polymers are partitioned into the bilayer with in first 160 ns of simulation. The individual bbM4 copolymers have no in-built facial amphiphilicity and exist in a predominantly random coil configuration in the water phase and also as a part of the aggregate. However, when partitioned into the bacterial membrane, the bbM4 polymers acquire a predominant FA conformation with cationic groups interacting with the head groups of lipid molecules and the hydrophobic tails of the polymer buried deep with in the membrane interior. This 'acquired' amphiphilicity sustains throughout the simulation time scale and validates earlier single-polymer simulations where a similar phenomenon was observed. This strongly supports our earlier results [2, 204] that presence of built-in amphiphilic structures with rigid scaffolds or programmed secondary conformation such as $\alpha$-helix of peptides is not a necessary condition for antimicrobial activity by polymers or peptides. It is rather their ability to facially segregate into cationic and hydrophobic groups, which facilitates efficient binding to the bacterial membranes. In the context of various antimicrobial mechanisms proposed in the literature, our results strongly support that at least for polymers with flexible backbones, antimicrobial mechanism combining the previously experimentally observed segregation of domains and current observations of phased manner of partitioning of polymers at the possible domain boundary defect sites may be a precursor to generally accepted membrane-destabilizing modes for antimicrobial action [230, 231].

# Chapter 4

# Dependence of methacrylate polymer interactions on model membrane composition

## 4.1  Introduction

The interaction of multiple methacrylate polymers with poPE-PG lipid membrane described in Chapter 3, yielded valuable information on the mechanism of partitioning of the bbM4 polymers into the lipid bilayer, conformation of the polymers in the membrane partitioned state, as well as the response of the bilayer in terms of structural and organizational properties. The key observations can be summarized as: (a) bbM4 polymers are released from the aggregate upon interactions with lipid membrane in a phased manner. The release of a polymer from aggregate onto the bilayer leaflet is associated with bbM4 - membrane energetic interactions turning more favorable compared to bbM4 polymer - aggregate interactions, (b) bbM4 polymers can adopt FA conformations in their membrane partitioned phase, and (c) bbM4 polymers can induce demixing of anionic and zwitterionic lipids in membranes, resulting in phase boundary defects such as thickness and

lipid tail order mismatches. Understanding of the mode of poPE-PG membrane desta-bilization, however, does not readily lead to a comprehensive knowledge of the mode(s) of antimicrobial action of bbM4 polymers. Many AMPs are characterized by the abil-ity to act through multiple antimicrobial modes of action under varying environmental conditions [3, 66, 68].

A crucial factor having direct influence on antimicrobial agent - membrane interactions is the lipid composition of the membranes. Changing the lipid compositions of membranes can be broadly classified into changes in (a) lipid head groups, and (b) lipid tails. In the context of antimicrobial agent - membrane interaction, the two types of changes can be envisaged to predominantly influence different stages in the antimicrobial action. The re-cruitment of antimicrobial agent molecules involves the recognition through long - range electrostatic interactions, followed by adsorption and partitioning of the agent molecule. The latter involves specific interactions with lipid head group atoms such as hydrogen bonding, in addition to electrostatic and vdW interactions. In recent studies, non-ideal packing of lipid head groups, leading to interfacial packing defects has also been sug-gested to play an important role in the partitioning of amphiphilic agent molecules to the membrane interior [4, 5]. The interactions of un-partitioned agent molecules with the membranes is thus essentially an interfacial phenomenon having greater dependence on the head group composition, compared to the composition of lipid tails. Partitioned agent molecules, however, interact extensively with the lipid hydrophobic tails. Changes in lipid tail composition has a strong influence on properties such as bilayer thickness and order in lipid tail [17]. Changes to such properties can critically alter the conformations of partitioned agent molecules, as well as their influence on the bilayer properties. How-ever, it is important to note that the overall impact of changes in lipid head group and tail compositions are unlikely to be exclusive.

In this chapter, the study of multiple bbM4 polymer - membrane interactions is extended to include membranes of varying lipid compositions. Retaining the lipid head groups

PE (phosphatidylethanolamine) and PG (phosphatidylglycerol) from the study detailed in Chapter 3, two membranes have been studied which differ in the degree of (un-)saturation of their acyl chains. These are abbreviated as doPE-PG and dpPE-PG in the rest of the thesis. The doPE-PG lipid membrane comprises of zwitterionic lipid DOPE and anionic lipid DOPG lipids, with mono-unsaturations in all lipid tails. The zwitterionic and anionic lipids in dpPE-PG lipid membrane are DPPE and DPPG respectively. All lipid tails of dpPE-PG lipid bilayer are saturated. dpPE-PG and doPE-PG are both models for bacterial membranes. A further lipid bilayer comprising of zwitterionic lipid DOPC and anionic lipid DOPG has been studied, abbreviated as doPC-PG. doPC-PG represents a model for a mammalian lipid membrane patch, but with similar electrostatics as its bacterial equivalent doPE-PG. The chemical structures of the individual lipids are described in section 2.2. In doPE-PG and doPC-PG membranes, the zwitterionic to anionic lipid ratio is 8:2. In dpPE-PG, the ratio is 7:3.

In the following, the interactions of an aggregate of four bbM4 AMPoly with the membrane patches is described. Special emphasis is laid on the influence of membrane lipid composition on the three key observations from bbM4 aggregate - poPE-PG interactions mentioned above. The results in section 4.3 are often posed in a comparative manner.

## 4.2   Model and Simulation method

Atomistic MD simulations under isothermal - isobaric (NPT) ensemble were performed to study the interactions of bbM4 polymer aggregates with membrane patches. Each leaflet of the membrane patches were comprised of 128 lipid molecules. The starting configuration of all membranes were taken from pre-equilibrated membrane patches constructed using CHARMM-GUI's Membrane Builder module [170, 215]. All membranes were adequately hydrated to 50 water molecules per lipid molecule, and $Na^+$ and $Cl^-$ ions were added to neutralize the systems and set salt concentration to 150 mM. At the initial stages

of the simulations, the membranes were subjected to planar, harmonic, and dihedral restraints, which were gradually reduced to zero over 0.8 ns. Following the same, each membrane patch was equilibrated for 50 ns, over which the energy, temperature, pressure and area per lipid were tested for convergence. Following initial fluctuations, the quantities were observed to be nearly constant during equilibration.

Following equilibration, bbM4 aggregate - membrane systems were prepared for the membranes by placing an aggregate of four bbM4 polymers close to one of the leaflets in the respective systems (referred to as the *upper* leaflet). The conformation of the aggregate was taken from our previous work, described in Chapter 3. Additional water was added to the bbM4 - membrane systems and further salts were added to restore the salt concentration to 150 mM. The bbM4 - membrane systems were simulated for 300 ns. Of these, the final 50 ns (250 - 300 ns) were treated as production runs. Each of the 50 ns equilibrated control membranes were also simulated for further 250 ns, resulting in control simulations of 300 ns. The last 50 ns were treated as production runs. All analyses, unless mentioned otherwise, were performed using production run data. Simulation package NAMD2.9 [165] was used to perform all simulations. CHARMM36 [172] force field was used for lipid atoms. Interaction parameters for bbM4 polymer atoms were taken from our published works [2, 204]. TIP3P [135] water model was used to simulate water and standard CHARMM parameters were used for Na$^+$ and Cl$^-$ ions [191].

Langevin Piston [218] was used to maintain pressure at 1 atm, while temperature was controlled through coupling to an external heat bath. The simulation temperature was maintained at 310.15 K for the doPE-PG and doPC-PG systems, and at 340.15 K for the dpPE-PG systems. Different temperatures were chosen so as to simulate all systems above their main phase transition temperature, in the disordered phase. Particle mesh Ewald method was used to compute long range electrostatic interactions. Lennard-Jones interactions were smoothly truncated beyond 12 $\mathring{A}$ using a switching function between 10 $\mathring{A}$ and 12 $\mathring{A}$. Timestep of 2 fs was used for all simulations. Visual Molecular Dynamics

(VMD) [171] was used extensively for visualization and analyses.
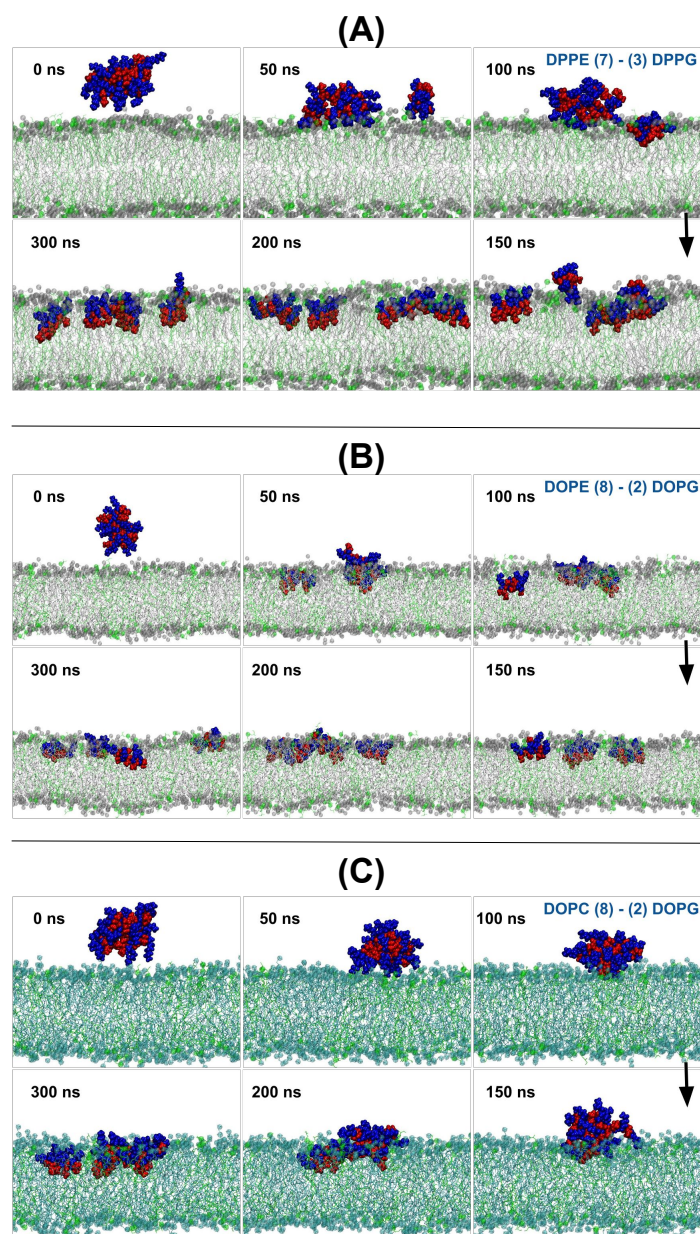


Figure 4.1: Snapshots of evolution of (A) bbM4 - dpPE-PG, (B) bbM4 - doPE-PG and (C) bbM4 - doPC-PG membrane systems. Water and ions are not shown for clarity. The cationic and hydrophobic groups of bbM4 polymers are shown in blue and red respectively.

## 4.3 Results

### 4.3.1 Interaction of bbM4 aggregate with model membranes

The bbM4 polymers, owing to their cationic moieties, interact favorably with anionic (PG) lipid molecules through long range electrostatic interactions. Such favorable electrostatics is considered to play an essential role in the selectivity of antimicrobial agents towards anionic microbial membranes compared to zwitterionic mammalian membranes [1]. For all the three systems studied, the aggregates of four bbM4 polymers were observed to quickly approach the membrane patches, and localize close to the proximal membrane leaflets. Following the contact with the bilayer leaflet, however, differences were observed in the stability of the aggregates, and the evolution of the three systems. Figure 4.1 shows the time evolution of the three bbM4 - membrane systems.

For the PE lipid head group containing membranes (dpPE-PG and doPE-PG), the mechanism of release of the polymers from the aggregate bears close resemblance to that observed with poPE-PG, described in section 3.3. As can be seen from Figures 4.1(A) and 4.1(B), the bbM4 polymer aggregates take up extended conformations upon contact with the bilayer leaflet, thus maximizing contact between polymer cationic side arms and lipid head group atoms. Subsequently, individual polymers are released onto the bilayer leaflets, which quickly partition into the bilayer. Upon contact with doPC-PG bilayer, however, the aggregate was not observed to readily adopt extended conformations, or form strong contacts with lipid head group atoms. As can be seen from Figure 4.1(C), the aggregate was observed to hover on top of the doPC-PG bilayer leaflet over the first 100 ns. During the same, transient contacts with head group atoms were observed through polymer cationic side arms. Strong aggregate - membrane contact was initiated, and the aggregate was anchored onto the membrane between 130 ns to 150 ns. The stable contact was observed to be formed by a polymer hydrophobic side arm, partially buried deeper than the head group region of the bilayer. Subsequent to this, the entire aggregate was

observed to partition into the doPC-PG membrane, over the interval of 150 ns to 240 ns. The partitioning was associated with conformational changes in the aggregate, through which the cationic moieties localized close to the head group atoms and the hydrophobic moieties were buried deeper within the bilayer interior. A single polymer was observed to be released from the aggregate during the partitioning event. The released polymer was observed to localize close to the partitioned aggregated polymers, transiently forming contacts with the same. At the end of the 300 ns of simulations, while the partitioned aggregate was observed to adopt extended conformations, the three polymers comprising the final aggregate were still in contact with one another (Figure 4.1(C, 300 ns)).
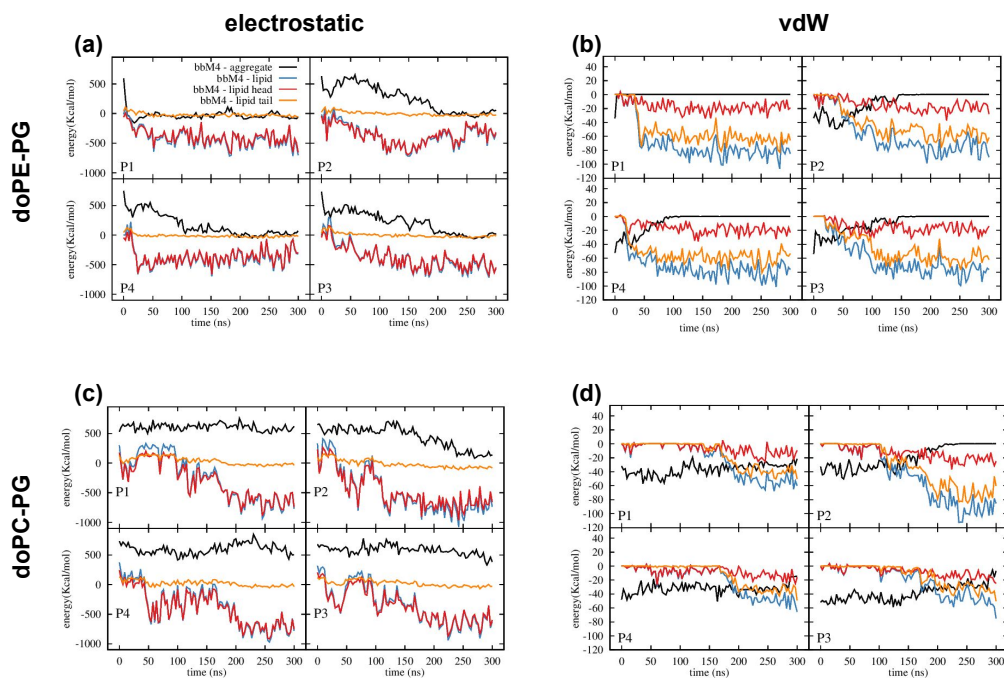


Figure 4.2: Pair interaction energies between each bbM4 polymer and aggregate (black), and between each bbM4 polymer and subensembles of membrane lipid atoms (all : blue, head group : red, tail : orange) computed as a function of time. (a,c) Electrostatic interactions with doPE-PG and doPC-PG membranes respectively. (b,d) vdW interactions with doPE-PG and doPC-PG membranes respectively.

Based on the mechanism of release of copolymer aggregate suggested in our prior study and described in section 3.3, the differences observed in the release of polymers from the aggregate should be reflected in the polymer - aggregate and polymer- bilayer interaction energies. To this effect, we computed the electrostatic and vdW interactions between

individual polymers and subensembles of lipid bilayer atoms, as well as between a polymer and the other three polymers in the system. Three subensembles of lipid atoms were chosen for the purpose,- (a) lipid head group atoms, (b) lipid acyl-chain atoms, and (c) all lipid atoms. The computed interaction energies for the bbM4 - doPE-PG and bbM4 - doPC-PG systems are shown in Figure 4.2. For the bbM4 - doPE-PG interactions, shown in Figures 4.2(a,b), the release of bbM4 polymers can be observed to coincide with bbM4 - membrane interactions becoming more favorable compared to bbM4 - aggregate interactions. The observation was observed to hold true for the bbM4 - dpPE-PG interactions too (results not shown). However, the proposition clearly does not hold for the bbM4 - doPC-PG interactions (Figures 4.2(c,d)). Over the 300 ns of simulation, the bbM4 - lipid interactions become more favorable compared to bbM4 - aggregate interactions for all polymers (P1, P2, P3, P4), but only polymer P2 was observed to be released from the aggregate. These results indicate that while energetic interactions with membrane lipids are important in the destabilization of bbM4 aggregates, other factors also contribute to the phased release of bbM4 polymers. From the plots in Figure 4.2, it can be clearly seen that electrostatic interactions between bbM4 polymers and lipid bilayers is dominated by the interactions with lipid head group atoms, while the vdW interactions have dominant contributions from the lipid tail atoms.

Recently, it has been suggested that the recruitment of amphiphilic molecules by lipid bilayers is modulated by the topography of membrane interfacial region [5]. At the core of the notion lies the concept of interfacial lipid packing defects, which result in the transient exposure of hydrophobic lipid tail atoms to hydrating water. It has been suggested that membrane active molecules are intrinsically capable of detecting such defects and favorably binding to the same [5]. The presence of conical lipids, with relatively small head groups compared to lipid tail cross section, have been shown to result in enhancement of such interfacial lipid packing defects [4]. Lipids with PE head groups are effectively conical in shape, and are characterized by negative intrinsic curvature. In comparison, the effective shapes of PC head group containing lipids are cylindrical, allowing them a
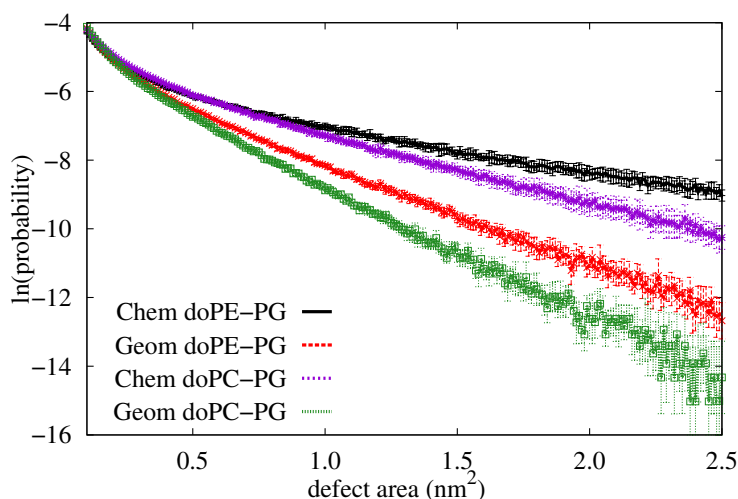
Figure 4.3: Semi-log plots showing the probability distributions of chemical and geometrical interfacial lipid packing defects for the doPE-PG and doPC-PG control membranes as a function of defect surface area. The presence of PE lipids can be observed to lead to greater abundance of both types of defects.

more effective packing in the planar bilayer phase. In our study, the bbM4 AMPoly were observed to make favorable contacts with doPE-PG lipid head group atoms to a considerably greater degree than doPC-PG lipid head group atoms in their adsorbed states. To study the influence of bilayer head group packing on the preferential binding contacts, the probability distributions of such interfacial surface lipid packing defects were computed for the two control bilayers (doPE-PG, doPC-PG) as a function of the defect surface area. The relative abundance of both chemical and geometric defects with greater exposed surface area was observed to be considerably greater for doPE-PG lipid bilayer, compared to doPC-PG. The distributions are shown in Figure 4.3. The results are in good agreement with the observations of preferential binding and phased release of bbM4 AMPoly in presence of doPE-PG lipid membrane.

## 4.3.2 Acquired amphiphilic conformations of bbM4 polymers

Methacrylate AMPoly are not characterized by designed built-in facial amphiphilicity such as $\alpha$-helix or $\beta$-sheet. However, they have been shown to have the ability to adopt to FA conformations upon interactions with poPE-PG lipid membranes. The robustness of
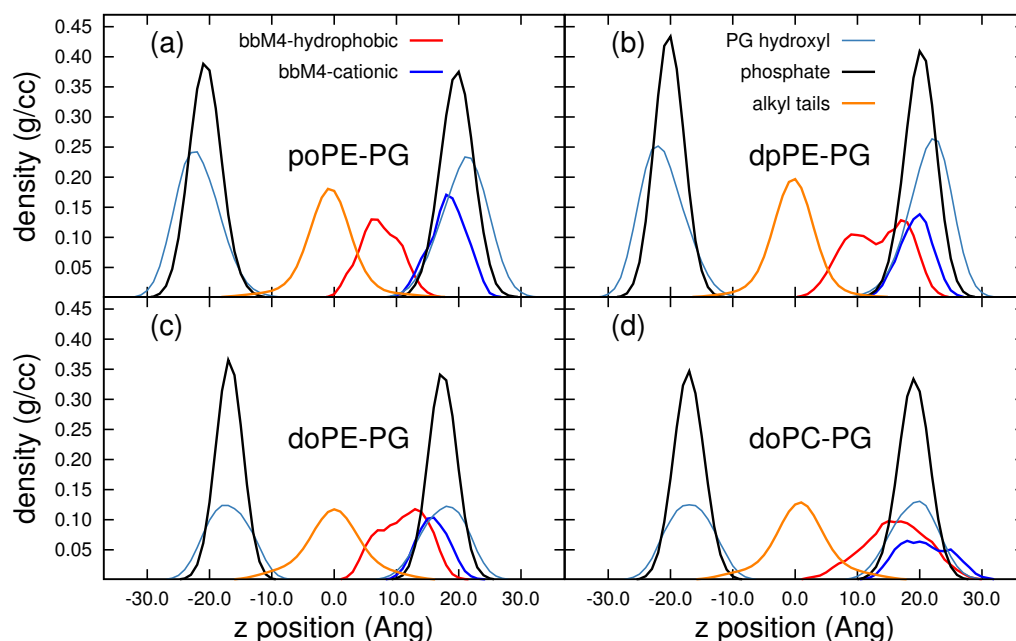
Figure 4.4: Density profiles of various system components along the direction of membrane normal (z-axis). The analyses were done over production run data for all systems. Results for bbM4 - dpPE-PG, bbM4 - doPE-PG and bbM4 - doPC-PG systems are shown in (b), (c), and (d) respectively. Results for bbM4 - poPE-PG system, detailed in Chapter 3, are included for comparison. In each figure, density profiles for cationic and hydrophobic moieties of the bbM4 polymer displaying most robust facial amphiphilicity in the corresponding system is shown.

facial amphiphilicity in membrane-bound conformations of methacrylate AMPoly have been mapped to their bactericidal activity [2]. In a FA conformation of bbM4 AMPoly, the cationic amine groups localize close to the interfacial lipid head group atoms, while the hydrophobic moieties are buried deeper within the membrane's hydrophobic interior. The extent of facial amphiphilicity can be studied by computing the density profiles of system components as a function of position along membrane normal. In the density profile, lesser overlap between the peaks corresponding to bbM4 cationic and hydrophobic (computed as the hydrophobic side chain's terminal groups) moieties indicates a more robust facial amphiphilicity. In Figure 4.4, the density profiles for the relevant bilayer constituents have been shown for poPE-PG, dpPE-PG doPE-PG and doPC-PG membranes, in presence of bbM4 AMPoly. Each system has four bbM4 polymers. For each system, den-

sity profile for the bbM4 polymer with most robust FA conformation observed has been shown in Figure 4.4. The profiles have been computed over (250 - 300) ns of simulation data. The plots for the poPE-PG membrane system are shown for completeness.

Figure 4.4(d) clearly shows that facial amphiphilicity of partitioned bbM4 polymers is not robust upon partition into doPC-PG membrane. The polymer for which the constituent density profiles are shown corresponds to the only bbM4 polymer released from the aggregate during the 300 ns simulation. The plots clearly show a high amount of overlap between the locations of cationic and hydrophobic moieties. Further, the polymer hydrophobic groups can also be observed to be located close to the interfacial region, with the density profiles for bbM4 hydrophobic groups, and bilayer hydroxyl and phosphate groups showing considerable overlap. For the other three polymers in the system, facial amphiphilicity was observed to be even further reduced. The bbM4 AMPoly can be seen to adopt FA conformations when partitioned into dpPE-PG and doPE-PG membranes (Figures 4.4(b,c)), albeit slightly reduced compared to conformations inside a poPE-PG membrane. The results indicate that FA conformations of bbM4 AMPoly are robust when partitioned into bacterial membranes, while less so in presence of mammalian membrane lipid species (PC). In the partitioned conformations, the polymers are anchored to the interfacial region through their cationic moieties. Plots in Figure 4.4 also show that the depth at which the polymers are anchored (peak position of bbM4 cationic groups), is deeper in bacterial membranes, compared to doPC-PG. It can thus be envisaged that bbM4 AMPoly have stronger interactions with poPE-PG, dpPE-PG and doPE-PG membrane lipids in their partitioned state, compared to doPC-PG. The signature can be expected to be reflected in the modulation of membrane properties.

### 4.3.3 Lateral distribution of membrane thickness

Presence of multiple bbM4 AMPoly was observed to introduce lateral inhomogeneity in local thickness in poPE-PG membranes. The lateral inhomogeneity was associated with

123
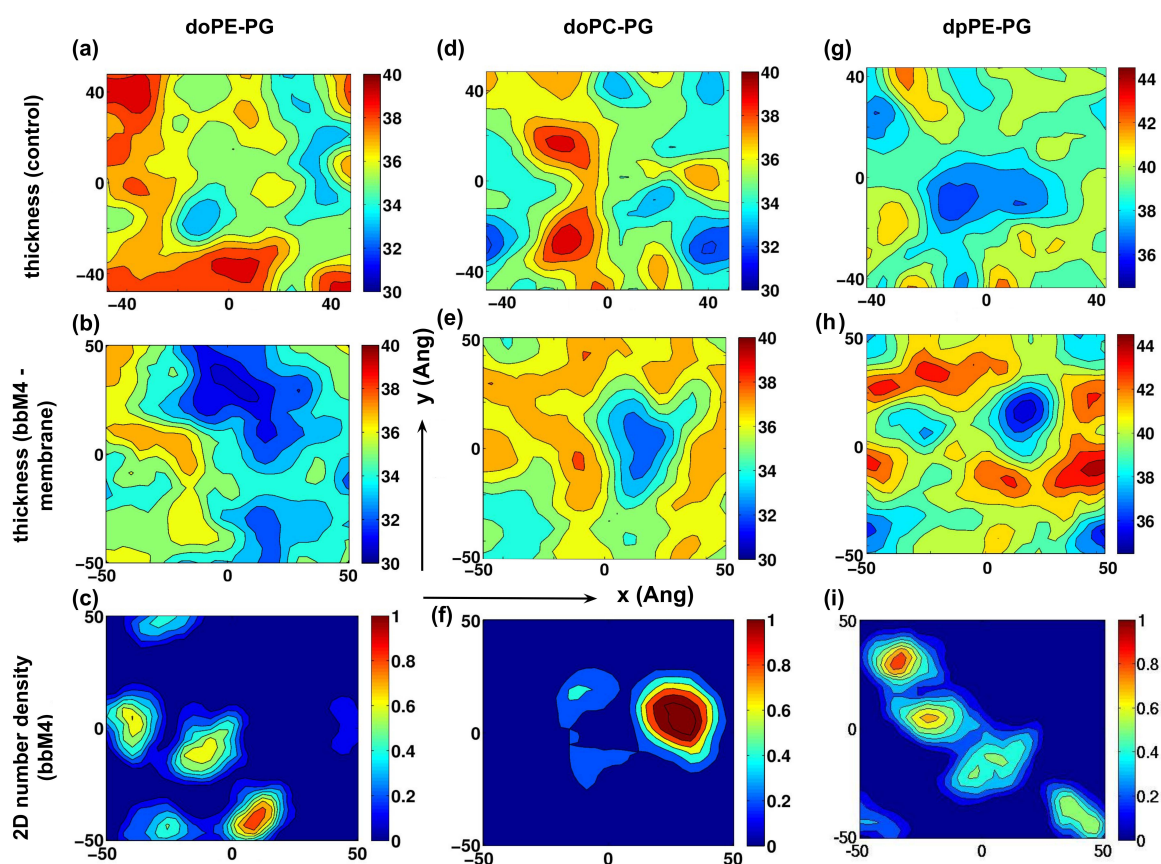
Figure 4.5: Contour plots showing the on-plane distributions of local membrane thickness for control (top row) and bbM4 - membrane (middle row) systems. The bottom row shows the on-plane (2D) number density distributions of the bbM4 AMPoly atoms. The left, center and right columns correspond to doPE-PG, doPC-PG and dpPE-PG membrane systems respectively. The X and Y axes represent co-ordinates along the bilayer-water interface. The analyses were done over (250 - 300) ns of simulation data.

coarsening of bilayer leaflet, resulting in onset of phase demixing of zwitterionic and anionic lipids. Upon interactions with bbM4 AMPoly, no such prominent phase demixing was observed to be introduced in the membranes discussed in this chapter. However, the presence of bbM4 AMPoly was observed to result in moderate lateral inhomogeneity in local membrane thickness in the dpPE-PG membrane. The lateral thickness profiles for control and bbM4 - membrane systems are shown in Figure 4.5, along with 2-dimensional number density distributions of the bbM4 AMPoly. Regions with higher local thickness in bbM4 - dpPE-PG system show close correlations with the distribution of bbM4 polymers, with regions away from the polymers characterized by reduced membrane thickness (Figures 4.5(h,i)). Also, the presence of bbM4 AMPoly is observed to result in enhanced

124

membrane thickness, compared to the control membrane (Figures 4.5(g,h)). While lateral inhomogeneity is thickness is also observed with the bbM4 - doPE-PG membrane interactions (Figure 4.5(b)), it is important to note that considerable inhomogeneity is observed to exist in the doPE-PG control membrane too (Figure 4.5(a)). An overall reduction in thickness of doPE-PG membrane is clearly observed upon interactions with bbM4 AMPoly. The reduction in membrane thickness is more prominent away from the locations of partitioned bbM4 polymers (Figures 4.5(a,b,c)). With close correlations between locally thick regions and the presence of bbM4 polymers, membrane destabilization through mismatches in local bilayer thickness can not be ruled out. No appreciable differences in lateral membrane thickness profile is observed with bbM4 - doPC-PG membrane interactions (Figure 4.5(d,e)), indicating that the polymers maintain a passive presence inside doPC-PG membranes.

## 4.4 Discussion

The results presented in this chapter are part of an ongoing work, and the understanding of bbM4 - membrane interactions is yet incomplete. However, the results indicate important differences in the interactions of bbM4 AMPoly with changes in membrane lipid composition. An aggregate of bbM4 AMPoly is observed to interact weakly with doPC-PG membrane, with weak contacts between polymer aggregate and lipid head groups in the adsorbed state. The vicinity of the membrane is not observed to have strong influence on the shape of the aggregate, whose partition into the doPC-PG membrane is facilitated only by hydrophobic group contacts. It can be envisaged, that in the absence of anionic PG lipid molecules, hence without favorable electrostatic interactions, stable adsorption of the aggregate on PC head group containing membranes is unlikely. Following partition, the bbM4 AMPoly are observed to maintain a passive presence inside the doPC-PG membrane. The partitioned bbM4 polymers do not show robust FA conformations, which is common to all effective antimicrobial agents.

The phased release of bbM4 AMPoly, which can facilitate easy partition of released polymers, is observed to be dependent on the head group compositions. With equivalent electrostatic interactions, phased release is observed with the presence of PE lipids, but not with PC lipids. The comparison of interfacial lipid packing defects observed with doPE-PG and doPC-PG lipid bilayers indicate at a likely connection between propensity for transient hydrophobic exposure and membrane binding of bbM4 AMPoly.

Mechanism of antimicrobial action through lateral inhomogeneity in membrane properties can not be ruled out for doPE-PG and dpPE-PG membranes. However, the mismatches in local membrane thicknesses have not been observed to be associated with demixing of anionic and zwitterionic lipids. A better understanding of the mode(s) of antimicrobial action of bbM4 AMPoly is part of the ongoing project.

# Chapter 5

# Interaction of side chain amphiphilic polymers with model bacterial membrane

## 5.1  Introduction

The role of cationic and hydrophobic moieties of antimicrobial agents on their membrane interactions have been discussed extensively in literature. It is well understood that the cationic groups are key to selective interactions of the antimicrobial agents with microbial membranes, over mammalian ones. The unfavorable exposure of hydrophobic groups to interfacial water drives the partitioning of the agent molecules into the membrane interior. Less understood are structural attributes such as the role of distribution of cationic and hydrophobic groups over the molecular structure. Natural, as well as synthetic molecules with well defined secondary structures such as $\alpha$-helix and $\beta$-sheet have been studied to understand the importance of secondary structural conformations. The results have indicated that well defined secondary structures are not essential for antimicrobial action. The ability to adopt to membrane bound conformations with facial amphiphilicity has

been observed to be key to effective microbial membrane destabilization. Accordingly, AMPoly with flexible backbones have been designed with varied distribution of cationic and hydrophobic groups. In Chapters 3 and 4, the membrane interactions with a class of flexible AMPoly have been discussed, in which cationic and hydrophobic groups are distributed along the polymer backbone [87, 232]. In this chapter, the polymers under study are characterized by side chain amphiphilicity. Each monomer of these homopolymers comprise of amphiphilic side chains, in which the cationic and hydrophobic moieties are distributed over distinct domains.

Apart from electrostatic and van der Waal (vdW) interactions, many antimicrobial agents are also capable of interacting with lipid head group atoms through specific interactions such as hydrogen bonding. For the agents of interest, the contributions from the hydrogen bonding interactions to the overall interaction energies are small compared with electrostatics and vdW. Nevertheless, such interactions are of vital importance in biology. It has been suggested in literature that the role of cationic groups, such as amines, of antimicrobial agents is not confined to electrostatic interactions. Methacrylate AMPoly with primary amine functional groups have been reported to have greater antimicrobial activity compared to ones with secondary and tertiary amines. Also, the antimicrobial activity of primary amine containing methacrylate polymers has been observed to be dependent on pH, hence the protonation state. Primary, secondary and tertiary amines are equivalent in electrostatics, but differ appreciably in their hydrogen bonding ability. These results thus indicate at the relevance of hydrogen bonding interaction between antimicrobial agents and lipid molecules [205, 206]. However, the role of hydrogen bonding interactions in antimicrobial agent - membrane interactions is not well understood.

In this chapter, results from atomistic MD simulation studies, performed to understand the interactions of isosteric amide and ester side chain amphiphilic polymers with a poPE-PG bacterial lipid membrane will be discussed. Four polymers with side chain amphiphilicity have been studied. Their chemical structures, and abbreviations used for them are shown

128
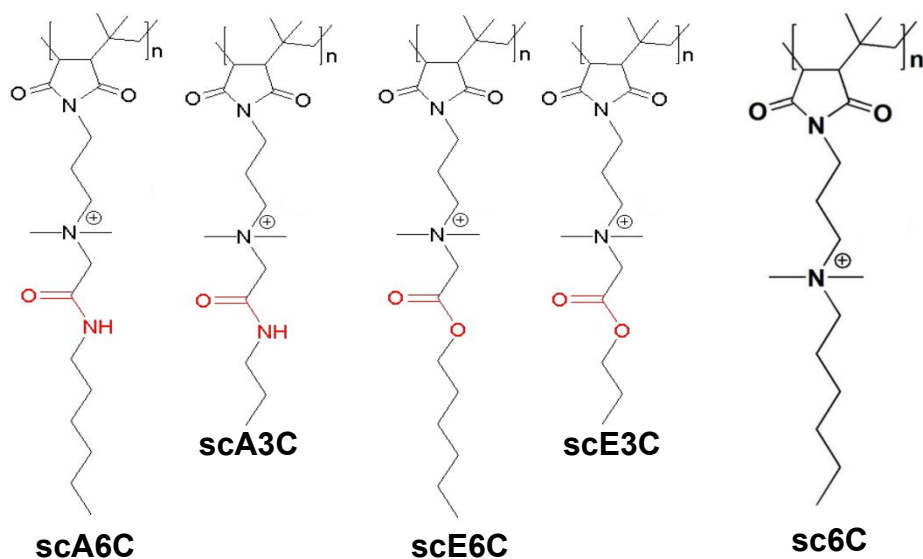
Figure 5.1: Chemical structures of side chain amphiphilic polymers shown along with the abbreviations used to denote them.

in Figure 5.1. These polymers have been recently designed, and are characterized by facile synthesis [87, 232]. Higher and lower alkyl chain amide (scA6C and scA3C) and ester (scE6C and scE3C) polymers were studied to understand the effect of hydrophobicity, as well as the isosteric replacement in their interaction with the membrane. More importantly, these studies were aimed at understanding the difference in the antibacterial efficacy of amide and ester containing polymers. Amide and ester moieties are equivalent in electrostatics, owing to similar charge densities, but differ in their hydrogen bonding ability. It can be envisaged that amide and ester functionalized polymers vary in their ability to form hydrogen bonds with the lipid head group atoms. A fifth polymer, abbreviated as sc6C (Figure 5.1), was also studied. sc6C polymer have the same backbone and cationic moieties as the other polymers, but have neither amide, nor ester functionality in their amphiphilic side chains. The content of this chapter is published in reference [232].

129

## 5.2   Model and Simulation method

Classical atomistic molecular dynamics (MD) simulations were performed using simulation package NAMD (versions 2.8 and 2.9) [165] to investigate the interactions of the individual polymer species with a poPE-PG bacterial membrane patch consisting of 90 POPE and 38 POPG lipid molecules. The membrane configuration used to construct the polymer - membrane systems was taken from a fully hydrated, 300 ns equilibrated membrane patch used in our previous published work [213]. Owing to such long equilibration, the last 50 ns (250 - 300 ns) of the simulation was used as control study to compute observables in absence of polymers. CHARMM force field CHARMM 36 [172], optimized to simulate tension-less bilayers was used for the lipid (POPE, POPG) molecules and force field parameters for the polymers were derived using the CGenFF program [192, 193]. TIP3P model was used for water and standard CHARMM parameters were used for ions ($Na^+$, $Cl^-$) [135, 191].

Each polymer has four representative polymeric chains with 12 monomers each. Equilibrium structures of the 12-monomer length polymers in aqueous environment were obtained by simulating single polymers in 150 mM NaCl solutions for 50 ns. Initial system sizes for such simulations were $68\mathring{A} \times 68\mathring{A} \times 68\mathring{A}$, containing 9500 water molecules. Polymer properties in aqueous environments were computed over the last 30 ns (20 - 50 ns) of simulation data. The polymer configurations at the end of 50 ns were extracted, replicated and used to construct the polymer - membrane systems. To construct each of the polymer - membrane systems, four polymers (of same chemical composition) were placed dispersed in the membrane plane (12 - 18) $\mathring{A}$ away along the membrane normal from one of the membrane leaflets (referred to as the upper leaflet). Additional water molecules were added so as to prevent the polymers from interacting strongly with the other bilayer leaflet (referred to as the lower leaflet), at least at the initial stages of simulations. Further, $Na^+$ and $Cl^-$ ions were added to neutralize the excess charges in the systems and set salt concentration at 150 mM. The number of atoms for the polymer - membrane systems

130

simulated was ~86,000. These systems were each simulated for 150 ns and stationary properties were computed over the last 20 ns (130 - 150 ns) of simulations, unless stated otherwise. All simulations were performed under isothermal - isobaric (NPT) conditions at a temperature of 310.15 K. Pressure was maintained at 1 atm using Langevin Piston [218]. Time step for all simulations was 2.0 fs. Long range electrostatic interactions were computed using particle-mesh Ewald (PME) and Lennard - Jones interactions were truncated beyond using a switching function between 10 $\mathring{A}$ and 12 $\mathring{A}$.

## 5.3 Results

### 5.3.1 Membrane bound polymer conformations and polymer - membrane energetics
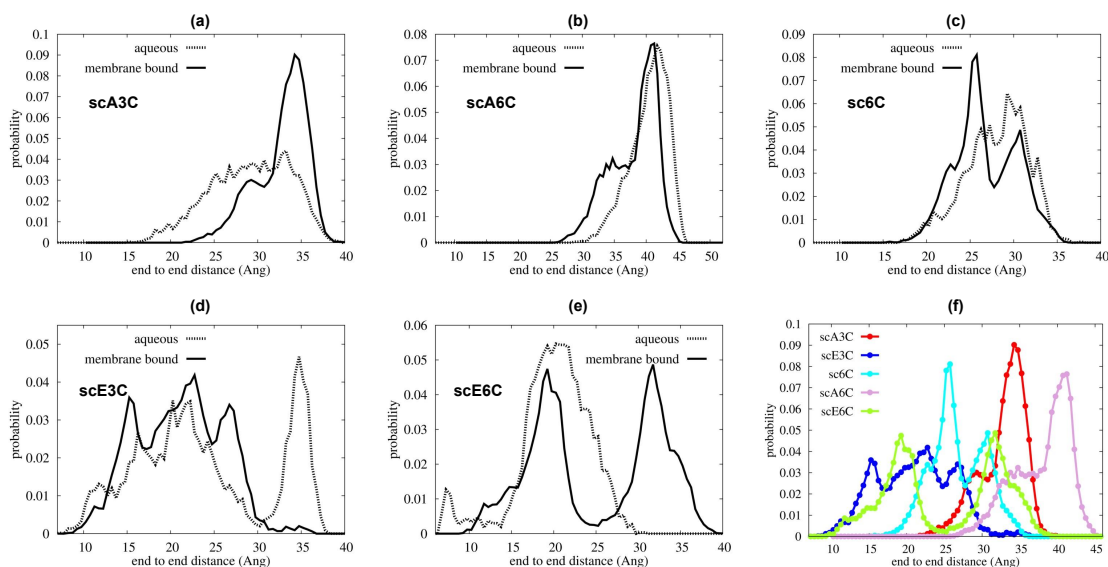


Figure 5.2: (a-e) End-to-end distance distributions for the various polymer species in their aqueous (dotted) and membrane bound (solid lines) states. (f) Comparison of end-to-end distance distributions for the polymers in their membrane bound states. The distances in the aqueous phases were computed over (30 - 50) ns simulation data from the respective AMPoly - 150 mM NaCl aqueous solution simulations. The distances in the membrane bound states were computed over (130 - 150) ns of respective AMPoly - poPE-PG system's simulation data.

Results after 150 ns simulations of amide and ester polymers with the lipid bilayers

showed interesting differences in their membrane - bound conformations as well as their interactions with the lipid head group atoms. The amide polymers (scA3C, scA6C) showed greater propensities to adopt extended conformations at the lipid interface, thus maximizing the number of contacts with lipid head groups, while their ester counterparts (scE3C, scE6C) polymer adopted considerably more compact conformations. Figure 5.2 (a-e) shows comparisons of the individual polymer conformations in their aqueous and membrane - bound states, through end-to-end distance distribution plots. End-to-end distance for a polymer has been computed as the distance between terminal C atoms in the polymer backbone. Figure 5.2 (f) shows comparison between end-to-end distances between polymers in their membrane bound states. Extended conformations were found to be induced to a considerably greater extent in amide polymer than ester counterpart upon interaction with the lipid membranes. Even sc6C did not have appreciable conformational changes compared to the amide polymers upon interaction with the lipid bilayer.
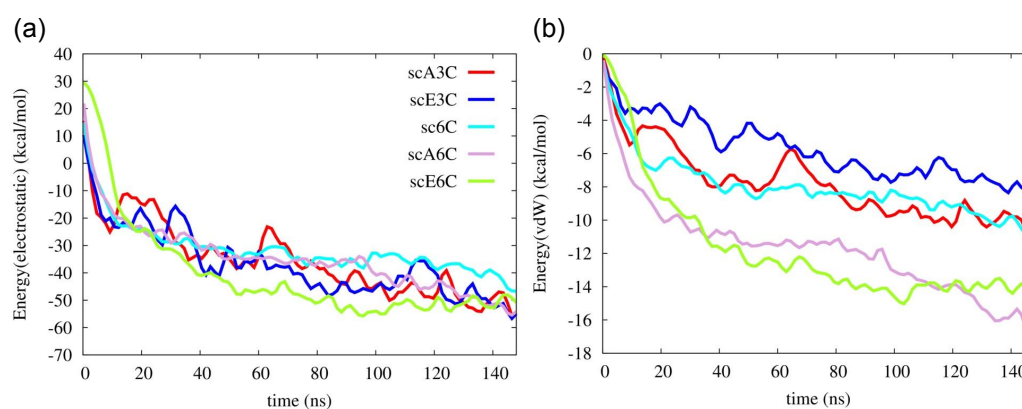


Figure 5.3: Pair interaction energies,- (a) electrostatic and (b) vdW between the various side chain amphiphilic AMPoly and poPE-PG membrane lipids, plotted as a function of simulation time.

Such differences in conformations indicate that these isosteric amide and ester polymers differ in the favorability of their interactions with bilayer lipids. To investigate the same, their interaction energies with the lipid bilayers were computed. The interaction energies have been computed in per sequestered side chain basis to keep them in same footing, since various polymers have different number of sequestered side arms after 150 ns of simulations. It can be seen from Figure 5.3(a) that the electrostatic interaction energies
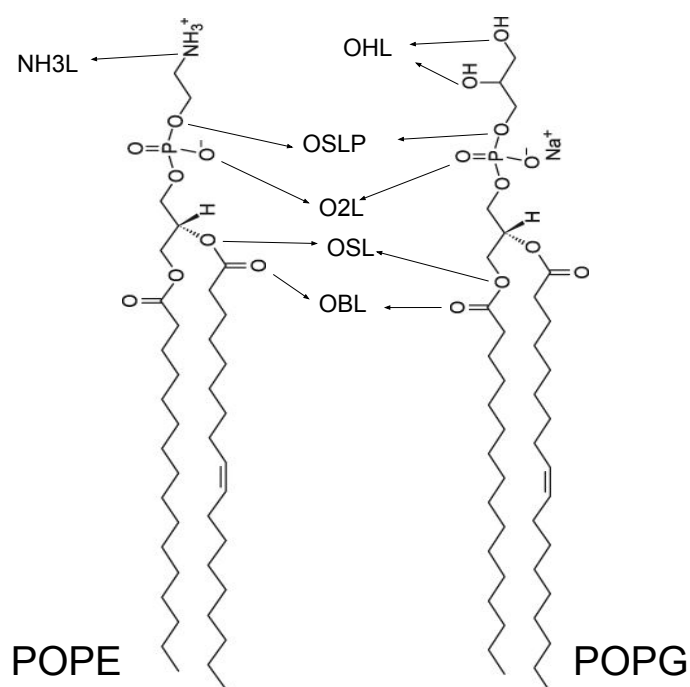
Figure 5.4: Hydrogen bond former atoms of POPE and POPG lipids. The types are shown following CHARMM atom types [172]

(more negative value indicating stronger interactions) of all the polymers were statistically equal. This is expected since the cationic charge density is constant in the present approach. However, vdW interaction energies, were observed to be dependent on length of alkyl chains, as well as functional group (Figure 5.3(b)). vdW interaction energies were more negative (hence more attractive) for scA3C and sc6C but were statistically less for scE3C. Trends observed in the plots for vdW interaction energies of scA6C and scE6C toward the later parts of the simulations (> 100 ns) also indicate that scA6C has more favorable vdW interactions with the poPE-PG membrane lipids compared to scE6C. vdW interaction energies are likely to incorporate a greater signature of interactions of partitioned side chains of these polymers with the hydrophobic lipid chains. This was observed to be consistent with the extent to which the polymers were inserted into the lipid bilayer.
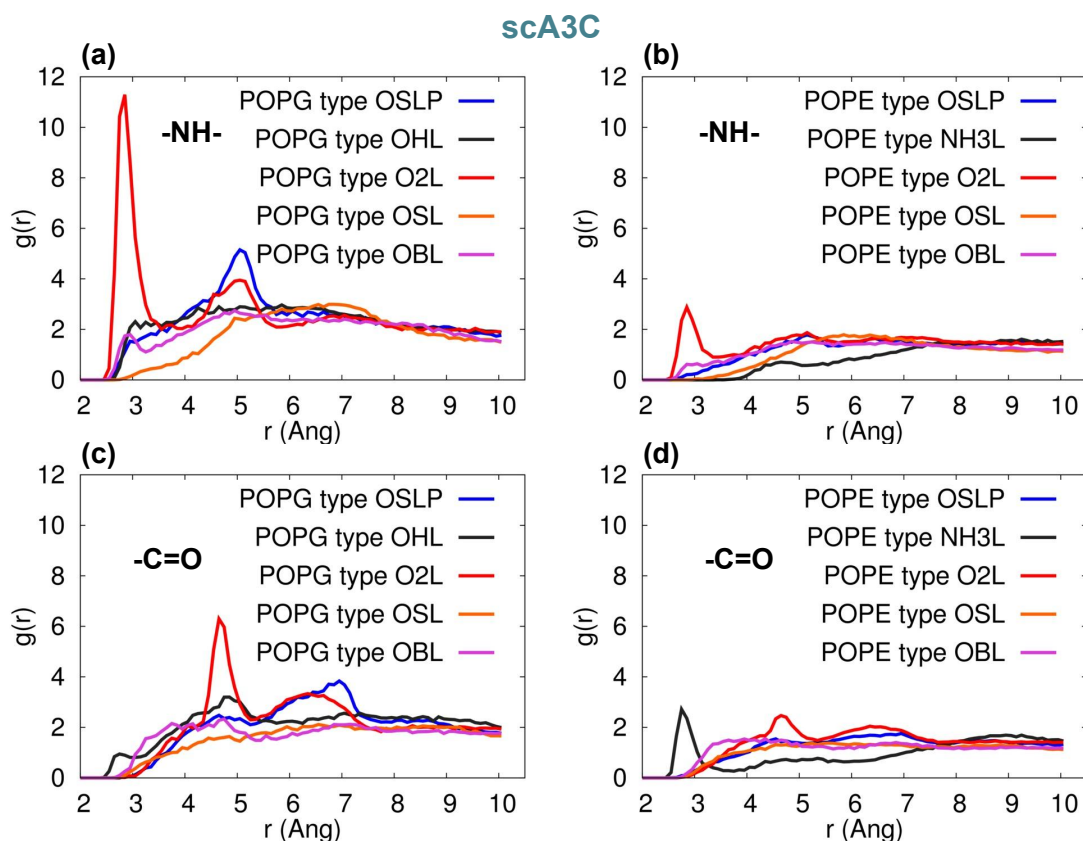
Figure 5.5: Radial distribution functions computed between the hydrogen bond formers of amide group (N from -NH-, and O from -C=O moieties) of scA3C AMPoly, and POPG and POPE lipid head groups' hydrogen bond former atoms (labels based on CHARMM atom types [172]). Preferential interactions with the oxygen atoms of the phosphate head groups of the POPG lipid molecules (red, (a)) can clearly be seen. The amide groups also interact preferentially, albeit weaker, with the phosphate head groups (red, (b)) and ammonium moieties (black, (d)) of POPE lipid molecules.

## 5.3.2  Preferential interactions and hydrogen bonding

The differences in the ability of isosteric polymer species to form hydrogen bonds with the lipid head group atoms were probed through direct computations of number of hydrogen bonds. The positional order in the spatial distribution of hydrogen bond forming lipid head group atoms in the neighborhood of amide and ester moieties has also been calculated. Conventionally, in atomistic MD simulations, hydrogen bonds are calculated using geometric criteria and the same was used in the present cases (donor-acceptor distance $\leq 4.0\text{Å}$ and donor-H-acceptor angle $\leq 60°$. The amide polymers have displayed a greater propensity to form hydrogen bonds compared to their ester counterparts, both in the overall number of hydrogen bonds formed and the number of sequestered side arms

134

observed to be involved in the formation of said bonds (Table 5.1). The propensity of

| polymer | No. hydrogen bonds | No. of side arms involved |
|---------|--------------------|---------------------------|
| scA3C | 34280 | 25537 |
| scA6C | 48100 | 33499 |
| scE3C | 8343 | 7709 |
| scE6C | 15492 | 14402 |
| sc6C | 4035 | 4000 |

Table 5.1: Number of hydrogen bonds formed by the polymers with lipid head group atoms, calculated over the last 20ns (130-150ns) of simulation.

atomic species' to act as hydrogen bonded partners is portrayed in their radial distribution function, or two point density correlation function (g(r)). Radial distribution functions have been computed between the amide and ester groups' hydrogen bond formers and the same from lipid head group atoms and are interpret in the following as their relative affinities in forming hydrogen bonds.

The amide group (-NH- and -C=O moieties) of the amide polymers interact through strong hydrogen bonds with the oxygen atoms of the phosphate head groups of the POPG lipid molecules, as seen in Figures 5.5 and 5.6 (the atom types are explicitly shown in 5.4). The amide groups also form hydrogen bonds, albeit weaker, with the oxygen atoms of phosphate head groups and ammonium moieties of POPE lipid molecules. On the other hand, the carbonyl group of their ester counterparts has no strong interactions with POPG molecules (Figure 5.7(b,d), and form weak hydrogen bonds with ammonium moieties of only POPE (Figure 5.7(a,c). sc6C forms the lowest number of hydrogen bonds, likely due to the backbone imide groups. These results suggest that the amide polymers have strong interactions, whereas the ester polymers are devoid of any preferentially favorable interactions with the negatively charged POPG lipids. These results also support the observation of more stretched conformations of amide polymers.
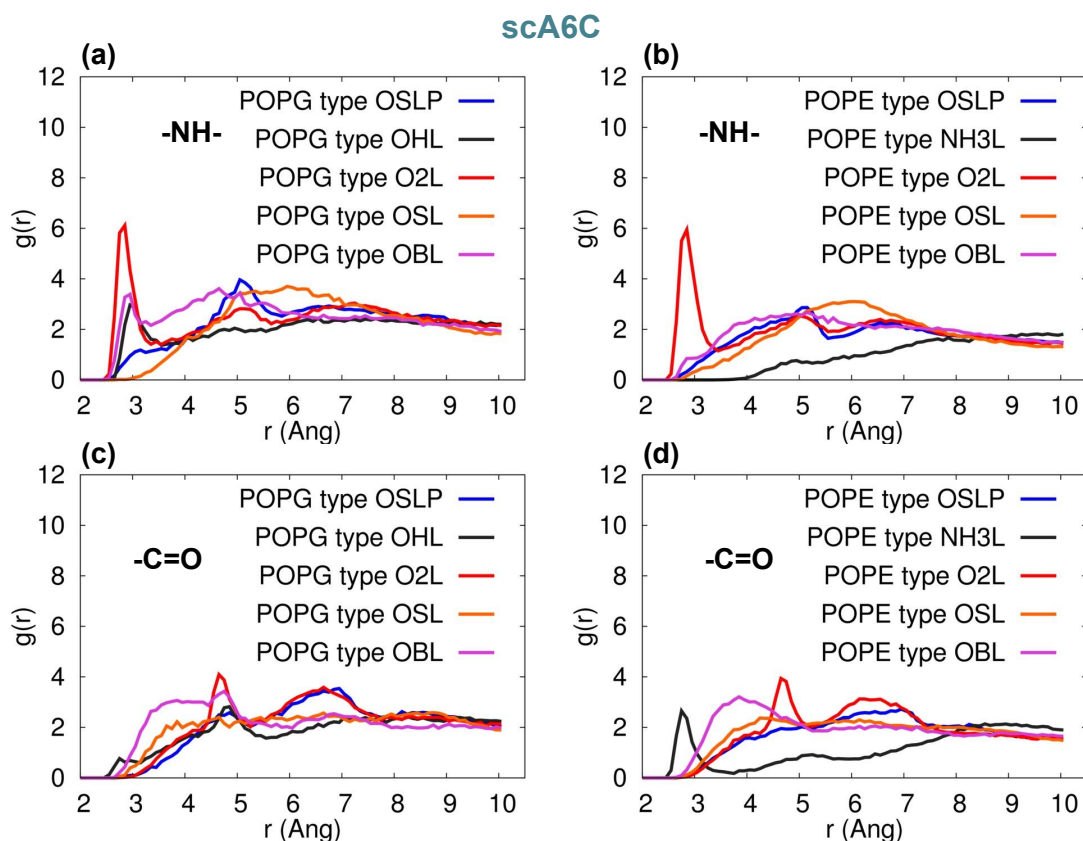
Figure 5.6: Radial distribution functions computed between the hydrogen bond formers of amide group (N from -NH-, and O from -C=O moieties) of scA6C AMPoly, and POPG and POPE lipid head groups' hydrogen bond former atoms (labels based on CHARMM atom types [172]). Preferential interactions with the oxygen atoms of the phosphate head groups of the POPG and POPE lipid molecules (red, (a,b)) can be seen. In addition, plots in (a) show additional preferential interactions with POPG lipid head group moieties (purple, black), which are absent for POPE (b). The amide groups also interact preferentially, albeit weakly, with the ammonium moieties (black, (d)) of POPE lipid molecules.

## 5.3.3    Polymer induced reorganizations of membrane lipids

The discernible differences in lipid - amide polymer and lipid - ester polymer interactions described above are further reflected in the relative ability of isosteric polymers in inducing structural reorganizations of the bilayer lipids. The number density distributions of amide and ester containing polymers, and POPG molecules in the upper leaflet of the corresponding polymer - membrane systems are shown in Figure 5.8. It can clearly be seen that the location of amide polymers and POPG clusters are well correlated and the amide polymers seem to have the ability to reorganize the upper leaflets of the bacterial membranes through favorable interactions between the partitioned side chains and the POPG

136
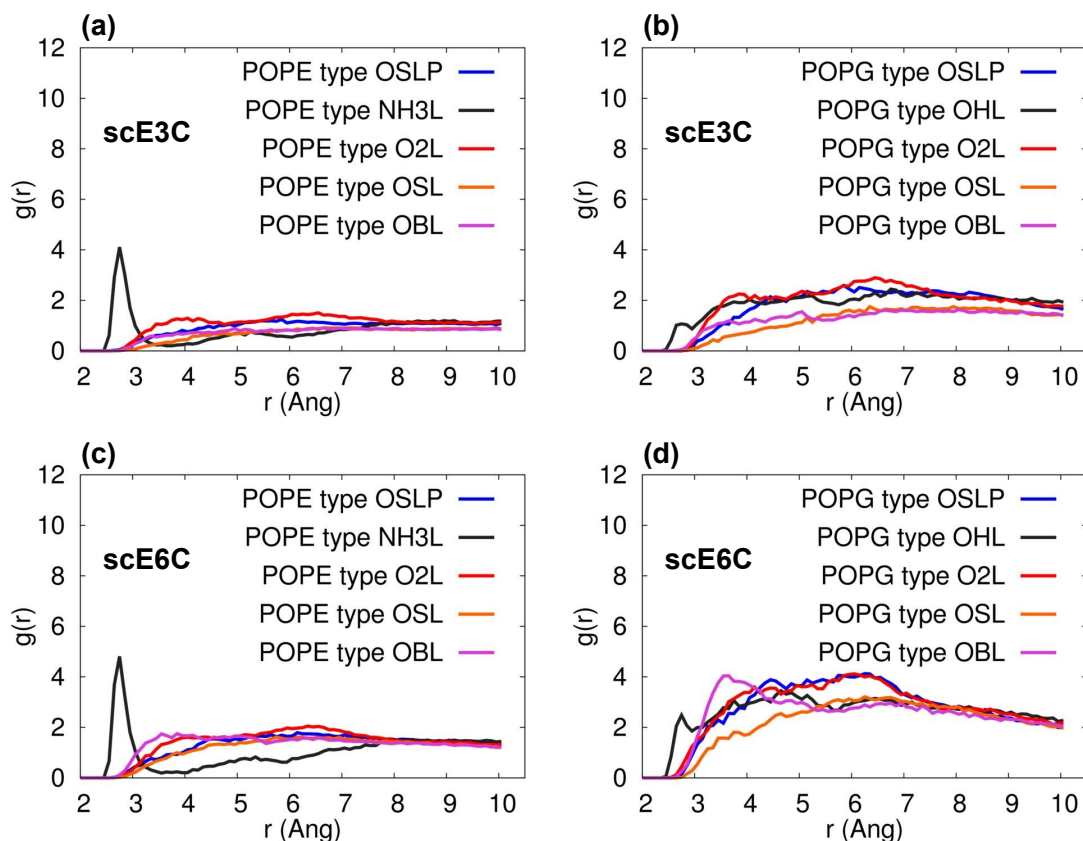
**Figure 5.7:** Radial distribution functions computed between the carbonyl groups of scE3C and scE6C AMPoly, and POPG and POPE lipid head groups' hydrogen bond former atoms (labels based on CHARMM atom types [172]). The only (weak) preferential interactions observed are with ammonium moieties (black, (a,c)) of POPE lipid molecules.

lipid molecules. With equivalent electrostatics in play, the results highlight that weaker interactions such as hydrogen bonding can have significant influence on antimicrobial agent - membrane interactions.

## 5.4 Discussion

Experimental results have shown that the amide containing side chain amphiphilic AM-Poly have greater antimicrobial efficacy compared to their ester counterparts. These MD simulations support the potent antibacterial efficacy of amide polymers due to the culmination of various stronger interactions with the bacterial cell membranes. The additional hydrogen bonding ability of the amide polymers has been observed to modulate
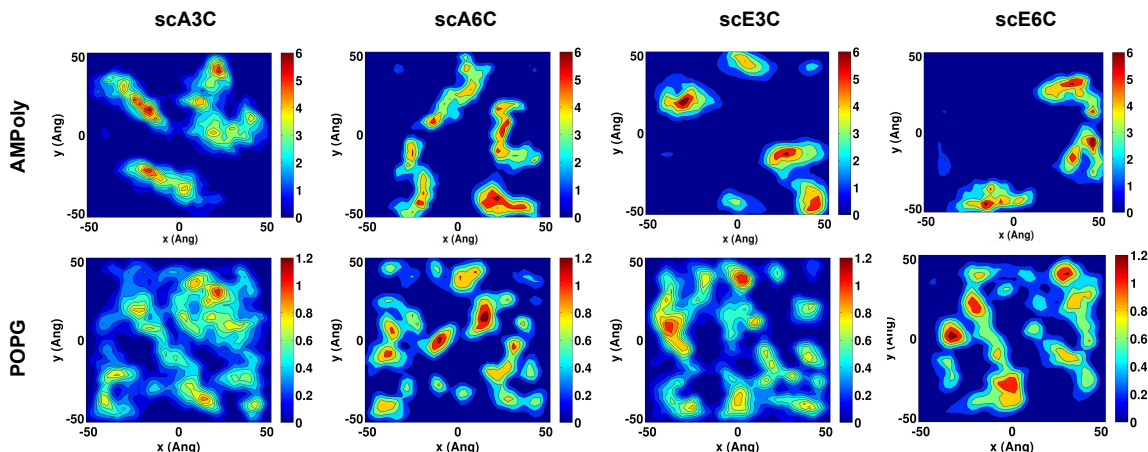
Figure 5.8: 2D number density plots for AMPoly (top row) and POPG lipids in the upper leaflets of the corresponding AMPoly - poPE-PG systems (bottom row). The plots indicate efficient sequestering of POPG lipids by amide AMPoly (scA3C, scA6C).

the membrane - adsorbed conformations, allowing for extended conformations and hence greater number of contacts with lipid head groups. Extended conformations at the membrane - water interface is known to facilitate partitioning of AMPoly into bacterial membranes [2]. The preferentially favorable interactions of the amide polymers with membrane lipids, compared to their ester counterparts is also observed to facilitate effective sequestering of anionic lipids by the former. The results signify the importance of hydrogen bonding interactions in antimicrobial agent - lipid membrane interactions, in addition to non-specific interactions such as electrostatics and vdW.

# Chapter 6

# Effect of simple solutes on the long range dipolar correlations in liquid water

## 6.1   Introduction

Water is generally accepted as a highly structured liquid. The molecular origin of the structure can be mapped to the existence of extensive hydrogen bond network among water molecules, and its incessant, picosecond time-scale fluctuations [7, 150]. Several short-range and long-range structural correlations originating from the same have been discussed in section 1.3. In nature, water rarely exists in its neat, or solute-free form. Commonly known as the *universal solvent*, water dissolves / solvates a wide variety of solutes, ranging from simple inorganic ions, atmospheric pollutants, to biological macro-molecules and their aggregates [10, 147, 233]. Study of chemically diverse solutes have shown that specific solute - solvent interactions such as hydrogen bonding (or the absence of it), locally un-screened electrostatic interactions *etc.* can critically modulate the local structure of water close to the solutes [15, 234, 235]. Another important distinction among

the solutes is their size, which is especially relevant when water interacts with hydrophobic or mixed hydrophobic - hydrophilic surfaces. Considering local structure, studies have shown that water molecules can effectively reorganize around small hydrophobes with no appreciable loss in their hydrogen bond connectivity. However the modification to the hydrogen bond network, when exposed to hydrophobic solutes or surfaces that are at least an order of magnitude larger than the inter - water molecule separations, involves substantial loss of hydrogen bonds. The loss of hydrogen bonds has a profound impact on water structure, and comes with a considerable loss in entropy of the water molecules [110, 113, 144, 236, 237].

A related observation in nature is that large hydrophobic solutes quickly aggregate in water, while small solutes such as methane are appreciably more solvable. It is widely recognized that the aggregation of hydrophobes in water, also known as the *hydrophobic effect*, has contributions from the structure and entropy of water in addition to the energetic favorability [110, 237]. Extensive studies have probed the connection between local water structure and thermodynamic stability of water around hydrophobes, and the hydrophobic effect. However, studies have indicated that modulation to short-range structural properties of water, such as density correlations and the orientational ordering of water molecules, die off within a depth of ~ $10\mathring{A}$ into the aqueous phase [238–240]. While these can partially account for the final collapse of hydrophobes, they are insufficient in accounting for long-range interactions, such as recognition and approach to such short separations. Experiments indicate that the strength of interactions between hydrophobes, over the spatial range of tens to a couple of hundreds of angstroms, decays mono-exponentially and is independent of the chemical composition of the hydrophobes [16, 241]. An understanding of long range dipolar correlations, such as $l(r)$ (see sections 1.3.4 and 2.4), allows us to probe water structure over such relevant length-scales.

The most commonly found solutes in water are simple inorganic ions (dissolved salts). Generally comparable in size with water molecules, their influence on water structure can

be envisaged to be determined by their charge density. Ions have the ability to modulate water structure through preferential electrostatic interactions with either hydrogens, or the lone pairs of the water molecules. Over decades, effort has been made to characterize the effect of dissolved salts on the structure of water based on the ability of the ions to enhance or reduce the same [10, 143]. Consequently, ions have often been characterized as *structure makers* and *structure breakers*. The nomenclature was originally proposed to explain enhanced / reduced solubilities of biomolecules such as proteins in aqueous solutions. However, structure making and breaking by ions has often been evoked to classify their influence on short-range structure of water, such as radial distribution functions, and hydrogen bonding of solvation shell waters. This putative notion has been recently subjected to considerable criticism, primarily owing to the absence of an unambiguous definition of structure in water [9, 242, 243].

In this chapter, results are presented on the effect of multiple salts (CsCl, KCl, NaCl and MgCl$_2$) on dipolar correlations in water, for large system sizes using TIP4P-Ew and TIP3P water models. The results clearly demonstrate that structure making (and breaking) is not a generic concept, but crucially depends on the particular correlation in water. Without invoking a definition of structure, the consistency of our observations are discussed in a general framework motivated by the sum rule for water and associated orientational entropy (see section 1.3.4). For the same, we invoke electrostatics driven orientational stratification of water molecules situated close to the ions. To quantify the same, a solute - dipole correlation is defined, which is a trivial extension of the oxygen - dipole correlation discussed in section 2.4. Finally, as a first extension to the case of non - ionic solutes, we contrast the effects observed for single salt molecules dissolved in water with the same for a methane molecule and show that hydrophilic and hydrophobic impurities of comparable sizes differ characteristically in their effects on the long range orientational correlations in water. The implications of this observation is discussed in the context of hydrophobic effect. The content of this chapter is published in reference [244].

## 6.2   Model and Simulation method

### Dipolar correlations

The orientational correlation functions ($t(r)$ and $l(r)$) and the position - dipole correlation ($d(r)$), involving dipole vectors of water molecules, were defined in section 2.4. The definitions are briefly revisited in the following for consistency. Additionally, a correlation similar to $d(r)$, involving the presence of ions are introduced.

### dipole - dipole correlations

Let $\hat{\mu}$ denote the normalized dipole vector of a water molecule. $t(r)$ and $l(r)$ correlations among any two water molecules, whose oxygen atoms are situated at $\mathbf{r_1}$ and $\mathbf{r_2}$ are defined as,

$$t(r) = \langle \hat{\mu}(\mathbf{r_1}).\hat{\mu}(\mathbf{r_2}) \rangle \tag{6.1}$$

$$l(r) = \langle \hat{\mu}(\mathbf{r_1}).\hat{\mathbf{r}}\,\hat{\mu}(\mathbf{r_2}).\hat{\mathbf{r}} \rangle \ . \tag{6.2}$$

### position - dipole correlations

The oxygen - dipole correlation ($d(r)$) is defined as

$$d(r) = \langle \hat{\mu}(\mathbf{r_1}).\,\hat{\mathbf{r}}\rho(\mathbf{r_2}) \rangle \tag{6.3}$$

where $\rho(\mathbf{r})$ takes a value of 1 or 0 depending on presence or absence of oxygen atom at $\mathbf{r}$ [11]. Similarly, the solute - dipole correlation can be defined through the same expression, where the density field for oxygen atoms ($\rho(\mathbf{r})$) is replaced by the same for a solute species. The oxygen - dipole and solute - dipole correlations represent the propensity for alignment of the dipole vector of a water molecule to the radially outward direction, when

observed from the position of another water molecule or a solute respectively.

## System setup

Classical atomistic molecular dynamics simulations were performed using simulation package NAMD 2.9 [165] using TIP4P-Ew [133] and TIP3P [135] water models. Recently developed parameters that correctly reproduce the right coordination number were used for simulating divalent $Mg^{2+}$ ions with TIP4P-Ew water model [245]. Rest of the monovalent ion parameters for simulating TIP4P-Ew systems were taken from extensively used halide and alkali ion parameters available in literature [246]. For simulating aqueous solutions using TIP3P water model, standard CHARMM parameters [191], used extensively in biomolecular systems, were used for all ions. Methane parameters were derived from aliphatic *sp3* carbon and nonpolar hydrogen parameters in CHARMM [188].

Given the longest correlation length is $\sim 24\mathring{A}$ for $l(r)$ dipolar correlations [11], cubic box lengths of $\gtrsim 50\mathring{A}$ need to be simulated for quantitative estimates of the same. As to enable the identification of any enhancement of the same, or the appearances of even longer correlation lengths, if any, considerably larger cubic boxes of dimensions $\approx 100\mathring{A} \times 100\mathring{A} \times 100\mathring{A}$ were simulated in the investigations of $t(r)$ and $l(r)$ correlations. Solute free water systems comprising of 36054 water molecules for TIP4P-Ew and 34194 water molecules for TIP3P were initially equilibrated for 5 ns under isothermal, isobaric (NPT) conditions under a pressure of 1 atm. The temperature was maintained at 298 K for TIP4P-Ew and at 305 K for TIP3P. The temperatures were chosen since 298 K is the conventional experimental temperature, while 305 K is often used to simulate biomolecular systems with TIP3P water model. The system configurations at the end of the NPT equilibration were used to generate 0.15 M and 1.0 M aqueous solutions of CsCl, NaCl, KCl and $MgCl_2$ using *autoionize* plugin of VMD [171]. The salt-water systems were further equilibrated for 5 ns under NPT conditions (pressure 1 atm; temperature 298 K and 305 K for TIP4P-Ew and TIP3P respectively). All systems, including solute free water systems were equili-

brated for further 5 ns under NVE conditions resulting in total equilibration time of 10 ns for each system. Following equilibration, production runs for all systems were carried out for additional 10 ns, over which the system configurations were written every 4 ps. The analyses for each system were performed on the 2500 uncorrelated system configurations thus generated.

For comparative study of effects of single hydrophilic versus hydrophobic solutes, and the analyses of $d(r)$ correlations, a pre-equilibrated water box of dimensions $\approx 50\mathring{A} \times 50\mathring{A} \times 50\mathring{A}$ was extracted from the 10 ns equilibrated configuration of the $\approx 100\mathring{A} \times 100\mathring{A} \times 100\mathring{A}$ water box for TIP4P-Ew water model. Single $MgCl_2$, NaCl and $CH_4$ molecules were added to the same to construct dilute (1 solute molecule in ~4100 water molecules) solutions. All four systems were further equilibrated for 2 ns under NPT conditions (pressure 1 atm; temperature 298 K) followed by 3 ns under NVE. Production runs for 10 ns were then carried out for each of the three systems under NVE conditions, generating 5000 configurations for analyses. Ion pairing effects were not observed for the salt solutions studied.

For the NPT equilibration stages, constant pressure and temperature were maintained using Langevin Piston [218] and temperature coupling to external reservoir respectively. Timesteps of 1 fs and 2 fs were used for simulating systems with TIP4P-Ew and TIP3P water model respectively. For all simulations, long range electrostatic interactions were computed using particle mesh Ewald (PME) and Lennard-Jones interactions were smoothly truncated beyond $12\mathring{A}$ through the use of switching functions between $10\mathring{A}$ and $12\mathring{A}$.

## 6.3 Results

In this section, observations on the effects of studied solutes on the dipolar correlations $t(r)$, $l(r)$ and $d(r)$ are described. In subsections 6.3.1 and 6.3.2, the effects of salts on the $t(r)$ and $l(r)$ correlations at salt concentrations of 0.15 M and 1.0 M are detailed. In

subsection 6.3.3, the $d(r)$ correlation is described, both in absence of salts and around cationic species. The section is concluded by comparing results for the presence of single molecules of NaCl, $MgCl_2$ and $CH_4$ in subsection 6.3.4.
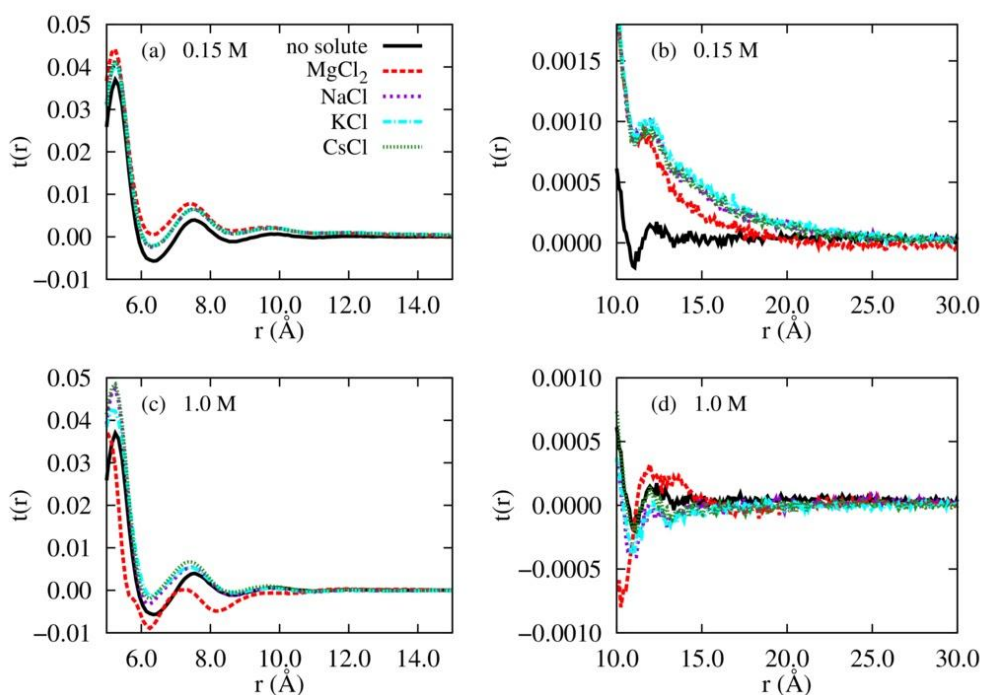
Figure 6.1: *t(r)* correlation functions for systems with (A) TIP4P-Ew and (B) TIP3P water models at 0.15 M and 1.0 M salt concentrations. In all plots, the curve for water in absence of solutes is shown in (solid, black) line. The same are shown in (dashed, red), (dotted, purple), (dash-dot, cyan) and (small dots, green) for MgCl$_2$, NaCl, KCl and CsCl solutions respectively.

## 6.3.1 Effect of salts on trace correlations

Computed $t(r)$ correlation functions for systems with TIP4P-Ew and TIP3P water models are shown in Figures 6.1(A) and 6.1(B) respectively. For clarity of comparison, the plots have been shown for $r \geq 5\mathring{A}$. Results for the two water models are in good qualitative agreement. Also in agreement with prior results for solute free liquid water [11, 120], $t(r)$ shows oscillatory solvation structure over radial separations below $14\mathring{A}$ and vanishes beyond the same. All salts at low concentration (0.15 M) enhance $t(r)$ in comparison with solute free water at both smaller ($\leq 10\mathring{A}$) and larger ($\geq 10\mathring{A}$) separations (Figures 6.1(A)(a,b), (B)(a,b)). At smaller separations, the enhancement is observed to be most pronounced in the presence of $MgCl_2$. The other salts studied (NaCl, KCl and CsCl) are observed to induce smaller, roughly equal enhancements in $t(r)$. Beyond $10\mathring{A}$, however, the effects are reversed with NaCl, KCl and CsCl resulting in a greater enhancement in $t(r)$ over $MgCl_2$. Further, all salts at 0.15 M concentration can clearly be observed to lead to an enhancement in the range of $t(r)$, being non-vanishing till $\sim 18\mathring{A}$ for $MgCl_2$ and $\sim 24\mathring{A}$ for the rest. No appreciable shift in peak positions is observed at 0.15 M concentration for all salts.

At 1.0 M concentration, the effect of $MgCl_2$ can be observed to be substantially different from that of the other salts, as can be seen in Figures 6.1((A)(c), (B)(c)). While NaCl, KCl and CsCl still result in an enhancement of $t(r)$ over that for solute free water for smaller separations, $MgCl_2$ leads to a reduction of the same beyond the first solvation shell. The effect is most prominently observable beyond the second solvation peak, where presence of $MgCl_2$ results in an anticorrelation in the $t(r)$ part of dipolar correlations. Effects of NaCl, KCl and CsCl are also distinguishable at the higher concentration, with CsCl resulting in a greater enhancement in peak heights for $t(r)$ over NaCl and KCl. The positions of the second and third solvation peaks are visibly shifted to left for all salts, the shift being maximum for $MgCl_2$. Further, the appearance of a quasi long range nature in $t(r)$ at the lower concentration (0.15 M) is washed off at the higher (1.0 M)

(Figures 6.1((A)(d), (B)(d))). The concentration dependent enhancing / reducing effect observed for $MgCl_2$ is in good agreement with reported results [120] for $CaCl_2$ which was also observed to affect enhancement in $t(r)$ at 0.25 M concentration followed by similar anticorrelations at the concentration of 1.56 M. The trait thus appears to be a general characteristics for salts with strongly solvated cations capable of inducing strong perturbations in the orientation of water molecules.

## 6.3.2  Effect of salts on longitudinal correlations

Longitudinal correlations $l(r)$ are of greater interest over $t(r)$ in the study of long range dipolar correlations in water since $l(r)$ can be described as a truly long range correlation with an exponential decay [11]. In solute free liquid water at ambient conditions, $l(r)$ has been shown [11] to exhibit solvation peaks till $14\mathring{A}$, beyond which it decays exponentially with longest correlation length of $\sim 24\mathring{A}$ and is non-vanishing even at $75\mathring{A}$. It is always positive in solute free water and decays in an oscillatory manner. The characteristics of this function are closely shared by another long range angular correlation function computable using classical density functional theory calculations [140], further strengthening the likely existence of long range orientationally correlated domains of water molecules. It has been suggested from HRS observations that long range orientational correlations in molecular liquids are expressed through propagating waves in molecular reorientation instead of diffusional orientation of molecules [247]. $l(r)$ as well as the stated angular correlation function [140] are thus in qualitative agreement with HRS results. Recently, correlations from HRS measurements have been directly compared to $l(r)$ and a linear combination of it with $t(r)$, computed using MD simulations [12].

Results have been in qualitative agreement with similar asymptotic behavior. However, the oscillatory nature of the correlations computed using molecular simulations have not been reflected in the HRS results. A direct quantitative comparison with the experimental results is still not possible since (a) system dimensions studied using HRS are well

148

beyond the scope of atomistic simulations [139] and (b) HRS does not provide explicit information of microscopic correlations among molecular dipoles [140].

Computed $l(r)$ correlations for systems with TIP4P-Ew and TIP3P water models are shown in Figures 6.2(A) and 6.2(B) respectively. As with $t(r)$, the plots have been shown for $r \geq 5\overset{\circ}{A}$. Given the system sizes ($\sim 100 \times 100 \times 100\overset{\circ}{A}^3$) studied, the correlations have been computed upto $48\overset{\circ}{A}$ separations. The results for solute free water has been observed to be consistent with prior results [11, 120]. All salts have been observed to induce reduction in both the strength and range of $l(r)$ correlations at both the concentrations studied. The reduction is more prominent at the higher salt concentration (1.0 M) studied. At 0.15 M salt concentrations, the $l(r)$ correlations for salt - water systems retain the essential solvation structures of solute free $l(r)$, such as the positions of solvation peaks and the absence of anticorrelation. However, the long range the decay of the correlations, which are bi-exponential for solute free water, are severely effected even at 0.15 M salt concentration (Figures 6.2((A)(a,b), (B)(a,b))). The longest correlation length $\sim 24\overset{\circ}{A}$ for solute free water is not observed for any of the salts, even at 0.15 M concentrations. The correlation lengths have been obtained by fitting $l(r)$ for $r > 12\overset{\circ}{A}$ to a bi-exponential or a mono-exponential ($a_2 = 0$, for salt - water systems) function of Ornstein-Zernike kind [248].

$$l(r) = \frac{a_1}{r} \exp(-r/r_1) + \frac{a_2}{r} \exp(-r/r_2) \tag{6.4}$$

The fit results are shown in Table 6.1 for both TIP4P-Ew and TIP3P water models. Within the limitations of model dependence, the results from both water models are in good agreement. The comparable effects of NaCl, KCl and CsCl are reflected in the correlation lengths too.
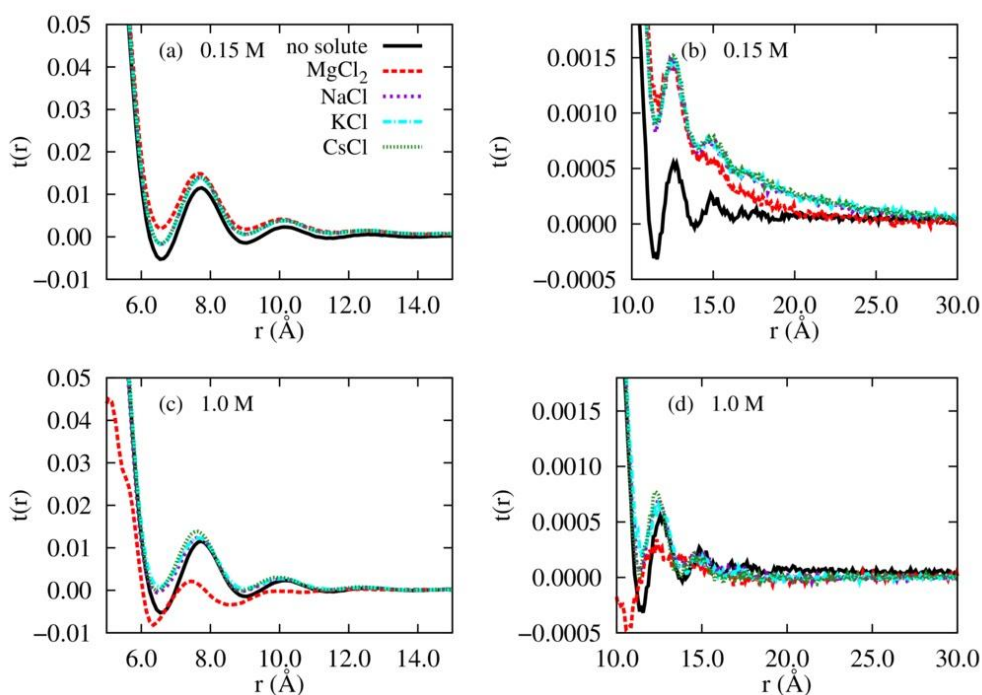
149
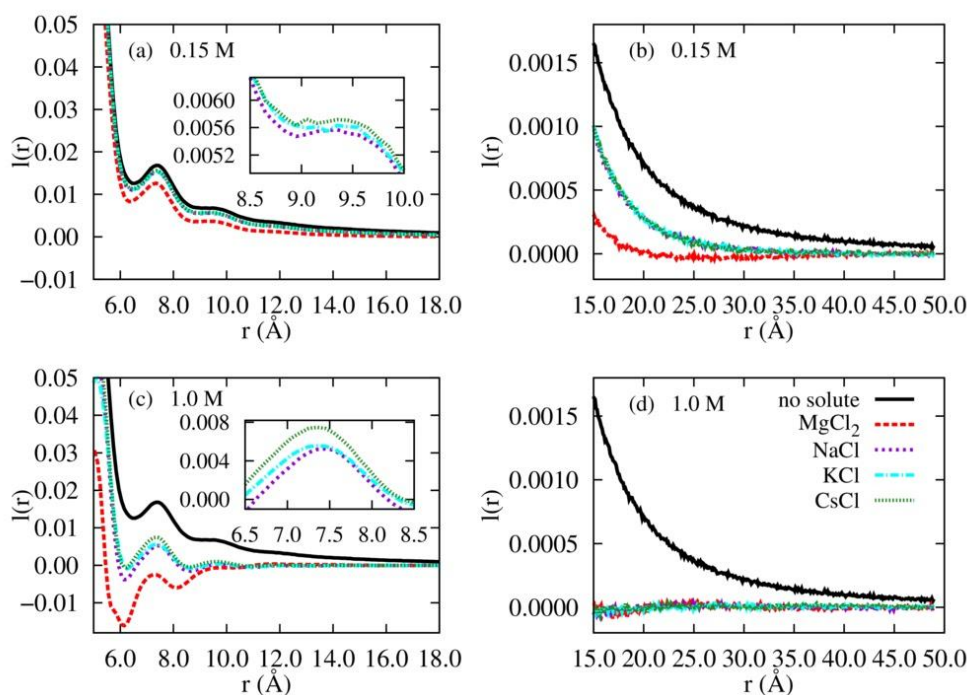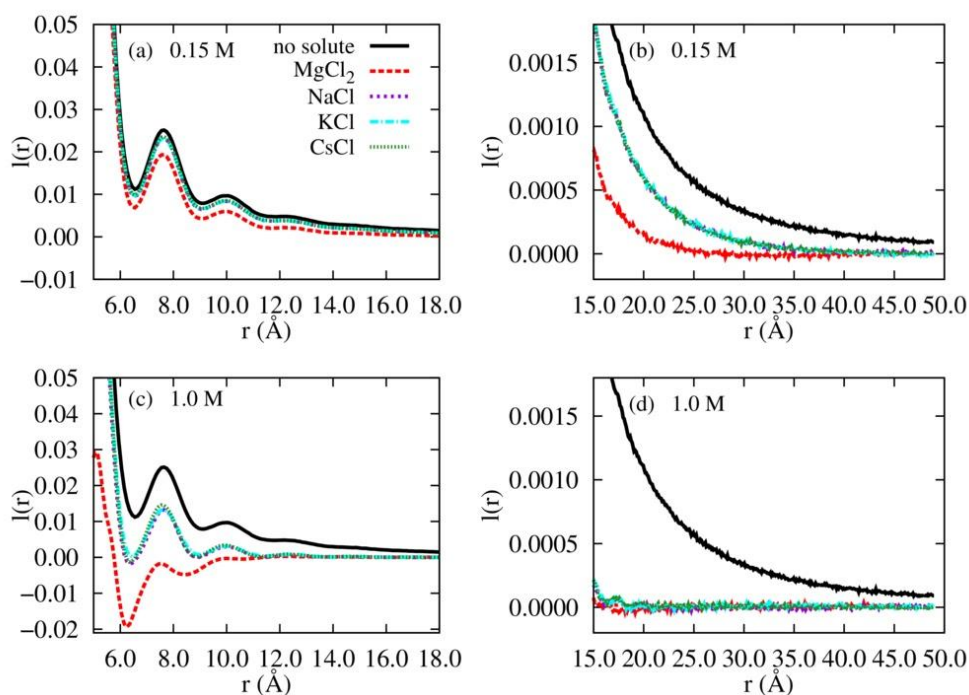
Figure 6.2: *l(r)* correlation functions for systems with (A) TIP4P-Ew and (B) TIP3P water models at 0.15 M and 1.0 M salt concentrations. In all plots, the curve for water in absence of solutes is shown in (solid, black) line. The same are shown in (dashed, red), (dotted, purple), (dash-dot, cyan) and (small dots, green) for MgCl$_2$, NaCl, KCl and CsCl solutions respectively.

| water model | salt (concentration) | $a_1$ (AU*) | $r_1$ (Å) | $a_2$ (AU*) | $r_2$ (Å) |
|---|---|---|---|---|---|
| TIP4P-Ew | none | 0.31 (± 0.01) | 4.82 (± 0.08) | 0.0207 (± 0.0008) | 24.0 (± 0.6) |
| | CsCl (0.15 M) | 0.321 (± 0.004) | 4.93 (± 0.02) | | |
| | KCl (O.15 M) | 0.34 (± 0.01) | 4.82 (± 0.03) | | |
| | NaCl (O.15 M) | 0.34 (± 0.01) | 4.77 (± 0.03) | | |
| | MgCl$_2$ (O.15 M) | 0.74 (± 0.04) | 2.94 (± 0.04) | | |
| TIP3P | none | 0.34 (± 0.01) | 5.24 (± 0.12) | 0.026 (± 0.001) | 24.8 (± 0.9) |
| | CsCl (0.15 M) | 0.344 (± 0.006) | 5.95 (± 0.04) | | |
| | KCl (O.15 M) | 0.359 (± 0.006) | 5.93 (± 0.04) | | |
| | NaCl (O.15 M) | 0.323 (± 0.005) | 6.10 (± 0.04) | | |
| | MgCl$_2$ (O.15 M) | 0.82 (± 0.04) | 3.01 (± 0.03) | | |

Table 6.1: Numerical fitting results for $l(r)$ for TIP4P-Ew and TIP3P water model systems. For the higher (1.0 M) salt concentration, all salts result in disappearance of the long range component of $l(r)$. The numbers within parenthesis represent the numerical fitting error estimates. The results for TIP4P-Ew and TIP3P water models are at 298K and 305K respectively.
* Arbitrary Units.

While the correlation lengths of $l(r)$, computed for individual salt - water systems, can not distinguish the relative effects of NaCl, KCl and CsCl, their relative influences are discernible even at 0.15 M concentrations through their solvation peaks (as shown in the inset of Figure 6.2(A)(a) for the third solvation peak). Owing to the common choice of anion (Cl$^-$), the cations studied can be ordered based on their relative effects on the longitudinal correlation $l(r)$. In terms of effects on $l(r)$, for both 0.15 M and 1.0 M salt concentrations, the trend is observed to be Cs$^+$ <K$^+$ <Na$^+$ <Mg$^{2+}$.

At the higher concentration of 1.0 M, salts are observed to severely reduce the $l(r)$ correlations. The absence of anticorrelations in $l(r)$ is observably lost for MgCl$_2$ and NaCl as seen from Figures 6.2((A)(c), (B)(c)). Closer scrutiny of curves for KCl and CsCl also indicate anticorrelated regions, especially with TIP4P-Ew water model. The trends ensure that at higher concentrations, all studied salts would result in negatively correlated regions in $l(r)$ profile. Salts studied have not been observed to have any appreciable effect on the positions of observable solvation peaks in $l(r)$, except for MgCl$_2$, which is observed to induce small shift in peak positions to smaller separations. Most notably, however, the long range nature of $l(r)$ visibly disappears within 1.0 M concentrations for all salts studied (Figures 6.2((A)(d), (B)(d)), fit results in Table 6.1 show that the long range component vanishes even at 0.15 M). The long range behavior of $l(r)$ correlations in liquid water was

shown to be predominantly governed by local fluctuations in the underlying hydrogen bond network of water [11]. Observed effects of salts on $l(r)$ thus clearly indicate that the salts studied induce perturbations in the hydrogen bond network of water,- especially MgCl$_2$, for which the magnitude of effect indicates at highly non-local effects owing to the presence of strongly solvated Mg$^{2+}$ ions.

### 6.3.3  Effect of salts on position - dipolar orientational correlations
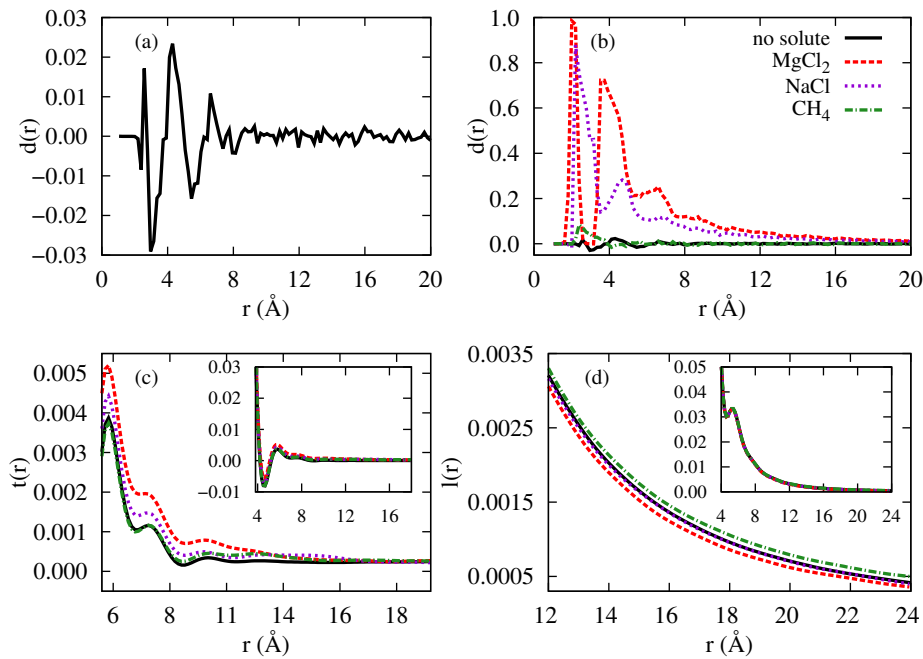


Figure 6.3: (a) oxygen - dipole correlation for solute free water. (b) Comparison of $d(r)$ (oxygen - dipole / solute - dipole) correlations as seen by a water molecule in absence of solutes, a methane molecule and a lone cation (with counterion(s)) in a water-box. (c) $t(r)$ and (d) $l(r)$ correlations for the systems shown in panel (b) (inset plots : comparisons shown over larger ranges in $r$). Curves for solute free water are plotted using (solid, black) lines. Curves for MgCl$_2$, NaCl and CH$_4$ are plotted using (large dots, red), (small dots, purple) and (dash-dots, green) respectively.

The position - dipole correlations have been computed using TIP4P-Ew water model alone. The oxygen - dipole correlation $d(r)$ for solute free liquid water is observed to display oscillatory solvation structure at small radial separations below $14\mathring{A}$ and vanish beyond the same (Figure 6.3(a)). The result is in good agreement with prior observations of the same correlation [11]. Dissolved ions have strong electrostatic interactions with water molecules in their first few solvation shells. The solute - dipole correlations for

ionic species are thus expected to deviate widely from the oxygen - dipole correlations in solute free water. Further, the nature of the correlations is expected to vary strongly between cationic and anionic species owing to their preferential interactions with the oxygen and hydrogen atoms of a water molecule respectively. The charge density of the ions can also be envisaged to play a critical role in the patterning of water molecules around ions. Thus, the solute - dipole correlations for ions are likely to be highly ion specific, and the same can have important consequences on the connectivity, as well as the dynamics of the hydrogen bond network both within and beyond the first few solvation shells. Rich literature exists on ion specific effects on the structure and dynamics of water molecules, encompassing both local and non-local effects [14, 243, 249–253]. In the following, we investigate the effects of the presence of a single divalent ($Mg^{2+}$) or monovalent ($Na^+$) cation (with requisite $Cl^-$ anion(s) for charge neutrality) on the orientational behavior of water around them and compare the same with solute free water $d(r)$ correlations. To retain similar statistics for solute free water and salt - water systems, the $d(r)$ calculation for solute free water was carried out by considering a single *tagged* water molecule at the center of the simulation box (since the same for salt - water systems can be carried out only over a single cation per frame). The results of the analyses are shown in Figures 6.3(a,b). $d(r)$ for solute free water with TIP4P-Ew water model is observed to reproduce all qualitative trends of the same, previously reported with TIP5P water model [11].

As can be clearly seen from Figure 6.3(b), the presence of a cation has a significant effect on the orientation of water dipoles, causing them to align along the radial vector. The effect is strongest for the first solvation shell waters and gradually falls off with distance, with solvation peak structure. The correlation is long range, being non-vanishing at > $14\mathring{A}$, at least when single salt molecules are present in a box of water. Interestingly, solute - dipole $d(r)$ for ionic solutes falls off faster than the charge oscillations within spheres of increasing radii around ions (Figure 6.4), indicating that the neighboring water molecules (hence hydrogen bonding) also have considerable effects on the structuring of water molecules around ions. The divalent cation ($Mg^{2+}$) has a stronger effect compared

to the monovalent one (Na$^+$), while both result in ~2 orders of magnitude enhancement over $d(r)$ correlations in solute free water. Further, anticorrelated regions present for solute free water are absent when observed from ion sites.
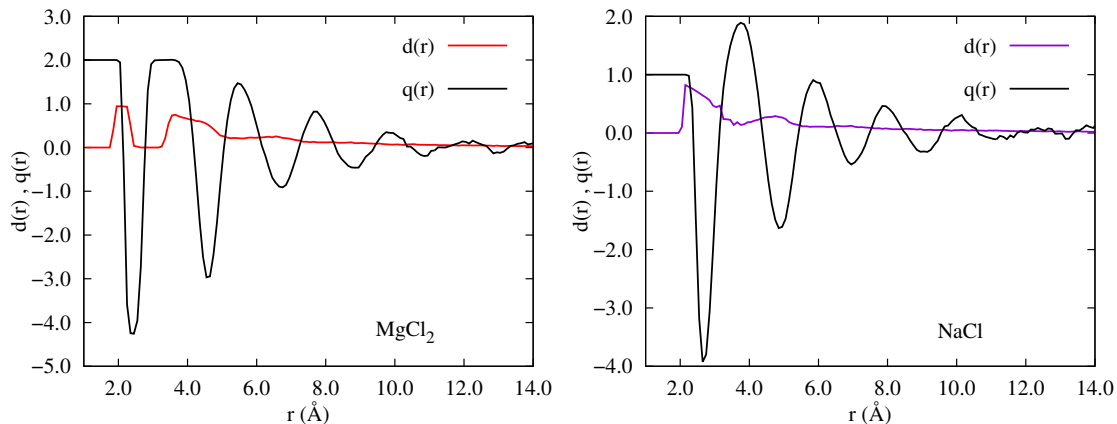


Figure 6.4: Comparison of ion - dipole ($d(r)$) correlations with net charge within a sphere of radius $r$ around the cations ($q(r)$). The charge is shown in units of $e$, the charge of an electron. $d(r)$ correlations around both Mg$^{2+}$ and Na$^+$ ions disappear faster than the oscillation of uncompensated charges within a sphere about the cations.

Such preferential patterning of water molecules' dipoles, or equivalently of hydrogen bonding arms, around each ion can have important consequences on the long range dipolar correlations. As a consequence of the patterning, orientation fluctuations of neighboring water molecules are restricted as compared to those in solute free water. Such local perturbations to the underlying dynamics of hydrogen bond network is coupled to the long range orientational correlations, and more generally to the orientational entropy of the liquid, through the sum rule [141, 144]. The ions can thus be envisaged as decorrelating centers, which along with their regions of influence, effectively screen bulk like water molecules from one another,- thus causing a decrease in the range of (ensemble averaged) long range correlations. The spatial extent of region of influence, as well as the strength of the patterning are critically related to the charge density of the ions [253]. Thus, strongly solvated ions can be expected to affect the long range orientational correlations to a greater extent than weakly solvated ones. With increasing salt concentration, there is likely to be a two-fold effect. Trivially, there is an enhanced fraction of water in the orientationally restricted regions of influence, whose orientational fluctuations are

suppressed. Further, an enhancement in the number of such de-correlation centers with increasing number of ions can be expected to result in a more effective screening. Our observations are generally consistent with such effects, with the exception of enhancement in $t(r)$ at lower salt concentrations.

Interestingly, the decay of the solute - dipole correlation around both $Na^+$ and $Mg^{2+}$ ions show similar long range behavior. Fitting the $d(r)$ correlations for them for $r \geq 10\mathring{A}$ with the fit function defined in equation 5 ($a_2 = 0$), yields correlation lengths of $(9.45\pm0.42)$ for $Na^+$ and $(8.81\pm0.28)$ for $Mg^{2+}$. This indicates that, while the effects of ions on the orientations of first few solvation shell waters is strongly governed by the valency and charge density of the ions, the approach to pure water-like orientation can be independent of such parameters.

## 6.3.4   Comparison of effects : hydrophilic and hydrophobic solute

At the lowest concentration of solutes studied, with only one solute molecule among ~4100 water molecules, the effects of the solutes on the dipolar correlations $t(r)$ and $l(r)$ are expected to be extremely small. As shown in the inset plots of Figures 6.3(c,d), the correlations only differ marginally from that in absence of solutes [1]. However, the long range parts of the correlations $t(r)$ and $l(r)$ can still be seen to be capable of distinguishing the effects of individual solute molecules, further emphasizing the applicability of the correlations in investigating orientational correlations among water molecules (Figure 6.3(c,d)). The $t(r)$ correlations for NaCl and $MgCl_2$ can be seen to have the same qualitative differences as observed at 0.15 M concentration, both among themselves and with water in absence of solutes. $t(r)$ correlation for $CH_4$ is observed to be almost identical to that for solute free water, with indications of enhanced structuring, especially at larger separations. $l(r)$ correlation for $CH_4$, however shows clear differences, being en-

---

[1]In the presence of a single solute, various correlations d(r), l(r) and t(r) have no dependance on position and orientations of the solute molecules, as these have been averaged over all possible configurations.

hanced compared to solute free water. $l(r)$ correlation can be observed to be reduced for MgCl$_2$, and comparable for NaCl when compared to solute free water. The results clearly show that small hydrophilic and hydrophobic solutes have contrasting effects on the long range orientational correlations among water molecules,- the former causing reduction and the latter leading to enhancement. $d(r)$ correlation around CH$_4$ shows no long range preferential orientation, as expected from its charge neutrality and size.

## 6.4   Discussion

The results described above indicate that the presence of dissolved salts (ions) leads to considerable changes in the dipolar correlations, that are both salt species and concentration dependent. The effects on the trace and longitudinal parts of the dipolar correlations are considerably varied. Varied responses of the $t(r)$ and $l(r)$ parts of the dipolar correlations to the presence of salts at lower concentration (0.15M), as well as the concentration dependent enhancement or reduction of the $t(r)$ part for the presence of the same salt (MgCl$_2$) have been observed in this study. This bolsters the criticism of the prevalent classification of ions along the lines of structure making and breaking, without defining an unambiguous connection between the observable(s) and structural changes.

The long range exponential decay of the longitudinal correlation observed for solute free water is greatly reduced in the presence of salts, completely vanishing at the higher concentration studied. The reduction in the long range longitudinal correlation in presence of ions can be explained by considering ion locations as de-correlation centers. Within their regions of influence, ions result in orientational stratification of water molecules and a consequent restriction in their orientational fluctuations. Such local perturbations are coupled to the long range dynamics of the underlying hydrogen bond network through the sum rule. As a result, long range orientational correlations, whose molecular origin lies in the inherent fluctuations of the hydrogen bond network, get suppressed.

The contrasting effects of hydrophilic and hydrophobic solutes on long range $l(r)$ correlations can have interesting implications in understanding the long range $(10 - 100\,\mathring{A})$ component of hydrophobic force. It was suggested in our earlier publication that $l(r)$ correlations can lead to a shape dependent attraction between two hydrophobic surfaces at large distances of separation [11], decaying with a correlation length of $\sim 12\mathring{A}$. Experimental evidences have shown that the force between hydrophobic surfaces, acting in spatial separation between $(10 - 100\,\mathring{A})$, is exponential in nature, and the range, as well as the magnitude of the same is reduced in presence of ionic impurities [16]. Our observations of reduction in the range of $l(r)$ correlations is consistent with the same. The observations for methane can not be extended to extended hydrophobic surfaces in a straightforward manner. However, sum rule for water dictates that long range $l(r)$ correlations in the presence of extended hydrophobic surfaces would be considerably altered compared to the same for water in absence of impurities, owing to the presence of dangling bonds at hydrophobic surfaces. Future research would be directed at studying the effects of larger hydrophobes as well as surfactants and osmolytes on the discussed correlations.

# Chapter 7

# Effect of salts on water dynamics beyond the first ion solvation shells

## 7.1 Introduction

The importance of (long-range) structural correlations in liquid water, and the effects of dissolved ions on the same has been discussed in Chapter 6 in the context of biologically relevant processes such as the hydrophobic effect. At the heart of the long-range correlations, as with short-range structural correlations in liquid water, is the highly connected and fluctuating network of hydrogen bonds. The fluctuations in the hydrogen bond network, allowing dominant contribution to the configurational entropy of the liquid, are enabled by the incessant reorientational motions of water molecules. The reorientation of a water molecule is associated with a change in hydrogen bonding partners, as well as coordination through nearest neighbors [13, 150]. Local environment, such as the presence of solutes and interfaces, is known to have a strong effect on the reorientational dynamics of neighboring water molecules. Water can not form hydrogen bonds with hydrophobes. Hence, the presence of hydrophobic exposure severely restricts the conformations of neighboring water molecules,- thus inducing moderate reorientational

slowing [113, 254]. For ionic solutes in water, the orientations of the first solvation shell waters are restricted through electrostatic ordering. The electrostatic ordering constrains the dipole vectors and OH- arms of water molecules respectively in the neighborhood of cationic and anionic species'. Depending on the charge density, dissolved ions can thus induce weak to strong slowing effects on the reorientations of first solvation shell water molecules, and this slowdown is preferentially reflected in the reorientations of dipole vectors, or OH- arms [255, 256].

A debated question in the scientific community is whether the presence of dissolved ions can induce reorientational slowing of water molecules beyond their first solvation shells. Such an effect is described as long-range dynamical effects of salts, or dissolved ions. Spectroscopic techniques have been instrumental in probing the cooperative ion solvation mechanism and consequent long-range structural and dynamical effects of certain salts, or ion combinations, on water [14, 243, 249, 250, 255–257]. Earlier experiments suggested that the effect of ions on dynamical properties of water is largely restricted to their first solvation shell [258, 259]. However, recent experiments, using a combination of femtosecond time resolved infrared (fs-IR) and dielectric relaxation spectroscopy, have shown the existence of a fraction of reorientationally slow water molecules well beyond the first solvation shells of dissolved $MgSO_4$ ions [14, 255]. In these experiments, two sub-populations of water molecules were identified for various salts: one with reorientation timescales comparable to pure water (~2.6 ps) and the other showing characteristically slower reorientations (~10 ps). The fraction of total water molecules contributing to the sub-population of slow-water molecules was seen to increase with increase in salt concentration for all salts and the magnitude of increase was observed to be highly dependent on ion combinations, being largest for combinations of strongly solvated ion species ($Mg^{2+}$, $SO_4^{2-}$).

Long-range effects of ions on the reorientational dynamics of water molecules can have importance in a vast number of complex processes, including processes of biological and

environmental relevance [233, 260, 261]. Of especial importance is the Hofmeister effect, which includes highly ion-specific effects on aggregation dynamics of proteins [147, 262]. Proposed by Franz Hofmeister over a century ago, the Hofmeister series (distinct for cations and anions) classifies ions in the order of their ability to salt out or salt in proteins in aqueous solutions. The ordering of the ions, however, is not limited to solubility of proteins. The same order has been observed in other biologically and environmentally relevant processes,- such as interface propensity of ions at a aqueous - hydrophobic interface [261, 263]. In spite of extensive research, the physical origin of the Hofmeister series is yet unknown. Long range effects of ions on the structural and dynamical properties of liquid water has recently been suggested as a likely explanation to Hofmeister effect [243].

Despite the recent experimental results [14], the existence of long-range dynamical effects of salts, beyond first solvation shell, is controversial owing to results from other experimental as well as simulation studies which suggest the contrary [15, 202, 252, 258, 259, 264, 264–266]. While an intense cooperative slowdown of water reorientation has been observed in presence of ions with high charge densities, the range of presence of slow water molecules has been found to be confined to the first solvation shell of the ions [15, 202, 252, 259, 264, 266]. The focus of the work reported here is on the extended hydrogen bond network in bulk water, and the domain formation and existence of 'defect water molecules' at boundaries of such domains, when salt is added. Instead of classifying water molecules based on radially varying spherical solvation shells around ions, sub-populations depending on whether they are bulk-like or defect water molecules are considered. Using MD simulations, evidence is presented for for reorientational slowdown of water molecules well beyond the first solvation shell for solutions of $MgCl_2$, and effect of salt concentration on the same. For CsCl-water solutions, no significant effect on reorientational dynamics of water (irrespective of CsCl concentration) was found, which is in good agreement with the Hofmeister series. The content of this chapter is published in reference [251].

## 7.2 Methods and simulation details

### 7.2.1 System Setup

Classical atomistic MD simulations were performed with TIP4P-Ew [133] and TIP3P [135] water models and using simulation package NAMD 2.9 [165]. For simulations involving TIP4P-Ew water model, recently developed parameters for divalent ion $Mg^{2+}$ and optimized for correct coordination number [245] were used. Monovalent ($Cl^-$, $Cs^+$) ion parameters for the TIP4P-Ew simulations were taken from extensively used halide and alkali ion parameters [246]. Standard CHARMM parameters were used for all ions [191] while simulating with TIP3P water. All systems were first equilibrated under constant pressure and temperature (NPT) and further under constant volume and energy (NVE) conditions. Production runs for all systems were performed under NVE conditions. For the NPT simulations, pressure was maintained at 1 atm using Langevin Piston [218] and temperature coupling to external heat bath was used to maintain temperature at 298 K for simulations with TIP4P-Ew model and at 305 K for TIP3P. Lennard-Jones interactions were smoothly truncated with cutoff $12\,\mathring{A}$ using switching function between $10\,\mathring{A}$ and $12\,\mathring{A}$. Long-range electrostatic interactions were computed using particle mesh Ewald (PME) method. Timesteps of 1 and 2 fs were used for simulations involving TIP4P-Ew and TIP3P models respectively.

*TIP4P-Ew water systems :* Initially a $54\mathring{A} \times 54\mathring{A} \times 54\mathring{A}$ box of water containing 5251 water molecules was equilibrated for 5 ns under NPT conditions and further for 4 ns under NVE. *Autoionize* plugin of VMD [171] was used to produce $MgCl_2$ (2 M, 3 M, 4 M) and CsCl (3 M, 4 M) solutions from this equilibrated configuration and each of the salt-water systems was equilibrated for 5 ns under NPT conditions and further for 4 ns under NVE. Thus, including the water box in absence of solutes, each of the six systems involving TIP4P-Ew water were equilibrated for a total of 9 ns.

*TIP3P water systems :* Initially a $50\mathring{A} \times 50\mathring{A} \times 50\mathring{A}$ box of water containing 4972 water

molecules was equilibrated for 10 ns under NPT conditions. *Autoionize* plugin of VMD was used to produce salt solutions of the same concentrations as for TIP4P-Ew water molecules from this equilibrated configuration and each of these salt-water systems was equilibrated for 15 ns under NPT conditions. The salt free water system was further simulated for 5 ns, resulting in 15 ns NPT equilibration simulations for each of the six systems considered. All above systems were equilibrated for further 9 ns under NVE conditions resulting in total equilibration time of 24 ns for systems involving TIP3P water.

| system | water model | num. water | num. cation | num. anion | system dimensions ($\mathring{A}^3$) |
|---|---|---|---|---|---|
| solute free water | TIP4P-Ew | 5251 | 0 | 0 | 54.2×54.2×54.2 |
| | TIP3P | 4972 | 0 | 0 | 52.8×52.8×52.8 |
| 2 M MgCl$_2$ solution | TIP4P-Ew | 4648 | 201 | 402 | 53.4×53.4×53.4 |
| | TIP3P | 4414 | 186 | 372 | 51.6×51.6×51.6 |
| 3 M MgCl$_2$ solution | TIP4P-Ew | 4348 | 301 | 602 | 53.0×53.0×53.0 |
| | TIP3P | 4135 | 279 | 558 | 51.1×51.1×51.1 |
| 4 M MgCl$_2$ solution | TIP4P-Ew | 4045 | 402 | 804 | 52.8×52.8×52.8 |
| | TIP3P | 3856 | 372 | 744 | 50.6×50.6×50.6 |
| 3 M CsCl solution | TIP4P-Ew | 4649 | 301 | 301 | 54.3×54.3×54.3 |
| | TIP3P | 4414 | 279 | 279 | 53.1×53.1×53.1 |
| 4 M CsCl solution | TIP4P-Ew | 4447 | 402 | 402 | 54.3×54.3×54.3 |
| | TIP3P | 4228 | 372 | 372 | 53.2×53.2×53.2 |

Table 7.1: Details of the systems studied. The simulation box dimensions in the table are after equilibration of all systems.

Table 7.1 includes further details of system setup for the various systems studied. Relatively high salt concentrations of salt were chosen in this reported study based on recently studied experimental concentrations [255, 265], as well as to account for good statistics. For computation of reorientational autocorrelation functions and other observables, production runs of 1 ns each were carried out for all systems under NVE conditions, with system configurations saved every 0.1 ps. All the dynamical analyses were performed over the last 0.5 ns of the production run data.

## 7.2.2 Water domain identification

To identify hydrogen bond (O-O distance $\leq 3.8\mathring{A}$ and H-O··H angle $\leq 60°$ definition of hydrogen bond was used) network domains in all the twelve systems considered in this report, each system configuration was divided into multiple overlapping slabs along each of the three orthonormal directions. Over each such slab, hydrogen bonded domains of water molecules were identified. The criterion for inclusion of water molecules to a single domain is the existence of a bidirected path between every pair, via a network of hydrogen bonds formed by water molecules in the same slab. Using this definition of water domain, it was observed that for salt free water all values of slab thickness $\geq 2.7\mathring{A}$ consistently resulted in a single spanning domain along the slab. Addition of salt to the water systems resulted in formation of multiple water domains, even when higher values of slab thickness ($4\mathring{A}$) were considered. The size distributions of different domains of TIP4P-Ew and TIP3P water systems, for a slab thickness of $4\mathring{A}$ are shown in Figure 7.1. The distributions for the two water models are in qualitative agreement. From the figures, it can be seen that for the case of salt free water, a single spanning domain exists. With the addition of $MgCl_2$ salt, the size distribution of water domains depends on the concentration. For 2 M salt concentration, the domain size distribution is similar to the salt free water case, with additional appearance of smaller sized water domains. When the concentration of $MgCl_2$ is increased to 3 M and above, the domain size distribution differs significantly from that of salt free water. No single spanning domain remains in the system and the system primarily consists of many domains of water molecules of varying size distribution. Ion specific local structural effects on water has been widely studied in the literature [259, 267–271]. High charge density ions have been known to exert strong patterning effects on first solvation shell water molecules, leading to a reduction in water-water hydrogen bonding [111, 272, 273]. The domain size distributions in CsCl-water systems, in contrast to $MgCl_2$-water systems, is very similar to the salt free water system even at 4 M concentration consistent with a recent ab initio MD study of other low-charge

density salts such as NaCl and CsI [274].
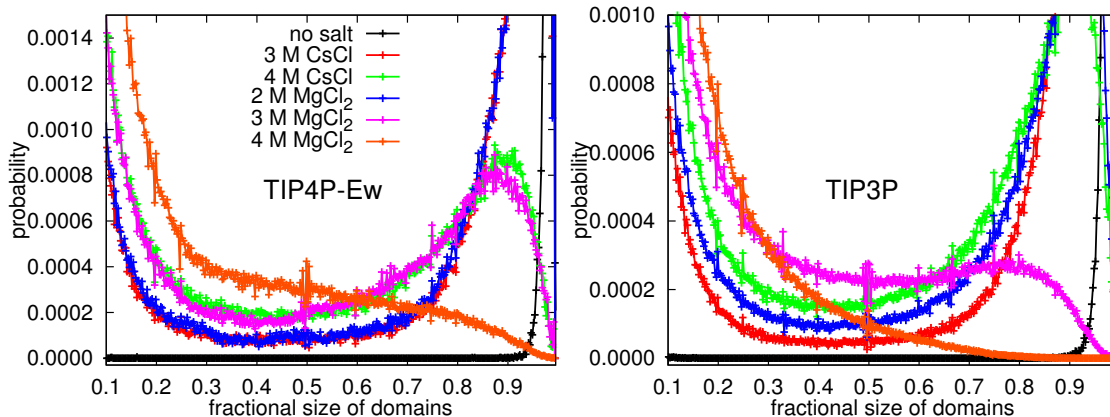


Figure 7.1: Domain size distribution plots scaled to [0, 1] for all systems with TIP4P-Ew (left) and TIP3P (right) water models. Slab thickness is 4Å. The distributions are averaged over 5000 frames and 0.5 ns of simulation data in each case.

Following the identification of domains, water molecules residing at the domain boundaries were identified and recorded for all the three orthonormal directions. From this data, the water molecules which appear in all the three lists, corresponding to three orthonormal directions, are identified and labeled defect water molecules. This set of defect water molecules, however, may contain water molecules which are within the first solvation shell of any ions. From this superset of defect water molecules, a subset of water molecules which are not within the first solvation shell of any ion were identified, which are referred to henceforth as *waterD* (salt free water is referred to as *waterP*). A further sub-population of defect water molecules were also identified : water molecules which are at domain boundaries in any two orthonormal directions (instead of three) and not in the first solvation shell of ions. These will be referred as *waterD2*. They constitute a more relaxed definition of defect water molecules, and their sub-population size would be larger than that of *waterD* at moderate salt concentrations.

The probability distribution of local tetrahedral order parameter ($Q$) was computed for *waterP* and sub-populations *waterD* for systems involving TIP4P-Ew model of water. $Q$ for a water molecule is defined as [275]

$$Q = 1 - \frac{3}{8} \sum_{j=1}^{3} \sum_{k=j+1}^{4} \left( cos\,\Psi_{jk} + \frac{1}{3} \right)^2 \qquad (7.1)$$

where $\Psi_{jk}$ is the angle formed by the lines joining the oxygen atom of a given molecule and those of its nearest neighbors $j$ and $k$ ($\leq 4$). $Q$ takes values 1 and 0 for ideal tetrahedral structures and ideal gas respectively.

## 7.3 Results

### 7.3.1 Tetrahedrality and hydrogen bonding
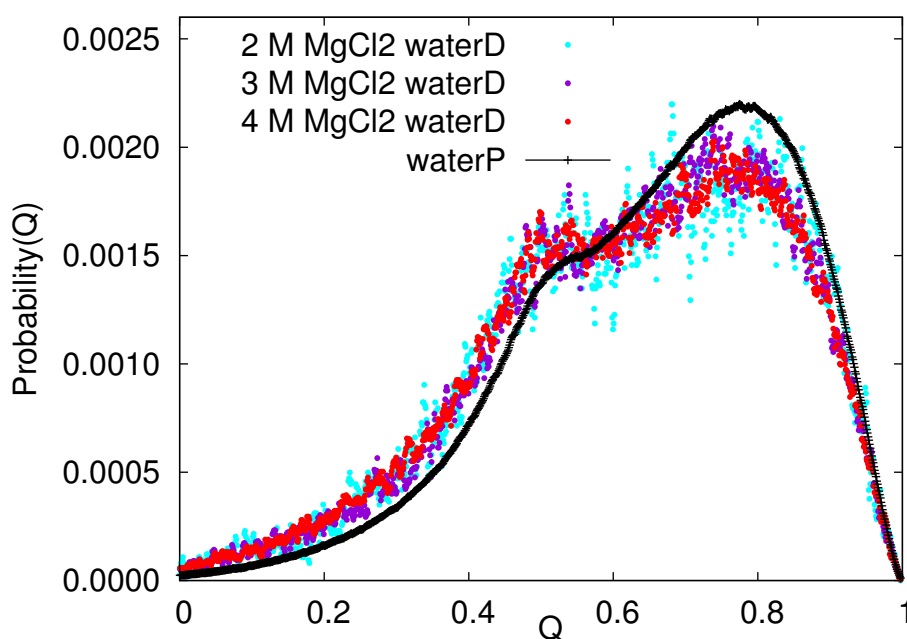


Figure 7.2: Probability distribution for local tetrahedral order parameter ($Q$) values obtained for salt free water molecules (waterP) and defect water molecules (waterD) for 2 M, 3 M, 4 M MgCl$_2$ with TIP4P-Ew water model (NVE simulation following NPT (T = 298K) simulation). The data for CsCl were found to be very noisy owing to low statistics and hence have not been included. The data are averaged over 5000 frames and 0.5 ns of simulation. Following initial calculation using binwidth 0.001, the data were smoothed by assigning each bin the average value of five neighboring bins including itself.

Figure 7.2 shows the probability distributions of local tetrahedral order parameter for *waterP*, and sub-populations *waterD* in MgCl$_2$ salt solutions. The data obtained for *waterD* in CsCl solutions were very noisy owing to low statistics (small number of defect wa-

ters molecules), and have not been included in the figure. The tetrahedrality results, in conjunction with hydrogen bonds per water molecules, suggest that the sub-population of *waterD* molecules differ significantly from salt free water molecules. Typical bimodal distributions [7, 275] observed for both *waterP* and *waterD*, are shifted towards lower tetrahedrality for the latter. The reduced tetrahedrality was observed to be associated with lower number of hydrogen bonds. The average number of hydrogen bonds per defect water molecule (*waterD*) were found to be less than 2.

## 7.3.2  Reorientational dynamics beyond first ion solvation shells
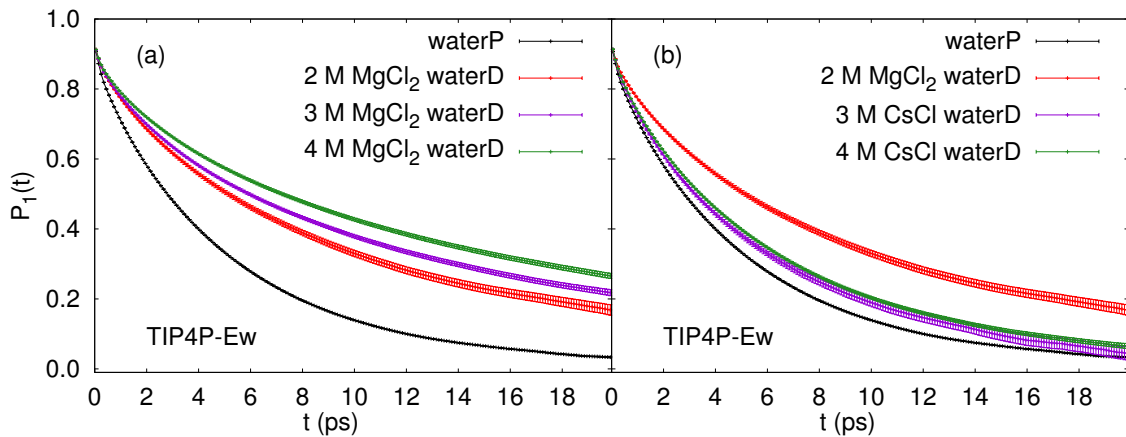


Figure 7.3: Plots for $P_1(t)$ for *waterD* in the presence of (a) MgCl$_2$ and (b) CsCl at the concentrations studied, and with TIP4P-Ew water model. In plot (b), the curve for 2 M MgCl$_2$ has been repeated for comparison. In both plots, $P_1(t)$ for *waterP* has been shown in black. The error bars in all plots have been magnified 5 times.

Reorientation autocorrelation functions $P_1(t)$ and $P_2(t)$ defined as first and second Legendre polynomials of water dipole vector ($\hat{\mu}$), a unit bisector of the H-O-H angle, were computed for various sub-populations of water molecules over 20 ps:

$$P_1(t) = \langle \hat{\mu}(t).\hat{\mu}(0) \rangle \qquad (7.2)$$

$$P_2(t) = \langle \frac{1}{2}(3cos^2(\hat{\mu}(t).\hat{\mu}(0)) - 1) \rangle \qquad (7.3)$$

where the angular brackets denote average over number of water molecules in each sub-

population and time. The errors for $P_1(t)$ and $P_2(t)$ have been obtained by computing standard deviations using block averages.
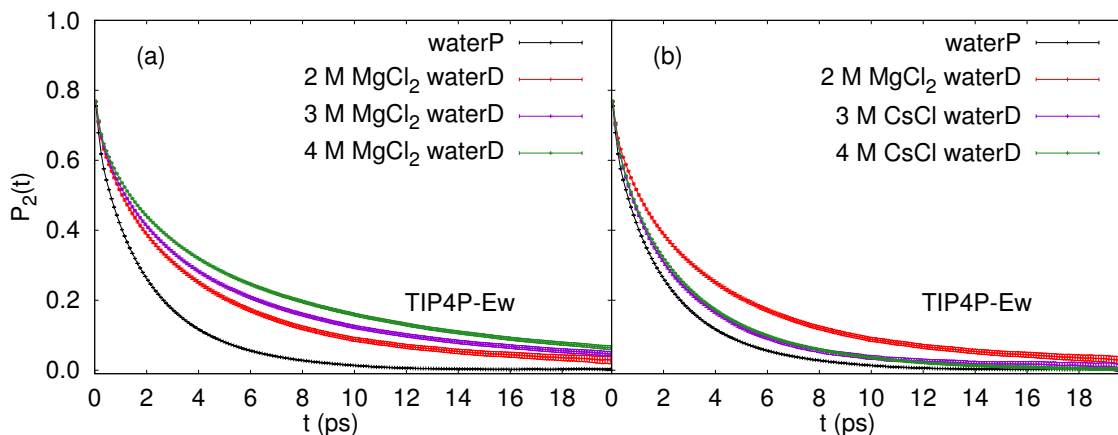


Figure 7.4: Plots for $P_2(t)$ for *waterD* in the presence of (a) MgCl$_2$ and (b) CsCl at the concentrations studied, and with TIP4P-Ew water model. In plot (b), the curve for 2 M MgCl$_2$ has been repeated for comparison. In both plots, $P_2(t)$ for *waterP* has been shown in black. The error bars in all plots have been magnified 5 times.

The computed correlation functions $P_1(t)$ for salt free water and MgCl$_2$ solutions using TIP4P-Ew water model are plotted in Figure 7.3(a). A significant slowing down of re-orientational times for sub-population *waterD* as a function of salt concentration can be seen from the figure. These results suggest that 'slow water molecules' exist beyond the first solvation shell of both cations and anions. Earlier experiments and simulations show that the propensity of formation of ion-water clusters is higher at higher concentration of salts in water [276]. Water molecules trapped in such clusters can experience very slow reorientational times. It is to be noted that though the salt concentrations considered in the reported study are high, the sampling of sub-population *waterD* will not include such trapped water molecules, by definition. The *waterD* molecules considered can, at best, be part of three solvent separated ion pairs. Extensive studies of the reorientation of water molecules have shown that autocorrelation functions of a body-set vector, including dipole vector, of water molecules involve distinct time scales [13, 148, 150, 277, 278]. A fast, sub-picosecond decay due to librational motion followed by a slower component that can be attributed to structural changes such as hydrogen bond exchange and reorientations of hydrogen bonded water molecules. Multi-exponential functions thus serve as

168

good fit functions for such correlations and they have been fit to either bi- ($A_3 = 0$) or

tri-exponential functions of the form

$$P_{1/2}(t) = A_1 exp(-\frac{t}{\tau_1}) + A_2 exp(-\frac{t}{\tau_2}) + A_3 exp(-\frac{t}{\tau_3}) \tag{7.4}$$

depending on the system. However, the attribution of specific physical processes to these
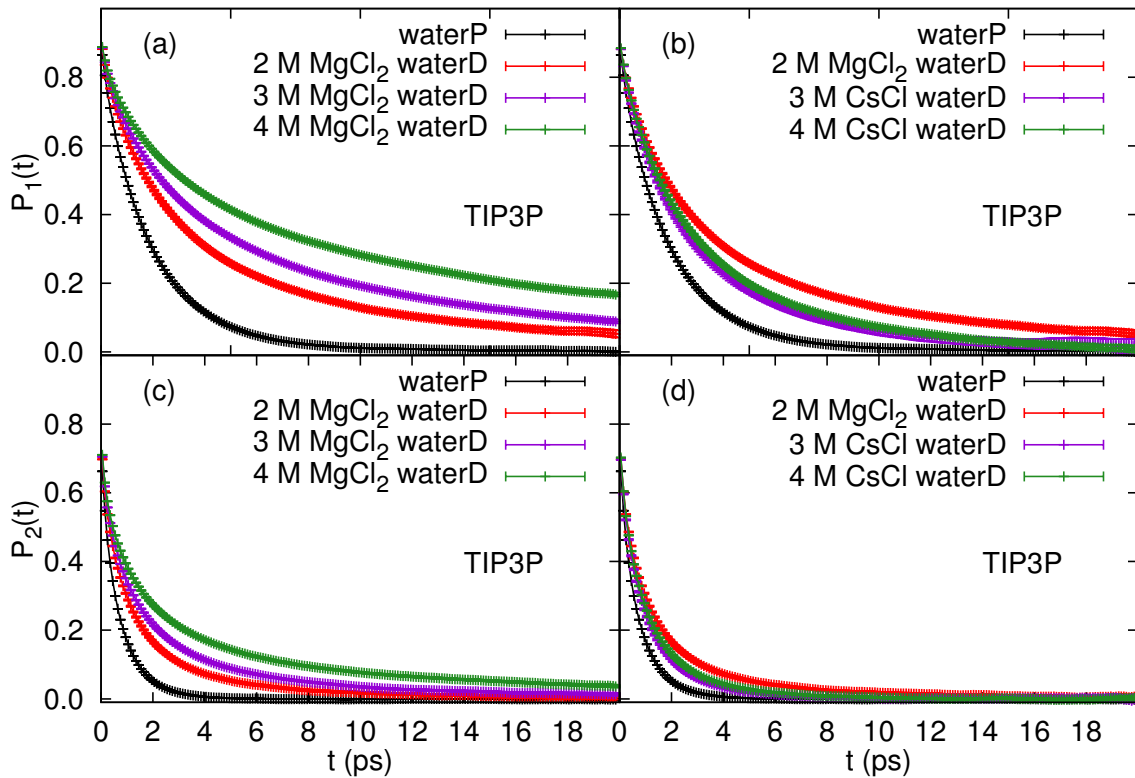


**Figure 7.5:** Plots for $P_1(t)$ (a,b) and $P_2(t)$ (c,d) for sub-population *waterD* of water molecules, with TIP3P water model. In all plots, curves for *waterP* have been shown in black. The error bars in all plots have been magnified 5 times.

time constants is not attempted in this report. A bi-exponential function ($A_3 = 0$) was

the best fit for reorientational time curves for the salt free water case. In the presence of

$MgCl_2$, a tri-exponential function was found to be more appropriate, with dynamics of

defect water molecules introducing a new time scale into the problem. The decay times

($\tau_3$) are much larger than the slowest component of orientational relaxation for salt free

water and show an increase with the concentration of $MgCl_2$ salt. These results are shown

in Table 7.2. Simulation results show that for the largest concentration of $MgCl_2$ studied

(4 M), the longest mode in decay time for defect water molecules, which are beyond first solvation shell of any ions, is as high as 21 ps.

| salt | sub-population | $A_1$ | $\tau_1$ | $A_2$ | $\tau_2$ | $A_3$ | $\tau_3$ |
|------|----------------|-------|----------|-------|----------|-------|----------|
| none | | 0.078(0.002) | 0.329(0.052) | 0.848(0.002) | 5.333(0.034) | | |
| MgCl$_2$ | (2 M,*waterD*) | 0.052(0.004) | 0.209(0.058) | 0.262(0.003) | 3.538(0.031) | 0.615(0.002) | 15.027(0.002) |
| | (3 M,*waterD*) | 0.049(0.003) | 0.192(0.028) | 0.222(0.003) | 3.010(0.016) | 0.656(0.003) | 17.654(0.001) |
| | (4 M,*waterD*) | 0.050(0.002) | 0.206(0.024) | 0.197(0.002) | 2.980(0.017) | 0.682(0.002) | 20.818(0.001) |
| CsCl | (3 M,*waterD*) | 0.044(0.004) | 0.188(0.307) | 0.169(0.005) | 1.917(0.039) | 0.720(0.003) | 7.476(0.002) |
| | (4 M,*waterD*) | 0.052(0.003) | 0.232(0.031) | 0.235(0.009) | 2.788(0.022) | 0.644(0.002) | 8.506(0.002) |

Table 7.2: Water reorientational time constants (for $P_1(t)$) with TIP4P-Ew water model (under NVE conditions following NPT (T = 298K) simulations) for salt free water molecules and *waterD* sub-population in the presence of salt using tri-exponential fits. All time constants are in picoseconds. The numbers within parentheses indicate fir errors. Eg., 0.078(0.002) stands for (0.078 ± 0.002).
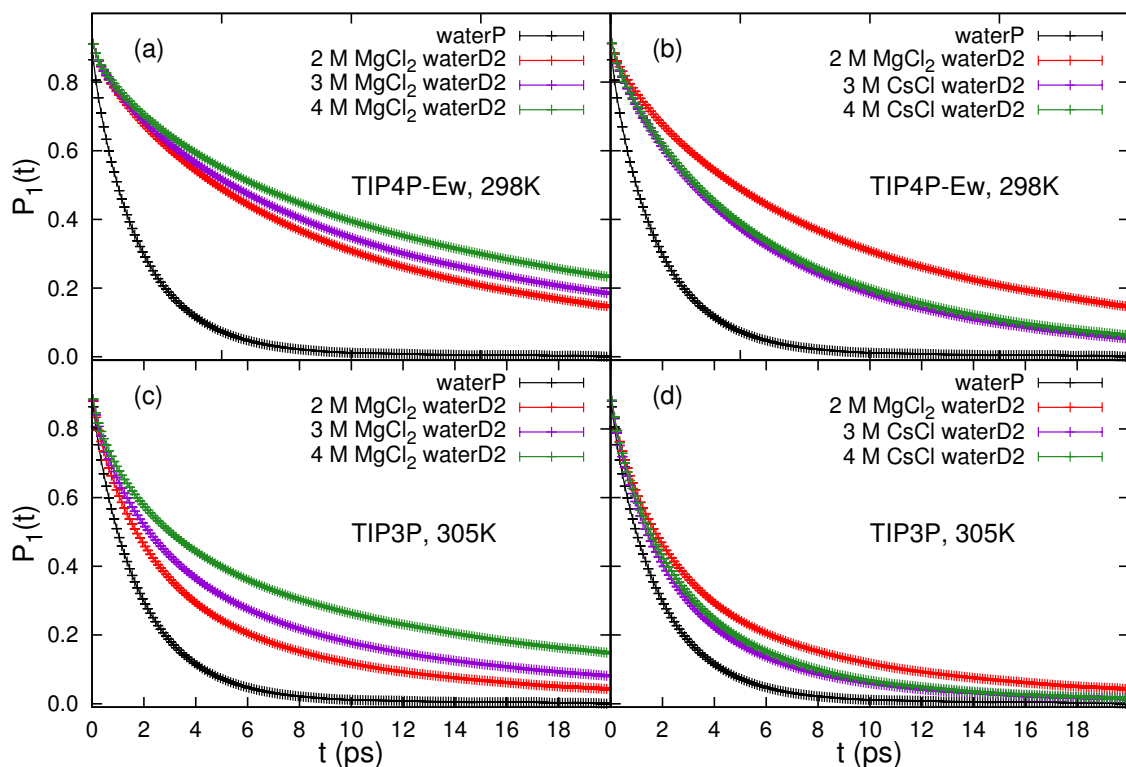


Figure 7.6: Plots for $P_1(t)$ for sub-population *waterD2* of water molecules, with TIP4P-Ew (a,b) and TIP3P (c,d) water models. In all plots, curves for *waterP* have been shown in black. The error bars in all plots have been magnified 5 times.

The $P_1(t)$ curves for CsCl salt solutions are plotted in Figure 7.3(b). For CsCl, the deviation from the case of salt free water is much less significant compared to effects of MgCl$_2$ and independent of salt concentration. The $P_1(t)$ curves for CsCl are also fit with a tri-exponential function and the values are given in Table 7.2. The anion used in both

170

the salts, $Cl^-$, is known to be weakly solvated ion and such anions are expected to affect the dynamics of OH vector preferentially over dipole vectors of water molecule [255]. Thus the observed difference in reorientational dynamics between the two cations reported here, $Mg^{2+}$ and $Cs^+$ reflect the difference between a strongly solvated vs a weakly solvated cation, while both have the same counterion.

Trends described above for correlations $P_1(t)$ with TIP4P-Ew water model have been observed with correlations $P_2(t)$ too. Further, the results for TIP3P water model have been observed to be in good qualitative agreement. Plots $P_2(t)$ for TIP4P-Ew are shown in Figures 7.4. Plots for both $P_1(t)$ and $P_2(t)$ for TIP3P are shown in Figure 7.5. Similar differences between $Mg^{2+}$ and $Cs^+$ are observed for the sub-population of water molecules *waterD2* as well, and the plots are shown in Figure 7.6 for both water models used, through correlation function $P_1(t)$. The reorientational time constants obtained for $P_2(t)$ for sub-population *waterD* for TIP4P-Ew, and $P_{1/2}(t)$ for TIP3P water models are given in Table 7.3. These results seem to be consistent with the ordering of cations in well-known Hofmeister series [255].

Table 7.3: Water reorientational time constants obtained. All time constants are in picoseconds. The numbers within parentheses indicate fit errors. Eg., 0.202 (0.003) stands for (0.202 ± 0.003).

| water model | T (K)* | ensemble | autocorr. f″ | salt | sub-population | $A_1$ | $\tau_1$ | $A_2$ | $\tau_2$ | $A_3$ | $\tau_3$ |
|---|---|---|---|---|---|---|---|---|---|---|---|
| TIP4P-Ew | 298 | NVE | $P_2(t)$ | none | (2 M,waterD) | 0.202 (0.003) | 0.305 (0.047) | 0.593 (0.003) | 2.480 (0.022) | | |
| | | | | MgCl$_2$ | (3 M,waterD) | 0.130 (0.001) | 0.196 (0.034) | 0.382 (0.007) | 2.315 (0.014) | 0.295 (0.008) | 8.158 (0.003) |
| | | | | | (4 M,waterD) | 0.122 (0.001) | 0.190 (0.043) | 0.336 (0.003) | 2.239 (0.022) | 0.348 (0.003) | 9.629 (0.002) |
| | | | | CsCl | (2 M,waterD) | 0.116 (0.001) | 0.184 (0.022) | 0.283 (0.002) | 2.232 (0.035) | 0.406 (0.002) | 10.601 (0.001) |
| | | | | | (3 M,waterD) | 0.151 (0.002) | 0.245 (0.069) | 0.513 (0.004) | 2.177 (0.063) | 0.144 (0.096) | 5.682 (1.468) |
| | | | | | (4 M,waterD) | 0.120 (0.001) | 0.191 (0.083) | 0.258 (0.003) | 1.344 (0.031) | 0.433 (0.004) | 4.976 (1.128) |
| | 305 | NVE | $P_1(t)$ | none | (2 M,waterD) | 0.153 (0.004) | 0.555 (0.052) | 0.741 (0.004) | 2.171 (0.032) | | |
| | | | | MgCl$_2$ | (3 M,waterD) | 0.072 (0.002) | 0.234 (0.048) | 0.499 (0.003) | 2.175 (0.024) | 0.338 (0.003) | 10.182 (0.002) |
| | | | | | (4 M,waterD) | 0.074 (0.002) | 0.234 (0.042) | 0.406 (0.002) | 2.274 (0.019) | 0.430 (0.002) | 12.177 (0.002) |
| | | | | CsCl | (2 M,waterD) | 0.078 (0.002) | 0.240 (0.017) | 0.348 (0.002) | 2.471 (0.026) | 0.485 (0.002) | 17.922 (0.001) |
| | | | | | (3 M,waterD) | 0.060 (0.002) | 0.225 (0.472) | 0.511 (0.006) | 1.845 (0.049) | 0.340 (0.004) | 5.742 (0.008) |
| | | | | | (4 M,waterD) | 0.058 (0.001) | 0.207 (0.044) | 0.428 (0.004) | 1.768 (0.024) | 0.427 (0.002) | 5.764 (0.002) |
| | | | $P_2(t)$ | none | (2 M,waterD) | 0.207 (0.003) | 0.229 (0.046) | 0.526 (0.003) | 0.922 (0.022) | | |
| | | | | MgCl$_2$ | (3 M,waterD) | 0.182 (0.006) | 0.208 (0.012) | 0.460 (0.002) | 1.215 (0.008) | 0.114 (0.002) | 5.433 (0.024) |
| | | | | | (4 M,waterD) | 0.190 (0.006) | 0.221 (0.024) | 0.423 (0.007) | 1.474 (0.012) | 0.145 (0.006) | 7.821 (0.020) |
| | | | | CsCl | (2 M,waterD) | 0.195 (0.092) | 0.236 (0.022) | 0.385 (0.004) | 1.798 (0.026) | 0.178 (0.005) | 10.069 (0.038) |
| | | | | | (3 M,waterD) | 0.014 (0.006) | 0.172 (0.064) | 0.459 (0.008) | 0.869 (0.096) | 0.160 (0.012) | 2.346 (0.034) |
| | | | | | (4 M,waterD) | 0.144 (0.005) | 0.173 (0.082) | 0.443 (0.006) | 0.902 (0.066) | 0.178 (0.008) | 2.599 (0.086) |
| TIP3P | 305 | NPT | $P_1(t)$ | none | (2 M,waterD) | 0.127 (0.004) | 0.588 (0.048) | 0.761 (0.002) | 2.272 (0.026) | | |
| | | | | MgCl$_2$ | (3 M,waterD) | 0.071 (0.002) | 0.439 (0.062) | 0.464 (0.002) | 2.446 (0.022) | 0.355 (0.003) | 10.731 (0.002) |
| | | | | | (4 M,waterD) | 0.078 (0.001) | 0.463 (0.034) | 0.424 (0.002) | 2.846 (0.013) | 0.388 (0.003) | 14.957 (0.001) |
| | | | | CsCl | (2 M,waterD) | 0.088 (0.002) | 0.561 (0.020) | 0.347 (0.002) | 3.280 (0.014) | 0.452 (0.003) | 22.081 (0.001) |
| | | | | | (3 M,waterD) | 0.049 (0.002) | 0.204 (0.539) | 0.455 (0.004) | 1.671 (0.056) | 0.404 (0.005) | 5.110 (0.003) |
| | | | | | (4 M,waterD) | 0.067 (0.001) | 0.428 (0.042) | 0.512 (0.003) | 2.160 (0.020) | 0.315 (0.004) | 6.250 (0.002) |
| | | | $P_2(t)$ | none | (2 M,waterD) | 0.209 (0.006) | 0.235 (0.034) | 0.529 (0.005) | 0.925 (0.018) | | |
| | | | | MgCl$_2$ | (3 M,waterD) | 0.181 (0.004) | 0.212 (0.052) | 0.460 (0.004) | 1.308 (0.008) | 0.121 (.004) | 6.082 (0.024) |
| | | | | | (4 M,waterD) | 0.197 (0.004) | 0.236 (0.038) | 0.429 (0.005) | 1.653 (0.016) | 0.135 (0.006) | 8.768 (0.028) |
| | | | | CsCl | (2 M,waterD) | 0.191 (0.008) | 0.238 (0.044) | 0.382 (0.004) | 1.868 (0.014) | 0.191 (0.005) | 13.382 (0.033) |
| | | | | | (3 M,waterD) | 0.170 (0.006) | 0.199 (0.066) | 0.529 (0.007) | 1.042 (0.027) | 0.062 (0.008) | 3.422 (0.062) |
| | | | | | (4 M,waterD) | 0.157 (0.006) | 0.188 (0.036) | 0.441 (0.010) | 0.958 (0.031) | 0.167 (0.014) | 3.485 (0.068) |

* Temperatures mentioned are for NPT equilibration runs, followed by NVE simulations.

### 7.3.3 Hydration number and fraction of slow water molecules

| water model | salt,conc. | $N_{\hat{\mu}}$ | $f_{\frac{slow}{bulk}}$ | $f_{(\frac{slow}{bulk},defect)}$ |
|---|---|---|---|---|
| | MgCl$_2$, 2 M | 7.28 | 0.19 | 0.06 |
| | MgCl$_2$, 3 M | 7.05 | 0.41 | 0.26 |
| TIP4P-Ew | MgCl$_2$, 4 M | 6.71 | 0.80 | 0.34 |
| | CsCl, 3 M | 5.91 | 0.05 | 0.03 |
| | CsCl, 4 M | 5.80 | 0.15 | 0.10 |
| | MgCl$_2$, 2 M | 7.1 | 0.18 | 0.02 |
| | MgCl$_2$, 3 M | 7.2 | 0.59 | 0.35 |
| TIP3P | MgCl$_2$, 4 M | 7.0 | 0.95 | 0.44 |
| | CsCl, 3 M | 5.7 | 0.04 | 0.02 |
| | CsCl, 4 M | 5.7 | 0.10 | 0.07 |

Table 7.4: Approximate values of quantities $N_{\hat{\mu}}$, $f_{\frac{slow}{bulk}}$ and $f_{(\frac{slow}{bulk},defect)}$ obtained with TIP4P-Ew and TIP3P water models (under NVE conditions following NPT simulations). The data are averaged over 5000 frames and 0.5 ns of simulation time.

Two dynamical quantities, which can be measured experimentally, related to ion solvation are the solvation number ($N_{\hat{\mu}}$), defined as the number of moles of slow water dipoles per mole of dissolved salt and fraction of slow water molecules relative to bulk-like water ($f_{\frac{slow}{bulk}}$) [14, 255]. The slow water molecules identified in the experiments are independent of structural definition of solvation shells and can contain water molecules within and outside the first solvation shells of ions. To be consistent with the experiments, a similar definition of slow water molecules was adopted which entails including water molecules in the first solvation shell of cations along with two sub-populations *waterD* and *waterD2*. Further, simulations allow a new dynamical quantity $f_{(\frac{slow}{bulk},defect)}$ to be computed, which is difficult to measure experimentally. $f_{(\frac{slow}{bulk},defect)}$ measures the fraction of slow water molecules beyond first solvation shell of ions relative to bulk-like water. The $N_{\hat{\mu}}$, $f_{\frac{slow}{bulk}}$ and $f_{(\frac{slow}{bulk},defect)}$ for both MgCl$_2$ and CsCl solutions are given in Table 7.4. It has been suggested that the typical hydration number, $N_{\hat{\mu}}$, for many ions is around 6 and any value greater than this number indicates presence of long-range effects of ions [14]. Experiments on salt solutions containing both strongly solvated cations and anions show a large $N_{\hat{\mu}}$ value of the order of 18 and this has been suggested as a strong indication of cooperative slow down of water dynamics beyond first solvation shells of such ions [14]. In the reported study the $N_{\hat{\mu}}$ values for MgCl$_2$ for all the three concentrations studied is 7, indicating the

existence of the long-range effect of $Mg^{2+}$ ions in the presence of $Cl^-$, albeit weaker than when the counterion is $SO_4^{2-}$. The $N_{\hat{\mu}}$ values for CsCl were found to be less than 6.

| r (Å) | TIP4P-Ew, T = 298K | | | | | TIP3P T = 305K | | | | |
|---|---|---|---|---|---|---|---|---|---|---|
| | $MgCl_2$ | | | CsCl | | $MgCl_2$ | | | CsCl | |
| | 2 M | 3 M | 4 M | 3 M | 4 M | 2 M | 3 M | 4 M | 3 M | 4 M |
| 1.75 | 1.05 | 1.53 | 2.07 | | | 0.56 | 1.33 | 2.03 | | |
| 2.25 | 0.89 | 1.15 | 1.51 | | | 0.52 | 1.22 | 1.86 | | |
| 2.75 | 0.42 | 0.73 | 0.74 | 0.07 | 0.15 | 0.22 | 0.92 | 2.45 | 0.04 | 0.12 |
| 3.25 | 0.22 | 0.28 | 0.62 | 0.06 | 0.14 | 0.12 | 0.27 | 0.48 | 0.04 | 0.11 |
| 3.75 | 0.15 | 0.17 | 0.34 | 0.05 | 0.12 | 0.12 | 0.24 | 0.42 | 0.03 | 0.10 |
| 4.25 | 0.09 | 0.16 | 0.33 | 0.04 | 0.11 | 0.11 | 0.24 | 0.39 | 0.03 | 0.09 |
| 4.75 | 0.08 | 0.14 | 0.31 | 0.04 | 0.10 | 0.10 | 0.22 | 0.38 | 0.03 | 0.09 |
| 5.25 | 0.07 | 0.11 | 0.21 | 0.03 | 0.09 | 0.08 | | | 0.03 | 0.07 |
| 5.75 | 0.05 | 0.09 | | 0.02 | 0.07 | | | | 0.02 | 0.06 |

Table 7.5: $f_{\left(\frac{slow}{bulk}\right)}$ values calculated in NVE ensemble for various spatial separations (r) from the cationic species (binwidth = $0.5\mathring{A}$). The data are averaged over 5000 frames and 0.5 ns of simulation for TIP4P-Ew water model (NVE simulation following NPT (T = 298K) simulation)) and over 5000 frames and 1 ns of simulation for TIP3P (NVE simulation following NPT (T = 305K) simulation).

From Table 7.4, it can also be seen that the fraction of slow water molecules relative to bulk-like water, beyond first solvation shell ($f_{\left(\frac{slow}{bulk},defect\right)}$) for 2 M $MgCl_2$ is only 0.06. This small value may suggest why long-range effects of strongly solvated cations were not conclusively found in earlier simulations. A snap shot of $MgCl_2$-TIP4P-Ew water system for 2 M salt concentration is shown in Figure 7.7. The defect water molecules, which are beyond the first solvation shell of any ions are shown as van der Waals spheres and it can be seen that they form a small fraction of total number of water molecules in the system. Values of $f_{\frac{slow}{bulk}}$ as a function of radial distance from cations was computed and are given in Table 7.5. Within 2.5 $\mathring{A}$, a typical radial distance defining first solvation shell, the fraction of slow water molecules to bulk $f_{\frac{slow}{bulk}}$ for 2 M $MgCl_2$ concentration is 0.89. This value drops to 0.22 just above 3 $\mathring{A}$ and progressively decreases beyond first solvation shell. However the non-zero values of $f_{\frac{slow}{bulk}}$ well beyond first and second solvation shells of $Mg^{2+}$ ions even at 2 M concentration indicate delocalized presence of slow water molecules. Similar trends are observed for TIP3P water model as well. These results suggest that classifying water molecules around multiple ions, at moderate to high concentrations, using an oft-used definition of radially varying solvation shells may not
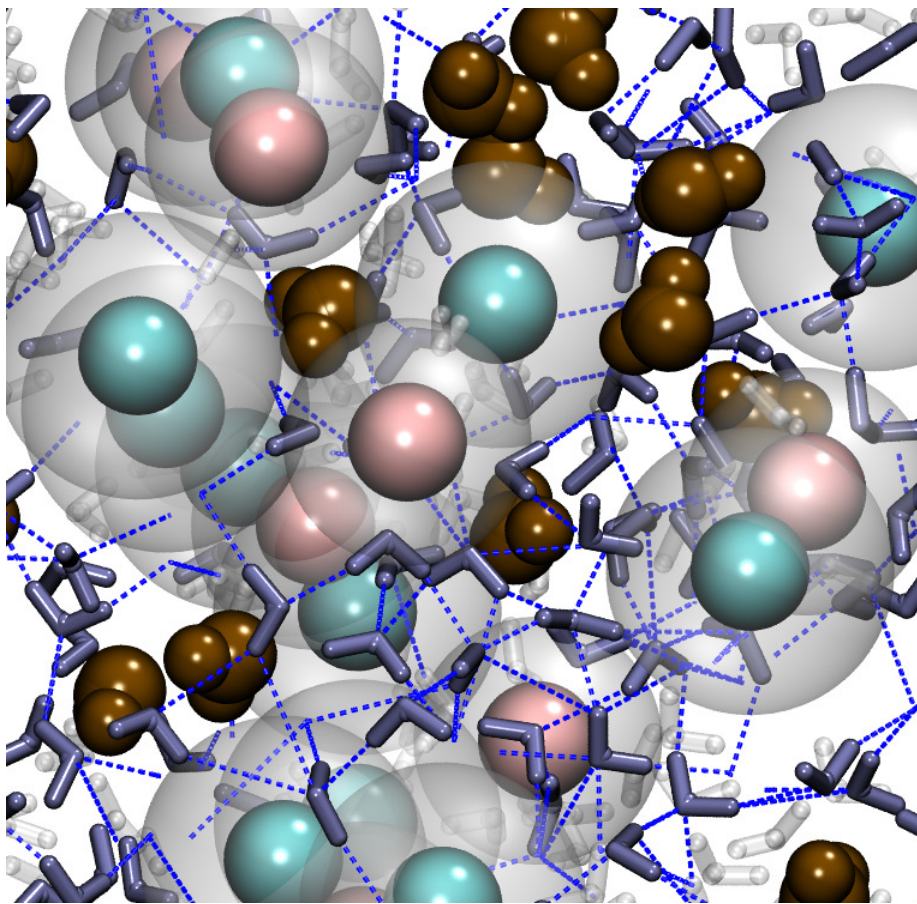
Figure 7.7: Snapshot of part of $MgCl_2$-water system at 2 M salt concentration. The $Mg^{2+}$ and $Cl^-$ ions are shown as cyan and pink spheres. The first solvation shells (2.5 $\mathring{A}$ radius) around the ions are also shown as transparent spheres. The defect water molecules, *waterD*, which are not within the first solvation shell are shown in vdW representation in brown and the other water molecules are shown in stick representation (transparent for water molecules in the first solvation shell of ions). The hydrogen bond network among water molecules is also shown.

be able to capture this small fraction of slow water molecules. The definition of defect water molecules *waterD* used in the reported study can capture these small fraction of slow water molecules and suggest long-range effects of strongly solvated cations such as $Mg^{2+}$. It can also be seen from the Table 7.4 that this fraction of defect water molecules increases with concentration and a significant jump occurs in such fraction from 2 M to 4 M (0.19 to 0.80). This suggests that a global network of defect water molecules may occur at higher salt concentrations. The values of $f_{\frac{slow}{bulk}}$ and $f_{(\frac{slow}{bulk}, defect)}$ for CsCl salt solutions are very small, consistent with results in Figure 7.7.

175

## 7.4  Discussion

MD simulation results in the reported study support the concentration dependent effects of strongly solvated ion species ($Mg^{2+}$) on the reorientational dynamics of water molecules beyond the first solvation shell. A likely mechanism for the same has been suggested in terms of salt induced defects in the underlying hydrogen bond network of water, which is in agreement with concepts of ion induced patterning of water at long distances. While the actual number of water molecules beyond first solvation shell of ions that exhibit slow reorientational times is a small fraction of the total water molecules, especially at low concentrations, they have been found at large spatial separations from the ions. The fractional number has been observed to increase monotonically with increase in the concentration of $MgCl_2$. It is to be noted that the long-range effect of $Mg^{2+}$ ions in the presence of a weakly solvated counterion $Cl^-$ is smaller than experimentally observed effects in the presence of $SO_4^{2-}$ [14], but not insignificant. Comparison with weakly solvated cationic species ($Cs^+$) has been seen to be in agreement with the Hofmeister series. The results in the present study are obtained with two non-polarizable models of water. The long-range effect of dissolved ions on water dynamics has also been observed in a recent MD simulation study using polarizable models for water and ions [279].

# Bibliography

[1] M. Zasloff, "Antimicrobial peptides of multicellular organisms," *Nature*, vol. 415, no. 6870, pp. 389–395, 2002.

[2] E. F. Palermo, S. Vemparala, and K. Kuroda, "Cationic spacer arm design strategy for control of antimicrobial activity and conformation of amphiphilic methacrylate random copolymers," *Biomacromolecules*, vol. 13, no. 5, pp. 1632–1641, 2012.

[3] L. T. Nguyen, E. F. Haney, and H. J. Vogel, "The expanding scope of antimicrobial peptide structures and their modes of action," *Trends in Biotechnology*, vol. 29, no. 9, pp. 464–472, 2011.

[4] L. Vamparys, R. Gautier, S. Vanni, W. D. Bennett, D. P. Tieleman, B. Antonny, C. Etchebest, and P. Fuchs, "Conical lipids in flat bilayers induce packing defects similar to that induced by positive curvature," *Biophysical Journal*, vol. 104, no. 3, pp. 585 – 593, 2013.

[5] S. Vanni, H. Hirose, H. Barelli, B. Antonny, and R. Gautier, "A sub-nanometre view of how membrane curvature and composition modulate lipid packing and protein recruitment," *Nature communications*, vol. 5, 2014.

[6] R. F. Epand, B. P. Mowery, S. E. Lee, S. S. Stahl, R. I. Lehrer, S. H. Gellman, and R. M. Epand, "Dual mechanism of bacterial lethality for a cationic sequence-random copolymer that mimics host-defense antimicrobial peptides," *Journal of Molecular Biology*, vol. 379, no. 1, pp. 38 – 50, 2008.

[7] P. Kumar, S. V. Buldyrev, and H. E. Stanley, "A tetrahedral entropy for water," *Proceedings of the National Academy of Sciences*, vol. 106, no. 52, pp. 22130–22134, 2009.

[8] T. Head-Gordon and G. Hura, "Water structure from scattering experiments and simulation," *Chemical Reviews*, vol. 102, no. 8, pp. 2651–2670, 2002.

[9] P. Ball and J. E. Hallsworth, "Water structure and chaotropicity: their uses, abuses and biological implications," *Physical Chemistry Chemical Physics*, vol. 17, no. 13, pp. 8297–8305, 2015.

[10] Y. Marcus, "Effect of ions on the structure of water: structure making and breaking," *Chemical Reviews*, vol. 109, no. 3, pp. 1346–1370, 2009.

[11] J. M. P. Kanth, S. Vemparala, and R. Anishetty, "Long-distance correlations in molecular orientations of liquid water and shape-dependent hydrophobic force," *Physical Review E*, vol. 81, no. 2, p. 021201, 2010.

[12] D. P. Shelton, "Long-range orientation correlation in dipolar liquids probed by hyper-Rayleigh scattering," *The Journal of Chemical Physics*, vol. 143, no. 13, p. 134503, 2015.

[13] D. Laage and J. T. Hynes, "On the molecular mechanism of water reorientation," *The Journal of Physical Chemistry B*, vol. 112, no. 45, pp. 14230–14242, 2008.

[14] K. J. Tielrooij, N. Garcia-Araez, M. Bonn, and H. J. Bakker, "Cooperativity in ion hydration," *Science*, vol. 328, no. 5981, pp. 1006–1009, 2010.

[15] G. Stirnemann, E. Wernersson, P. Jungwirth, and D. Laage, "Mechanisms of acceleration and retardation of water dynamics by ions," *Journal of the American Chemical Society*, vol. 135, no. 32, pp. 11824–11831, 2013.

[16] E. E. Meyer, K. J. Rosenberg, and J. Israelachvili, "Recent progress in understanding hydrophobic interactions," *Proceedings of the National Academy of Sciences*, vol. 103, no. 43, pp. 15739–15746, 2006.

[17] O. G. Mouritsen, *Life-as a matter of fat*. Springer, 2005.

[18] D. B. N. Lee, N. Jamgotchian, S. G. Allen, M. B. Abeles, and H. J. Ward, "A lipid-protein hybrid model for tight junction," *American Journal of Physiology - Renal Physiology*, vol. 295, no. 6, pp. F1601–F1612, 2008.

[19] O. G. Mouritsen and M. Bloom, "Models of lipid-protein interactions in membranes," *Annual Review of Biophysics and Biomolecular Structure*, vol. 22, no. 1, pp. 145–171, 1993.

[20] A. W. Smith, "Lipid-protein interactions in biological membranes: a dynamic perspective," *Biochimica et Biophysica Acta (BBA) - Biomembranes*, vol. 1818, no. 2, pp. 172–177, 2012.

[21] R. Faller, *BPH241 Lecture Notes*. University of California, Davis, April, 2015.

[22] J. F. Nagle and S. Tristram-Nagle, "Lipid bilayer structure," *Current Opinion in Structural Biology*, vol. 10, no. 4, pp. 474–480, 2000.

[23] A. E. Blaurock and T. J. McIntosh, "Structure of the crystalline bilayer in the subgel phase of dipalmitoylphosphatidylglycerol," *Biochemistry*, vol. 25, no. 2, pp. 299–305, 1986.

[24] J. Katsaras, V. A. Raghunathan, E. J. Dufourc, and J. Dufourcq, "Evidence for a two-dimensional molecular lattice in subgel phase dppc bilayers," *Biochemistry*, vol. 34, no. 14, pp. 4684–4688, 1995.

[25] W. J. Sun, S. Tristram-Nagle, R. M. Suter, and J. F. Nagle, "Structure of the ripple phase in lecithin bilayers," *Proceedings of the National Academy of Sciences*, vol. 93, no. 14, pp. 7008–7012, 1996.

[26] S. Mukherjee and F. R. Maxfield, "Membrane domains," *Annual Review of Cell and Developmental Biology*, vol. 20, no. 1, pp. 839–866, 2004.

[27] G. Cevc, "How membrane chain-melting phase-transition temperature is affected by the lipid chain asymmetry and degree of unsaturation: an effective chain-length model," *Biochemistry*, vol. 30, no. 29, pp. 7186–7193, 1991.

[28] J. M. Seddon, R. H. Templer, N. A. Warrender, Z. Huang, G. Cevc, and D. Marsh, "Phosphatidylcholine-fatty acid membranes: effects of headgroup hydration on the phase behaviour and structural parameters of the gel and inverse hexagonal (HII) phases," *Biochimica et Biophysica Acta (BBA) - Biomembranes*, vol. 1327, no. 1, pp. 131 – 147, 1997.

[29] T. P. W. McMullen, R. N. A. H. Lewis, and R. N. McElhaney, "Cholesterol-phospholipid interactions, the liquid-ordered phase and lipid rafts in model and biological membranes," *Current Opinion in Colloid & Interface Science*, vol. 8, no. 6, pp. 459 – 468, 2004.

[30] F. de Meyer and B. Smit, "Effect of cholesterol on the structure of a phospholipid bilayer," vol. 106, no. 10, pp. 3654–3658, 2009.

[31] G. Khelashvili, G. Pabst, and D. Harries, "Cholesterol orientation and tilt modulus in DMPC bilayers," *The Journal of Physical Chemistry B*, vol. 114, no. 22, pp. 7524–7534, 2010.

[32] D. P. Tieleman, S. J. Marrink, and H. J. C. Berendsen, "A computer perspective of membranes: molecular dynamics studies of lipid bilayer systems," *Biochimica et Biophysica Acta (BBA) - Reviews on Biomembranes*, vol. 1331, no. 3, pp. 235 – 270, 1997.

[33] P. A. Janmey and P. K. J. Kinnunen, "Biophysical properties of lipids and dynamic membranes," *Trends in Cell Biology*, vol. 16, no. 10, pp. 538 – 546, 2006.

[34] R. S. Cantor, "Lateral pressures in cell membranes: a mechanism for modulation of protein function," *The Journal of Physical Chemistry B*, vol. 101, no. 10, pp. 1723–1725, 1997.

[35] R. S. Cantor, "The lateral pressure profile in membranes: a physical mechanism of general anesthesia," *Biochemistry*, vol. 36, no. 9, pp. 2339–2344, 1997.

[36] A. Polley and S. Vemparala, "Partitioning of ethanol in multi-component membranes: effects on membrane structure," *Chemistry and Physics of Lipids*, vol. 166, pp. 1 – 11, 2013.

[37] M. S. P. Sansom and P. C. Biggin, *Molecular simulations and biomembranes: from biophysics to function.* No. 20, Royal Society of Chemistry, 2010.

[38] J. Gullingsrud and K. Schulten, "Lipid bilayer pressure profiles and mechanosensitive channel gating," *Biophysical Journal*, vol. 86, no. 6, pp. 3496 – 3509, 2004.

[39] J. Katsaras, "Structure of the subgel (Lc') and gel (L$_\beta$') phases of oriented dipalmitoylphosphatidylcholine multibilayers," *The Journal of Physical Chemistry*, vol. 99, no. 12, pp. 4141–4147, 1995.

[40] J. F. Nagle and S. Tristram-Nagle, "Structure of lipid bilayers," *Biochimica et Biophysica Acta (BBA) - Reviews on Biomembranes*, vol. 1469, no. 3, pp. 159–195, 2000.

[41] R. S. Armen, O. D. Uitto, and S. E. Feller, "Phospholipid component volumes: determination and application to bilayer structure calculations," *Biophysical Journal*, vol. 75, no. 2, pp. 734 – 744, 1998.

[42] M. C. Wiener and S. H. White, "Structure of a fluid dioleoylphosphatidylcholine bilayer determined by joint refinement of X-ray and neutron diffraction data. III. Complete structure," *Biophysical Journal*, vol. 61, no. 2, pp. 434 – 447, 1992.

[43] J. F. Nagle, R. Zhang, S. Tristram-Nagle, W. Sun, H. I. Petrache, and R. M. Suter, "X-ray structure determination of fully hydrated $L_\alpha$ phase dipalmitoylphosphatidylcholine bilayers," *Biophysical Journal*, vol. 70, no. 3, pp. 1419 – 1431, 1996.

[44] S. Tristram-Nagle, H. I. Petrache, and J. F. Nagle, "Structure and interactions of fully hydrated dioleoylphosphatidylcholine bilayers," *Biophysical Journal*, vol. 75, no. 2, pp. 917 – 925, 1998.

[45] S. Tristram-Nagle and J. F. Nagle, "Lipid bilayers: thermodynamics, structure, fluctuations, and interactions," *Chemistry and Physics of Lipids*, vol. 127, no. 1, pp. 3 – 14, 2004.

[46] A. Tardieu, V. Luzzati, and F. C. Reman, "Structure and polymorphism of the hydrocarbon chains of lipids: a study of lecithin-water phases," *Journal of Molecular Biology*, vol. 75, no. 4, pp. 711 – 733, 1973.

[47] R. P. Rand and V. A. Parsegian, "Hydration forces between phospholipid bilayers," *Biochimica et Biophysica Acta (BBA) - Reviews on Biomembranes*, vol. 988, no. 3, pp. 351 – 376, 1989.

[48] R. Zhang, S. Tristram-Nagle, W. Sun, R. L. Headrick, T. C. Irving, R. M. Suter, and J. F. Nagle, "Small-angle X-ray scattering from lipid bilayers is well described by modified Caillé theory but not by paracrystalline theory," *Biophysical Journal*, vol. 70, no. 1, pp. 349 – 357, 1996.

[49] L. S. Vermeer, B. L. de Groot, V. Réat, A. Milon, and J. Czaplicki, "Acyl chain order parameter profiles in phospholipid bilayers: computation from molecular dynamics simulations and comparison with $^2$H NMR experiments," *European Biophysics Journal*, vol. 36, no. 8, pp. 919–931, 2007.

[50] M. A. McCabe and S. R. Wassail, "Rapid deconvolution of NMR powder spectra by weighted fast Fourier transformation," *Solid State Nuclear Magnetic Resonance*, vol. 10, no. 1, pp. 53 – 61, 1997.

[51] M. Renault, V. Réat, M. Sugawara, P. Demange, E. Phez, J. Teissie, M. Piotto, and A. Milon, "Giant vesicles as an efficient intermediate for $^2$H NMR analyses of proteoliposomes in water suspension and in oriented lipid bilayers," *Comptes Rendus Chimie*, vol. 9, no. 3-4, pp. 401 – 407, 2006.

[52] R. L. Thurmond, G. Lindblom, and M. F. Brown, "Curvature, order, and dynamics of lipid hexagonal phases studied by deuterium NMR spectroscopy," *Biochemistry*, vol. 32, no. 20, pp. 5394–5410, 1993.

[53] H. I. Petrache, S. W. Dodd, and M. F. Brown, "Area per lipid and acyl length distributions in fluid phosphatidylcholines determined by $^2$H NMR spectroscopy," *Biophysical Journal*, vol. 79, no. 6, pp. 3172 – 3192, 2000.

[54] M. A. Alonso and J. Millán, "The role of lipid rafts in signalling and membrane trafficking in T lymphocytes," *Journal of Cell Science*, vol. 114, no. 22, pp. 3957–3965, 2001.

[55] M. Leslie, "Do lipid rafts exist?," *Science*, vol. 334, no. 6059, pp. 1046–1047, 2011.

[56] R. M. Epand and R. F. Epand, "Lipid domains in bacterial membranes and the action of antimicrobial agents," *Biochimica et Biophysica Acta (BBA) - Biomembranes*, vol. 1788, no. 1, pp. 289 – 294, 2009.

[57] A. Arouri, M. Dathe, and A. Blume, "Peptide induced demixing in PG/PE lipid mixtures: a mechanism for the specificity of antimicrobial peptides towards bacterial membranes?," *Biochimica et Biophysica Acta (BBA) - Biomembranes*, vol. 1788, no. 3, pp. 650 – 659, 2009.

[58] E. Gorter and F. J. E. M. Grendel, "On bimolecular layers of lipoids on the chromocytes of the blood," *The Journal of experimental medicine*, vol. 41, no. 4, pp. 439–443, 1925.

[59] "The fluid-mosaic model of membrane structure: still relevant to understanding the structure, function and dynamics of biological membranes after more than 40 years," *Biochimica et Biophysica Acta (BBA) - Biomembranes*, vol. 1838, no. 6.

[60] O. G. Mouritsen and K. Jørgensen, "Problems and paradigms: dynamic lipid-bilayer heterogeneity: a mesoscopic vehicle for membrane function?," *BioEssays*, vol. 14, no. 2, pp. 129–136, 1992.

[61] J. N. Israelachvili, "Refinement of the fluid-mosaic model of membrane structure," *Biochimica et Biophysica Acta (BBA) - Biomembranes*, vol. 469, no. 2, pp. 221 – 225, 1977.

[62] R. Lipowsky and E. Sackmann, *Structure and dynamics of membranes*: *I. From cells to vesicles/ II. Generic and specific interactions*, vol. 1. Elsevier, 1995.

[63] G. D. Wright, "The antibiotic resistome: the nexus of chemical and genetic diversity," *Nature Reviews Microbiology*, vol. 5, no. 3, pp. 175–186, 2007.

[64] J. B. Mcphee and R. E. W. Hancock, "Function and therapeutic potential of host defence peptides," *Journal of Peptide Science*, vol. 11, no. 11, pp. 677–687, 2005.

[65] R. E. W. Hancock and H.-G. Sahl, "Antimicrobial and host-defense peptides as new anti-infective therapeutic strategies," *Nature Biotechnology*, vol. 24, no. 12, pp. 1551–1557, 2006.

[66] H. Jenssen, P. Hamill, and R. E. W. Hancock, "Peptide antimicrobial agents," *Clinical Microbiology Reviews*, vol. 19, no. 3, pp. 491–511, 2006.

[67] F. Harris, S. R. Dennison, and D. A. Phoenix, "Anionic antimicrobial peptides from eukaryotic organisms," *Current Protein & Peptide Science*, vol. 10, no. 6, pp. 585–606, 2009.

[68] A. Peschel and H.-G. Sahl, "The co-evolution of host cationic antimicrobial peptides and microbial resistance," *Nature Reviews Microbiology*, vol. 4, no. 7, pp. 529–536, 2006.

[69] B. M. Peters, M. E. Shirtliff, and M. A. Jabra-Rizk, "Antimicrobial peptides: primeval molecules or future drugs?," *Public Library of Science*: *Pathogens*, vol. 6, pp. 1–4, 10 2010.

[70] H. G. Boman, "Peptide antibiotics and their role in innate immunity," *Annual Review of Immunology*, vol. 13, pp. 61–92, 1995.

[71] M.-D. Seo, H.-S. Won, J.-H. Kim, T. Mishig-Ochir, and B.-J. Lee, "Antimicrobial peptides for therapeutic applications: a review," *Molecules*, vol. 17, no. 10, pp. 12276–12286, 2012.

[72] V. Teixeira, M. J. Feio, and M. Bastos, "Role of lipids in the interaction of antimicrobial peptides with membranes," *Progress in Lipid Research*, vol. 51, no. 2, pp. 149 – 177, 2012.

[73] C. M. Goodman, S. Choi, S. Shandler, and W. F. DeGrado, "Foldamers as versatile frameworks for the design and evolution of function," *Nature Chemical Biology*, vol. 3, no. 5, pp. 252–262, 2007.

[74] M. A. Schmitt, B. Weisblum, and S. H. Gellman, "Interplay among folding, sequence, and lipophilicity in the antibacterial and hemolytic activities of $\alpha/\beta$-peptides," *Journal of the American Chemical Society*, vol. 129, no. 2, pp. 417–428, 2007.

[75] S. Riedl, D. Zweytick, and K. Lohner, "Membrane-active host defense peptides – challenges and perspectives for the development of novel anticancer drugs," *Chemistry and Physics of Lipids*, vol. 164, no. 8, pp. 766 – 781, 2011.

[76] T. L. Raguse, E. A. Porter, B. Weisblum, and S. H. Gellman, "Structure-activity studies of 14-helical antimicrobial $\beta$-peptides: probing the relationship between conformational stability and antimicrobial potency," *Journal of the American Chemical Society*, vol. 124, no. 43, pp. 12774–12785, 2002.

[77] P. S. Farmer and E. J. Ariëns, "Speculations on the design of nonpeptidic peptidomimetics," *Trends in Pharmacological Sciences*, vol. 3, no. 0, pp. 362 – 365, 1982.

[78] E. A. Porter, B. Weisblum, and S. H. Gellman, "Mimicry of host-defense peptides by unnatural oligomers: antimicrobial $\beta$-peptides," *Journal of the American Chemical Society*, vol. 124, no. 25, pp. 7324–7330, 2002.

[79] Y. Hamuro, J. P. Schneider, and W. F. DeGrado, "De novo design of antibacterial $\beta$-peptides," *Journal of the American Chemical Society*, vol. 121, no. 51, pp. 12200–12201, 1999.

[80] F. Sgolastra, B. M. deRonde, J. M. Sarapas, A. Som, and G. N. Tew, "Designing mimics of membrane active proteins," *Accounts of Chemical Research*, vol. 46, no. 12, pp. 2977–2987, 2013.

[81] L. Arnt, K. Nusslein, and G. N. Tew, "Nonhemolytic abiogenic polymers as antimicrobial peptide mimics," *Journal of Polymer Science Part A*: *Polymer Chemistry*, vol. 42, no. 15, pp. 3860–3864, 2004.

[82] G. N. Tew, D. Liu, B. Chen, R. J. Doerksen, J. Kaplan, P. J. Carroll, M. L. Klein, and W. F. DeGrado, "De novo design of biomimetic antimicrobial polymers," *Proceedings of the National Academy of Sciences*, vol. 99, no. 8, pp. 5110–5114, 2002.

[83] M. F. Ilker, K. Nusslein, G. N. Tew, and E. B. Coughlin, "Tuning the hemolytic and antibacterial activities of amphiphilic polynorbornene derivatives," *Journal of the American Chemical Society*, vol. 126, no. 48, pp. 15870–15875, 2004.

[84] K. Kuroda and G. A. Caputo, "Antimicrobial polymers as synthetic mimics of host-defense peptides," *Wiley Interdisciplinary Reviews*: *Nanomedicine and Nanobiotechnology*, vol. 5, no. 1, pp. 49–66, 2013.

[85] K. Kuroda and W. F. DeGrado, "Amphiphilic polymethacrylate derivatives as antimicrobial agents," *Journal of the American Chemical Society*, vol. 127, no. 12, pp. 4128–4129, 2005.

[86] T. Ikeda and S. Tazuke, "Biologically active polycations : antimicrobial activities of poly[trialkyl (vinylbenzyl) ammonium chloride]-type polycations," *Die Makromolekulare Chemie Rapid Communications*, vol. 4, no. 7, pp. 459–461, 1983.

[87] D. S. S. M. Uppu, P. Akkapeddi, G. B. Manjunath, V. Yarlagadda, J. Hoque, and J. Haldar, "Polymers with tunable side-chain amphiphilicity as non-hemolytic antibacterial agents," *Chemical Communications*, vol. 49, no. 82, pp. 9389–9391, 2013.

[88] E.-R. Kenawy, S. D. Worley, and R. Broughton, "The chemistry and applications of antimicrobial polymers: a state-of-the-art review," *Biomacromolecules*, vol. 8, no. 5, pp. 1359–1384, 2007.

[89] P. Li, X. Li, R. Saravanan, C. M. Li, and S. S. J. Leong, "Antimicrobial macromolecules: synthesis methods and future applications," *RSC Advances*, vol. 2, pp. 4031–4044, 2012.

[90] K. Kuroda, G. Caputo, and W. DeGrado, "The role of hydrophobicity in the antimicrobial and hemolytic activities of polymethacrylate derivatives," *Chemistry - A European Journal*, vol. 15, no. 5, pp. 1123–1133, 2009.

[91] Y. Oda, S. Kanaoka, T. Sato, S. Aoshima, and K. Kuroda, "Block versus random amphiphilic copolymers as antibacterial agents," *Biomacromolecules*, vol. 12, no. 10, pp. 3581–3591, 2011.

[92] J. M. Lagaron, M. J. Ocio, and A. Lopez-Rubio, *Antimicrobial polymers*. John Wiley & Sons, 2011.

[93] K. Glinel, P. Thebault, V. Humblot, C. M. Pradier, and T. Jouenne, "Antibacterial surfaces developed from bio-inspired approaches," *Acta Biomaterialia*, vol. 8, no. 5, pp. 1670–1684, 2012.

[94] K. Matsuzaki, K. Sugishita, N. Ishibe, M. Ueha, S. Nakata, K. Miyajima, and R. M. Epand, "Relationship of membrane curvature to the formation of pores by magainin 2," *Biochemistry*, vol. 37, no. 34, pp. 11856–11863, 1998.

[95] M. R. Yeaman and N. Y. Yount, "Mechanisms of antimicrobial peptide action and resistance," *Pharmacological Reviews*, vol. 55, no. 1, pp. 27–55, 2003.

[96] K. A. Brogden, "Antimicrobial peptides: pore formers or metabolic inhibitors in bacteria?," *Nature reviews. Microbiology*, vol. 3, pp. 238–250, 2005.

[97] K. Matsuzaki, O. Murase, N. Fujii, and K. Miyajima, "An antimicrobial peptide, magainin 2, induced rapid flip-flop of phospholipids coupled with pore formation and peptide translocation," *Biochemistry*, vol. 35, no. 35, pp. 11361–11368, 1996.

[98] R. Mani, S. D. Cady, M. Tang, A. J. Waring, R. I. Lehrer, and M. Hong, "Membrane-dependent oligomeric structure and pore formation of a $\beta$-hairpin antimicrobial peptide in lipid bilayers from solid-state NMR," *Proceedings of the National Academy of Sciences*, vol. 103, no. 44, pp. 16242–16247, 2006.

[99] E. S. Salnikov, M. D. Zotti, F. Formaggio, X. Li, C. Toniolo, J. D. J. O'Neil, J. Raap, S. A. Dzuba, and B. Bechinger, "Alamethicin topology in phospholipid

membranes by oriented solid-state NMR and EPR spectroscopies: a comparison," *The Journal of Physical Chemistry B*, vol. 113, no. 10, pp. 3034–3042, 2009.

[100] S. Archer, J. Ellena, and D. Cafiso, "Dynamics and aggregation of the peptide ion channel alamethicin. measurements using spin-labeled peptides," *Biophysical Journal*, vol. 60, no. 2, pp. 389 – 398, 1991.

[101] H. Leontiadou, A. E. Mark, and S. J. Marrink, "Antimicrobial peptides in action," *Journal of the American Chemical Society*, vol. 128, no. 37, pp. 12156–12161, 2006.

[102] M. Wu, E. Maier, R. Benz, and R. E. W. Hancock, "Mechanism of interaction of different classes of cationic antimicrobial peptides with planar bilayers and with the cytoplasmic membrane of escherichia coli," *Biochemistry*, vol. 38, no. 22, pp. 7235–7242, 1999.

[103] http://www.sklogwiki.org/SklogWiki/index.php/Lennard-Jones_model .

[104] https://en.wikipedia.org/wiki/Structure_of_liquids_and_glasses .

[105] http://www1.lsbu.ac.uk/water/water_phase_diagram.html .

[106] E. Schneck, F. Sedlmeier, and R. R. Netz, "Hydration repulsion between biomembranes results from an interplay of dehydration and depolarization," *Proceedings of the National Academy of Sciences*, vol. 109, no. 36, pp. 14405–14409, 2012.

[107] P. M. Kasson, E. Lindahl, and V. S. Pande, "Water ordering at membrane interfaces controls fusion dynamics," *Journal of the American Chemical Society*, vol. 133, no. 11, pp. 3812–3815, 2011.

[108] E. Tajkhorshid, P. Nollert, M. Ø. Jensen, L. J. W. Miercke, J. O'Connell, R. M. Stroud, and K. Schulten, "Control of the selectivity of the aquaporin water channel family by global orientational tuning," *Science*, vol. 296, no. 5567, pp. 525–530, 2002.

[109] A. Horner, F. Zocher, J. Preiner, N. Ollinger, C. Siligan, S. A. Akimov, and P. Pohl, "The mobility of single-file water molecules is governed by the number of H-bonds they may form with channel-lining residues," *Science Advances*, vol. 1, no. 2, 2015.

[110] D. Chandler, "Interfaces and the driving force of hydrophobic assembly," *Nature*, vol. 437, no. 7059, pp. 640 – 647, 2005.

[111] K. A. Dill, T. M. Truskett, V. Vlachy, and B. Hribar-Lee, "Modeling water, the hydrophobic effect, and ion solvation," *Annual Review of Biophysics and Biomolecular Structure*, vol. 34, no. 1, pp. 173–199, 2005.

[112] N. Agmon, "The grotthuss mechanism," *Chemical Physics Letters*, vol. 244, no. 5-6, pp. 456 – 462, 1995.

[113] G. Stirnemann, P. J. Rossky, J. T. Hynes, and D. Laage, "Water reorientation, hydrogen-bond dynamics and 2D-IR spectroscopy next to an extended hydrophobic surface," *Faraday Discussions*, vol. 146, pp. 263–281, 2010.

[114] D. S. Eisenberg and W. Kauzmann, *The structure and properties of water*. New York: Oxford University Press, 1969.

[115] J. Zielkiewicz, "Structural properties of water: comparison of the SPC, SPCE, TIP4P, and TIP5P models of water," *The Journal of Chemical Physics*, vol. 123, no. 10, p. 104501, 2005.

[116] H. E. Stanley, S. V. Buldyrev, O. Mishima, M. R. Sadr-Lahijany, A. Scala, and F. W. Starr, "Unsolved mysteries of water in its liquid and glassy phases," *Journal of Physics*: *Condensed Matter*, vol. 12, no. 8A, p. A403, 2000.

[117] H. P. Bennetto and E. F. Caldin, "Solvent effects on the kinetics of the reactions of nickel(II) and cobalt(II) ions with 2,2′-bipyridyl and 2,2′,2″-terpyridyl," *Journal of the Chemical Society A*: *Inorganic, Physical, Theoretical*, pp. 2191–2198, 1971.

[118] Y. Marcus, "The structuredness of water at elevated temperatures along the saturation line," *Journal of Molecular Liquids*, vol. 79, no. 2, pp. 151 – 165, 1999.

[119] A. K. Soper, "The radial distribution functions of water as derived from radiation total scattering experiments: is there anything we can say for sure?," *International Scholarly Research Notices Physical Chemistry*, vol. 2013, p. 279463, 2013.

[120] C. Zhang and G. Galli, "Dipolar correlations in liquid water," *The Journal of Chemical Physics*, vol. 141, no. 8, p. 084504, 2014.

[121] P. Mark and L. Nilsson, "Structure and dynamics of the TIP3P, SPC, and SPC/E water models at 298 k," *The Journal of Physical Chemistry A*, vol. 105, no. 43, pp. 9954–9960, 2001.

[122] A. K. Soper, "The radial distribution functions of water and ice from 220 to 673 K and at pressures up to 400 MPa," *Chemical Physics*, vol. 258, no. 2-3, pp. 121 – 137, 2000.

[123] R. L. McGreevy and L. Pusztai, "Reverse monte carlo simulation: a new technique for the determination of disordered structures," *Molecular Simulation*, vol. 1, no. 6, pp. 359–367, 1988.

[124] R. Kumar, J. R. Schmidt, and J. L. Skinner, "Hydrogen bonding definitions and dynamics in liquid water," *The Journal of Chemical Physics*, vol. 126, no. 20, p. 204107, 2007.

[125] D. Xenides, B. R. Randolf, and B. M. Rode, "Hydrogen bonding in liquid water: an ab initio QM/MM MD simulation study," *Journal of Molecular Liquids*, vol. 123, no. 2-3, pp. 61–67, 2006.

[126] G. E. Walrafen, "Effects of equilibrium H-bond distance and angle changes on Raman intensities from water," *The Journal of Chemical Physics*, vol. 120, no. 10, pp. 4868–4876, 2004.

[127] P. Wernet, D. Nordlund, U. Bergmann, M. Cavalleri, M. Odelius, H. Ogasawara, L. A. Näslund, T. K. Hirsch, L. Ojamäe, P. Glatzel, L. G. M. Pettersson, and A. Nilsson, "The structure of the first coordination shell in liquid water," *Science*, vol. 304, no. 5673, pp. 995–999, 2004.

[128] U. Bergmann, A. Di Cicco, P. Wernet, E. Principi, P. Glatzel, and A. Nilsson, "Nearest-neighbor oxygen distances in liquid water and ice observed by X-ray Raman based extended X-ray absorption fine structure," *The Journal of Chemical Physics*, vol. 127, no. 17, p. 174504, 2007.

[129] J. D. Smith, C. D. Cappa, K. R. Wilson, B. M. Messer, R. C. Cohen, and R. J. Saykally, "Energetics of hydrogen bond network rearrangements in liquid water," *Science*, vol. 306, no. 5697, pp. 851–853, 2004.

[130] J. D. Smith, C. D. Cappa, B. M. Messer, W. S. Drisdell, R. C. Cohen, and R. J. Saykally, "Probing the local structure of liquid water by X-ray absorption spectroscopy," *The Journal of Physical Chemistry B*, vol. 110, no. 40, pp. 20038–20045, 2006.

[131]  http://www.dynamicscience.com.au/tester/solutions1/chemistry/watr.html  .

[132] J. A. Sellberg, C. Huang, T. A. McQueen, N. D. Loh, H. Laksmono, D. Schlesinger, R. G. Sierra, D. Nordlund, C. Y. Hampton, D. Starodub, *et al.*, "Ultrafast X-ray probing of water structure below the homogeneous ice nucleation temperature," *Nature*, vol. 510, no. 7505, pp. 381–384, 2014.

[133] H. W. Horn, W. C. Swope, J. W. Pitera, J. D. Madura, T. J. Dick, G. L. Hura, and T. Head-Gordon, "Development of an improved four-site water model for biomolecular simulations: TIP4P-Ew," *The Journal of Chemical Physics*, vol. 120, no. 20, pp. 9665–9678, 2004.

[134] M. W. Mahoney and W. L. Jorgensen, "A five-site model for liquid water and the reproduction of the density anomaly by rigid, nonpolarizable potential functions," *The Journal of Chemical Physics*, vol. 112, no. 20, pp. 8910–8922, 2000.

[135] W. L. Jorgensen, J. Chandrasekhar, J. D. Madura, R. W. Impey, and M. L. Klein, "Comparison of simple potential functions for simulating liquid water," *The Journal of Chemical Physics*, vol. 79, no. 2, pp. 926–935, 1983.

[136] J. M. Sorenson, G. Hura, R. M. Glaeser, and T. Head-Gordon, "What can X-ray scattering tell us about the radial distribution functions of water?," *The Journal of Chemical Physics*, vol. 113, no. 20, pp. 9149–9161, 2000.

[137] D. P. Shelton, "Long-range orientation correlation in liquids," *The Journal of Chemical Physics*, vol. 136, no. 4, p. 044503, 2012.

[138] D. P. Shelton, "Hyper-Rayleigh scattering from correlated molecules," *The Journal of Chemical Physics*, vol. 138, no. 15, p. 154502, 2013.

[139] D. P. Shelton, "Long-range orientation correlation in water," *The Journal of Chemical Physics*, vol. 141, no. 22, p. 224506, 2014.

[140] Y. Liu and J. Wu, "Communication: long-range angular correlations in liquid water," *The Journal of Chemical Physics*, vol. 139, no. 4, p. 041103, 2013.

[141] J. M. P. Kanth and R. Anishetty, "Molecular mean field theory for liquid water," *Physica A: Statistical Mechanics and its Applications*, vol. 391, no. 3, pp. 439 – 455, 2012.

[142] K. F. Rinne, S. Gekle, and R. R. Netz, "Ion-specific solvation water dynamics: single water versus collective water effects," *The Journal of Physical Chemistry A*, vol. 118, no. 50, pp. 11667–11677, 2014.

[143] A. Tongraar, K. R. Liedl, and B. M. Rode, "Born-oppenheimer ab initio QM/MM dynamics simulations of $Na^+$ and $K^+$ in water: from structure making to struc-

ture breaking effects," *The Journal of Physical Chemistry A*, vol. 102, no. 50, pp. 10340–10347, 1998.

[144] J. M. P. Kanth and R. Anishetty, "Hydrophobic force, a Casimir-like effect due to hydrogen-bond fluctuations," *Physica A*: *Statistical Mechanics and its Applications*, vol. 392, no. 20, pp. 4804 – 4823, 2013.

[145] G. Mathias and P. Tavan, "Angular resolution and range of dipole-dipole correlations in water," *The Journal of Chemical Physics*, vol. 120, no. 9, pp. 4393–4403, 2004.

[146] D. C. Elton and M. V. Fernández-Serra, "Polar nanoregions in water: a study of the dielectric properties of TIP4P/2005, TIP4P/2005f and TTM3F," *The Journal of Chemical Physics*, vol. 140, no. 12, p. 124504, 2014.

[147] W. Kunz, J. Henle, and B. W. Ninham, "'Zur Lehre von der Wirkung der Salze' (about the science of the effect of salts): Franz Hofmeister's historical papers," *Current Opinion in Colloid & Interface Science*, vol. 9, no. 1-2, pp. 19–37, 2004.

[148] D. Laage, G. Stirnemann, F. Sterpone, R. Rey, and J. T. Hynes, "Reorientation and allied dynamics in water and aqueous solutions," *Annual Review of Physical Chemistry*, vol. 62, no. 1, pp. 395–416, 2011.

[149] B. Geil, T. M. Kirschgen, and F. Fujara, "Mechanism of proton transport in hexagonal ice," *Physical Review B*, vol. 72, p. 014304, 2005.

[150] D. Laage and J. T. Hynes, "A molecular jump mechanism of water reorientation," *Science*, vol. 311, no. 5762, pp. 832–835, 2006.

[151] A. Fernández and R. S. Berry, "Proteins with H-bond packing defects are highly interactive with lipid bilayers: implications for amyloidogenesis," *Proceedings of the National Academy of Sciences*, vol. 100, no. 5, pp. 2391–2396, 2003.

[152] R. Pomès and B. Roux, "Structure and dynamics of a proton wire: a theoretical study of H$^+$ translocation along the single-file water chain in the gramicidin A channel," *Biophysical Journal*, vol. 71, no. 1, pp. 19 – 39, 1996.

[153] C. Rønne, P.-O. Åstrand, and S. R. Keiding, "THz spectroscopy of liquid H$_2$O and D$_2$O," *Physical Review Letters*, vol. 82, pp. 2888–2891, 1999.

[154] K. Winkler, J. Lindner, H. Bürsing, and P. Vöhringer, "Ultrafast Raman-induced Kerr-effect of water: single molecule versus collective motions," *The Journal of Chemical Physics*, vol. 113, no. 11, pp. 4674–4682, 2000.

[155] C. J. Fecko, J. J. Loparo, S. T. Roberts, and A. Tokmakoff, "Local hydrogen bonding dynamics and collective reorganization in water: ultrafast infrared spectroscopy of HOD/D$_2$O," *The Journal of Chemical Physics*, vol. 122, no. 5, p. 054506, 2005.

[156] H. J. Bakker, Y. L. A. Rezus, and R. L. A. Timmer, "Molecular reorientation of liquid water studied with femtosecond midinfrared spectroscopy," *The Journal of Physical Chemistry A*, vol. 112, no. 46, pp. 11523–11534, 2008.

[157] H. J. Bakker and J. L. Skinner, "Vibrational spectroscopy as a probe of structure and dynamics in liquid water," *Chemical Reviews*, vol. 110, no. 3, pp. 1498–1517, 2010.

[158] A. Abragam, *The principles of nuclear magnetism*. No. 32, Oxford university press, 1961.

[159] J. Qvist and B. Halle, "Thermal signature of hydrophobic hydration dynamics," *Journal of the American Chemical Society*, vol. 130, no. 31, pp. 10345–10353, 2008.

[160] D. Di Cola, A. Deriu, M. Sampoli, and A. Torcini, "Proton dynamics in supercooled water by molecular dynamics simulations and quasielastic neutron scattering," *The Journal of Chemical Physics*, vol. 104, no. 11, pp. 4223–4232, 1996.

[161] A. Beneduci, "Which is the effective time scale of the fast Debye relaxation process in water?," *Journal of Molecular Liquids*, vol. 138, no. 1-3, pp. 55 – 60, 2008.

[162] P. Debye, *Polar molecules*. The Chemical Catalog Company: New York, 1929.

[163] J. D. Eaves, J. J. Loparo, C. J. Fecko, S. T. Roberts, A. Tokmakoff, and P. L. Geissler, "Hydrogen bonds in liquid water are broken only fleetingly," *Proceedings of the National Academy of Sciences of the United States of America*, vol. 102, no. 37, pp. 13019–13022, 2005.

[164] T. Hansson, C. Oostenbrink, and W. F. van Gunsteren, "Molecular dynamics simulations," *Current Opinion in Structural Biology*, vol. 12, no. 2, pp. 190 – 196, 2002.

[165] J. C. Phillips, R. Braun, W. Wang, J. Gumbart, E. Tajkhorshid, E. Villa, C. Chipot, R. D. Skeel, L. Kale, and K. Schulten, "Scalable molecular dynamics with NAMD," *Journal of Computational Chemistry*, vol. 26, no. 16, pp. 1781 – 1802, 2005.

[166] H. J. C. Berendsen, D. van der Spoel, and R. van Drunen, "Gromacs: a message-passing parallel molecular dynamics implementation," *Computer Physics Communications*, vol. 91, no. 1, pp. 43 – 56, 1995.

[167] D. A. Case, R. M. Betz, W. Botello-Smith, D. S. Cerutti, *et al. AMBER 2016, University of California, San Francisco*.

[168] S. Plimpton, "Fast parallel algorithms for short-range molecular dynamics," *Journal of Computational Physics*, vol. 117, no. 1, pp. 1 – 19, 1995.

[169] H. M. Berman, J. Westbrook, Z. Feng, G. Gilliland, T. Bhat, H. Weissig, I. N. Shindyalov, and P. E. Bourne, "The protein data bank," *Nucleic acids research*, vol. 28, no. 1, pp. 235–242, 2000.

[170] http://www.charmm-gui.org/?doc=input/membrane .

[171] W. Humphrey, A. Dalke, and K. Schulten, "VMD: visual molecular dynamics," *Journal of Molecular Graphics*, vol. 14, no. 1, pp. 33 – 38, 1996.

[172] J. B. Klauda, R. M. Venable, J. A. Freites, J. W. O' Connor, D. J. Tobias, C. Mondragon-Ramirez, I. Vorobyov, A. D. MacKerell, and R. W. Pastor, "Update of the CHARMM all-atom additive force field for lipids: validation on six lipid types," *The Journal of Physical Chemistry B*, vol. 114, no. 23, pp. 7830–7843, 2010.

[173] W. L. Jorgensen, D. S. Maxwell, and J. Tirado-Rives, "Development and testing of the opls all-atom force field on conformational energetics and properties of organic liquids," *Journal of the American Chemical Society*, vol. 118, no. 45, pp. 11225–11236, 1996.

[174] Y.-P. Pang, "Use of 1-4 interaction scaling factors to control the conformational equilibrium between $\alpha$-helix and $\beta$-strand," *Biochemical and Biophysical Research Communications*, vol. 457, no. 2, pp. 183 – 186, 2015.

[175] D. Boda and D. Henderson, "The effects of deviations from Lorentz-Berthelot rules on the properties of a simple mixture," *Molecular Physics*, vol. 106, no. 20, pp. 2367–2370, 2008.

[176] D. Frenkel and B. Smit, *Understanding molecular simulation*: *from algorithms to applications*, vol. 1. Academic press, 2001.

[177] T. Darden, D. York, and L. Pedersen, "Particle mesh Ewald: an $N \cdot log(N)$ method for Ewald sums in large systems," *The Journal of Chemical Physics*, vol. 98, no. 12, pp. 10089–10092, 1993.

[178] L. Kalé, R. Skeel, M. Bhandarkar, R. Brunner, A. Gursoy, N. Krawetz, J. Phillips, A. Shinozaki, K. Varadarajan, and K. Schulten, "NAMD2: greater scalability for parallel molecular dynamics," *Journal of Computational Physics*, vol. 151, no. 1, pp. 283 – 312, 1999.

[179] T. Dauxois, S. Ruffo, E. Arimondo, and M. Wilkens, *Dynamics and Thermodynamics of Systems with Long Range Interactions.* Springer-Verlag Berlin Heidelberg, 2002.

[180] D. J. Tobias, K. Tu, and M. L. Klein, "Atomic-scale molecular dynamics simulations of lipid membranes," *Current Opinion in Colloid & Interface Science*, vol. 2, no. 1, pp. 15 – 26, 1997.

[181] S. E. Feller, "Molecular dynamics simulations of lipid bilayers," *Current Opinion in Colloid & Interface Science*, vol. 5, no. 3 - 4, pp. 217 – 223, 2000.

[182] S. W. Chiu, M. Clark, V. Balaji, S. Subramaniam, H. L. Scott, and E. Jakobsson, "Incorporation of surface tension into molecular dynamics simulation of an interface: a fluid phase lipid bilayer membrane," *Biophysical Journal*, vol. 69, no. 4, pp. 1230 – 1245, 1995.

[183] S. E. Feller and R. W. Pastor, "On simulating lipid bilayers with an applied surface tension: periodic boundary conditions and undulations," *Biophysical Journal*, vol. 71, no. 3, pp. 1350 – 1355, 1996.

[184] F. Jähnig, "What is the surface tension of a lipid bilayer membrane?," *Biophysical Journal*, vol. 71, no. 3, pp. 1348 – 1349, 1996.

[185] R. W. Pastor and A. D. MacKerell Jr., "Development of the CHARMM force field for lipids," *The Journal of Physical Chemistry Letters*, vol. 2, no. 13, pp. 1526–1532, 2011.

[186] H. J. C. Berendsen, J. P. M. Postma, W. F. van Gunsteren, A. DiNola, and J. R. Haak, "Molecular dynamics with coupling to an external bath," *The Journal of Chemical Physics*, vol. 81, no. 8, pp. 3684–3690, 1984.

[187] M. Sprik and M. L. Klein, "A polarizable model for water using distributed charge sites," *The Journal of Chemical Physics*, vol. 89, no. 12, pp. 7556–7560, 1988.

[188] R. B. Best, X. Zhu, J. Shim, P. E. M. Lopes, J. Mittal, M. Feig, and A. D. MacKerell Jr., "Optimization of the additive CHARMM all-atom protein force field targeting improved sampling of the backbone $\phi$, $\psi$ and side-chain $\chi_1$ and $\chi_2$ dihedral angles," *Journal of Chemical Theory and Computation*, vol. 8, no. 9, pp. 3257–3273, 2012.

[189] S. O. Nielsen, C. F. Lopez, G. Srinivas, and M. L. Klein, "Coarse grain models and the computer simulation of soft materials," *Journal of Physics*: *Condensed Matter*, vol. 16, no. 15, p. R481, 2004.

[190] A. D. MacKerell and N. K. Banavali, "All-atom empirical force field for nucleic acids: II. application to molecular dynamics simulations of DNA and RNA in solution," *Journal of Computational Chemistry*, vol. 21, no. 2, pp. 105–120, 2000.

[191] A. D. MacKerell Jr., D. Bashford, M. Bellott, R. L. Dunbrack, *et al.*, "All-atom empirical potential for molecular modeling and dynamics studies of proteins," *The Journal of Physical Chemistry B*, vol. 102, no. 18, pp. 3586–3616, 1998.

[192] A. D. MacKerell Jr., D. Bashford, and M. t. Bellott, "All-atom empirical potential for molecular modeling and dynamics studies of proteins," *The Journal of Physical Chemistry B*, vol. 102, no. 18, pp. 3586–3616, 1998.

[193] K. Vanommeslaeghe, E. Prabhu Raman, and A. D. MacKerell Jr., "Automation of the CHARMM general force field (CGenFF) II: assignment of bonded parameters and partial atomic charges," *Journal of Chemical Information and Modeling*, vol. 52, no. 12, pp. 3155–3168, 2012.

[194] H. A. Boumann, J. Gubbens, M. C. Koorengevel, C.-S. Oh, C. E. Martin, A. J. R. Heck, J. Patton-Vogt, S. A. Henry, B. de Kruijff, and A. I. P. M. de Kroon, "Depletion of phosphatidylcholine in yeast induces shortening and increased saturation of the lipid acyl chains: evidence for regulation of intrinsic membrane curvature in a eukaryote," *Molecular Biology of the Cell*, vol. 17, no. 2, pp. 1006–1017, 2006.

[195] http://www1.lsbu.ac.uk/water/water_models.html .

[196] B. Guillot, "A reappraisal of what we have learnt during three decades of computer simulations on water," *Journal of Molecular Liquids*, vol. 101, no. 1, pp. 219 – 260, 2002.

[197] K. R. Hadley and C. McCabe, "Coarse-grained molecular models of water: a review," *Molecular Simulation*, vol. 38, no. 8-9, pp. 671–681, 2012.

[198] S. O. Yesylevskyy, L. V. Schäfer, D. Sengupta, and S. J. Marrink, "Polarizable water model for the coarse-grained MARTINI force field," *PLOS Computational Biology*, vol. 6, no. 6, p. e1000810, 2010.

[199] S. J. Marrink, H. J. Risselada, S. Yefimov, D. P. Tieleman, and H. de Vries, A, "The MARTINI force field: Coarse grained model for biomolecular simulations," *The Journal of Physical Chemistry B*, vol. 111, no. 27, pp. 7812–7824, 2007.

[200] S. V. Bennun, M. I. Hoopes, C. Xing, and R. Faller, "Coarse-grained modeling of lipids," *Chemistry and Physics of Lipids*, vol. 159, no. 2, pp. 59 – 66, 2009.

[201] J. Hoshen and R. Kopelman, "Percolation and cluster distribution. I. Cluster multiple labeling technique and critical concentration algorithm," *Physical Review B*, vol. 14, no. 8, pp. 3438–3445, 1976.

[202] A. Vila Verde and R. Lipowsky, "Cooperative slowdown of water rotation near densely charged ions is intense but short-ranged," *The Journal of Physical Chemistry B*, vol. 117, no. 36, pp. 10556–10566, 2013.

[203] I. Sovadinova, E. F. Palermo, M. Urban, P. Mpiga, G. A. Caputo, and K. Kuroda, "Activity and mechanism of antimicrobial peptide-mimetic amphiphilic polymethacrylate derivatives," *Polymers*, vol. 3, no. 3, pp. 1512 – 1532, 2011.

[204] I. Ivanov, S. Vemparala, V. Pophristic, K. Kuroda, W. F. DeGrado, J. A. McCammon, and M. L. Klein, "Characterization of nonbiological antimicrobial polymers

in aqueous solution and at water-lipid interfaces from all-atom molecular dynamics," *Journal of the American Chemical Society*, vol. 128, no. 6, pp. 1778–1779, 2006.

[205] E. F. Palermo and K. Kuroda, "Chemical structure of cationic groups in amphiphilic polymethacrylates modulates the antimicrobial and hemolytic activities," *Biomacromolecules*, vol. 10, no. 6, pp. 1416–1428, 2009.

[206] E. F. Palermo, D.-K. Lee, A. Ramamoorthy, and K. Kuroda, "Role of cationic group structure in membrane binding and disruption by amphiphilic copolymers," *The Journal of Physical Chemistry B*, vol. 115, no. 2, pp. 366–375, 2011.

[207] L. M. Thoma, B. R. Boles, and K. Kuroda, "Cationic methacrylate polymers as topical antimicrobial agents against staphylococcus aureus nasal colonization," *Biomacromolecules*, vol. 15, no. 8, pp. 2933–2943, 2014.

[208] E. F. Palermo, S. Vemparala, and K. Kuroda, *Antimicrobial Polymers*: *Molecular Design as Synthetic Mimics of Host-Defense Peptides*, ch. 20, pp. 319–330.

[209] C. W. Avery, E. F. Palermo, A. McLaughlin, K. Kuroda, and Z. Chen, "Investigations of the interactions between synthetic antimicrobial polymers and substrate-supported lipid bilayers using sum frequency generation vibrational spectroscopy," *Analytical Chemistry*, vol. 83, no. 4, pp. 1342–1349, 2011.

[210] A. A. Polyansky, R. Ramaswamy, P. E. Volynsky, I. F. Sbalzarini, S. J. Marrink, and R. G. Efremov, "Antimicrobial peptides induce growth of phosphatidylglycerol domains in a model bacterial membrane," *The Journal of Physical Chemistry Letters*, vol. 1, no. 20, pp. 3108–3111, 2010.

[211] G. A. Caputo and E. London, "Cumulative effects of amino acid substitutions and hydrophobic mismatch upon the transmembrane stability and conformation of hydrophobic $\alpha$-helices," *Biochemistry*, vol. 42, no. 11, pp. 3275–3285, 2003.

[212] S. Jaud, M. Fernández-Vidal, I. Nilsson, N. M. Meindl-Beinker, N. C. Hübner, D. J. Tobias, G. von Heijne, and S. H. White, "Insertion of short transmembrane helices by the Sec61 translocon," *Proceedings of the National Academy of Sciences*, vol. 106, no. 28, pp. 11588–11593, 2009.

[213] U. Baul, K. Kuroda, and S. Vemparala, "Interaction of multiple biomimetic antimicrobial polymers with model bacterial membranes," *The Journal of Chemical Physics*, vol. 141, no. 8, p. 084902, 2014.

[214] A. Som and G. N. Tew, "Influence of lipid composition on membrane activity of antimicrobial phenylene ethynylene oligomers," *The Journal of Physical Chemistry B*, vol. 112, no. 11, pp. 3495–3502, 2008.

[215] S. Jo, J. B. Lim, J. B. Klauda, and W. Im, "CHARMM-GUI membrane builder for mixed bilayers and its application to yeast membranes," *Biophysical Journal*, vol. 97, no. 1, pp. 50 – 58, 2009.

[216] A. A. Polyansky, R. Ramaswamy, P. E. Volynsky, I. F. Sbalzarini, S. J. Marrink, and R. G. Efremov, "Antimicrobial peptides induce growth of phosphatidylglycerol domains in a model bacterial membrane," *The Journal of Physical Chemistry Letters*, vol. 1, no. 20, pp. 3108–3111, 2010.

[217] H. M. Seeger, G. Marino, A. Alessandrini, and P. Facci, "Effect of physical parameters on the main phase transition of supported lipid bilayers," *Biophysical Journal*, vol. 97, no. 4, pp. 1067–1076, 2009.

[218] S. E. Feller, Y. Zhang, R. W. Pastor, and B. R. Brooks, "Constant pressure molecular dynamics simulation: the Langevin piston method," *The Journal of Chemical Physics*, vol. 103, no. 11, pp. 4613–4621, 1995.

[219] J. N. Horn, J. D. Sengillo, D. Lin, T. D. Romo, and A. Grossfield, "Characterization of a potent antimicrobial lipopeptide via coarse-grained molecular dynamics,"

*Biochimica et Biophysica Acta (BBA) - Biomembranes*, vol. 1818, no. 2, pp. 212 – 218, 2012.

[220] J. A. Killian and G. von Heijne, "How proteins adapt to a membrane-water interface," *Trends in Biochemical Sciences*, vol. 25, no. 9, pp. 429–434, 2000.

[221] V. K. Mishra, M. N. Palgunachari, J. P. Segrest, and G. M. Anantharamaiah, "Interactions of synthetic peptide analogs of the class a amphipathic helix with lipids. evidence for the snorkel hypothesis," *The Journal of Biological Chemistry*, vol. 269, pp. 7185–7191, 1994.

[222] R. F. Epand, M. A. Schmitt, S. H. Gellman, and R. M. Epand, "Role of membrane lipids in the mechanism of bacterial species selective toxicity by two $\alpha/\beta$-antimicrobial peptides," *Biochimica et Biophysica Acta (BBA) - Biomembranes*, vol. 1758, no. 9, pp. 1343–1350, 2006.

[223] H. Khandelia, B. Loubet, A. Olzynska, P. Jurkiewicz, and M. Hof, "Pairing of cholesterol with oxidized phospholipid species in lipid bilayers," *Soft Matter*, vol. 10, pp. 639–647, 2014.

[224] E. Lindahl and O. Edholm, "Spatial and energetic-entropic decomposition of surface tension in lipid bilayers from molecular dynamics simulations," *The Journal of Chemical Physics*, vol. 113, no. 9, pp. 3882–3893, 2000.

[225] M. Patra, "Lateral pressure profiles in cholesterol-DPPC bilayers," *European Biophysics Journal*, vol. 35, no. 1, pp. 79–88, 2005.

[226] E. Terama, O. H. S. Ollila, E. Salonen, A. C. Rowat, C. Trandum, P. Westh, M. Patra, M. Karttunen, and I. Vattulainen, "Influence of ethanol on lipid membranes: from lateral pressure profiles to dynamics and partitioning," *The Journal of Physical Chemistry B*, vol. 112, no. 13, pp. 4131–4139, 2008.

[227] H. Saito, M. Iwayama, H. Takagi, M. Nishimura, T. Miyakawa, K. Kawaguchi, M. Takasu, T. Mizukami, and H. Nagao, "Molecular dynamics study of gramicidin a in lipid bilayer: structure and lateral pressure profile," *International Journal of Quantum Chemistry*, vol. 112, no. 24, pp. 3834–3839, 2012.

[228] R. M. Epand, S. Rotem, A. Mor, B. Berno, and R. F. Epand, "Bacterial membranes as predictors of antimicrobial potency," *Journal of the American Chemical Society*, vol. 130, no. 43, pp. 14346–14352, 2008.

[229] J. N. Horn, T. D. Romo, and A. Grossfield, "Simulating the mechanism of antimicrobial lipopeptides with all-atom molecular dynamics," *Biochemistry*, vol. 52, no. 33, pp. 5604–5610, 2013.

[230] W. Kopec, J. Telenius, and H. Khandelia, "Molecular dynamics simulations of the interactions of medicinal plant extracts and drugs with lipid bilayer membranes," *FEBS Journal*, vol. 280, pp. 2785–2805, 2013.

[231] K. Hu, N. W. Schmidt, R. Zhu, Y. Jiang, G. H. Lai, G. Wei, E. F. Palermo, K. Kuroda, G. C. L. Wong, and L. Yang, "A critical evaluation of random copolymer mimesis of homogeneous antimicrobial peptides," *Macromolecules*, vol. 46, no. 5, pp. 1908–1915, 2013.

[232] D. S. S. M. Uppu, M. M. Konai, U. Baul, P. Singh, T. K. Siersma, S. Samaddar, S. Vemparala, L. W. Hamoen, C. Narayana, and J. Haldar, "Isosteric substitution in cationic-amphiphilic polymers reveals an important role for hydrogen bonding in bacterial membrane interactions," *Chemical Science*, 2016.

[233] R. J. Buszek, J. S. Francisco, and J. M. Anglada, "Water effects on atmospheric reactions," *International Reviews in Physical Chemistry*, vol. 30, no. 3, pp. 335–369, 2011.

[234] D. R. Martin and D. V. Matyushov, "Hydration shells of proteins probed by depolarized light scattering and dielectric spectroscopy: orientational structure is sig-

nificant, positional structure is not," *The Journal of Chemical Physics*, vol. 141, no. 22, p. 22D501, 2014.

[235] S. Roy, S. M. Gruenbaum, and J. L. Skinner, "Theoretical vibrational sum-frequency generation spectroscopy of water near lipid and surfactant monolayer interfaces. ii. two-dimensional spectra," *The Journal of Chemical Physics*, vol. 141, no. 22, p. 22D505, 2014.

[236] X. Huang, C. J. Margulis, and B. J. Berne, "Do molecules as small as neopentane induce a hydrophobic response similar to that of large hydrophobic surfaces?," *The Journal of Physical Chemistry B*, vol. 107, no. 42, pp. 11742–11748, 2003.

[237] A. Godec and F. Merzel, "Physical origin underlying the entropy loss upon hydrophobic hydration," *Journal of the American Chemical Society*, vol. 134, no. 42, pp. 17574–17581, 2012.

[238] I. I. Vaisman, F. K. Brown, and A. Tropsha, "Distance dependence of water structure around model solutes," *The Journal of Physical Chemistry*, vol. 98, no. 21, pp. 5559–5564, 1994.

[239] D. Bandyopadhyay and N. Choudhury, "Characterizing hydrophobicity at the nanoscale: a molecular dynamics simulation study," *The Journal of Chemical Physics*, vol. 136, no. 22, p. 224505, 2012.

[240] X. Huang, R. Zhou, and B. J. Berne, "Drying and hydrophobic collapse of paraffin plates," *The Journal of Physical Chemistry B*, vol. 109, no. 8, pp. 3546–3552, 2005.

[241] M. U. Hammer, T. H. Anderson, A. Chaimovich, M. S. Shell, and J. Israelachvili, "The search for the hydrophobic force law," *Faraday Discussions*, vol. 146, pp. 299–308, 2010.

[242] P. Gallo, D. Corradini, and M. Rovere, "Ion hydration and structural properties of water in aqueous solutions at normal and supercooled conditions: a test of the

structure making and breaking concept," *Physical Chemistry Chemical Physics*, vol. 13, pp. 19814–19822, 2011.

[243] D. Paschek and R. Ludwig, "Specific ion effects on water structure and dynamics beyond the first hydration shell," *Angewandte Chemie International Edition*, vol. 50, no. 2, pp. 352–353, 2011.

[244] U. Baul, J. M. P. Kanth, R. Anishetty, and S. Vemparala, "Effect of simple solutes on the long range dipolar correlations in liquid water," *The Journal of Chemical Physics*, vol. 144, no. 10, p. 104502, 2016.

[245] P. Li, B. P. Roberts, D. K. Chakravorty, and K. M. Merz, "Rational design of particle mesh Ewald compatible Lennard-Jones parameters for +2 metal cations in explicit solvent," *Journal of Chemical Theory and Computation*, vol. 9, no. 6, pp. 2733–2748, 2013.

[246] I. S. Joung and T. E. Cheatham, "Determination of alkali and halide monovalent ion parameters for use in explicitly solvated biomolecular simulations," *The Journal of Physical Chemistry B*, vol. 112, no. 30, pp. 9020–9041, 2008.

[247] D. P. Shelton and P. Kaatz, "Librons observed in liquid acetonitrile by hyper-Rayleigh scattering," *Physical Review Letters*, vol. 84, pp. 1224–1227, 2000.

[248] N. H. March and M. P. Tosi, *Introduction to liquid state physics*. World Scientific, 2002.

[249] J. T. O'Brien, J. S. Prell, M. F. Bush, and E. R. Williams, "Sulfate ion patterns water at long distance," *Journal of the American Chemical Society*, vol. 132, no. 24, pp. 8248–8249, 2010.

[250] J. S. Prell, J. T. O'Brien, and E. R. Williams, "Structural and electric field effects of ions in aqueous nanodrops," *Journal of the American Chemical Society*, vol. 133, no. 13, pp. 4810–4818, 2011.

[251] U. Baul and S. Vemparala, "Ion hydration and associated defects in hydrogen bond network of water: observation of reorientationally slow water molecules beyond first hydration shell in aqueous solutions of $MgCl_2$," *Physical Review E*, vol. 91, p. 012114, Jan 2015.

[252] L. Yang, Y. Fan, and Y. Q. Gao, "Differences of cations and anions: their hydration, surface adsorption, and impact on water dynamics," *The Journal of Physical Chemistry B*, vol. 115, no. 43, pp. 12456–12465, 2011.

[253] S. J. Irudayam and R. H. Henchman, "Long-range hydrogen-bond structure in aqueous solutions and the vapor-water interface," *The Journal of Chemical Physics*, vol. 137, no. 3, p. 034508, 2012.

[254] D. Laage, G. Stirnemann, and J. T. Hynes, "Why water reorientation slows without iceberg formation around hydrophobic solutes," *The Journal of Physical Chemistry B*, vol. 113, no. 8, pp. 2428–2435, 2009.

[255] K. J. Tielrooij, S. T. van der Post, J. Hunger, M. Bonn, and H. J. Bakker, "Anisotropic water reorientation around ions," *The Journal of Physical Chemistry B*, vol. 115, no. 43, pp. 12638–12647, 2011.

[256] S. T. van der Post and H. J. Bakker, "The combined effect of cations and anions on the dynamics of water," *Physical Chemistry Chemical Physics*, vol. 14, no. 18, pp. 6280–6288, 2012.

[257] J. T. O'Brien and E. R. Williams, "Effects of ions on hydrogen-bonding water networks in large aqueous nanodrops," *Journal of the American Chemical Society*, vol. 134, no. 24, pp. 10228–10236, 2012.

[258] A. W. Omta, M. F. Kropman, S. Woutersen, and H. J. Bakker, "Influence of ions on the hydrogen-bond structure in liquid water," *The Journal of Chemical Physics*, vol. 119, no. 23, pp. 12457–12461, 2003.

[259] A. W. Omta, M. F. Kropman, S. Woutersen, and H. J. Bakker, "Negligible effect of ions on the hydrogen-bond structure in liquid water," *Science*, vol. 301, no. 5631, pp. 347–349, 2003.

[260] P. L. Nostro and B. W. Ninham, "Hofmeister phenomena: an update on ion specificity in biology," *Chemical Reviews*, vol. 112, no. 4, pp. 2286–2322, 2012.

[261] P. Jungwirth and D. J. Tobias, "Specific ion effects at the air/water interface," *Chemical Reviews*, vol. 106, no. 4, pp. 1259–1281, 2006.

[262] F. Hofmeister, "Zur lehre von der wirkung der salze," *Archiv for Experimentelle Pathologie und Pharmakologie*, vol. 24, pp. 247–260, 1888.

[263] D. E. Otten, P. R. Shaffer, P. L. Geissler, and R. J. Saykally, "Elucidating the mechanism of selective ion adsorption to the liquid water surface," *Proceedings of the National Academy of Sciences*, vol. 109, no. 3, pp. 701–705, 2012.

[264] S. Funkner, G. Niehues, D. A. Schmidt, M. Heyden, G. Schwaab, K. M. Callahan, D. J. Tobias, and M. Havenith, "Watching the low-frequency motions in aqueous salt solutions: the terahertz vibrational signatures of hydrated ions," *Journal of the American Chemical Society*, vol. 134, no. 2, pp. 1030–1035, 2011.

[265] C. H. Giammanco, D. B. Wong, and M. D. Fayer, "Water dynamics in divalent and monovalent concentrated salt solutions," *The Journal of Physical Chemistry B*, vol. 116, no. 46, pp. 13781–13792, 2012.

[266] Y.-S. Lin, B. M. Auer, and J. L. Skinner, "Water structure, dynamics, and vibrational spectroscopy in sodium bromide solutions," *The Journal of Chemical Physics*, vol. 131, no. 14, p. 144511, 2009.

[267] C. D. Cappa, J. D. Smith, B. M. Messer, R. C. Cohen, and R. J. Saykally, "Effects of cations on the hydrogen bond network of liquid water: New results from X-ray

absorption spectroscopy of liquid microjets," *The Journal of Physical Chemistry B*, vol. 110, no. 11, pp. 5301–5309, 2006.

[268] L. A. Näslund, D. C. Edwards, P. Wernet, U. Bergmann, H. Ogasawara, L. G. M. Pettersson, S. Myneni, and A. Nilsson, "X-ray absorption spectroscopy study of the hydrogen bond network in the bulk water of aqueous solutions," *The Journal of Physical Chemistry A*, vol. 109, no. 27, pp. 5995–6002, 2005.

[269] P. B. Petersen and R. J. Saykally, "Probing the interfacial structure of aqueous electrolytes with femtosecond second harmonic generation spectroscopy," *The Journal of Physical Chemistry B*, vol. 110, no. 29, pp. 14060–14073, 2006.

[270] J. D. Smith, R. J. Saykally, and P. L. Geissler, "The effects of dissolved halide anions on hydrogen bonding in liquid water," *Journal of the American Chemical Society*, vol. 129, no. 45, pp. 13847–13856, 2007.

[271] R. Leberman and A. K. Soper, "Effect of high salt concentrations on water structure," *Nature*, vol. 378, no. 6555, pp. 364–366, 1995.

[272] A. S. Thomas and A. H. Elcock, "Molecular dynamics simulations of hydrophobic associations in aqueous salt solutions indicate a connection between water hydrogen bonding and the hofmeister effect," *Journal of the American Chemical Society*, vol. 129, no. 48, pp. 14887–14898, 2007.

[273] H. Shinto, S. Morisada, and K. Higashitani, "Potentials of mean force for hydrophilic - hydrophobic solute pairs in water," *Journal of Chemical Engineering of Japan*, vol. 38, no. 7, pp. 465–477, 2005.

[274] Y. Ding, A. A. Hassanali, and M. Parrinello, "Anomalous water diffusion in salt solutions," *Proceedings of the National Academy of Sciences*, vol. 111, no. 9, pp. 3310–3315, 2014.

[275] J. R. Errington and P. G. Debenedetti, "Relationship between structural order and the anomalies of liquid water," *Nature*, vol. 409, no. 6818, pp. 318–321, 2001.

[276] C. Allolio, N. Salas-Illanes, Y. S. Desmukh, M. R. Hansen, and D. Sebastiani, "H-bonding competition and clustering in aqueous LiI," *The Journal of Physical Chemistry B*, vol. 117, no. 34, pp. 9939–9946, 2013.

[277] D. Laage and J. T. Hynes, "Do more strongly hydrogen-bonded water molecules reorient more slowly?," *Chemical Physics Letters*, vol. 433, no. 1-3, pp. 80–85, 2006.

[278] A. Vila Verde, P. G. Bolhuis, and R. K. Campen, "Statics and dynamics of free and hydrogen-bonded oh groups at the air/water interface," *The Journal of Physical Chemistry B*, vol. 116, no. 31, pp. 9467–9481, 2012.

[279] A. Vila Verde, M. Santer, and R. Lipowsky, "Solvent-shared pairs of densely charged ions induce intense but short-range supra-additive slowdown of water rotation," *Physical Chemistry Chemical Physics*, vol. 18, pp. 1918–1930, 2016.